UNIVERISTÀ DI PISA

SCIENZE MATEMATICHE, FISICHE E DELLA NATURA

Corso di Laurea Magistrale in Fisica

TESI DI LAUREA MAGISTRALE

22 Luglio 2016

The new drift chamber of the MEG-II experiment, in search for lepton flavor violations

Candidato:
Marco Chiappini

Relatori:
Prof. Alessandro Baldini
Prof. Fabrizio Cei

Anno Accademico 2015–2016

Abstract

The MEG experiment represents the state of the art in the search for the possible existence of the Charged Lepton Flavor Violating (CLFV) decay $\mu^+ \to e^+\gamma$. This process is completely prohibited in the framework of the Minimal Standard Model (SM) of Particle Physics and practically forbidden also in the SM extensions including neutrino masses and oscillations, but is foreseen in many other extensions, as SUperSYmmetry (SUSY) and Grand Unified Theories (GUT). The predicted Branching Ratios (BR) are not far from the current experimental sensitivities and the discovery of such a decay would be an indisputable proof of the existence of New Physics Beyond the Standard Model (BSM).

The MEG collaboration has presented the final results of the experiment, exploiting the full statistics collected during the 2009-2013 data taking period at the Paul Scherrer Institut (PSI), which provides the most intense continuous low-energy muon beam in the world, up to 10^8 μ^+/s. The analysis of the complete data set, corresponding to a total number of $\approx 7.5 \times 10^{14}$ muons stopped in the target at a stopping rate of 3×10^7 μ^+/s, has resulted in the new best upper limit on the BR($\mu^+ \to e^+\gamma$) $\leq 4.2 \times 10^{-13}$ at 90% Confidence Level (C.L.). This value is a factor of ≈ 30 better than the previously published limit set by the MEGA experiment and improves the former MEG limit: BR($\mu^+ \to e^+\gamma$) $\leq 5.7 \times 10^{-13}$ at 90% C.L. based on 2009-2011 data analysis.

Although the MEG experiment set the most stringent constraint on the $\mu^+ \to e^+\gamma$ BR to date, it has practically reached its ultimate level of sensitivity, limited by the resolutions on the measurement of the kinematic variables of the two decay products. Therefore an upgrade (MEG-II) of the current experimental apparatus has been approved and is presently under construction. It aims at reaching a sensitivity enhancement of at least one order of magnitude compared to the final MEG results, in three years of data taking, by improving the detector figures of merit and the muon stopping rate.

This thesis is structured as follows. After a brief theoretical introduction to Flavor Physics, with particular emphasis on the Lepton Flavor Violation (LFV) in the muon sector, an overview of the MEG experiment is presented. Starting from the experimental

apparatus, the final MEG data analysis is described, ending with the presentation of the current best upper limit on the $\mu^+ \to e^+\gamma$ BR. Afterwards, a detailed description of the MEG detectors upgrade is provided. It consists in improving the performance of the Liquid Xenon (LXe) calorimeter by enhancing its geometrical acceptance and granularity through new photo-detectors (SiPM) and in developing and installing a new drift chamber, as well as a new positrons time detector (Timing Counter) featuring a scintillating multi-tiles configuration. The new drift chamber is designed to overcome the limitations of the MEG e^+ tracker and guarantee the proper operation at high rates with long-term detector stability. In fact, during the MEG-II data taking the muon rate on the stopping target will be more than doubled, up to 7×10^7 Hz. This also requires the design of a new trigger and DAQ electronics, capable of handling the increased number of readout channels, while maintaining a high bandwidth.

A whole Chapter is dedicated to the main item of the thesis: the MEG-II CYLindrical Drift CHamber (CYLDCH). It features a unique volume covering the whole azimuthal angle around the muon stopping target and a total length of ≈ 2 meters which improves the geometric acceptance for signal positrons and allows the use of a new tracking procedure. This one is designed to follow the e^+ tracks up to Timing Counter and to match the information provided by the two individual detectors in order to determine the positrons kinematic variables more accurately and to minimize the background sources. The high-granularity of the new MEG-II CYLDCH is ensured by ten layers of drift cells, defined by 13056 wires arranged in a stereo configuration and filled with a low-mass (85:15) Helium:Isobutane gas mixture. This minimizes the material budget in the sensitive volume, thus reducing the total radiation length down to 1.5×10^{-3} X_0 and the Multiple Coulomb Scattering (MCS) contribution. Particular emphasis is put on the drift chamber geometry, focusing on the design and detector construction, which is a direct responsability of the MEG-II Pisa group. The CYLDCH assembly is performed in the San Piero a Grado (Pisa) facility of the Istituto Nazionale di Fisica Nucleare (INFN).

In the next Chapter a description of a new Pattern Recognition (PR) algorithm for the new MEG-II CYLDCH is reported, together with the analysis of its performance in simulated experimental conditions close to that of the MEG-II data taking. Finally, in the following Chapter, the Track Fitting toolkit which will be used during the second phase of the MEG experiment is described, together with a study of the momentum and angular resolutions expected for MEG-II.

At the end, possible further improvements and a brief review of the MEG-II experiment potentialities and expected time schedule are presented in the conclusions.

Contents

Chapter 1

Introduction

The state of the art in particle physics can be summarized as follows. On one side the Standard Model (SM) has had strong support from the Higgs boson discovery and the absence of any clear signal of New Physics (NP) at the LHC. The SM description includes three of the four fundamental interactions (electromagnetic, weak and strong) and its predictions have been confirmed by all the current experimental precision measurements which are showing the physical reality of the relation $m_i = \lambda_i v$ between the fermion masses m_i and their couplings λ_i to the Higgs boson. The vacuum expectation value of the Higgs potential v represents the electro-weak symmetry breaking energy scale and can be written in term of the Fermi constant G_F for the weak interactions as: $v = (1/(\sqrt{2}G_F))^{1/2} \approx 246$ GeV.

On the opposite side the several problems that the Standard Model (SM) is not able to solve can be divided in two categories.

Theoretical:

- gravitation is not taken into account;
- hierarchy problem of the Higgs scalar mass and its loop divergence;
- the great number of free parameters λ_i of the theory that account for the observed masses and mixings of quarks and leptons.

Observational:

- it can not explain the Dark Matter (DM) of non-baryonic nature and the barion (matter-antimatter) asymmetry in the universe;
- neutrino mixing and neutrino masses;

- cosmological problems related with inflation: there was some period of time in the early universe when energy density with a negative equation of state, typically associated with a scalar field called *inflaton*, dominated the universe.

1.1 Introduction to Flavor Physics

Flavor physics has always played a key role in the development of our knowledge of fundamental interactions leading to several remarkable predictions, from the existence of the charm quark and the presence of a third generation of quarks to stringent constraints on new interactions. In this unstable equilibrium and with the possible discovery of new particles at the LHC in the first phase of its operation at higher energies and luminosities, it is therefore of fundamental importance for the future development in the field of elementary particle physics to continue improving the theoretical and experimental tools needed to study flavor physics.

Modern particle physics research can be divided in two main branches:

- the search for the direct production of new particles and the observation of new flavor physics interactions related to physics Beyond the Standard Model (BSM). This is the so-called **Energy Frontier** of particle physics and it is compatible with current or even achievable energies of the LHC in the TeV range. It consists in directly accessing new degrees of freedom and exploiting the full luminosity of the High-Luminosity-LHC (HL-LHC) in order to increase the precision on flavor observables by at least one order of magnitude with respect to the current results. The LHC at CERN explores in particular the domain of the EW symmetry breaking, the nature of the Higgs boson and the existence of new particles, for instance the super-symmetric partners of the SM particles. Any new particle produced in direct detection experiments could provide a precise determination of the NP Lagrangian.

- A completely complementary approach exploits precision measurements of extremely rare known processes in order to find deviations from the theoretical predictions. Indirect search of NP has some advantages: allows to probe, constrain or exclude many physics models simulataneously and allows to find the new particles as *virtual particles* in t-channel processes. This is the so-called **Intensity Frontier** of particle physics in which ad hoc experiments can explore highest energy scales, up to $10^{4\div5}$ TeV, by exploiting high statistics and well controlled experimental conditions, both unattainable at the LHC by general-purpose experiments. The most important probes are: $\Delta F = 2$ transitions, where F can be the strangeness

S, the charmness C or the bottomness B; $l \to l'$ transitions ($\mu \to e$ or $\tau \to \mu$); the Electric Dipole Moments (EDM), either of the electron or neutron.

Grand Unification Theories (GUT) predict that all the interactions are unified at the M_{GUT} scale ($\approx 10^{15}$ GeV). In general, BSM theories like SUperSYmmetry (SUSY) aim at formulating an universal theory containing the SM as an effective low-energy theory.

In processes involving QCD interactions a theoretical description can be provided by means of an effective theory in which the short-distance interaction, carried by the heavy vector bosons, can be computed with perturbative techniques, while the long-distance QCD interaction is treated in a non-perturbative way. In the framework of an effective theory, the Lagrangian of the entire process can be factorized in a form made up of a series of couplings C_i and local operators $\mathcal{O}_i$ [3] [4]:

$$\mathcal{L}_{EFF} \sim G_F \sum_i C_i(\mu, M_V)\mathcal{O}_i(\mu) \tag{1.1}$$

where μ is the energy scale, M_V is the mass of the heavy mediators responsible for the short-distance interaction, G_F is the Fermi constant for the weak interactions and C_i are the so-called Wilson coefficients. The quantity μ, beyond playing the role of energy scale, assumes in this context also the meaning of a factorization scale. What is factorized is the dependence on the various physical effects arising at the different energy scales. The Wilson coefficients $C_i(\mu, M_V)$, as coupling constants, depend only on the high-energy part of the full theory, namely on energies $> \mu$. On the other hand, the low-energy dynamics, at energies $< \mu$, is encoded in the operators $\mathcal{O}_i(\mu)$.

NP processes can enter the process, for instance by modifying the Wilson coefficients of the SM or adding new operators not present in the SM. In the search for NP, good candidates could be processes involving loops since they are already suppressed in the SM, thus a deviation from the SM predictions could be a hint of New Physics Beyond the Standard Model. Better if these processes involve leptons or photons since generally their Branching Ratios (BR) are cleaner to predict.

In the quark sector, it is of interest to know what is possible to achieve with an extension of the SM with an effective description of flavor physics close to the Cabibbo-Kobayashi-Maskawa (CKM) one, based on flavor symmetries and on their possible breaking pattern only, i.e. without referring to specific models or dynamical assumptions. In the CKM-like picture of flavor physics, the origin of the flavor symmetries breaking patterns is unknown at a fundamental level, but one could take this patterns as a low energy property of a basic theory, described by an effective Lagrangian. In these effective field

theories the operators which describe the flavor breaking can be written with specific combinations of the CKM matrix V_{CKM} elements ($\xi_{ij} = V_{tj}V_{ti}^*$) and are the same that operate in the SM. A possible example goes under the name of Minimal Flavor Violation (MFV) [8]. By using this model, it is possible to translate the experimental constraints into allowed ranges for the Wilson coefficients, parametrized as [2]:

$$C_i(\Lambda) = \frac{F_i L_i}{\Lambda^2} \tag{1.2}$$

where Λ is the NP scale, F_i is a function of the NP flavor couplings and L_i is a loop factor. Figure 1.1 shows the lower bounds on NP scale at 95% probability, assuming strongly coupled new physics ($F_i L_i \sim 1$), with no flavor suppression derived from mixing and CP violation, from $\Delta F = 2$ processes in neutral K, D, B_d, B_s meson systems. These bounds can be translated into less stringent constraints on the NP scale models featuring weak interactions and/or some kind of flavor suppression.

In the quark sector, given the current moderate precision achieved due to QCD parameters approximations, new flavor physics phenomena may be related to NP in the TeV range. In fact the coupling to new physics could be lower than 1 or flavor suppression due to mixing and/or CP violation could happen. The current overall status of flavor measurements still shows consistency with the CKM picture of flavor physics, allowing BSM contributions with an uncertainty at $20 \div 30\%$ level [2]. The present level of precision has been attained in the last 15 years of experiments, but is not yet comparable with the standards in other areas of particle physics (for instance QED) and clearly motivates one keeps improving on it. The current results are nevertheless already significant enough to require that some mechanism be active to keep any flavor violation under control at the TeV scale. In the next years a great improvement in Lattice-QCD (L-QCD) simulations are expected, leading to a significant reduction of the QCD uncertainties down to $1 \div 0.1\%$ [2].

1.1.1 Lepton Flavor Violation (LFV)

In the Standard Model hadronic flavor transitions arise from the misalignment between the kinetic and the Yukawa terms in the Lagrangian. The unitary matrices for Left-Handed (LH) up-quarks and Right-Handed (RH) down-quarks are generally different inducing the flavor mixing in the charged weak interactions. These are described by the Cabibbo-Kobayashi-Maskawa unitary matrix (V_{CKM}). Its elements represent how likely a quark from a specific family is expected to turn into a different quark of a possibly different family.

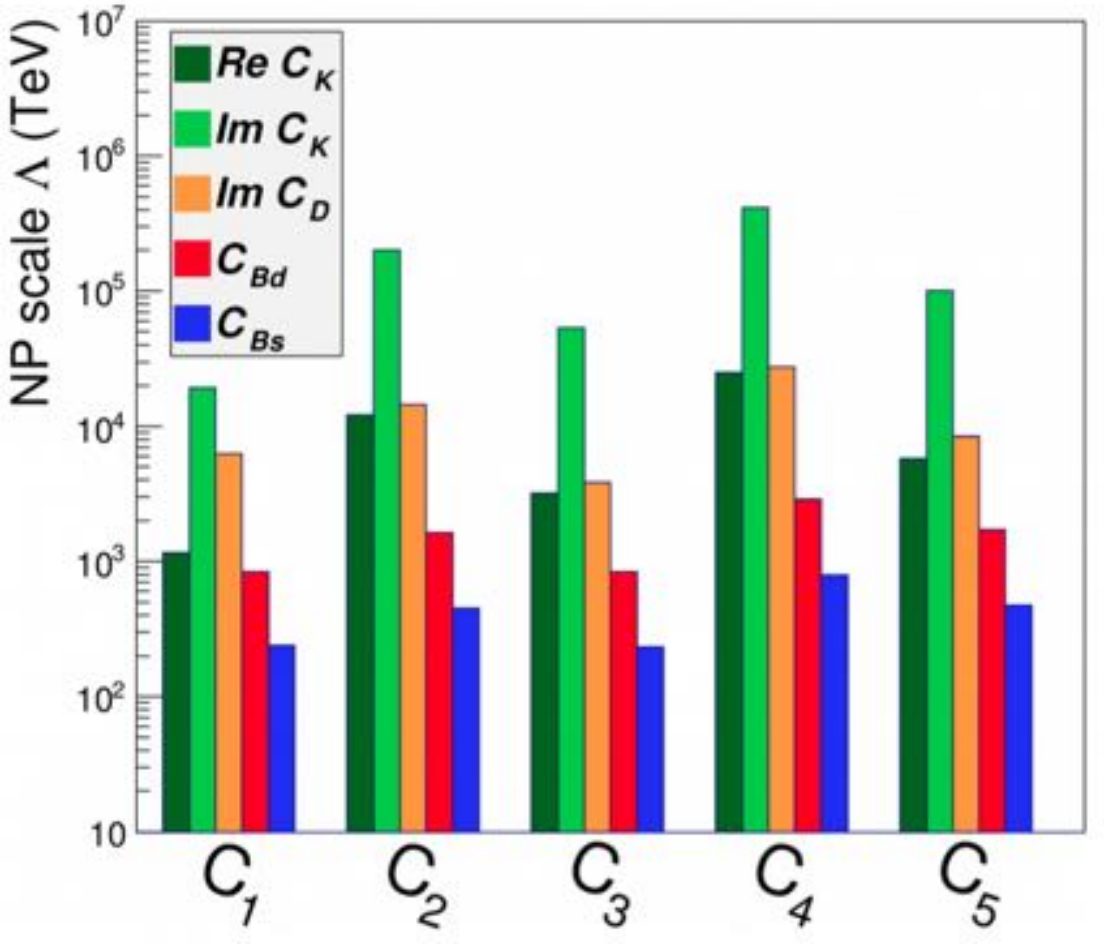

Figure 1.1: Lower bounds on New Physics (NP) scale at 95% probability, assuming strongly coupled new physics, from $\Delta F = 2$ ($F = S, C, B$) processes in neutral K, D, B_d, B_s meson systems.

In the lepton sector, since SM neutrinos are massless, the mass matrix is fully diagonalized by an unitary transformation for the LH lepton doublet and the RH lepton singlet. Therefore the lepton flavor is defined in the mass diagonalized basis: L_e, L_μ, L_τ and the lepton flavor is conserved for each generation. As a consequence it is possible to rotate indipendently the fields in the kinetic and in the Yukawa part of the Lagrangian without having to introduce a CKM-like matrix. In the pure SM framework the LFV processes are forbidden ($\mathrm{BR}_{LFV} = 0$) at all the orders of the theory and transitions between charged and neutral leptons preserve flavor, as is observed in nature.

However flavor transitions between neutral leptons have been observed in the phenomenon of neutrino oscillations by several experiments. Lepton flavor oscillations on

neutrino side lead to the fact that neutrinos have mass $m_i \neq 0$ and thus to a non-diagonal unitary mixing matrix U_{PMNS} (Pontecorvo-Maki-Nakagawa-Sakata) between mass eigenstates and flavor eigenstates:

$$\nu_l = \sum_{i=1}^{3} (U_{PMNS})_{li}\, \nu_i \tag{1.3}$$

where $l = e, \mu, \tau$ are the flavor eigenstates and $i = 1, 2, 3$ are the mass eigenstates.

Neutrino oscillations imply the non conservation of the lepton flavor number. It is natural to assume that lepton flavor is not conserved also in transitions involving charged leptons, even though the SM contribution due to neutrino mixing is negligible.

1.2 Charged Lepton Flavor Violation (CLFV)

Charged Lepton Flavor Violaiton (CLFV) searches are of particular interest because of the possibility to carry out clean measurements which are at the same time free of theoretical background. In the case of observation they could give a clear piece of evidence of physics BSM, but even in the case of non observation they establish strong limits for the development of new theories. On the other hand such searches are difficult to be carried out at general-purpose machines and detectors, thus dedicated detectors and even dedicated accelerators or storage rings have to be exploited or designed for the future.

The search for the CLFV is expected to make a significant step forward in the next few years. An international program of CLFV explorations exists, with experiments recently completed, currently running and soon to be constructed in the United States, Japan and Europe. These include:

- the completion of the MEG (Mu-E-Gamma) experiment [17] [16] [52] [51] (see Chapter 2) at Paul Scherrer Institut (PSI) and its upgrade MEG-II [1] (see Chapter 3 and the following Chapters);

- the proposed Mu3e [37] [38] search at PSI. The current experimental limit dates back to the SINDRUM experiment at PSI in 1988 [33] and is $\mathrm{BR}(\mu^+ \to e^+e^-e^+) \leq 1 \times 10^{-12}$ at 90% Confidence Level (C.L.). The expected improvements could allow to reach the 10^{-16} level;

- new searches of muon to electron conversion (Mu2e [39] [40] at Fermilab, COMET [41] [42] [43] [44] [45] at J-PARC). The measurement of the neutrinoless μ^- to e^-

conversion rate in presence of a nucleus is defined relatively to the ordinary capture of the muon on the nucleus as follows:

$$R_{\mu e} = \frac{R(\mu^- + A(Z,N) \to e^- + A(Z,N))}{R(\mu^- + A(Z,N) \to \nu_\mu + A(Z-1,N))} \tag{1.4}$$

The best limit on $R_{\mu e}$ is 7×10^{-13} (on gold) as obtained by the SINDRUM II experiment at PSI in 2006 [34]. The expected improvements could allow to reach the 10^{-16} level in the BR($\mu^- N \to e^- N$);

- studies of τ decay at SuperKEKB [49] (see also Section 1.2.2). The present best experimental limits on LFV τ decays come from measurements at the B-factories. The results presented in Figure 1.3 come from a sample of $\approx 5 \times 10^8$ (BaBar) and $\approx 9 \times 10^8$ (Belle) $\tau\bar{\tau}$ pairs and summarize the B-factories searches for LFV τ lepton decay modes. Future improvements could allow to increase the number of $\tau\bar{\tau}$ events up to $\approx 5 \times 10^{10}$ leading to reach the 10^{-9} level with the Belle II experiment, capable of probing an entire range of decays;

- constraints on the existence of $\Delta L_i = \pm 2$ processes (L lepton number) could be set by muonium-antimuonium conversion [46] [47] [48].

1.2.1 LFV at High Energy Colliders

In principle, CLFV signatures could be observed at the LHC if supersymmetric particles were discovered. They naturally generate LFV couplings in slepton mass matrix. Consequently if sleptons are light enough to be produced in pairs, different lepton flavors could show up in decay chains such as: $l^+l^- \to l^+l^-\chi^0\chi^0$.

New particles could also be reconstructed from resonance peaks if they have lepton-violating tree couplings ($H \to ll'$ or $Z \to ll'$). Due to the existing bounds on flavor changing processes, these LFV decays are small and difficult to detect above the large background from WW-production with subsequent leptonic decays. However with high enough luminosities the LHC can go beyond the LEP bounds on LFV Z decays. In addition, at possible future e^+e^- circular colliders ultimate limits could be set thanks to planned $\approx 10^{13} Z$ bosons decays.

1.2.2 LFV in τ Sector

Searches for lepton-flavor violating τ decays are among the probes of NP at present and future high luminosity flavor factories. The large τ mass implies many possible final

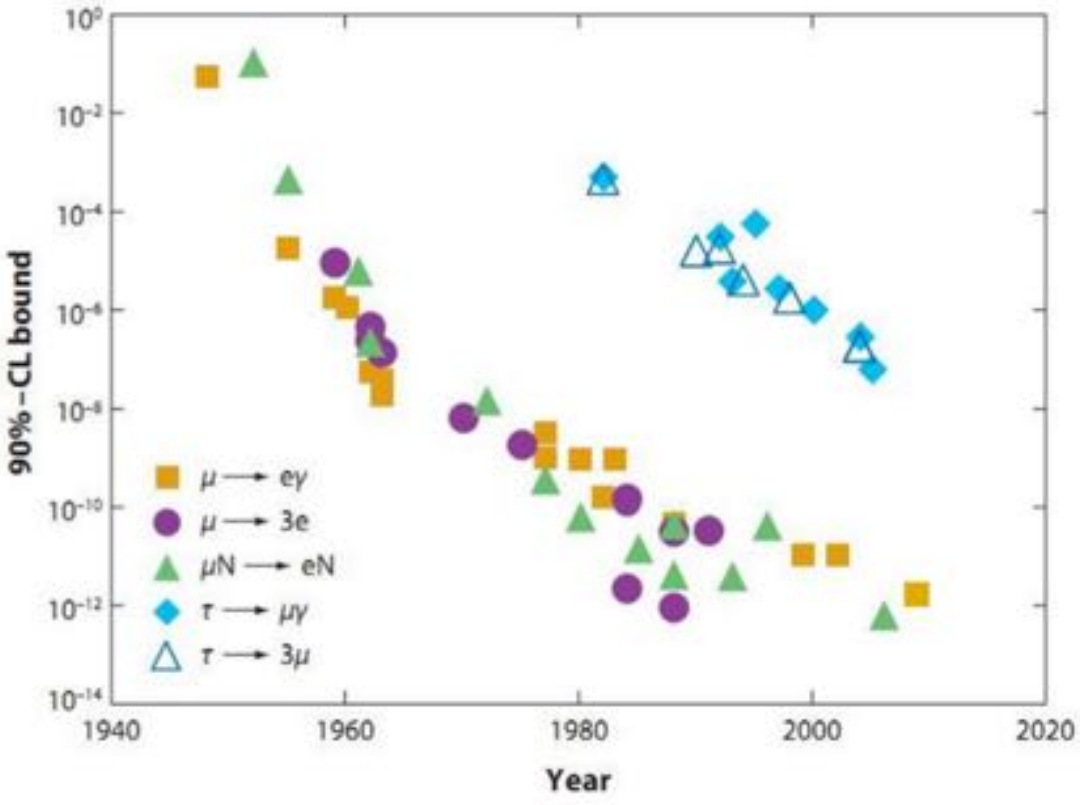

Figure 1.2: Summary of the experimental searches for CLFV processes as a function of the years.

states besides the natural $\tau \to e\gamma$, $\tau \to \mu\gamma$ or $\tau \to 3e$, $\tau \to 3\mu$. The BR for LFV τ decays is generally predicted to be larger compared to those of the muon, by a power of m_τ/m_μ. In fact, according to SUSY, the BR for the $\mu \to e\gamma$ decay process can be written in terms of the mixing angle ($\theta_{\tilde{e}\tilde{\mu}}$) between the first two sleptons generations and results proportional to [6] [7]:

$$\mathrm{BR}(\mu \to e\gamma) \sim \frac{\alpha^3 \pi \theta^2_{\tilde{e}\tilde{\mu}}}{G_F^2 \tilde{m}^4} \tan^2(\beta) \quad (\tilde{m} \text{ typical SUSY mass}) \tag{1.5}$$

where $\tan(\beta)$ is defined as the ratio of the two vacuum expectation values of the two neutral Higgses predicted by the Minimal Supersymmetric Standard Model (MSSM). The formula can be easily generalized to the process $\tau \to \mu\gamma$ and the ratio:

$$\frac{\mathrm{BR}(\tau \to \mu\gamma)}{\mathrm{BR}(\mu \to e\gamma)} \sim \frac{\theta^2_{\tilde{\mu}\tilde{\tau}}}{\theta^2_{\tilde{e}\tilde{\mu}}} \tag{1.6}$$

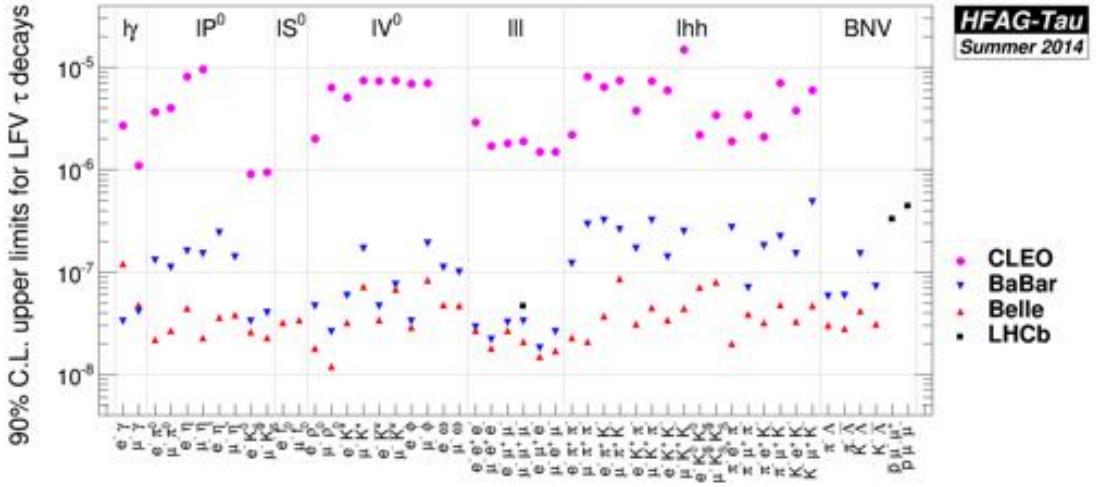

Figure 1.3: Summary of the B-factories searches for LFV τ lepton decay modes.

ranges from 500 to 10^4 depending on the model considered. It can be evaluated by modeling the slepton mixing matrix in analogy to the quark and neutrino sector mixing matrix: a CKM-like parameterization with $\theta_{\tilde{e}\tilde{\mu}} \sim V_{dt}V_{st}$, $\theta_{\tilde{\mu}\tilde{\tau}} \sim V_{bt}V_{st}$; a PMNS-like parameterization with $\theta_{\tilde{e}\tilde{\mu}} \sim U_{e3}U_{\mu 3}$, $\theta_{\tilde{\mu}\tilde{\tau}} \sim U_{\mu 3}U_{\tau 3}$. Despite the larger BRs the number of produced τ's and the experimental backgrounds spoil this advantage. In fact the experimental sensitivity in the muon sector results several orders of magnitude higher ($\approx 10^5$), more than compensating the difference in the BRs. At the end the experimental reach in both τ and μ LFV decays probe comparable regions of the parameter space of new theories.

LFV τ decays are searched for by tagging one of the τ's in the $e^+e^- \to \tau^+\tau^-$ event, dividing it in two hemispheres and considering each one as a possible candidate for the LFV decay under consideration. Despite all cuts and kinematical constraints, generally an irreducible background remains, for instance the initial state radiation $\tau^+\tau^-\gamma$ in the case of $\tau \to \mu\gamma$ searches. Future improvements could come from running at lower e^+e^- Center-of-Mass (CM) energy since the initial state radiation photon spectrum is suppressed for the typical gamma energies of the LFV processes.

1.2.3 Muon Sector

Muon physics has played a fundamental role in the costruction of the Standard Model (SM) of particle physics, especially in establishing the $V - A$ nature of the weak interactions and the validity of the QED. Nowadays muon physics has not yet exhausted its

potential.

The muon was discovered in 1937 by Neddermeier and Anderson [29] in a cloud chamber exposed to cosmic rays. Initially this particle was wrongly interpreted as the short-range strong force mediator predicted by Yukawa. Ten years later Conversi, Pancini and Piccioni [30] observed that muons behave like heavy electrons passing through matter being subject to the EM interaction but not the strong one. The first limit and the start to search for the LFV decays of this unstable particle was set by Pontecorvo and Hincks in 1948 [31] using cosmics: $\mathrm{BR}(\mu \to e\gamma) \leq 10\%$.

The muon mass and lifetime are $m_\mu = 105.6583715(35)$ MeV and $\tau_\mu = 2.1969811(22) \times 10^{-6}$ s respectively [55]. Precise measurements on the muon decay provide the best estimate for the Fermi constant $G_F = 1.16637(1) \times 10^{-5}$ GeV^{-2}. The SM muon decay modes are: $\mu^+ \to e^+\nu_e\bar{\nu}_\mu$ (Michel decay, $\approx 100\%$), $\mu^+ \to e^+\nu_e\bar{\nu}_\mu\gamma$ (Radiative Muon Decay (RMD), $(1.4 \pm 0.4)\%$ for $E_\gamma > 10$ MeV), $\mu^+ \to e^+\nu_e\bar{\nu}_\mu e^-e^+$ ($(3.4 \pm 0.4) \times 10^{-5}$).

CLFV explorations complement the direct searches of new particles and, among them, muon measurements in particular have the best sensitivity over the largest range of parameters space of many models of NP. In the muon sector over the years several experiments have taken place (Table 1.1), characterized by the use of muon beams of increasing intensity and improving detector resolutions, leading to continuosly increased sensitivities. Figure 1.4 shows, over the years, the CLFV searches improvements in the muon sector before the MEG experiment.

The discovery of the LFV in muon decays $\mu^+ \to e^+\gamma$, $\mu^+ \to e^+e^-e^+$ and $\mu^-N \to e^-N$ conversion in nuclei, would be an indisputable proof of the existence of new dynamics BSM. The predicted BRs are not far from the current experimental upper limits.

Process	$\mu^+ \to e^+\gamma$	$\mu^+ \to e^+e^-e^+$	$\mu^-N \to e^-N$
Background	accidental bkg	RMD with internal conversion accidental bkg	Decay-In-Orbit (DIO) beam-related π and $\bar{p}$ cosmic rays
Beam	Continuous	Continuos	Pulsed
Best limit	4.2×10^{-13} MEG (2016) [52] [51]	1×10^{-12} SINDRUM (1988) [33]	7×10^{-13} SINDRUM II (2006) [34]
Planned experiments	MEG-II at PSI [1]	Mu3e at PSI [37] [38]	Mu2e at Fermilab [39] [40], COMET at J-PARK [41] [42] [43] [44] [45]
Planned sensitivity	$\sim 10^{-14}$	$\sim 10^{-16}$	$\sim 10^{-16}$

Table 1.1: Comparison of muon CLFV experiments.

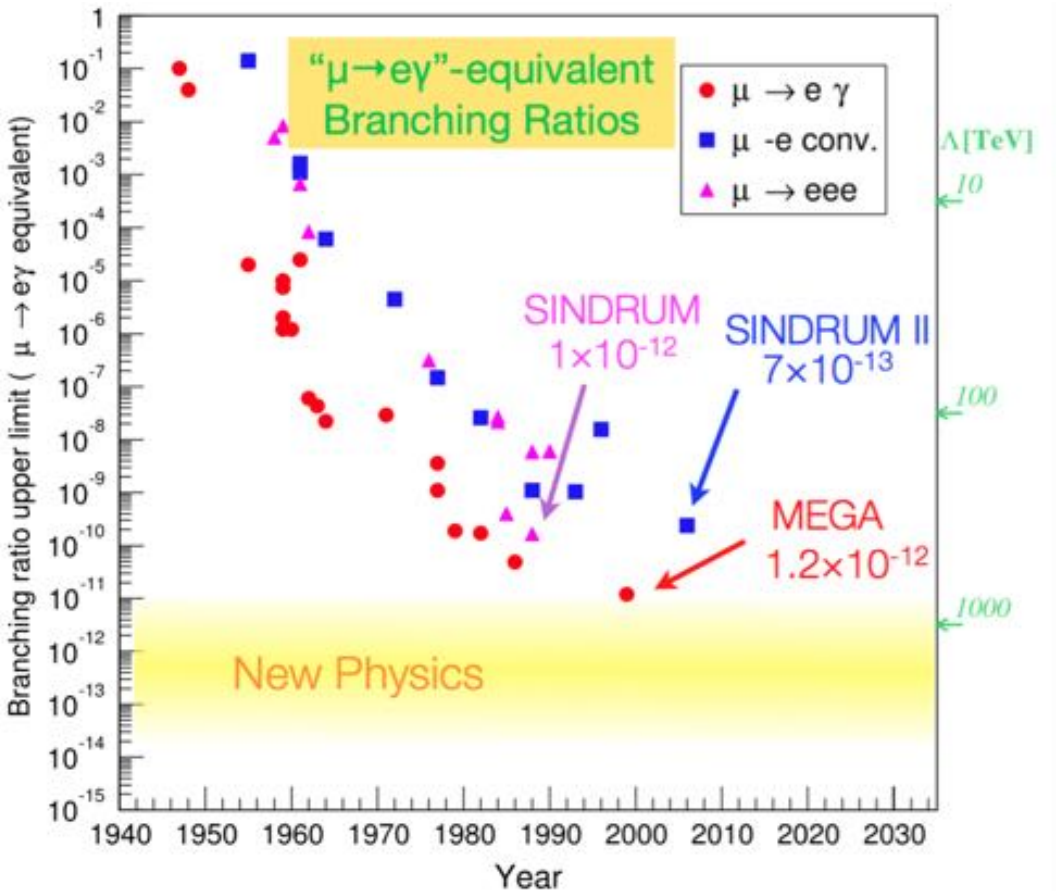

Figure 1.4: CLFV searches improvements in the muon sector before the MEG experiment as a function of the years.

Independently of the specific theory and model, CLFV transitions are related to new lepton-lepton couplings and effective operators. Some example processes are shown in Figure 1.5.

These processes can be divided in dipole amplitudes (the first three Feynman diagrams from the left) and four-fermion amplitudes (the last two diagrams). One can try to parametrize the interplay between the two diagrams by means of two parameters, Λ and k, in the following effective Lagrangian for leptons interactions [5] [6] [7] [2]:

$$\mathcal{L}_{CLFV} = \frac{m_\mu}{(k+1)\Lambda^2}\bar{\mu}_R\sigma_{\mu\nu}e_L F^{\mu\nu} + \frac{k}{(k+1)\Lambda^2}\bar{\mu}_L\gamma_\mu e_L(\bar{e}\gamma^\mu e) + h.c. \tag{1.7}$$

where L and R indicate the chirality of the different Standard Model (SM) fermion fields, $F^{\mu\nu}$ is the photon field strength and m_μ is the muon mass. Λ is the mass scale of

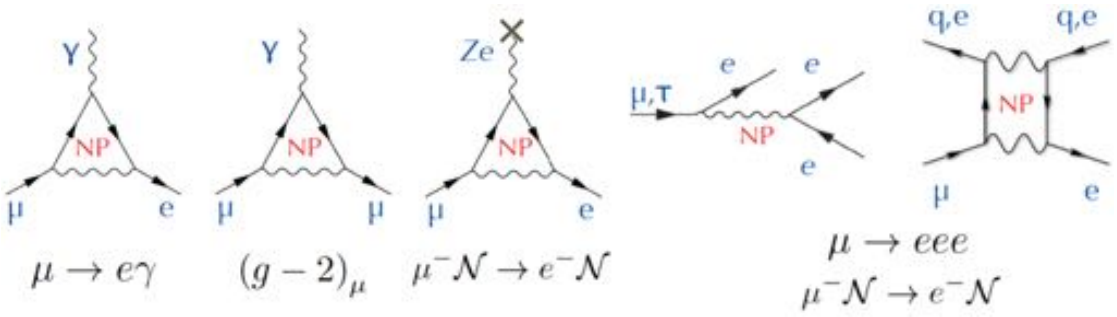

Figure 1.5: Schematic representation of vertices and interactions of some of CLFV processes in which New Physics (NP) contribution could be measurable.

the new physics and k is a dimentionless parameter that determines whether the dipole-like or the four-fermion interaction is dominant. It should be noted, as in [5], that in Equation 1.7 there may be several other terms which could interfere constructively or destructively. It has become commonplace in discussions to use Equation 1.7 to plot Λ vs. k. For $k << 1$ ($k >> 1$) the dipole-type (four-fermion) interaction dominates CLFV processes. Figure 1.6 summarizes the power of different searches to explore this parameters space.

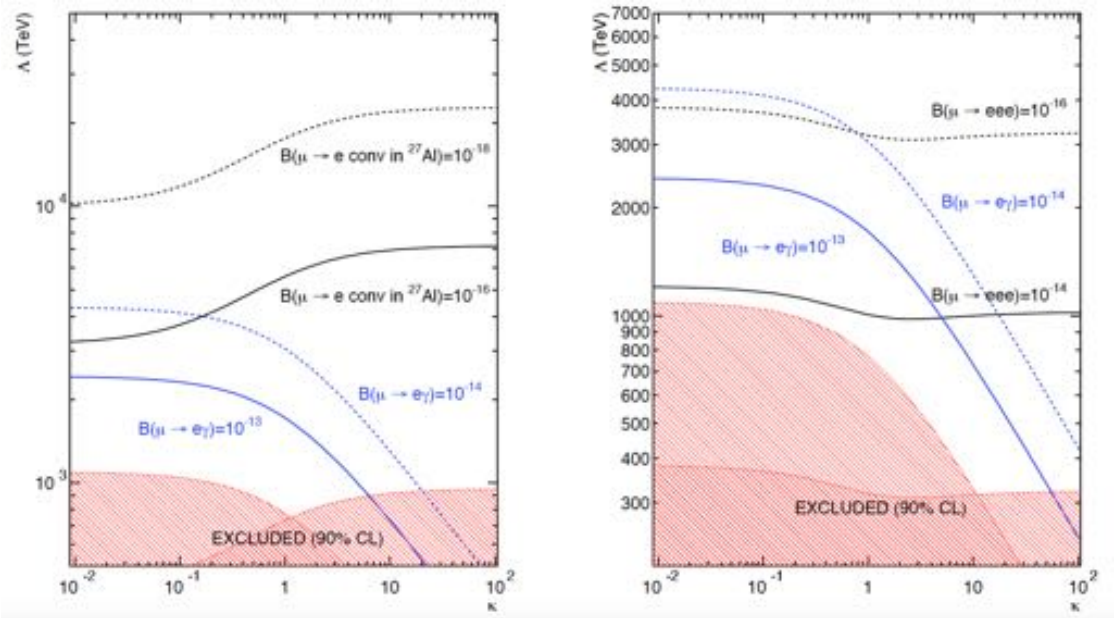

Figure 1.6: Sensitivity of the LFV processes $\mu \to e\gamma$, $\mu \to e$ and $\mu \to 3e$ to the scale of New Physics (NP) Λ as a function of the proportion of dipole versus four-fermion amplitude, parameterized by k.

As one can see a scale $\Lambda < 10^3$ TeV is already excluded by present limits, posing serious contraints on SM extensions, SUSY especially. The $\mu \to e\gamma$ decay is sensitive only in the dipole-dominating region, while the $\mu \to e$ conversion and the $\mu \to 3e$ decay receive contributions also from the four-fermion interactions. Nonetheless Λ is only an effective scale and is not immediately comparable to the mass M of new particles accessible by direct search. This dependence can be parametrized for the "loop" and "contact" interaction respectively as [2] [7]:

$$\frac{1}{\Lambda^2} \sim \frac{g_{BSM}^2 \alpha^2}{M^2} \; ; \quad \frac{1}{\Lambda^2} \sim \frac{g_{BSM}^2}{M^2} \tag{1.8}$$

where α is the fine-structure constant and g_{BSM} is the new Beyond the Standard Model (BSM) coupling. In both cases the real mass M tested by CLFV processes is significantly above that accessible at the LHC.

As apparent from Figure 1.6, the best upper limits would be obtained from the $\mu^+ \to e^+e^-e^+$ decay process or the $\mu^- N \to e^- N$ conversion in nuclei of heavy elements (BR $\approx 10^{-16}$, against BR $\approx 10^{-14}$ for $\mu \to e\gamma$). However the sensitivity to NP of these two processes is comparable to that of the $\mu^+ \to e^+\gamma$ decay because of the presence of a further electromagnetic vertex in the corresponding Feynman diagrams, as one can see from Figure 1.7.

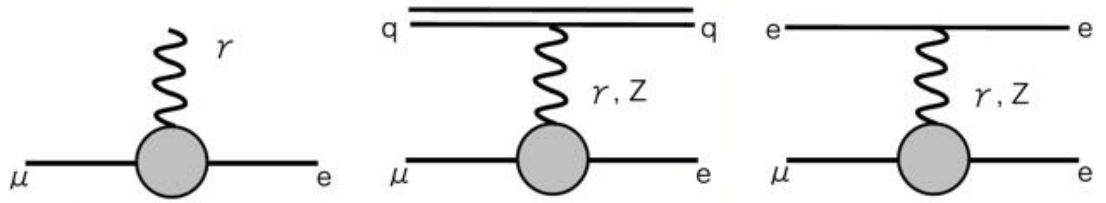

Figure 1.7: Feynman diagrams for the three principal processes in the CLFV exploration.

This leads to:

$$\frac{\mathrm{BR}(\mu^+ \to e^+e^-e^+)}{\mathrm{BR}(\mu^+ \to e^+\gamma)} \approx \frac{\mathrm{BR}(\mu^- N \to e^- N)}{\mathrm{BR}(\mu^+ \to e^+\gamma)} \sim \alpha \tag{1.9}$$

$\mu \to e\gamma$ History

In the Minimal Standard Model (MSM) extension including the neutrino oscillations, the $\mu \to e\gamma$ decay process becomes allowed with a BR $\neq 0$. If one looks at the Feynman diagrams of this process (Figure 1.8), it is clear that its amplitude is very extremely tiny

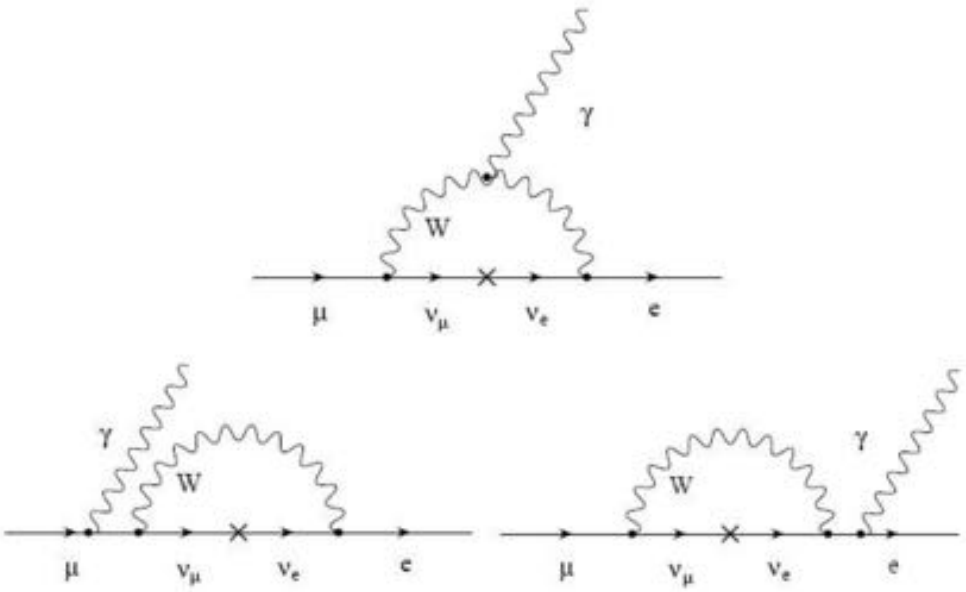

Figure 1.8: Feynman diagrams of the $\mu \to e\gamma$ decay process in the MSM extension including the neutrino oscillations. Its amplitude is very extremely tiny since the muon neutrino has to oscillate into an electron neutrino within a W vector boson lifetime.

since the muon neutrino has to oscillate into an electron neutrino within a W vector boson lifetime [5] [6] [7]:

$$\Gamma(\mu \to e\gamma) = \frac{\alpha G_F^2 m_\mu^5}{2048\pi^4} \left(\frac{\Delta m_{12}^2}{m_W^2}\right)^2 \sin^2\theta_{12} \cos^2\theta_{12} \tag{1.10}$$

where the identity $\sum_{i=1}^{3}(|V_{ei}^2 V_{\mu i}^2|^2) = \sin^2\theta_{12}\cos^2\theta_{12}$ is used. G_F is the Fermi constant for the weak interactions, m_μ is the muon mass and m_W is the mass of the W vector boson. In the two-states approximation θ_{12} is the mixing angle and $\Delta m_{12}^2 = m_1^2 - m_2^2$ is the difference between the two mass eigenstates. Considering the muon total decay width:

$$\Gamma_{TOT} = \frac{G_F^2 m_\mu^5}{192\pi^3} \quad \Rightarrow \quad \mathrm{BR}(\mu \to e\gamma) = 5 \times 10^{-48} (\Delta m_{12}^2[\mathrm{eV}^2])^2 \sin^2\theta_{12}\cos^2\theta_{12} \tag{1.11}$$

Given the measurement of Δm_{12}^2 and θ_{12} from KamLAND [32]:

$$\Delta m^2_{12} = 7.5 \times 10^{-5}\text{eV}^2; \quad \tan^2\theta_{12} = 0.44 \quad \Rightarrow \quad \text{BR}(\mu \to e\gamma) < 10^{-50} \tag{1.12}$$

which cannot be experimentally observed.

BSM theories predict additional particles and interactions that can enhance such process up to a measurable level. In particular SUSY-GUT extensions of the SM allow the $\mu^+ \to e^+\gamma$ decay to proceed with rates explorable by the MEG experiment (BR $\approx 10^{-14}$) [5]. SUSY main contributions in the LFV BRs are the non diagonal terms in the sleptons flavor matrix. A mismatch in the flavor basis between the leptons and sleptons mass matrix allows tree-level transitions between different leptons-sleptons generations (Figure 1.9).

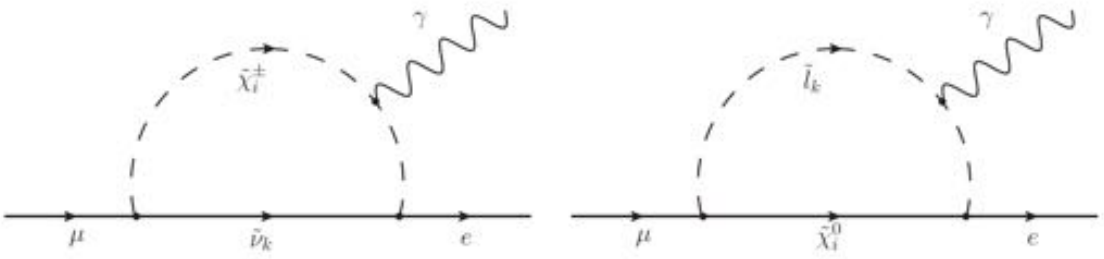

Figure 1.9: Feynman diagrams of the $\mu \to e\gamma$ decay process in the SUSY-GUT picture. On the left and on the right respectively, the slepton-chargino and slepton-neutralino contributions to the BR($\mu^+ \to e^+\gamma$).

Figure 1.10 shows the history of the searches for the $\mu \to e\gamma$ decay process with the improvement in sensitivity before the two last results from the MEG experiment. With the analysis of 2009-2011 data [17], the upper limit on the $\mu \to e\gamma$ decay process set by the MEG experiment was BR $\leq 5.7 \times 10^{-13}$ at 90% Confidence Level (C.L.). The final MEG results [52] [51] are presented in Section 2.3.

Year	90% CL on $\mathcal{B}(\mu \to e\gamma)$	Collaboration/Lab	Reference
1947	1.0×10^{-1}	Chalk River	Hincks and Pontecorvo [1948]
1948	.04	Washington University	Sard and Althaus [1948]
1955	2.0×10^{-5}	Nevis	Steinberger and Lokanathan [1955]
1959	7.5×10^{-6}	Liverpool	O'Keefe *et al.* [1959]
1959	2.0×10^{-6}	Nevis	Berley *et al.* [1959]
1959	1.0×10^{-5}	Rochester	Davis *et al.* [1959]
1959	1.2×10^{-6}	CERN	Ashkin *et al.* [1959]
1960	1.2×10^{-6}	LBL	Frankel *et al.* [1960]
1961	2.5×10^{-5}	Carnegie	Crittenden *et al.* [1961]
1962	1.9×10^{-7}	LBL	Frankel *et al.* [1962]
1962	6.0×10^{-8}	Nevis	Bartlett *et al.* [1962]
1963	4.3×10^{-8}	LBL	Frankel *et al.* [1963]
1964	2.2×10^{-8}	Chicago	Parker *et al.* [1964]
1971	2.9×10^{-8}	Dubna	Korenchenko *et al.* [1971]
1977	3.6×10^{-9}	TRIUMF	Depommier *et al.* [1977]
1977	1.1×10^{-9}	SIN	Povel *et al.* [1977]
1979	1.9×10^{-10}	LAMPF	Bowman *et al.* [1979]
1982	1.7×10^{-10}	LAMPF	Kinnison *et al.* [1982]
1986	4.9×10^{-11}	LAMPF/Crystal Box	Bolton *et al.* [1986, 1988]
1999	1.2×10^{-11}	LAMPF/MEGA	Brooks *et al.* [1999]
2010	2.8×10^{-11}	PSI/MEG	Adam *et al.* [2010]
2011	2.4×10^{-12}	PSI/MEG	Adam *et al.* [2011]

Figure 1.10: Experimental upper limit on $\mu \to e\gamma$ as a function of time before the two last results of the MEG experiment.

Chapter 2

The MEG Experiment

2.1 MEG Physics

2.1.1 $\mu \to e\gamma$ Decay Characterization

The phenomenology of the $\mu^+ \to e^+\gamma$ decay process is very simple and a representative picture of the signal event is shown in Figure 2.1. A positive muon[1] beam is stopped on a target and the decay products are observed in the laboratory system. Positive muons decay at rest thus the Center-of-Mass (CM) reference system coincides with the laboratory. The process is a two-body decay, then, apart from second-order corrections due to the fact that $m_e \neq 0$, the outgoing particles have $E = m_\mu/2$ and are emitted simultaneosly in a back-to-back direction. The signal consists in a photon and a positron of equal momentum emitted in collinear and temporal coincidence.

The four key observables that characterize the $\mu^+ \to e^+\gamma$ decay process are:

- the energy of the positron and the photon, E_e and E_γ respectively;
- the relative angle between the emission directions of the outgoing positron and photon, $\theta_{e\gamma}$;
- the relative time between the final state positron and photon, $t_{e\gamma}$.

2.1.2 Backgrounds

The sensitivity to the $\mu^+ \to e^+\gamma$ decay is given by the capability of the experimental apparatus to distinguish the two monochromatic, time coincident, back-to-back final state

[1] Because of the large nuclear capture cross section in matter for negative muons.

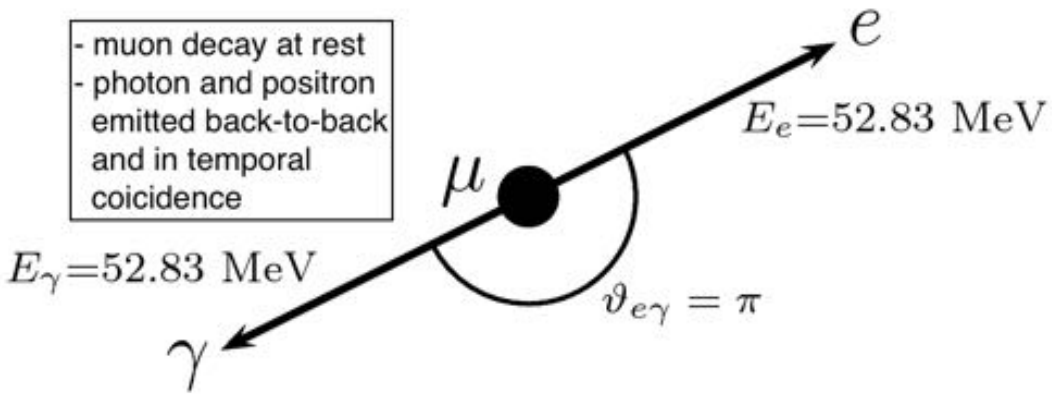

Figure 2.1: The kinematics of the $\mu^+ \to e^+\gamma$ decay process.

particles from the background (background rejection capability). In order to identity a muon decay event as a signal candidate, the MEG detectors have to accurately measure the four key quantities involved in the process. Two categories of background events can mimic the signal signature, thus a good angular, timing and energy resolutions are required.

Physics Background

The physics background is due to the Radiative Muon Decay (RMD) $\mu^+ \to e^+\nu_e\bar{\nu}_\mu\gamma$ where the photon and the positron are emitted back-to-back and small energy is carried out by the two neutrinos. This process is characterized by four time-coincident particles and it can mimic the two-body decay at the very end of the kinematic edge. The RMD rate R_{RMD} is proportional to the product $R_\mu \times \mathrm{BR}(\mu^+ \to e^+\nu_e\bar{\nu}_\mu\gamma)$ where R_μ is the muon beam intensity. The differential RMD width is usually expressed in terms of the reduced positron and photon energy and relative emission angle, respectively $x = 2E_e/m_\mu$, $y = 2E_\gamma/m_\mu$ and $z = \pi - \theta_{e\gamma}$. In the signal region ($x = 1$, $y = 1$ and $z = 0$) the width vanishes, but finite experimental resolutions introduce background events that limit the achievable sensitivity [5]. The probability of a background event to fall in the signal region is easily computed given the experimental resolutions δx, δy and δz and integrating the differential RMD width in the signal region smeared by the detectors resolutions. Resolutions of $\approx 1\%$ on both photon and positron energy are required to

keep the RMD rate at $\approx 10^{-15}$ level. Figure 2.2 shows the BR of the physics background from RMD as a function of the reduced e^+ (δx) and γ (δy) energy resolutions and the differential BR from RMD as a function of the reduced photon energy y.

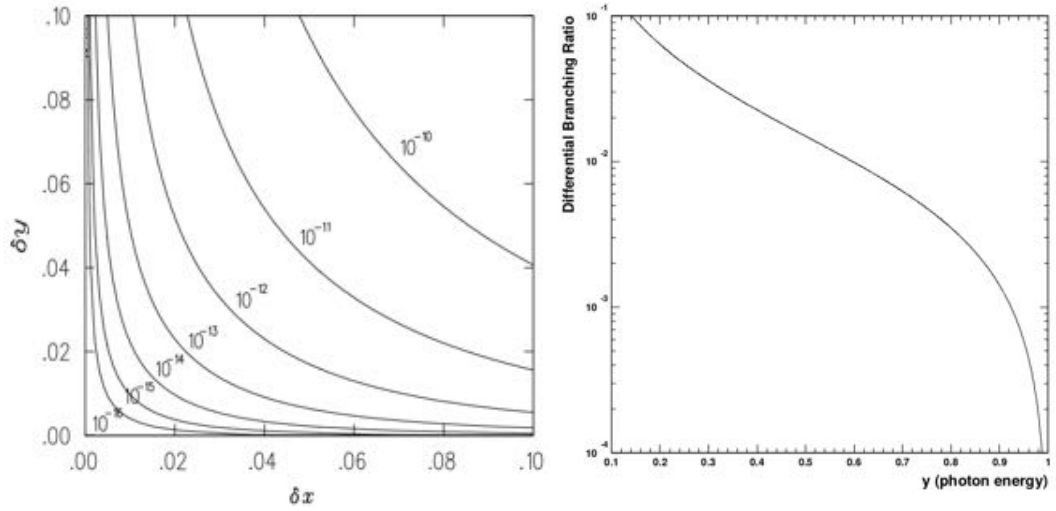

Figure 2.2: On the left: the BR from RMD as a function of the reduced e^+ (δx) and γ (δy) energy resolutions. On the right: the differential BR from RMD as a function of the reduced photon energy y.

Accidental Background

An accidental background event happens when a photon and a positron produced in two distinct processes are in accidental temporal coincidence and spatial collinearity. On one side, the pure muon beam exploited by the MEG experiment ensures that the unique source of positron is the muon decay (Michel positrons). On the other side, many sources of high energy photons pollute the experimental environment: RMD, positrons interacting in the detector materials (e^+ Annihilation-In-Flight (AIF), bremsstrahlung), neutrons interactions in the surrounding materials. All the contributions are proportional to the beam muon flux on the stopping target R_μ. The effective rate of accidental background events R_{acc} falling into the signal region is obtained using the reduced variables for the positron ($x = 2E_e/m_\mu$) and the photon ($y = 2E_\gamma/m_\mu$) energy and integrating over the corresponding energy spectra in the intervals $[1-\delta x, 1]$, $[1-\delta y, 1]$ [5]:

$$R_{acc} = R_\mu \times B_{acc} \sim R_\mu^2 \delta x (\delta y)^2 \delta t_{e\gamma} (\delta\theta_{e\gamma})^2 \tag{2.1}$$

where B_{acc} is the probability of a background event to be recognized as signal, i.e. the ratio between the number of accidental events interpreted as $\mu \to e\gamma$ to the total number of muon decays observed. The reduced positron and photon energy resolutions are respectively δx and δy, while $\delta t_{e\gamma}$ and $\delta\theta_{e\gamma}$ are the time and angular resolutions on the time-coincident back-to-back final state particles respectively. The accidental background rate R_{acc} increases quadratically with the muon rate R_μ delivered on the target, becoming predominant for intense muon beams. This is the case of MEG. For this reason the optimum muon beam for a $\mu \to e\gamma$ decay search is a continuous beam, which minimizes, for the same number of delivered muons, the number of accidental coincidences.

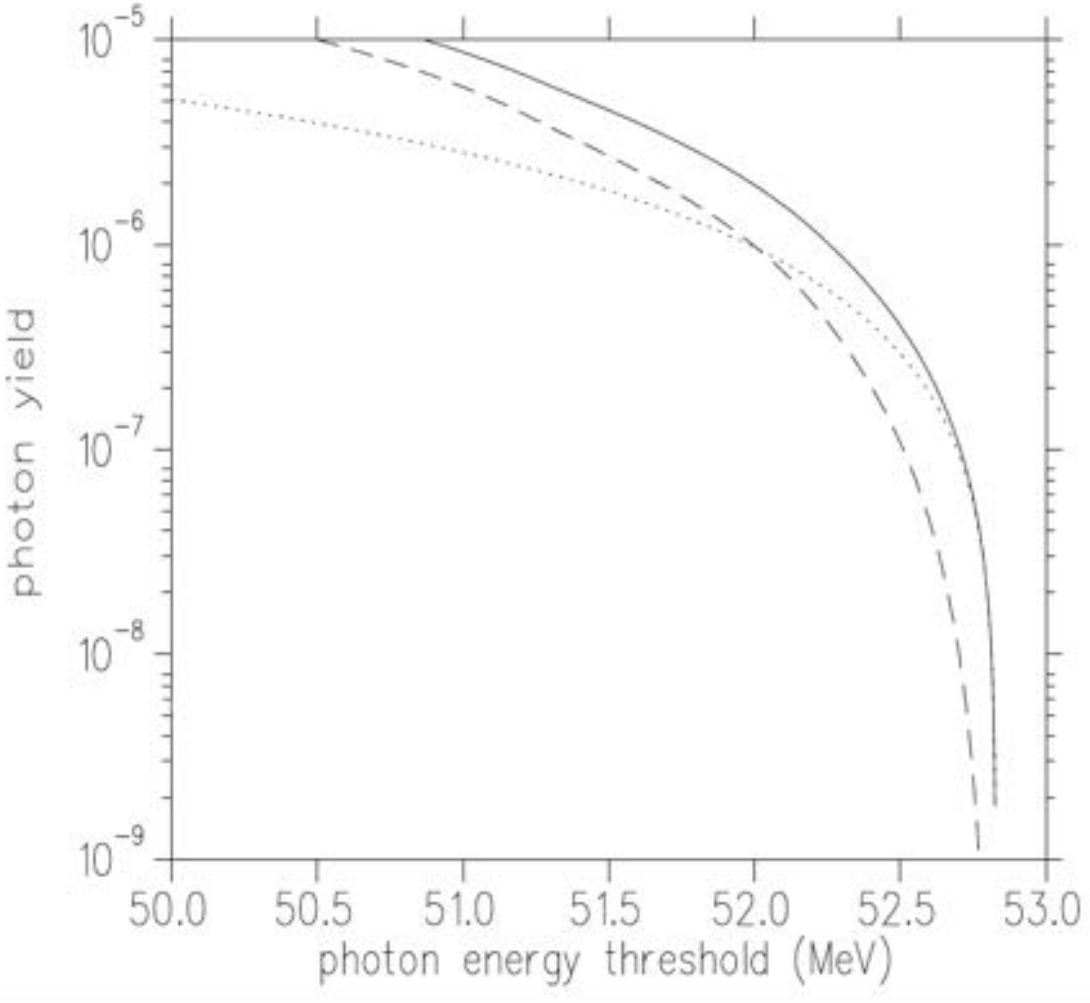

Figure 2.3: Contribution of AIF events (dashed line RMD, dotted line AIF) to the integrated rate of accidental background γ's as a function of the photon energy.

The RMD is not the only source of high energy γ's in the experimental area. Depending on the amount of material traversed by the decay positrons, even bremsstrahlung processes and e^+ annihilation in matter (AIF) are non-negligible contributors to the accidental background events. Figure 2.3 shows the AIF contribution to the total rate of accidental background γ's as a function of the photon energy.

The experiment sensitivity scales inversely with the statistics collected ($1/N_\mu$) only in case of background-free experiment, thus a considerable sensitivity improvement comes from the usage of intense muon sources. Nevertheless this is not true if the number of expected background events is greater than 1. Therefore, in order to limit the background, the detectors need to have the better possible performances in the measurement of the photon energy and the relative γ-e^+ direction since R_{acc} depends quadratically on these two observables. Obviously the positron energy resolution and time resolution are crucial too.

Variable	Design	Obtained
δE_e (keV)	200	380
$\delta\theta_e, \delta\phi_e$ (mrad)	5,5	9,11
Efficiency$_e$ (%)	90	40
δE_γ (%)	1.2	1.6
δPosition$_\gamma$ (mm)	4	5
$\delta t_{e\gamma}$ (ps)	65	120
Efficiency$_\gamma$ (%)	> 40	60

Table 2.1: Design and obtained detectors resolutions (1σ) and efficiencies for the MEG experiment.

In the Table 2.1 both the design and obtained detectors resolutions and efficiencies for the MEG experiment are listed. The trigger efficiency is $\approx 99\%$. As shown in Figure 2.4, with the resolutions reached by the MEG experiment (highlighted by the two red crosses), the dominant background source is the accidental one. This latter is at $\approx 10^{-14}$ level, while the physics background is maintained below $\approx 10^{-15}$ level, more than one order of magnitude below.

2.1.3 Single Event Sensitivity (SES)

Given the Branching Ratio for the $\mu \to e\gamma$ decay process BR($\mu \to e\gamma$), the average number of expected signal events $N(\mu \to e\gamma)$ in the case of a background-free experiment is:

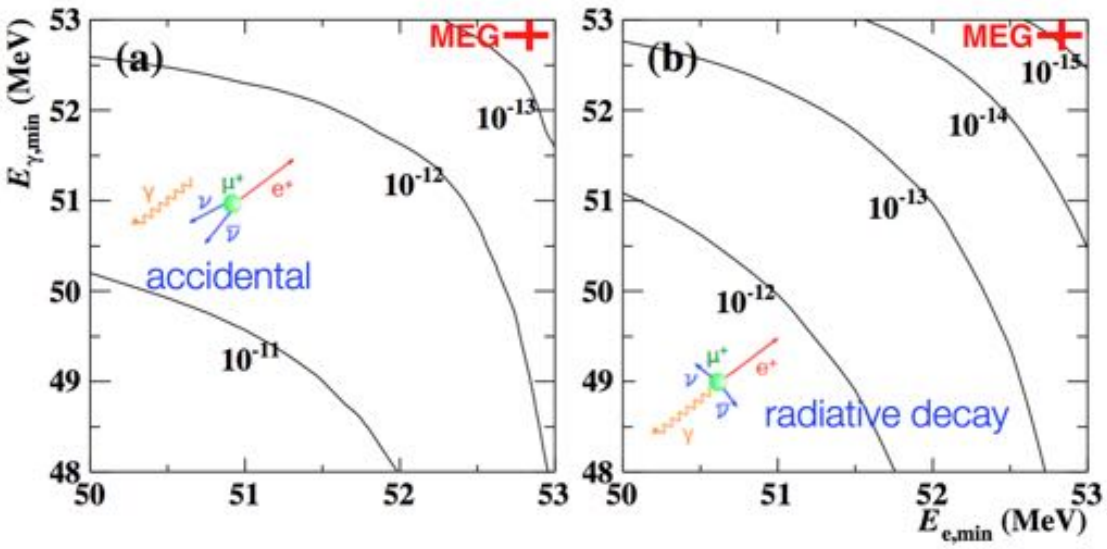

Figure 2.4: Isocurves for the two background sources in the MEG experimental environment in E_γ vs E_e planes. With the resolutions reached by the MEG experiment (highlighted by the two red crosses) the dominant background source is the accidental one.

$$N(\mu \to e\gamma) = \mathrm{BR}(\mu \to e\gamma) \times k = \mathrm{BR}(\mu \to e\gamma) \times \left(R_\mu T \frac{\Omega}{4\pi} \epsilon_e \epsilon_\gamma \epsilon_{sel} \right) \tag{2.2}$$

where k is the normalization factor, R_μ is the muon beam intensity, T is the data taking live time, $\Omega/(4\pi)$ the solid angle covered by the apparatus, ϵ_e and ϵ_γ the geometric efficiencies (related to detector geometry and materials) for positron and photons, i.e. the probability that they reach the respective detectors and ϵ_{sel} the signal selection efficiency (related to experimental resolutions).

The Single Event Sensitivity (SES) is defined as the $\mathrm{BR}(\mu \to e\gamma)$ for which the average number of expected signal events is equal to 1 in absence of background. By imposing $N(\mu \to e\gamma) = 1$ in the previous formula one obtains:

$$\mathrm{SES} = \mathrm{BR}(\mu \to e\gamma \mid N(\mu \to e\gamma) = 1) = \frac{1}{k} = \frac{1}{R_\mu T \Omega/(4\pi) \epsilon_e \epsilon_\gamma \epsilon_{sel}} \tag{2.3}$$

The SES is the inverse of the normalization parameter k. By using $\Omega/(4\pi) = 10\%$, $\epsilon_e = 90\%$, $\epsilon_\gamma = 60\%$, $\epsilon_{sel} = 70\%$, $T = 2.6 \times 10^7$ s and $R_\mu = 3 \times 10^7 \mu$/s, the expected Single Event Sensitivity for MEG is $\mathrm{SES} \approx 3.8 \times 10^{-14}$.

The value of the SES does not define the sensitivity of the experiment. This value

is calculated using the theory of probability. Given the true value of the $\tilde{\mathrm{BR}}(\mu \to e\gamma)$, the number of expected events follows a Poisson distribution with mean, given by Equation 2.2, $\tilde{N} = R_\mu T\Omega/(4\pi)\epsilon_e\epsilon_\gamma\epsilon_{sel}\tilde{\mathrm{BR}}(\mu \to e\gamma)$. If one defines N_{exp} as the number of detected signal events, this is a measurement of the true value $\tilde{N}$ extracted from the Poisson distribution. The strategy adopted by the MEG collaboration to extract a limit on the BR from the number of detected signal events is based on the frequentistic approach dictated by Feldman and Cousins [9]. In the case that any event is recognized as signal, the final limit reachable by the MEG experiment is BR $\leq 1.5 \times 10^{-13}$ at 90% Confidence Level (C.L.). Figure 2.5 shows the 90% confidence belt for the average number of expected events $\tilde{N}$ as a function of the number of detected signal events N_{exp} in presence of 0.5 background events. With $N_{exp} = 0$ the resulting upper limit on $\tilde{N} < 2$.

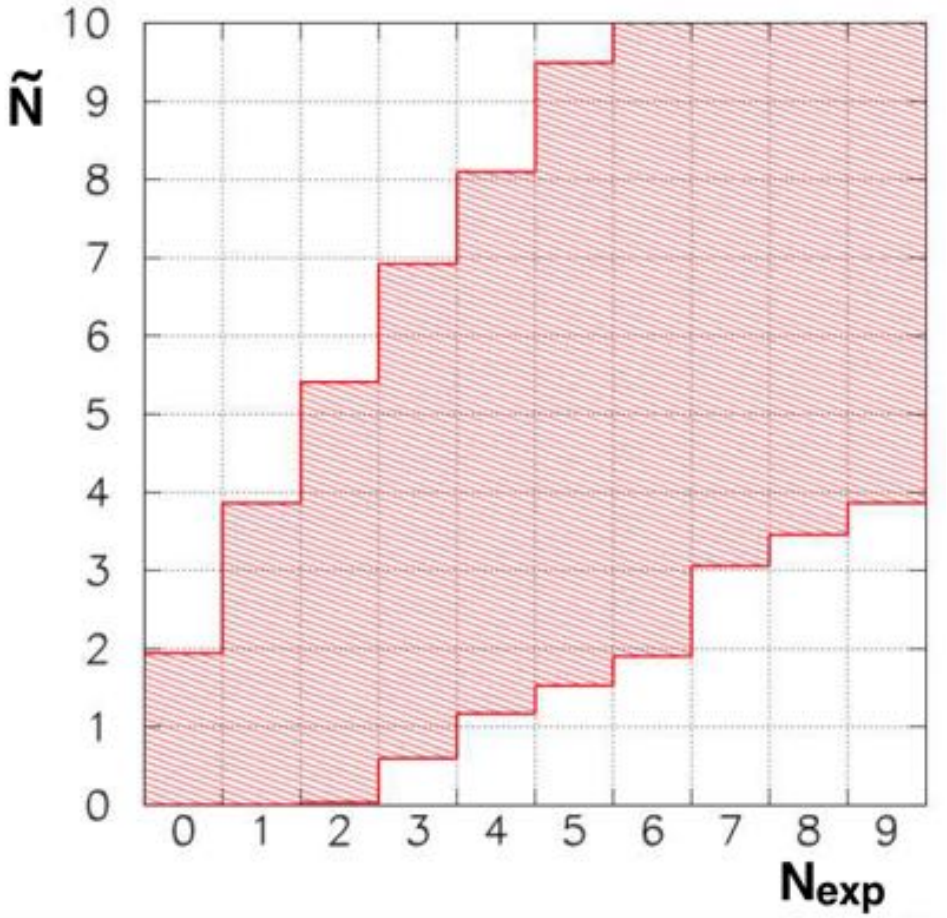

Figure 2.5: Confidence belt at 90% for the average number of expected events $\tilde{N}$ as a function of the number of detected signal events N_{exp} in presence of 0.5 background events.

2.2 The MEG experiment at PSI

The MEG experiment became operative in 2008 and data were taken from 2009 to 2013. The search for the extremely rare process $\mu \to e\gamma$ requires an extremely precise measurement of the kinematic variables of the decay products. This demand will become more stringent with increasing beam intensities to keep the accidental background under control. In fact the sensitivity to rare decay is in inverse proportion to the number of decays as the background is maintained below the signal.

The MEG experiment is hosted at the Paul Sherrer Institut (PSI) in Villigen (Figure 2.6 on the left), Switzerland, because, in order to explore Branching Ratio (BR) values well below the current predicted upper limits, the world's most powerful DC muons source is required ($> 10^8 \mu$/s). At PSI, in the 1.4 MW High-Intensity Proton Accelerator (HIPA) facility, a 590 MeV cyclotron (Figure 2.6 on the right) accelerates protons in a beam with an intensity of 1.8 mA.

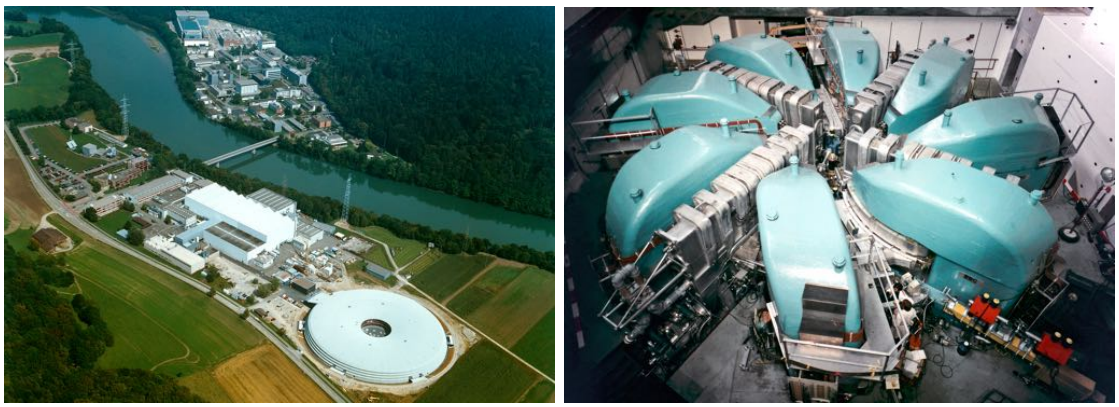

Figure 2.6: Left: aerial view of the Paul Sherrer Institut (PSI) in Villigen, Switzerland. Right: the 590 MeV cyclotron of the 1.4 MW High-Intensity Proton Accelerator (HIPA) facility at PSI.

The proton beam impinges on two rotating graphite targets (top left picture of Figure 2.7) in sequence, the M-target and the E-target, shaped like a truncated cone of half-open α tilted of the same angle α with respect to the beam axis. The rotation prevents the thermal stresses. The M-target has a thickness of 7 mm, while the E-target has a thickness of 40 or 60 mm. The two graphite targets branch seven beam lines, available simultaneously. Since the available energy is under the K meson production threshold, proton interactions mainly product pions. Pions decay in muons and electrons both inside the target and in flight. The muons from π decays at rest on the surface of the target are called *surface muons*. They have a momentum of 29.7 MeV/c due to two-body

decay kinematics and are totally polarized. However, due to the finite momentum-byte of the channel and the requirement to maximize the μ intensity, the momentum window is centered at approximately 28 MeV/c. At this momentum a significant increase of the μ^+ flux is observed (top right picture of Figure 2.7).

The MEG experiment exploits the πE5 beam line (bottom left picture of Figure 2.7) because its magnetic channel has the highest acceptance for surface muons. It is placed at 175° from the proton beam and collects positive particles (it can be also tuned to collect π^- for calibration purposes). Positrons are the most abundant particles in the beam (bottom right picture of Figure 2.7) and are swept away by an electrostatic separator (Wien filter) coupled to a lead collimator. This filter is located between two triplets of quadrupoles in order to focus the beam. In Table 2.2 the πE5 beam line properties are summarized. Simulation studies and experimental measurements led to the use of a superconducting Beam Transport Solenoid (BTS) as an additional element to couple the existing beam line to the magnet of the MEG spectrometer.

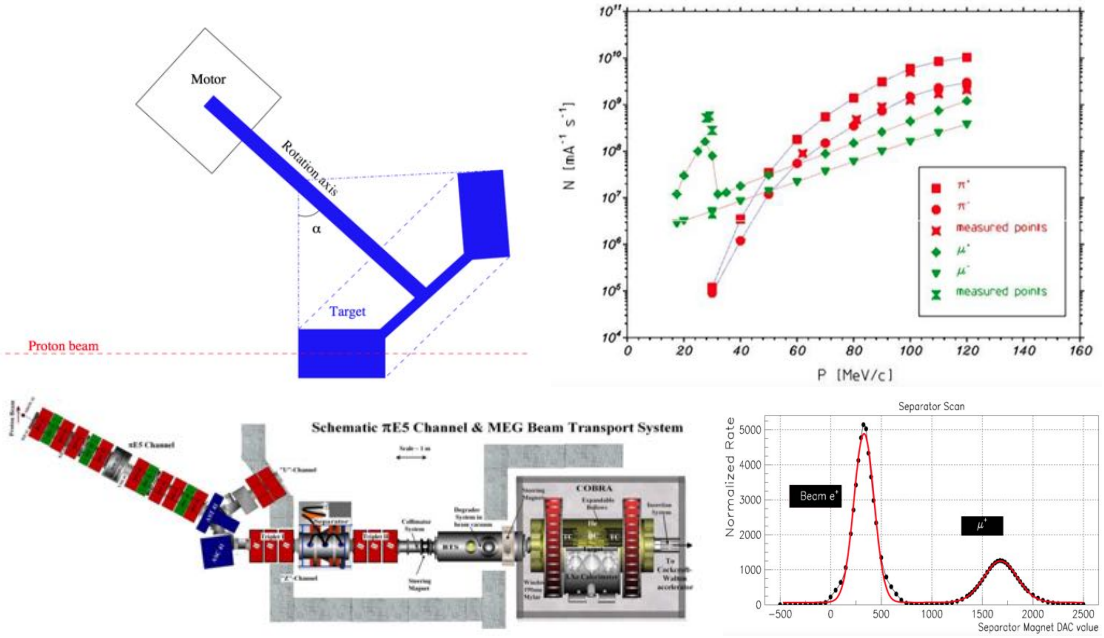

Figure 2.7: Top left: the rotating graphite targets. Top right: flux peak of the surface muons at $\approx$ 28 MeV/c. Bottom left: the πE5 magnetic channel which delivers μ^+ to the MEG detector. Bottom right: spatial separation between positrons (left peak) and muons (right peak) measured in the experimental area $\approx$ 2 m downstream from the electrostatic separator.

At the center of the experiment is located a polyethylene stopping target (Figure 2.8)

Beam line length	10.4 m
Momentum range	$20 \div 120$ MeV/c
Momentum resolution	2%
Solid Angle	150 msr
Beam spot (FWHM)	15×20 mm^2
Horizontal divergence (FWHM)	450 mrad
Vertical divergence (FWHM)	120 mrad

Table 2.2: Properties of the πE5 beam line.

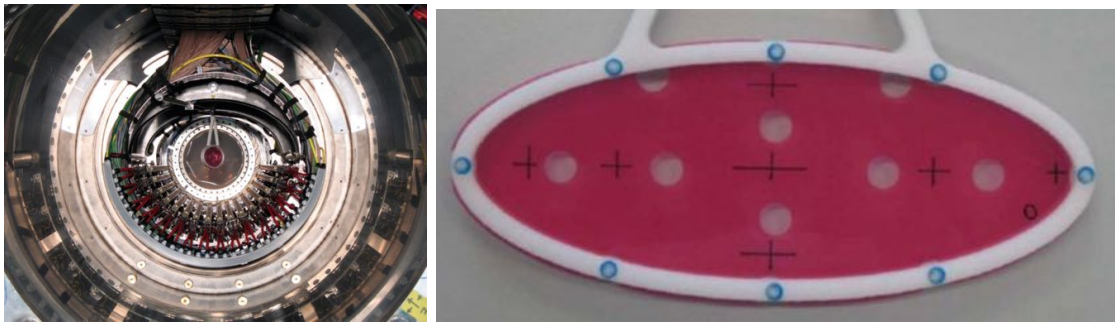

Figure 2.8: Left: picture of the muon stopping target at the center of the MEG apparatus. Right: the polyethylene elliptic stopping target held by the ROHACELL support structure. The crosses are used for alignment purposes, while the holes aligned horizontally and vertically are used to measure the tracking resolution on decay vertex reconstruction.

with an elliptical shape with semi-major and semi-minor axes of 10 cm and 4 cm respectively. The target is kept in the correct position by means of a ROHACELL[2] support structure. The reference system of the experiment has the origin at the center of the target, the z axis is directed along the beam direction, the y axis points upwards and finally the x axis completes the right-handed reference system. The azimuthal and the polar angles are indicated with ϕ and θ respectively. The range of the surface muons is of the order of 120 mg/cm^2 and the target thickness is 205 μm to prevent the Multiple Coulomb Scattering (MCS) of positrons in matter. Thus in order to maximize the fraction of stopped μ^+'s, inside the BTS a degrader consisting in a Mylar foil with a thickness of 300 μm is inserted to reduce the muons momentum before the particles are focused on the stopping target. The angle between the target and the beam is chosen to be 20.5°, so that the material seen by the muons is five times the range dispersion in polyethylene for 29 MeV/c μ's. On the other hand the material crossed by the decay positrons is

[2]Evonik Industries webpage about ROHACELL:
http://www.rohacell.com/product/rohacell/en/Pages/default.aspx

minimized and kept low by using a He atmosphere, so that positrons bremsstrahlung and Annihilation-In-Flight (AIF) as well as γ-ray conversion from Radiative Muon Decay (RMD) are minimized. The stopping efficiency is higher than 80%. The target is provided by seven crosses for alignment purposes and by six holes with a radius of 0.5 cm, aligned in horizontally and vertically, used to measure the tracking resolution on decay vertex reconstruction. The maximum beam intensity exploited by the MEG experiment is $2 \times 10^8 \mu$/s and the muons are focused on an ellipse of dimension $\sigma_x = \sigma_y \approx 5$ mm. The MCS in the material on the path from the BTS to the target spreads the dimensions of ≈ 10 mm on both axis. The final intensity is tuned to $3 \times 10^7 \mu$/s to match the rate capabilities of the tracking system.

2.2.1 Experimental Apparatus

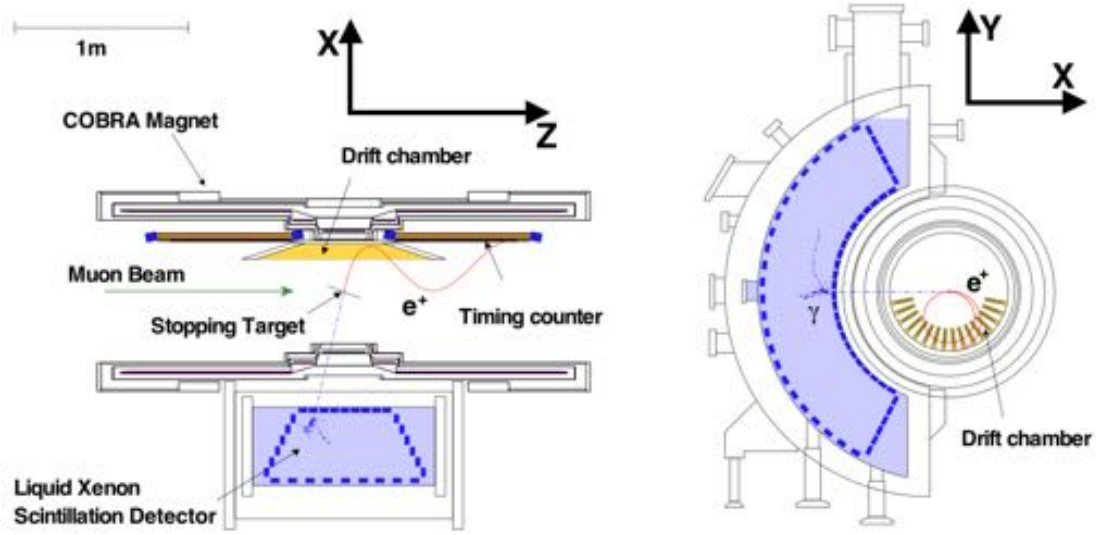

Figure 2.9: Schematic view of the MEG experiment with a signal event displayed.

In MEG for each of the two decay products a dedicated detection system is reserved. The photon is detected by means of a liquid Xenon Calorimeter (LXe) (see Section 2.2.1) which provides the energy, time and the direction of emission of the photon. The LXe is located in half-space at $x < 0$. Positrons are detected by two devices: a magnetic spectrometer consisting in a tracker made of a Drift Chambers (DC) array (see Section 2.2.1) immersed in a non-uniform solenoidal magnetic field provided by a superconducting magnet named COBRA (see Section 2.2.2) and a set of counters for time of flight measurements made of a scintillating bar hodoscope, the Timing Counter

(TC) (see Section 2.2.1). The tracking system defines the positron momentum and its direction of emission, while the TC measures the e^+ time. The DCs cover the same solid angle ($\approx 10\%$) of the LXe calorimeter: $|\cos\theta| < 0.35$ and $|\phi| < 60°$ for the polar and azimuthal angle respectively.

The MEG Drift Chambers (DC)

Figure 2.10: The MEG Drift Chamber (DC) modules. The zig-zag structure of the Vernier pads is highlighted: the cathode foils are divided in two sub-cathodes by etching the aluminum deposition.

The MEG magnetic spectrometer is made by 16 trapezoidal Drift Chambers (DC) immersed in the magnetic field generated by the COBRA magnet (Figure 2.10). The trapezoid base lengths are 40 cm and 104 cm respectively. The magnetic field geometry reduces the DCs overcrowding of the low momentum Michel positrons by one order of magnitude with respect to a pure solenoidal magnetic field configuration. The detectors are spaced by 10.6° intervals and the sensitive area ranges radially from $r = 19.3$ cm to $r = 27.9$ cm, covering longitudinally $|z| < 50$ cm. They are formed by two independent planes with a gap of 3 mm made of an array of alternating field and sense wires with a

pitch of 4.5 mm enclosed by two cathode foils spaced by 7 mm and made of a 12.5 μm thick polyamide layer with a 250 nm Al deposition. The anodes are Ni-Cr resistive wires shifted by half sense wire spacing to resolve the left-right ambiguity (Figure 2.11). The wire length spans from 82.8 cm to 37.6 cm, respectively the innermost and the outermost wire. The gas mixture filling the chamber volume is He-C_2H_6 (He-isobutane) 50:50. The ionization density is $\approx 65\ e^-$/cm for MIP particles with a radiation lenght $X_0 \approx 650$ m. Thanks to a low-mass construction the average amount of material seen by a positron is $\approx 2 \times 10^{-3}\ X_0$. The radial coordinate is measured by means of the time difference between the wire signals and the absolute track time is provided by the TC. The estimated resolution for the transverse direction is $\delta r \approx 200\ \mu$m. The longitudinal coordinate z is derived both, by the ratio of the charges collected at both ends of the hit wire (≈ 1 cm resolution), and by using the Vernier pad method (Figure **??**) with more accuracy. The cathode foils are divided in two sub-cathodes by etching the aluminum deposition. The induced charge on each 5 cm zig-zag shaped pad provides the z coordinate with a resolution of $\approx 550\ \mu$m. The accuracy in the determination of the impact parameter on a wire, is $\approx 210\ \mu$m. The angular resolution is determined by events where positrons made two turns in the DCs system, leading to $\sigma_\theta \approx 9.4$ mrad and $\sigma_\phi \approx 8.7$ mrad. The positron momentum resolution is measured exploiting the Michel spectrum endpoint. The fit function includes the theoretical Michel spectrum convolved with the detector acceptance and a Gaussian resolution, leading to $\sigma_P \approx 330$ keV.

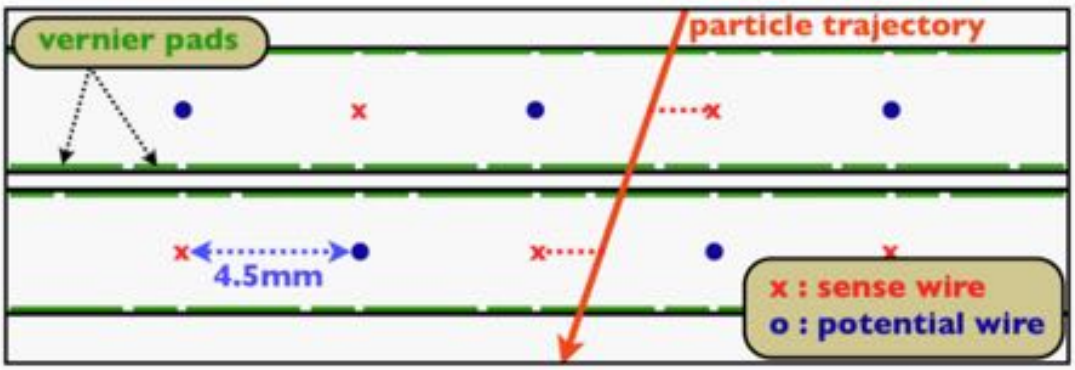

Figure 2.11: Schematic of the two detector planes in a Drift Chamber (DC) module.

The DCs operation stability, acceptance and the angular and momentum resolution are monitored through coherent Mott scattering of positrons on the carbon atoms of the polyethylene stopping target. The scattered positrons have an average momentum close to the incident one of 53 MeV/c with a measured $\sigma \approx 450$ keV/c (including the spread

in the incident positrons energy). A e^+ beam can be easily obtained by changing the working point of the electrostatic separator. The DC alignment is accomplished in two steps. The first consists in an optical survey based on reference markers, while the second in a software-based alignment (Millipede technique [25]) exploiting the reconstruction of the straight tracks from cosmic rays during COBRA shutdown. The resolution on the six Degrees Of Freedom (DOF) of each module is ≈ 0.2 mm (three positional DOF) and better than 150 μm (three rotational DOF) respectively.

The MEG Timing Counter (TC)

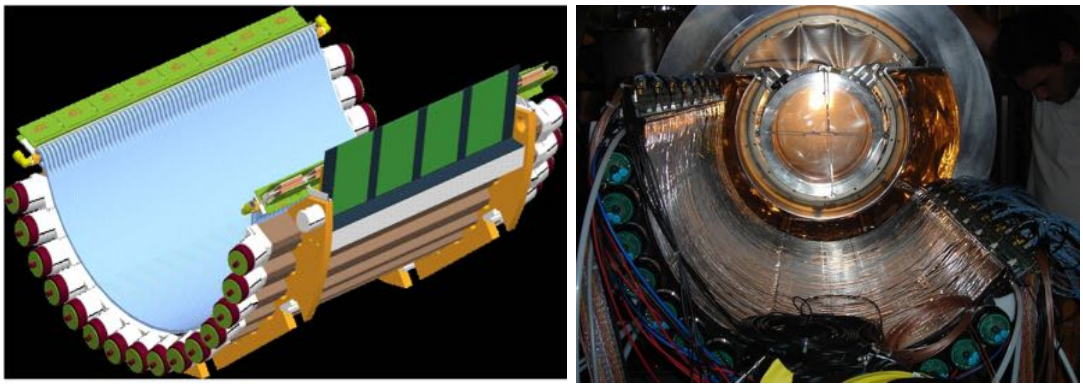

Figure 2.12: Scintillating bars and fibers of the MEG Timing Counter (TC).

The MEG Timing Counter (TC), showed in Figure 2.12, consists of two equal sections hosting 15 plastic scintillator bars (BC404) with a 4 cm square section and a length of 80 cm placed longitudinally. The symmetry is cylindrical along the z axis with a radius of 29.5 cm. The sections cover longitudinally 25 cm $\leq |z| \leq$ 95 cm and an interval of 145° for the azimuthal angle ϕ. A set of 256 scintillating fibers with a 0.5 cm square section and read out by Avalanche PhotoDiodes (APD) are oriented along the azimuthal direction covering the inner face. Given the geometry of the gradient magnetic field, positrons emitted within $|\cos\theta| < 0.35$ hit the TC after completing ≈ 1.5 turns in the r-ϕ plane. The scintillator bars are coupled at the ends to two 2" PhotoMultiplier Tubes (PMT) suitable to work in a high magnetic field environment. Even the PMT orientation is optimized to minimize the drop of performances due to the COBRA magnetic field. Moreover the TC is isolated from the DC He atmosphere through a plastic bag since otherwise the PMT lifetime dropped down. The combination of the signals from the two types of scintillators provided the bidimensional reconstruction of the impact point on TC with an online position and time resolutions of ≈ 5 cm and ≈ 2 ns respectively. The

offline time resolution is measured to be ≈ 60 ps through tracks hitting multiple bars, while the position resolution goes down to ≈ 0.5 cm.

The MEG Calorimeter (LXe)

Figure 2.13: The MEG Liquid Xenon (LXe) calorimeter with an interior view showing the PMTs during the assembly and a schematical 3D view showing a simulated electromagnetic shower from a signal γ.

A Liquid Xenon (LXe) calorimeter is used as γ-ray detector (Figure 2.13) and to date is the world's larger LXe scintillation detector (900 litres). Among the noble gases, the Xe has a high boiling point (165 K at 1 atm) and a high atomic number ($Z = 54$). Combined with a great density in liquid phase ($\rho_{LXe} = 2.95$ g/cm^3), these properties make it an excellent scintillator with a radiation lenght $X_0 = 2.77$ cm leading to a considerable compact size. The LXe extends radially 38.5 cm, corresponding to $\approx 14\ X_0$ and fully containing an electromagnetic shower from a signal γ-ray. The MEG calorimeter wants to combine the positive characteristics of both organic and inorganic scintillators: respectively the fast response and the high light yield. The short scintillation time reduces the probability of having pile-up events and gives a temporal resolution comparable with the experiment requirements. Furthermore the number of scintillation photons per unit of energy deposited is comparable to scintillator crystals leading to an excellent energy resolution without their slow response. About 20 eV are needed to have one scintillation photon. The γ's are emitted by the Xe_2^* excimer de-excitation and have a wavelength of 178 ± 13 nm, the so-called Vacuum UltraViolet (VUV) photons. This excimer exists

only in the excited state and not in the ground level. Moreover, the energy required to form the Xe first excited state is higher. Consequentely the Xe is transparent to its scintillation light with an absorption length $\gg 1$ m. A significant worsening in the LXe calorimeter uniform response and energy resolution is due to even small concentration of impurities (O_2 and H_2O) which induce light absorption. For this reason a complex Xe purification system was designed, operating on both gaseous and liquid phase. The VUV scintillation light is collected by 846 Hamamatsu R9299 2" PMTs, equipped with a synthetic quartz window, covering the six faces (Figure 2.13). The Quantum Efficiency (QE) is $\approx 15\%$.

The LXe calorimeter has a cylindrical symmetry around the muon stopping target so the photons produced in the muons decay at rest hit perpendicularly the inner face. The highest amount of energy is released near the inner surface, then here the photosensors density is higher (246 PMTs) with respect to the lateral and outer faces. The cryostat is far 65 cm from the target and extends 45 cm radially. The fiducial volume is ≈ 800 litres. The time resolution is measured to be about 67 ps while the energy resolution depends on the γ conversion depth: 2.7% within 8 mm from the inner face, 2% between 8 mm and 3 cm and 1.7% for deeper conversion.

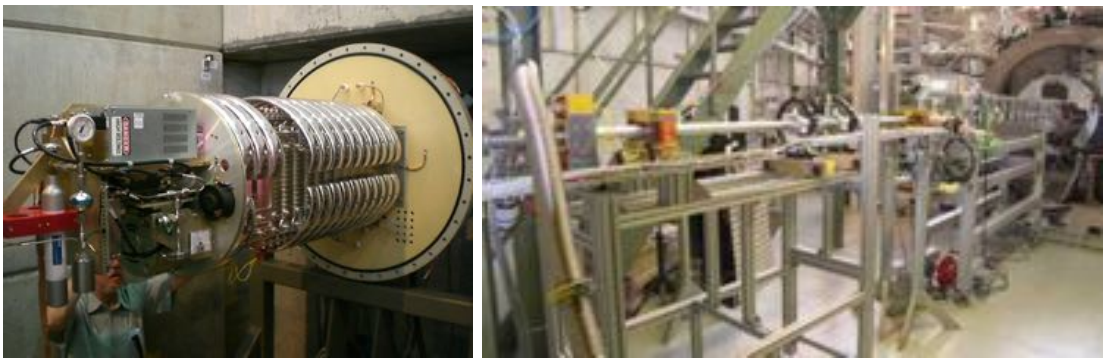

Figure 2.14: Left: the Cockroft-Walton (CW) proton accelerator. Right: the dedicated beam line which delivers the protons on the $Li_2B_4O_7$ target.

During the LXe operations, the stability and performances are continuously monitored via several dedicated calibration procedures. During the data taking period a daily-based calibration expolits a system of Light Emitting Diodes (LED) installed inside the detector, able to fully illuminate the calorimeter faces. In this way both the PMTs gain and stability are verified. In order to estimate the PMTs Quantum Efficiency (QE) and the LXe light absorption a weekly-based calibration is used. It is based on ^{241}Am α sources with a 200 Bq activity, deposited on five gold-plated 50 μm wires

immersed in the LXe. The 5.44 MeV energy of the α particles is completely deposited within a distance of about 40 μm from the sources so the energy and position are well defined. The calibration is obtained through a comparison between PMT measurements and MC simulations. Another weekly-based calibration procedure exploits a Cockroft-Walton (CW) proton accelerator. Once replaced the muon stopping target, through a dedicated beam line the sub-MeV protons are delivered on a $Li_2B_4O_7$ target and the CW can be tuned to induce a nuclear reaction with Li or B (Figure 2.14).

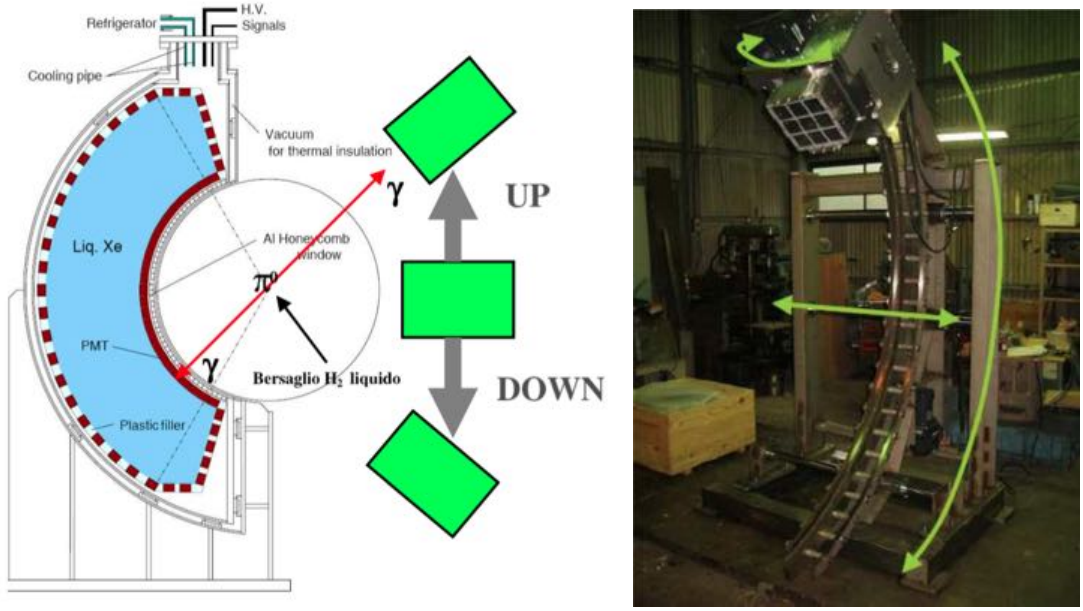

Figure 2.15: Left: schematic view of the experimental configuration during the $\pi^0 \to \gamma\gamma$ calibration. Right: the movable support for the auxiliary NaI calorimeter with the possible movements highlighted.

The Li resonance is used to determine the calorimeter energy scale through the final state 17.6 MeV photons. The B resonance gives the unique opportunity to determine the LXe-TC relative timing. In fact in this case the transition to the ground level occurs with the emission of 16.1 MeV γ's, but more frequently with the simultaneous emission of two γ's with an energy respectively of 11.7 MeV and 4.4 MeV. Once per year the LXe energy scale is calibrated near the signal energy. This calibration exploits the decay into two simultaneous γ's of neutral pions ($\pi^0 \to \gamma\gamma$) produced by charge exchange reactions of π^- on p ($\pi^- p \to \pi^0 n$). The πE5 beam line can be tuned to deliver 70 MeV/c π^- on a Liquid Hydrogen Target (LHT) positioned at the same location of the polyethylene muon stopping target. The final state π^0 has a kinetic energy of about 2.9

MeV so the relationship between the energy of the outgoing photons and their angle can be used to define the γ's energy once constrained their relative directions. Given the π^0 momentum in the laboratory, the two-body decay kinematics leads to a flat photon energy distribution 54.9 MeV $\leq E_\gamma \leq$ 82.9 MeV, with a minimum angle of 157° between the directions of emission of the two final state photons. In order to map the entire LXe inner face an auxiliary calorimeter mounted on a movable support is placed on the opposite side of the LXe calorimeter with respect to the LHT. It consists in a 3×3 matrix of NaI scintillating crystals read out by APDs. Finally, in order to determine the time resolution of the LXe calorimeter at the signal energy, a thin counter (0.3 X_0) consisting in a sandwich of fast plastic scintillators read out by four PMTs and lead plates is placed in front of the auxiliary calorimeter (Figure 2.15).

The MEG Trigger and DAQ

The πE5 beam line is capable of delivering $2 \times 10^8 \mu$/s on the stopping target at the maximum intensity. At this high decay rate a fast and efficient trigger system with a high pile-up rejection of the huge beam-related background is crucial for an experiment which aims to find ultra-rare events. A schematic view of the electronics and DAQ of the MEG experiment is shown in Figure 2.16.

In MEG the analog signals from all the detectors channels are collected. The electronics was designed accordingly to VME standard and it was arranged in 9 crates, each one with a dedicated read out online machine. Thanks to a triple buffer read out scheme the DAQ live time is $\geq 99\%$ for event rates up to 13 Hz. The individual DAQ boards were synchronized with a dedicated low-jitter 19.44 MHz clock. Moreover the use of Phase-Locked Loops (PLL) guaranteed the DAQ boards synchronization within $\approx 40 \div 50$ ps by removing the residual jitter. The DAQ software was based on the MIDAS (Maximum Integration Data Acquisition System) package. One of the most innovative approach in the DAQ system was the use of high frequency waveform digitizers for all ≈ 3000 readout channels, called Domino Ring Sampler 4 (DRS4) [26] [27], based on the Switched Capacitor Array technique. It was custom designed for MEG with the goal of storing waveforms with 1024 samples for each channel with signal above threshold. The waveforms sampling frequency is 1.6 GHz for the TC and the LXe, whose signals are used for firing the trigger, while 0.8 GHz for the DC. The stringent limit due to latency of the readout electronics prevents the use of any information from the DC. In fact the drift time of the ionization electrons toward the anode wires is too long. The achievable time resolution on the waveforms was $\approx$ 50 ps allowing pile-up reduction. Each waveform

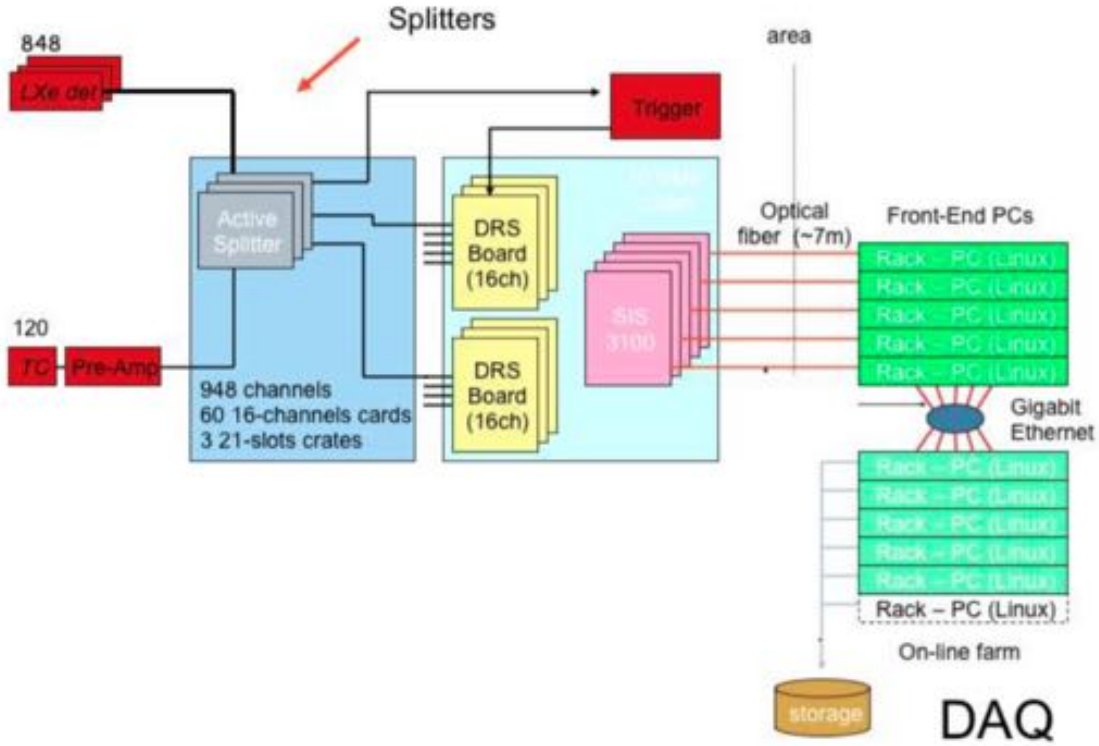

Figure 2.16: Schematic view of the electronics and DAQ of the MEG experiment.

is processed offline applying baseline subtraction, spectral analysis, noise filtering and digital constant fraction discrimination in order to optimise the information extraction and build the observables needed for the online event selection. The event size is reduced by means of the *bzip*2[3] algorithm down to ≈ 0.9 MB/event.

The trigger system has been designed, constructed and developed by the INFN Pisa group of the MEG experiment. A set of ancillary boards distributed a common 100 MHz clock signal to 50 VME custom boards arranged in a multi-layer system. The data transmission between different layers was operated by means of LVDS (Low-Voltage Differential Signaling) connections. At the lower level the boards operated a synchronous height pulse ADC conversion of the input signals. This allowed the determination of the signal amplitude a the permille level and timing within a few ns. At the middle level a basic event reconstruction was performed for the single detectors separately. At the higher level the information from different detectors is combined and estimates of the kinematic variables crucial for the trigger were obtained: the γ-ray energy and the

[3]http://www.bzip.org.

relative e^+-γ direction and timing. At this point the decision of firing the trigger signal was taken exploiting the large computation power of FPGAs (Field Programable Gate Arrays). The latency was $\approx$ 500 ns which is shorter than the DRS4 chip time depth ($\approx$ 600 ns). The signals used for the trigger selection come from the scintillating bars of the TC and the PMTs of the LXe calorimeter. Requirements were set on observables that could be computed in a very short time: the sum of the light collected by the PMTs of the inner and lateral faces of the calorimeter; the waveform and the position of the PMT with the largest signal; the hit scintillating bars of the TC. These quantities provide a rough estimate of the kinematic key parameters, respectively the energy, timing and direction of the photon originating in the target and the positron timing and momentum. In fact a positron hitting the TC has a momentum $p_{e^+} \geq 45$ MeV/c by construction. The trigger rate was kept below 10 Hz, thus the DAQ system was not overloaded.

The TC-LXe timing intercalibration is done by means of a Nb laser capable of emitting fast light pulses (10 ps). The laser excitation frequency can be tuned from 100 to 1000 Hz. The two wavelengths exploited are: 532 nm (second harmonic) for the TC and 266 nm (fourth harmonic) for the calorimeter. The laser system provides even a synchronization signal from the excitation with a jitter ≤ 5 ps. The laser beam is splitted and delivered, through optical paths with the same lengths, to the inner face of the calorimeter, the scintillating bars of the TC and to a reference PMT for the beam intensity normalization. The temporal difference between the rising edge of the signals from the LXe and the TC gives a measurement of the relative time offset between the two detectors whose signals are used for the trigger logic.

2.2.2 The COBRA Magnet

The COBRA (COnstant Bending RAdius) superconducting magnet (Figure 2.17) is capable of generating an axial gradient magnetic field with a cylindrical symmetry along the z axis. The maximum intensity, 1.27 Tesla, is at the center (z = 0) and it decreases while increasing $|z|$ down to 0.49 T near the endcaps (Figure 2.18).

The magnet consists of five coils with three different radii arranged in a step structure in order to obtain the gradient field adjusting the circulating current densities. The stray field could degrade the performance of the photon detectors of the LXe calorimeter (see Section 2.2.1), hence a pair of compensation coils surround the ends of COBRA to reduce the magnetic field to 50 Gauss level (Figure 2.18). Within the acceptance of the calorimeter, the amount of material of the magnet is $\approx 0.197\ X_0$. In a conventional solenoidal magnetic field the particle bending radius depends on the transverse momentum, i.e. it

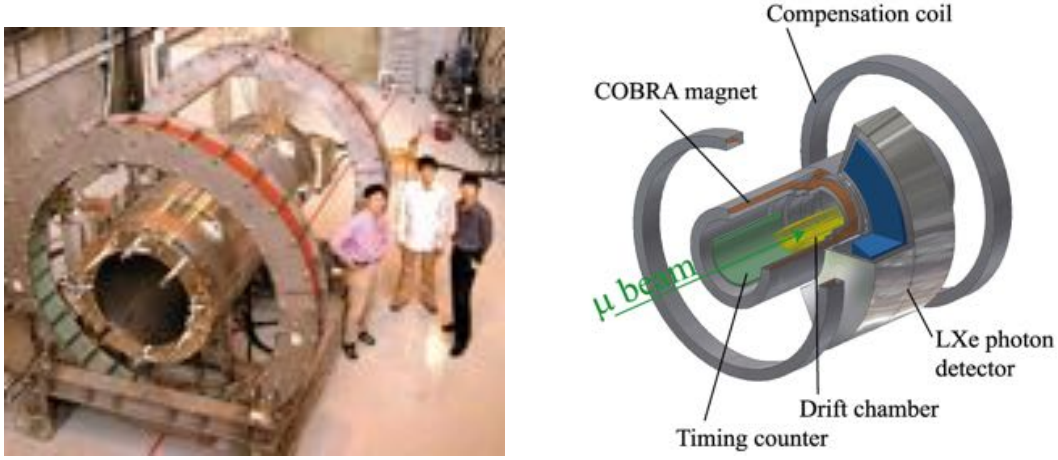

Figure 2.17: The COBRA (COnstant Bending RAdius) superconducting magnet.

depends on the emission angle of the particles, while thanks to the COBRA magnetic field configuration, the peculiarity is that the trajectory of the positrons emerging from the muon stopping target has a constant bending radius which only slightly depends on the emission angle, i.e. the particle bending radius depends almost exclusively by the total momentum (Figure 2.19). Another important feature is that the low-momentum positrons emitted at $\approx 90°$ with respect to the longitudinal axis are rapidly removed. The magnetic field map was obtained by measuring over 25000 points with a one dimensional Hall probe intercalibrated with a NMR probe. Over the entire volume the agreement with respect to theoretical prediction was found to be at 0.2%. The stability of the field was monitored with a NMR probe and it results stable within 20 ppm.

2.3 MEG Data Analysis

The physics data taking period for the MEG experiment spans from 2009 to 2013. The accumulated number of stopped muons in the target is shown in Figure 2.20 as a function of the years. As already mentioned in Section 2.1, the five key observables that characterized the $\mu^+ \to e^+\gamma$ decay process are:

- the measured energy of the final state positron (E_e) and photon (E_γ);
- the measured relative time between the positron and the photon ($t_{e\gamma}$);
- the relative polar ($\theta_{e\gamma}$) and azimuthal ($\phi_{e\gamma}$) angles between the measured emission directions of the outgoing positron and photon.

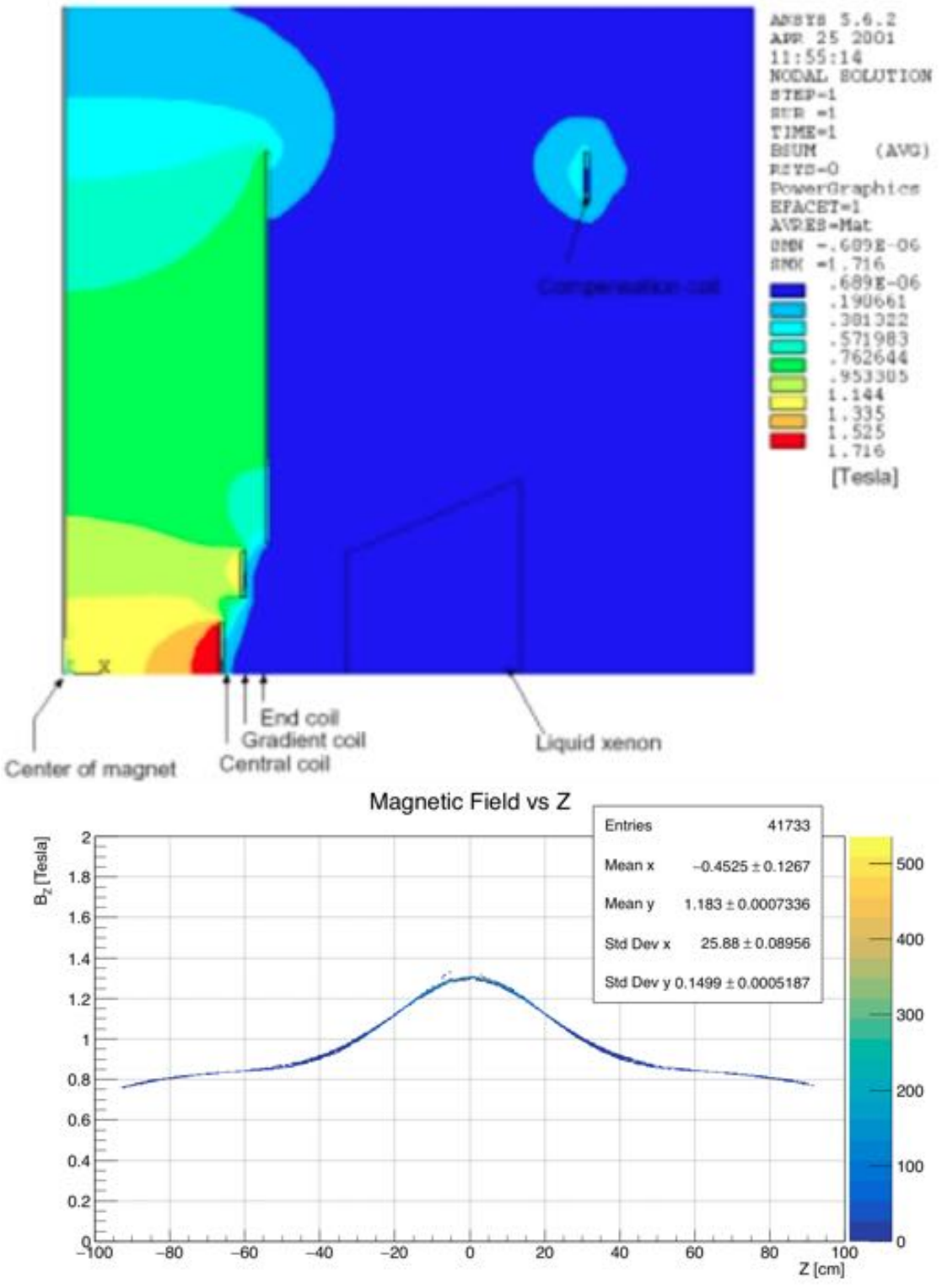

Figure 2.18: Above: COBRA gradient magnetic field intensity as a function of the position. Below: z component of the magnetic field B_z as a function of the z coordinate.

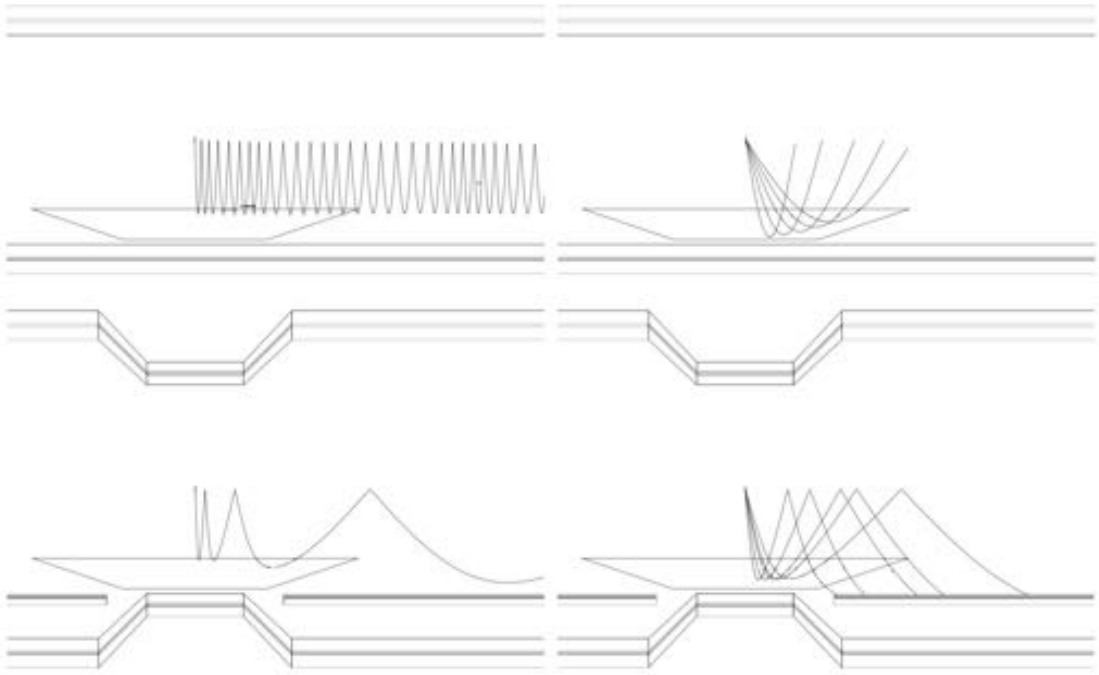

Figure 2.19: Above: monochromatic charged particle trajectory in a pure solenoidal magnetic field. Below: the same for the gradient magnetic field provided by the COBRA magnet. The left figures depict low-momentum positrons, while the right ones depict signal positrons emitted at different angles from the stopping target.

These five variables are aggregated in proper vectors for each event $\vec{e_i}$, and the distribution of the collected events is studied in terms of $\vec{e_i}$:

$$\vec{e_i} = (E_\gamma, E_e, t_{e\gamma}, \theta_{e\gamma}, \phi_{e\gamma}) \tag{2.4}$$

The approach of the MEG experiment to the measurement of the BR($\mu \to e\gamma$) is based on a **likelihood analysis** applied to a wide **blinding box**. A region in the $(E_\gamma, t_{e\gamma})$ plane is hidden to the collaboration immediately after a run is recorded. An automatic process removes the events inside a predefined region and writes them in separate files which are not open until the data analysis procedure is completely defined. This region is defined by the following restrictions based on the detectors resolutions on the photon energy (δE_γ) and on the γ-e^+ relative time ($\delta t_{e\gamma}$): $|t_{e\gamma}| < 3\delta t_{e\gamma}$ and $|E_\gamma - 52.83 \text{ MeV}| < 3\delta E_\gamma$. The blinding box is chosen large enough to fully contain the *signal region*, so that the final signal cuts may be chosen without bias as well. The blinding box for the MEG final analysis lies in the region defined by 48 MeV $\leq E_\gamma \leq$ 58

MeV and $|t_{e\gamma}| \leq 1$ ns.

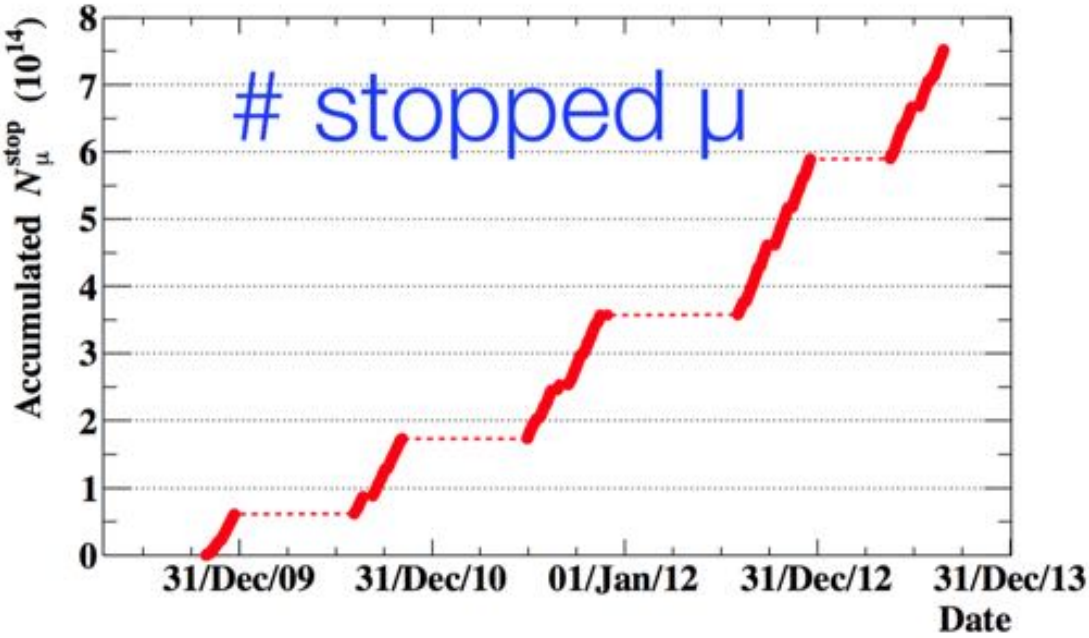

Figure 2.20: Accumulated number of stopped muons in the MEG polyethylene target as a function of the years.

2.3.1 Blind Analysis

A **blind analysis** is a measurement which is performed without looking at the answer. Blind analyses are the optimal way to reduce or eliminate *experimenter's bias*, the unintended biasing of a result in a particular direction. It is understood that bias may be intentional or unconscious, thus no dishonesty is implied by blinding.

A number of different blind analysis techniques have been used in nuclear and particle physics in recent years. The *hidden signal box* technique explicitly hides the signal region until the analysis is completed. This method is well suited to searches for rare processes, when the signal region is known in advance. This is exactly the case of the MEG experiment. Events in the signal region are kept hidden until the analysis method, selection cuts, and background estimates are fixed. Only when the analysis is essentially complete the blinding box (black rectangle in Figure 2.21) is opened and an upper limit or observation made.

The analysis algorithms are calibrated and optimized and the detector response functions are studied by using both calibration events when possible and data contained in

the sidebands of the blinding box. The sidebands are the regions in the $(E_\gamma, t_{e\gamma})$ plane surrounding the blinding box. There are two kinds of sidebands: the *time sidebands* are defined by the condition $|t_{e\gamma}| > 1$ ns; the *energy sideband* is defined by the condition 44 MeV $\leq E_\gamma \leq$ 48 MeV. The former are used to define the energy spectra for the accidental background events. The latter is populated by most of the RMD events which form an excess of events at $t_{e\gamma} = 0$ (Figure 2.21 and Figure 2.24). They are used to evaluate time resolution and offsets between the the LXe calorimeter and the TC and to extrapolate the number of RMDs in the **physics analysis window** (red rectangle in Figure 2.21), which is a bit smaller than the blinding box to avoid boundary effects.

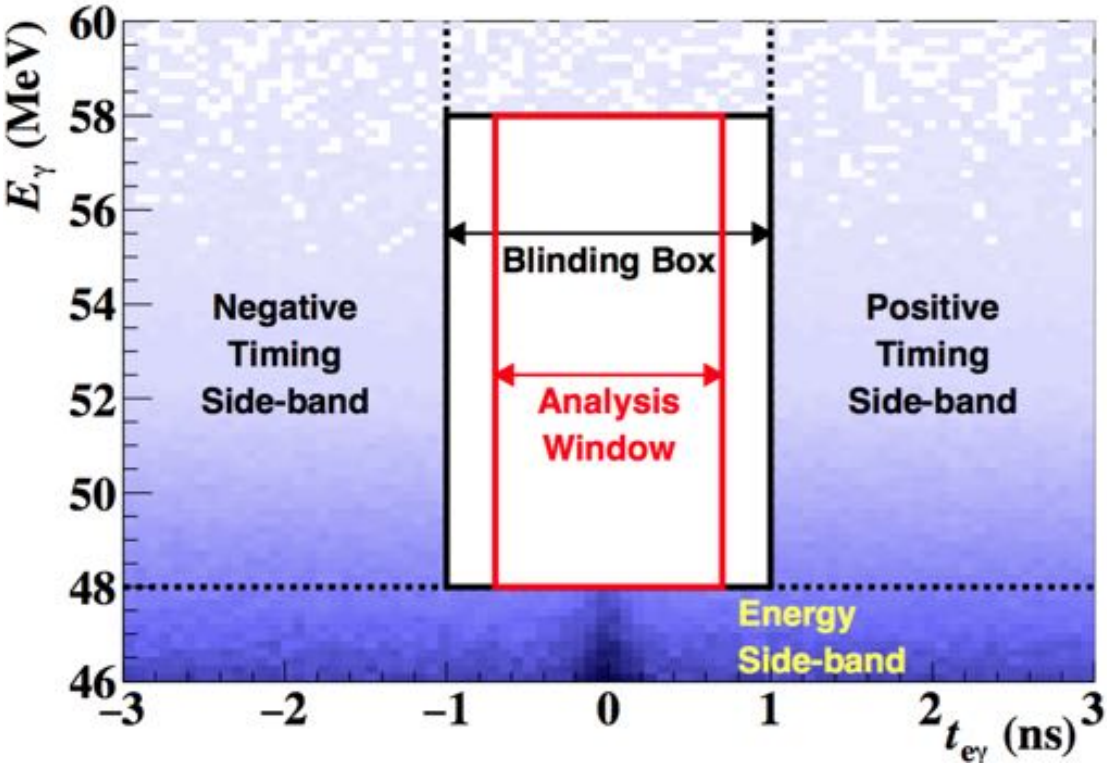

Figure 2.21: $(E_\gamma, t_{e\gamma})$ plane close to the $\mu^+ \to e^+\gamma$ signal region. The two *time sidebands* ($|t_{e\gamma}| > 1$ ns) and the *energy sideband* (44 MeV $< E_\gamma <$ 48 MeV) are highlighted, together with the *blinding box* (48 MeV $\leq E_\gamma \leq$ 58 MeV and $|t_{e\gamma}| \leq 1$ ns, black rectangle) and the *physics analysis window* (red rectangle). The excess of events at $t_{e\gamma} = 0$ is due to RMDs (Figure 2.24).

2.3.2 Probability Density Functions (PDF)

The first step of the analysis is the determination of the **Probability Density Functions (PDF)** for signal events $S(\vec{e_i})$, physics background from RMD events $R(\vec{e_i})$ and accidental background events $B(\vec{e_i})$. The PDFs are defined only inside the physics analysis window and are functions of the event vector $\vec{e_i}$ (Equation 2.4). For $S(\vec{e_i})$ and $B(\vec{e_i})$ each individual observable is independent from the others, therefore a factorization in five independent one-varible PDFs can be performed:

$$\begin{aligned} S(\vec{e}) &= S_{E_\gamma}(E_\gamma) \otimes S_{E_e}(E_e) \otimes S_{t_{e\gamma}}(t_{e\gamma}) \otimes S_{\theta_{e\gamma}}(\theta_{e\gamma}) \otimes S_{\phi_{e\gamma}}(\phi_{e\gamma}) \\ B(\vec{e}) &= B_{E_\gamma}(E_\gamma) \otimes B_{E_e}(E_e) \otimes B_{t_{e\gamma}}(t_{e\gamma}) \otimes B_{\theta_{e\gamma}}(\theta_{e\gamma}) \otimes B_{\phi_{e\gamma}}(\phi_{e\gamma}) \end{aligned} \tag{2.5}$$

For $R(\vec{e_i})$, energy and emission angle are correlated and thus one can factorize it only into two terms:

$$R(\vec{e}) = R_{kin}(E_\gamma, E_e, \theta_{e\gamma}, \phi_{e\gamma}) \otimes R_{t_{e\gamma}}(t_{e\gamma}) \tag{2.6}$$

A summary of the procedures for the PDFs determination is given below:

- $B_{t_{e\gamma}}$: it is the $t_{e\gamma}$ distribution of non-correlated positrons and photons (flat distribution);
- $R_{t_{e\gamma}}$, $S_{t_{e\gamma}}$: extracted from the fit to the time distribution of RMD events (Figure 2.24), since the outgoing final state particles are emitted simultaneously;
- R_{kin}: obtained from the theoretical RMD spectrum convoluted with the detectors resolutions;
- S_{E_e}, B_{E_e}: determined from the fit to the experimental positron energy distribution in the following way: the theoretical Michel spectrum is multiplied by the acceptance curve of the spectrometer and convolved with a Gaussian resolution function. The fit of the kinematic edge is used for S_{E_e}, while the whole curve is exploited for B_{E_e};
- S_{E_γ}, B_{E_γ}: the first PDF is extracted from the photon energy measured by the LXe calorimeter during the calibration runs with the $\pi^0 \to \gamma\gamma$ decays. The response of the detector is extrapolated to the signal region. The second PDF is obtained from the experimental photon energy distribution for events falling into the two time sidebands. The AIF contribution is taken into account;

- $S_{\theta_{e\gamma}}$, $S_{\phi_{e\gamma}}$: determined from the individual measured resolutions on the positron and photon angle by means of Monte Carlo simulations;

- $B_{\theta_{e\gamma}}$, $B_{\phi_{e\gamma}}$: extracted from all the sidebands data. The angular distributions for accidental background are expected to be flat. However detector acceptance effects slightly modify them.

After completing the optimization of the analysis algorithms and the background studies, the blinding box is opened and the likelihood analysis on the events populating the physics analysis window is performed.

2.3.3 Likelihood Fit

The number of signal N_{SIG}, RMD N_{RMD} and accidental N_{ACC} events is extracted by maximizing the following extended likelihood function $\mathcal{L}$, with N_{OBS} the number of events detected in the signal region and $N = N_{SIG} + N_{RMD} + N_{ACC}$:

$$\mathcal{L}(N_{SIG}, N_{RMD}, N_{ACC}) = \frac{e^{-N}}{N_{OBS}!} \prod_{i=1}^{N_{OBS}} [N_{SIG} S(\vec{e}_i) + N_{RMD} R(\vec{e}_i) + N_{ACC} B(\vec{e}_i)] \times \\ \times \exp\left[-\frac{(N_{RMD} - \langle N_{RMD} \rangle)^2}{2\sigma_{RMD}^2} \right] \times \exp\left[-\frac{(N_{ACC} - \langle N_{ACC} \rangle)^2}{2\sigma_{ACC}^2} \right] \tag{2.7}$$

where $\langle N_{RMD} \rangle$ and $\langle N_{ACC} \rangle$ are the estimated number of background events extrapolated to the signal region through the previous sidebands studies. The corresponding standard deviations of these numbers are σ_{RMD} and σ_{ACC} respectively. These two extrapolations are included in the likelihood analysis by means of the two gaussian terms in Equation 2.7. An example of the extrapolation of the number of RMD events from the energy sideband to the signal region is shown in Figure 2.22.

The results of the 5D likelihood fit to the events distribution in the physiscs analysis window is shown in Figure 2.23 for the 2009-2013 complete dataset. Here the experimental data (black points) are shown together with the 5D best fit function projected on each of the five kinematic variables (blue solid lines) characterizing the $\mu^+ \to e^+\gamma$ decay process. The individual best fits for signal in arbitrary scale (green filled areas) and RMD (red dashed-dotted lines) and accidental (magenta dashed lines) backgrounds are also reported. The last plot in the second row on the right shows the fit of a "control" variable $R_{SIG} = \log[S/(f_R R + f_B B)]$, where f_R and f_B are the fractions of RMD and accidental background events respectively (S, R and B are the PDFs for signal, RMD and accidental background events respectively).

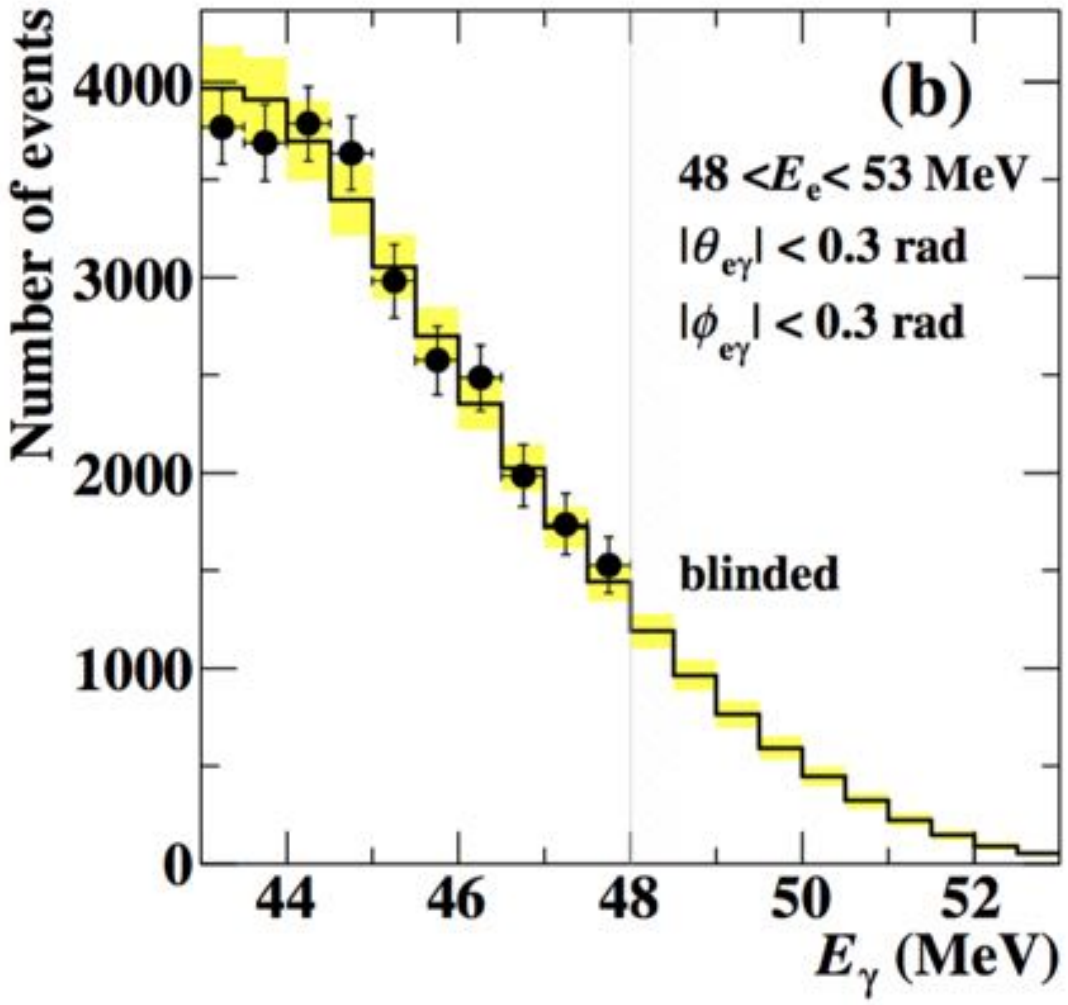

Figure 2.22: Example of extrapolation of the number of RMDs from the energy sideband to the signal region.

For the determination of the Branching Ratio BR($\mu \to e\gamma$), the number of detected events is normalized by using both the number of Michel positrons and the measured number of RMD events. The uncertainty in the BR estimate is $\approx 4\%$ by exploiting the combination of these two independent methods. The computation of the confidence interval is based on a frequentistic method [9] with a profile likelihood-ratio ordering where the number of RMD and accidental background events are treated as nuisance parameters.

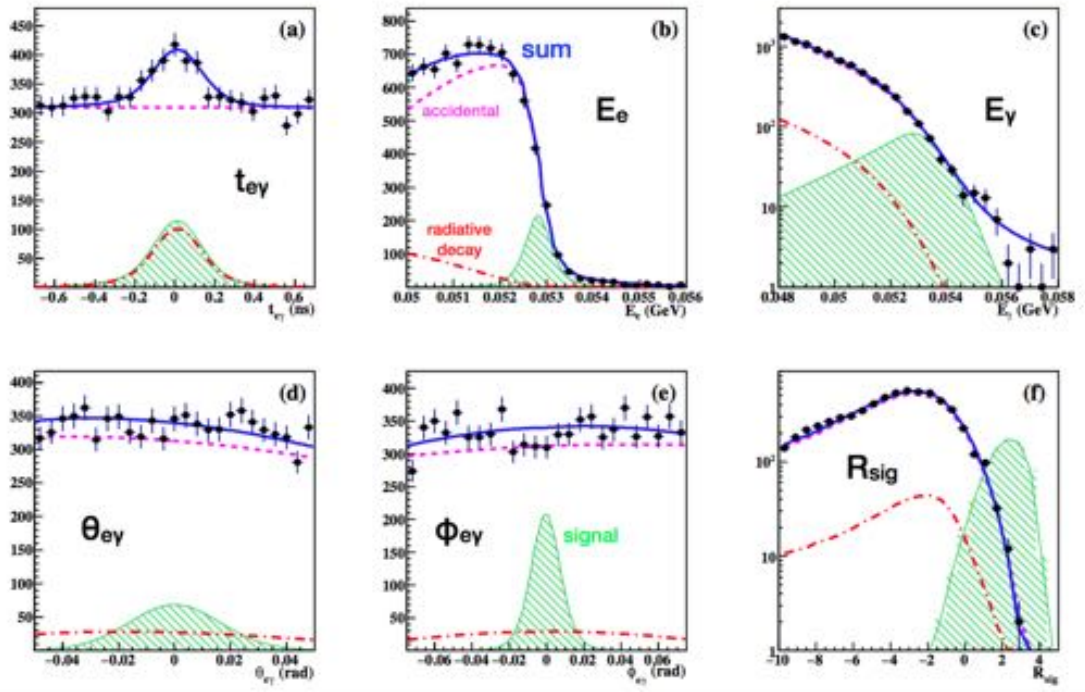

Figure 2.23: Results of the 5D likelihood fit to the events distribution in the physiscs analysis window for the 2009-2013 complete dataset. The experimental data (black points) are shown together with the 5D best fit function projected on each of the five kinematic variables (blue solid lines) characterizing the $\mu^+ \to e^+\gamma$ decay process. The individual best fits for signal in arbitrary scale (green filled areas) and RMD (red dashed-dot lines) and accidental (magenta dashed lines) backgrounds are also shown.

Radiative Muon Decay (RMD) Time Distribution

With the resolutions reached in the MEG experiment and exploiting the full statistics collected, the Radiative Muon Decay (RMD) events are clearly visible in the experimental distribution of the relative time between the final state positron and photon $t_{e\gamma}$ (Figure 2.24). In the early phase of the MEG experiment this peak was not visible due to low statistics and since the initial time resolution was poorer than the final one after several optimizations. The $t_{e\gamma}$ distribution in case of non-correlated e^+ and γ is expected to be flat.

The positron time is measured by the Timing Counter (TC) and corrected with the e^+ Time Of Flight (TOF) by exploiting the reconstructed trajectory. The photon time is measured by the Liquid Xe (LXe) calorimeter and corrected with the γ TOF from the conversion point. The histogram of Figure 2.24 is obtained with the following cuts on the

kinematic variables: 45 MeV $< E_e <$ 55 MeV, 40 MeV $< E_\gamma <$ 48 MeV, $|\theta_{e\gamma}| < 0.3$ rad, $|\phi_{e\gamma}| < 0.3$ rad. Once the aforementioned corrections are applied, the $t_{e\gamma}$ distribution is centered at zero within the experimental resolution: $\sigma_{t_{e\gamma}} = 130$ ps.

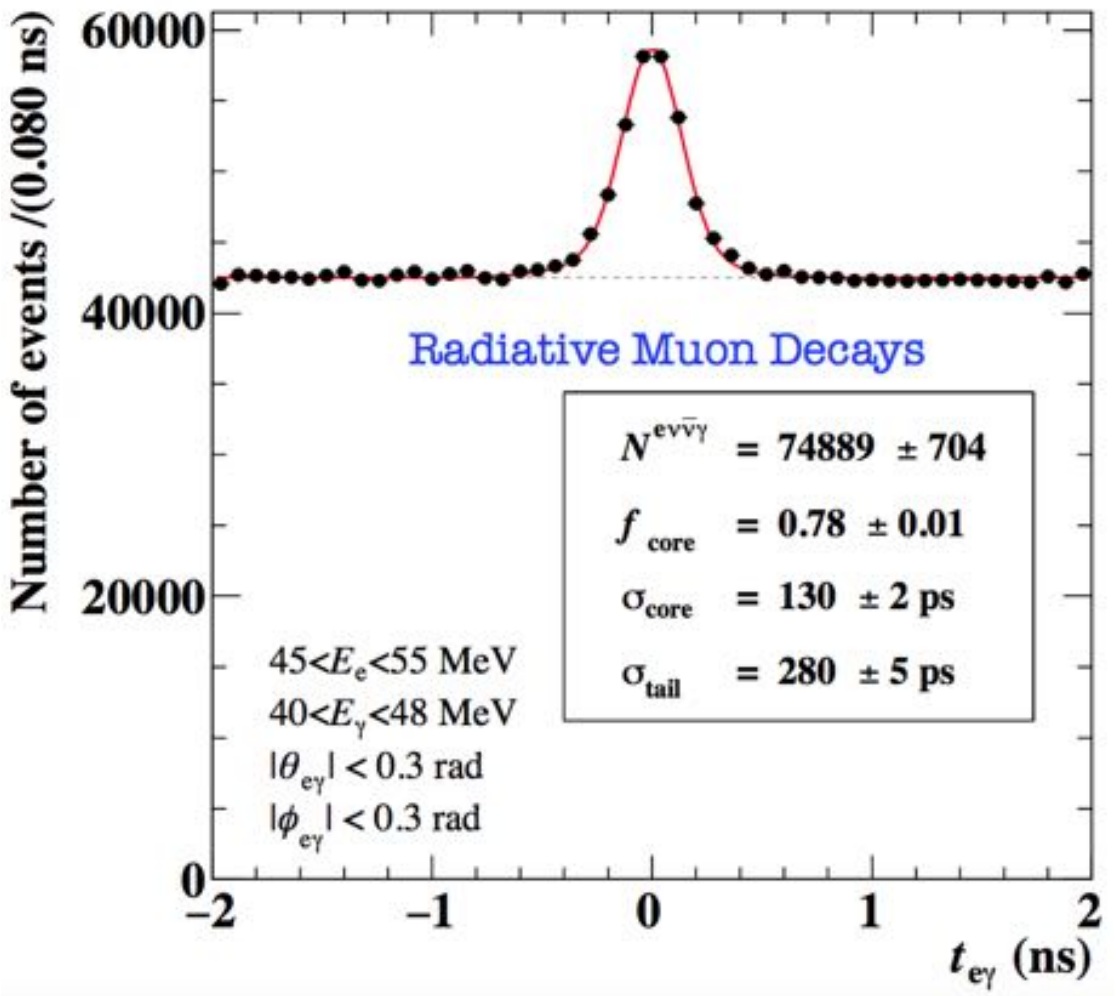

Figure 2.24: The RMD peak in the experimental distribution of the relative time between the final state positron and photon $t_{e\gamma}$.

2.3.4 Final Results of the MEG Experiment

The MEG collaboration has recently presented [52] [51] the final results of the MEG experiment exploiting the full statistics collected in ≈ 4 years of data taking, from 2009 to 2013, updating and lowering the previous upper limit on the $\mu^+ \to e^+\gamma$ decay process BR $\leq 5.7 \times 10^{-13}$ at 90% Confidence Level (C.L.) [17] with the analysis of 2009-2011

data and a total number of stopped muons in the target of $\approx 3.6 \times 10^{14}$ (half statistics). The new best upper limit is $\mathbf{BR}(\mu \to e\gamma) \leq 4.2 \times 10^{-13}$ **at** 90% **C.L.** (Figure 2.25 and Table 1.1), for a total number of stopped muons is $\approx 7.5 \times 10^{14}$. The improvement with respect to the previously published best limit set by the MEGA experiment [35] at the Los Alamos National Laboratory Meson Physics Facility (LAMPF) accelerator is by a factor of 30, with more than a factor of three in statistics.

With the MEG upgrade (MEG-II, see Chapter 3 and the following Chapters) an overall improvement on the BR($\mu \to e\gamma$) of at least one order of magnitude is expected (Figure 2.25 and Table 1.1).

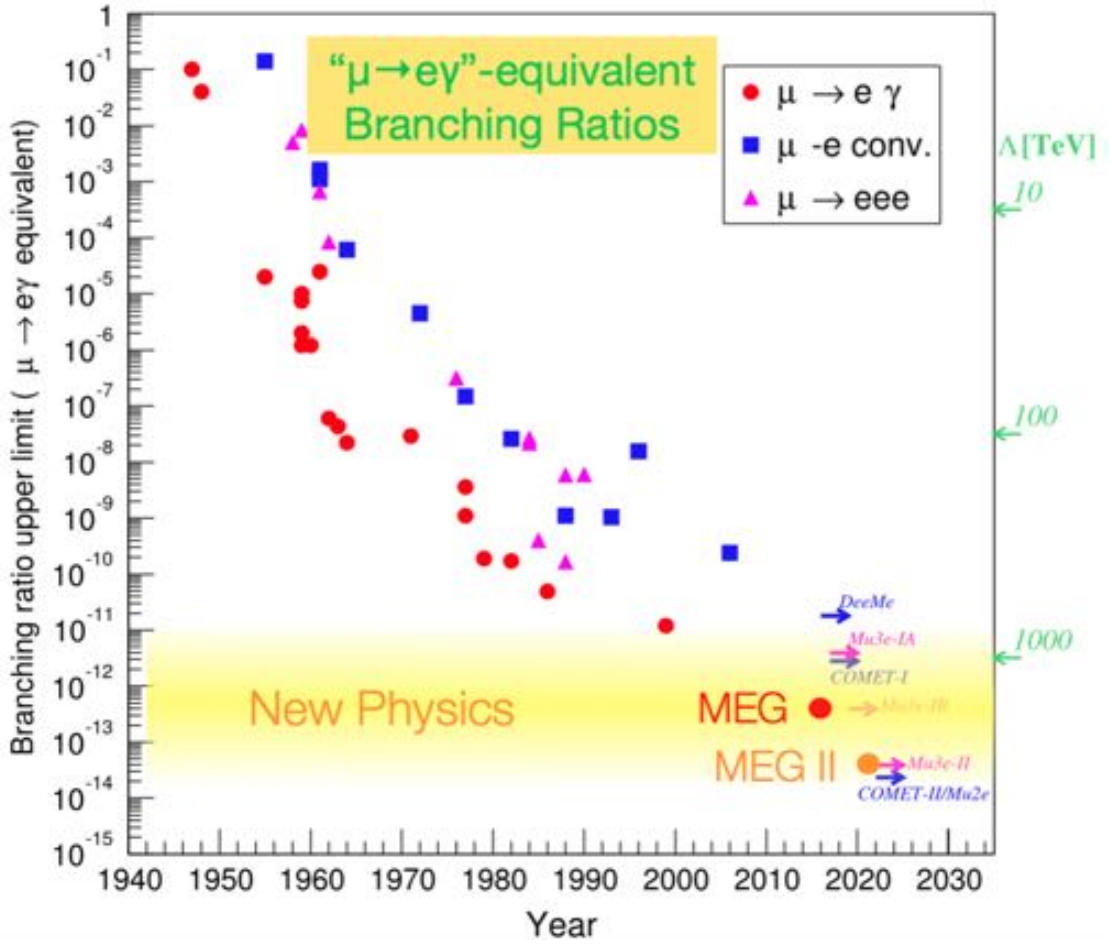

Figure 2.25: Sensitivity comparison between the last MEG results and the expected upper limits foreseen for MEG-II and the other main CLFV experiments.

In Figure 2.26 the events distribution for the complete MEG dataset in the signal region is shown with superimposed the contours of the confidence intervals at 68%, 90%

and 95% probability. The variables of interest are the reconstructed positron and photon energies E_e and E_γ, the reconstructed relative time $t_{e\gamma}$ between the final state particles emission and the reconstructed 3D angle $\Theta_{e\gamma}$ between the e^+ and γ directions of emission.. In the left plot is reported the plane (E_e,E_γ), while in the right plot the plane ($\cos\Theta_{e\gamma}$,$t_{e\gamma}$).

The background events seen close to the signal region do not allow to consider MEG as a background-free experiment any more. The resulting sensitivity would increase only with the square root of the data taking time.

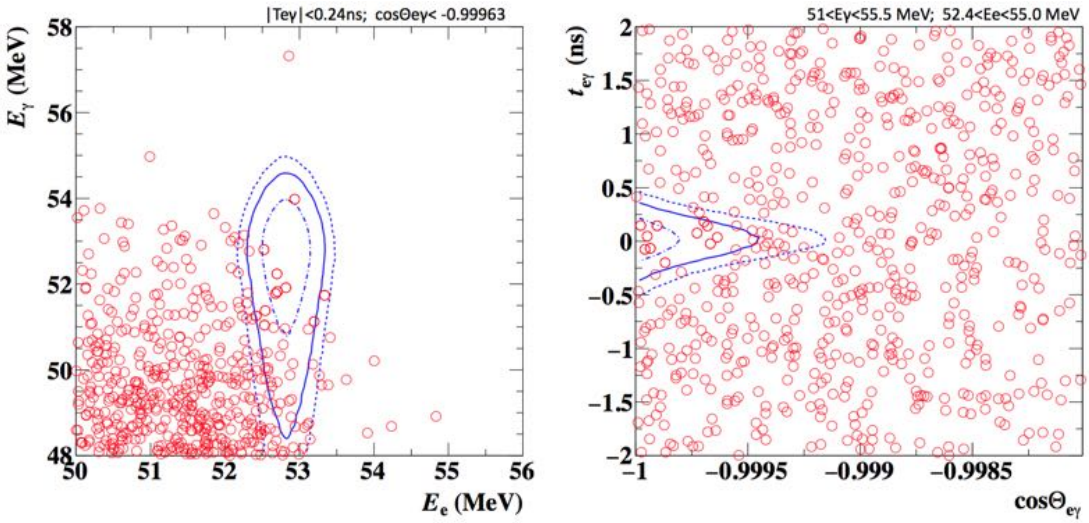

Figure 2.26: Events distribution for the complete MEG dataset in the signal region with superimposed the contours of the confidence intervals at 68%, 90% and 95% probability.

Chapter 3

The MEG Upgrade (MEG-II)

The MEG collaboration set the most stringent constraint on the $\mu^+ \to e^+\gamma$ Branching Ratio (BR) to date. Moreover MEG has imposed one of the tightest constraints on models predicting large LFV-enhancements through New Physics Beyond the Standard Model. The last MEG results [52] [51] have been obtained with the analysis of data collected in the entire data taking period, from 2009 to 2013. The new best upper limit is: $\mathrm{BR}(\mu \to e\gamma) \leq 4.2 \times 10^{-13}$ at 90% C.L., improving the previous constraint of 5.7×10^{-13} at 90% C.L. for the 2009-2011 data analysis [17].

From Figure 2.26, it is clear that the MEG experiment has practically reached its ultimate limit of sensitivity, limited by the resolutions on the kinematic variables of the two decay products. Background events are seen close to the signal region, lowering the experiment sensitivity which does not increase linearly with the acquired data anymore, but tends to saturate. In fact, the total number of stopped muons in the target is $\approx 3.5 \times 10^{14}$ and $\approx 7.5 \times 10^{14}$ for the 2009-2011 and the complete 2009-2013 data taking period respectively. The final doubled collected statistics resulted in an improvement in the $\mathrm{BR}(\mu \to e\gamma)$ upper limit of $\approx 36\%$.

By taking a look both at the design and measured MEG detectors performances, shown in Table 2.1, it is clear that the obtained resolutions, especially for the positrons spectrometer, are worse than expected. For this reason the continuation of the MEG experiment has been proposed and accepted by the PSI scientific committee in January, 2012. It is based on an upgrade of the current experiment which aims at a sensitivity enhancement on the $\mu^+ \to e^+\gamma$ decay process of at least one order of magnitude compared to the final MEG results for a running time of three years, assuming 180 data acquisition days per year.

The MEG upgrade, MEG-II from now on, relies on a series of improvements, which

include new detectors with better acceptances, efficiencies and performances and at the same time operations on the beam line and a new and optimized trigger and DAQ electronics:

1. increase the muons flux and the stopping efficiency on the target;
2. reduce the stopping target thickness;
3. replace the previous positron tracker (DC) with a new single volume drift chamber;
4. use a new tracking procedure which follows e^+'s until they hit the Timing Counter (TC);
5. replace the previous TC with a new highly segmented system;
6. extend the LXe calorimeter acceptance and efficiency;
7. improve the LXe performances;
8. implement new trigger and DAQ electronic boards.

Figure 3.1 shows a schematic overview of the previous MEG experiment compared to the upgrade MEG-II. The numbers refer to the items listed just above in the text.

3.1 Target and Beam Line

3.1.1 Target Thickness

The target thickness determines the intrinsic resolution on the determination of the relative angle between the photon and the positron. Reducing the thickness aims at minimizing the amount of material crossed by the decay photons and positrons and consequentely reduces the Multiple Coulomb Scattering (MCS) and the photon background production possibilities (Annihilation-In-Flight (AIF) and bremsstrahlung) of the outgoing positrons. Together with improved detectors, this leads to better momentum, time and angular resolutions in order to keep the accidental background at the lowest level despite the higher muon stopping rate foreseen for the MEG upgrade (see Section 3.1.2).

The crucial requirement is to maximize the **stopping density**, i.e. the maximal stopping rate in the thinnest possible target. Nevertheless the target thickness in related to the momentum of the incoming muons of the beam. The momentum is selected by the magnetic optics of the πE5 beam line. In MEG, muons originating from a layer of

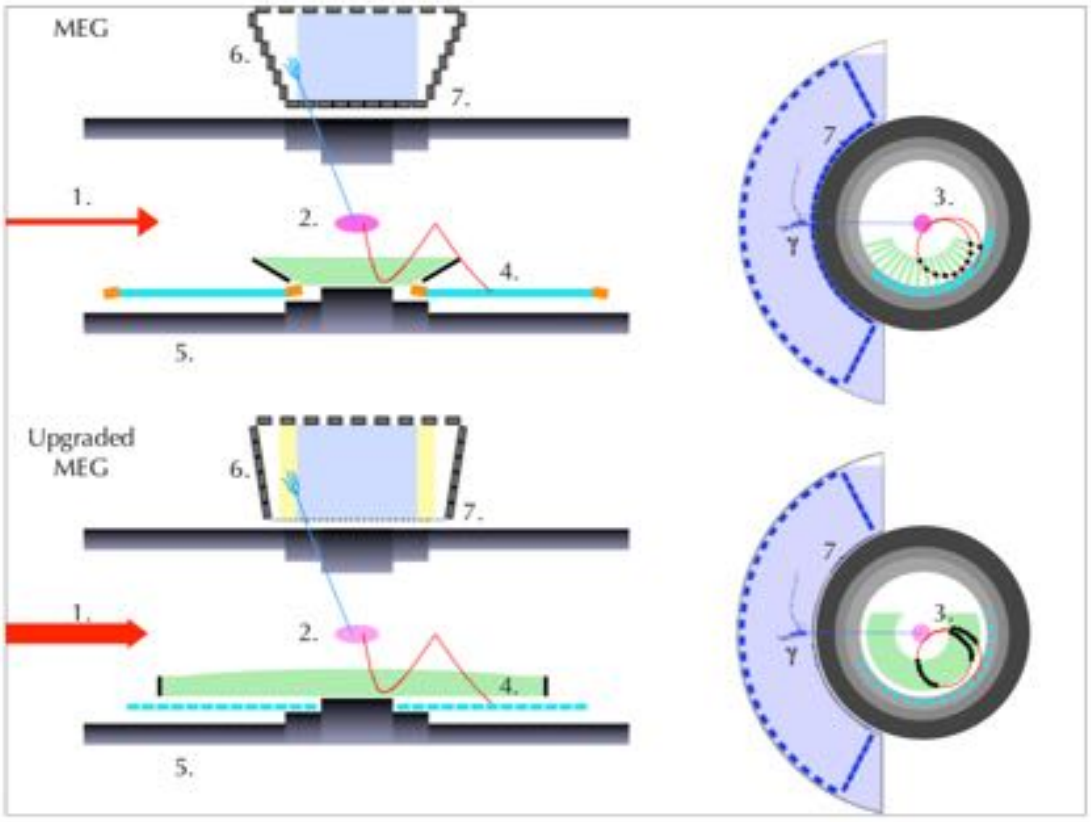

Figure 3.1: Schematic overview of the previous MEG experiment compared to the upgrade MEG-II. The numbers refer to the items listed in the text.

thickness equivalent to a few hundred of microns in the production target surface (*surface muons*) are transmitted and focussed on the stopping target. The total range straggling includes two components: the energy loss straggling of the traversed material (mainly the degrader, the target and the He gas) and the momentum-byte of the beam. For ≈ 30 MeV/c muons the first component contribution is a constant of about 9% of the range, while the range varies strongly with the momentum proportionally to $p^{3.5}$. The total range straggling ΔR_{TOT} is given by the following empirical formula:

$$\Delta R_{TOT} = M\sqrt{(9\%)^2 + \left(3.5\frac{\Delta p}{p}\right)^2}\, p^{3.5} \tag{3.1}$$

where M is a constant depending on the material and Δp is the momentum-byte.

From Equation 3.1 one can see that the most efficient way to reduce the straggling and hence the target thickness is by reducing the beam momentum, rather than lowering

the momentum-byte, due to the p power-law dependence. The central momentum for shallow muons is approximately 28 MeV/c, but the πE5 magnetic channel can be tuned to transmit muons with a momentum window centered at about 25 MeV/c. These are the so-called **sub-surface muons**, since the muon acceptance layer in the production target now lies below the surface. Monte Carlo (MC) simulation studies have shown that the Stopping Quality Factor (SQF), defined as the ratio of target stops to stops elsewhere, is better for sub-surface muons, which can be completely stopped in a target with a thickness of 160 μm at an angle of 15° with respect to the incoming muon beam. The MEG configuration is a target with a thickness of 205 μm placed at 20.5° with respect to the beam axis. Furthermore, the spatial separation between muons and beam positrons in the electrostatic separator (Wien filter) should also be enhanced due to the larger velocity difference in the case of sub-surface muons. Figure 3.2 shows the measured momentum spectrum for the muons provided by the πE5 beam line. The red curve is the fit to data, done with the theoretical $p^{3.5}$ distribution folded with a Gaussian resolution function. The blue and red (truncated) boxes, centered at $\approx$ 28 MeV/c and $\approx$ 25 MeV/c, show the full $\pm 3\sigma$ momentum spread for surface and sub-surface muons, respectively $\pm$2.7 MeV/c and $\pm$2.5 MeV/c.

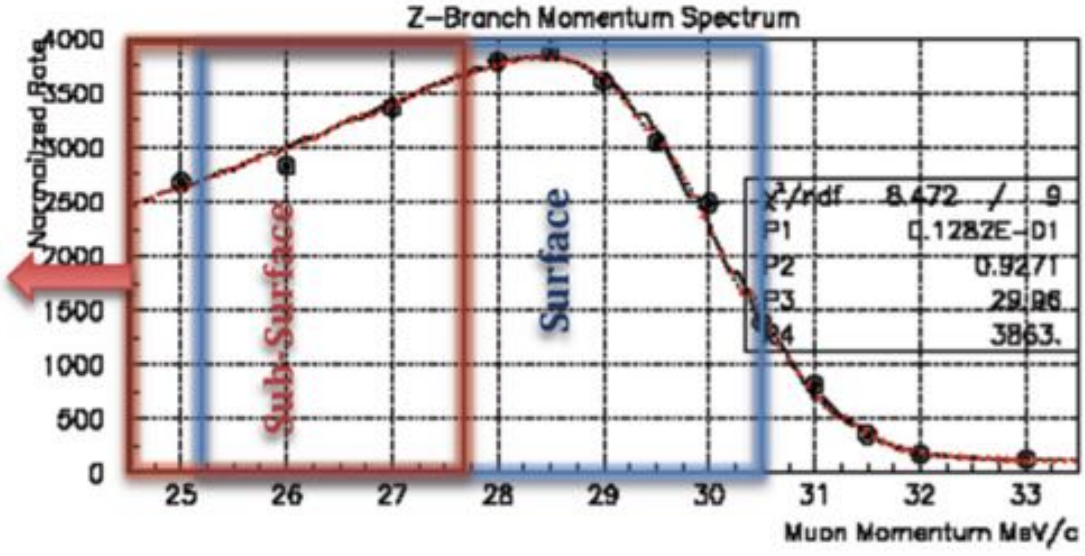

Figure 3.2: Measured momentum spectrum for the muons provided by the πE5 beam line. The red curve is the fit to data, done with the theoretical $p^{3.5}$ distribution folded with a Gaussian resolution function. The blue and red (truncated) rectangles, centered at $\approx$ 28 MeV/c and $\approx$ 25 MeV/c, show the full $\pm 3\sigma$ momentum spread for surface and sub-surface muons respectively.

During R&D studies several options for both the MEG-II stopping target thickness and position have been taken into account. Figure 3.3 shows the SQF as a function of the target thickness for both surface and sub-surface muons and two configurations (15° and 20.5°) for the target angle with respect to the beam axis (slant angle).

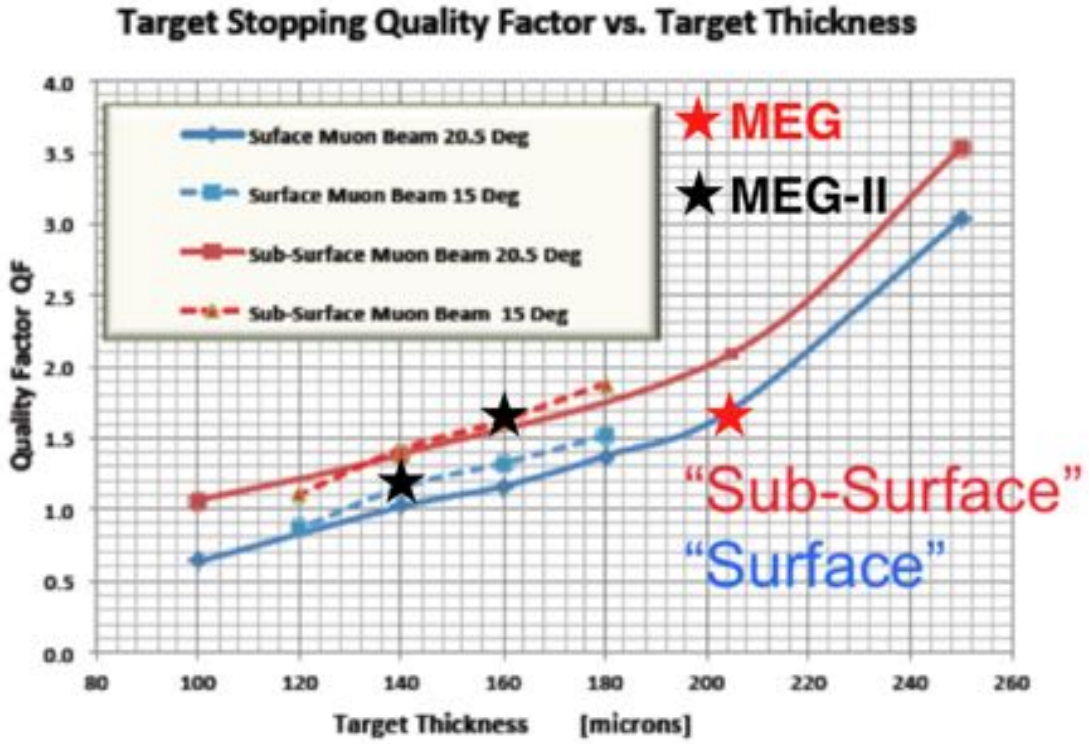

Figure 3.3: SQF as a function of the target thickness for both surface and sub-surface muons and two configurations (15° and 20.5°) for the target slant angle. The working point for MEG-I (red star) and the two possible MEG-II configurations (black stars) are highlighted.

In order to select a beam/target solution that will provide the optimal sensitivity, many factors must be considered such as the stopping rate, which influences the statistics, the central momentum and the momentum-byte, which determine the stopping distribution and optimal target size. This in turn dictates the amount of material encountered by both the incoming muons and the outgoing positrons and photons. All the previous considerations basically lead to two possible options for the MEG-II muon beam and stopping target: a surface muon beam with a 140 μm target thickness and an angle of 15°; a sub-surface muon beam with a 160 μm target thickness and an angle of 15°. These configurations are highlighted (black stars) in Figure 3.3, together with the configuration

used during the first phase of the MEG experiment (red star).

3.1.2 Muon Stopping Rate

The optimal signal sensitivity for the MEG experiment has been achieved for a muon stopping rate of 3×10^7 Hz, approximately a factor of three lower than the maximal rate achievable ($> 10^8$ Hz). However, thanks to higher rate capabilities of all the MEG-II detectors, together with improved detectors efficiencies and resolutions, an increase of the muon stopping rate up to 7×10^7 Hz is planned, more than twice that exploited during the first phase of the MEG experiment. Monte Carlo (MC) simulation studies have shown that with the upgraded detectors and the expected μ stopping rate, the sensitivity goal is achievable in three years of data taking.

3.2 The MEG-II Drift Chamber

By taking a look both at the design and measured MEG detectors performances, shown in Table 2.1, it is immediately evident that, while the LXe calorimeter and the TC almost met their requirements, the resolutions and efficiency of the DCs positron tracker are significantly worse than the design values. The consequences are also on the relative e^+-γ time, since $t_{e\gamma}$ contains the length of the positron track from the target to the TC, as reconstructed from the DCs. The positron tracking inefficiency for MEG is mainly due to the DC front-end electronic boards and mechanical support which intercept a large fraction of positrons on their path to the TC. Furthermore, the use of segmented cathode foils (Vernier pads) to reconstruct the z coordinate was partially limited by the low amplitude of the induced signals on the cathodes, making the z measurement more sensitive to the noise. Finally, the DC operation presented some instabilities. In fact, the use in a high radiation environment led to ageing-related problems with discharges preventing the use of some of the DC planes during part of the MEG data taking pariod.

All these issues convinced the MEG collaboration to design and build a new low-mass, single volume, high granularity stereo CYLindrical Drift CHamber (CYLDCH). The new tracker, presented in details in Chapter 4, is designed to overcome the previous limitations and ensure operation at high rates with a long-term detector stability. The reduced radiation length and the higher spatial resolution lead to substantial improvements in the efficiency, momentum and angular resolutions and consequentely a determination of the e^+ kinematic variables with a higher accuracy.

3.2.1 Single-Hit Resolution and Gas Mixture Choice

Charged particles are detected in drift chambers because they ionize the gas along their flight path. The energy required for ionization is very small, typically a few keV per cm of gas in normal conditions. The energy loss distribution for signal positrons passing through the gas mixture of new MEG-II CYLDCH is shown in Figure 5.9. The ionization electrons of every track segment drift through the gas and are amplified near the wires in avalanches. Electrical signals that contain information about the original location and ionization density of the track segment are recorded.

The particle trajectories are reconstructed by measuring the impact parameter of the track on sense wires. Generally the impact parameter is reconstructed from the drift distance of the first ionization cluster arriving on the anode wire. Because of the discreteness of ionization sites, the drift distance of the nearest cluster to the sense wire is always larger than the impact parameter (see the left picture of Figure 3.10). The estimate of the impact parameter from the drift distance has therefore a bias that depends on the mean free flight path for ionization: the larger the cluster density, the smaller the bias. The requirement of high transparency makes this effect particularly significant. In fact, for low mass drift chambers, the density of primary ionization clusters is very small and limits the drift chamber spatial resolution, especially for small cells and at small impact parameters. The effect is however mitigated in our case by the average polar angle of $\approx 50^\circ$ of the positrons trajectories, which results in a increase of $\approx 30\%$ of the total number of ionization clusters compared to normal incidence. In order to minimize the bias on the impact parameter the *Cluster Timing* technique, described in Section 3.2.3, will be used in MEG-II.

A basic parameter for the performances of drift chambers is the uncertainty for a single drift cell on the measured distance of closest approach of the particle to the anode, i.e. the single-hit resolution σ_{HIT}. The single-hit resolution, together with the high granularity and the low Multiple Coulomb Scattering (MCS) contribution, plays a fundamental role in the overall sensitivity of the MEG-II experiment, since it directly influences the positrons reconstructed kinematic variables.

Several prototypes were made in order to make a reliable project for the new drift chamber. Among them, one consisting in a system of three parallel copper drift tubes was used to get an estimate of the spatial resolution attainable as a function of the gas mixture. The tubes diameter is 8 mm and the length is 30 cm. The copper walls have a thickness of 200 μm. The three tubes are vertically aligned with the middle one slightly displaced on one side by $\Delta \approx 500$ μm. Anodes are 20 μm gold-plated tungsten wires

and are set at a high voltage of 1.5 kV. The sense wires connections occur inside brass boxes with gas tight connectors. The signals are read out by two Phillips 775 amplifiers (with a total gain of a factor 100 and a bandwidth of 1.8 GHz) and a Tektronix TDS7404 oscilloscope (with a bandwidth of 4 GHz). A cosmic ray telescope, composed of three plastic scintillators, is used to select cosmic ray muons. Two scintillators are placed just above and below the tubes, while the third is placed under a 3.5 cm-thick iron slab in order to select tracks as vertical as possible and to remove the low-energy component of cosmics. A schematical view of the 3-tubes prototype is shown in Figure 3.4. The distance between the through-going particle and the three sense wires as a function of the impinging cosmic ray angle θ for the two possible cases (depending on the sign of θ) is given by:

$$\begin{cases} b_1 = A \sin\theta \\ b_2 = (A + l) \sin\theta \pm \Delta \cos\theta \\ b_3 = (A + 2l) \sin\theta \end{cases} \tag{3.2}$$

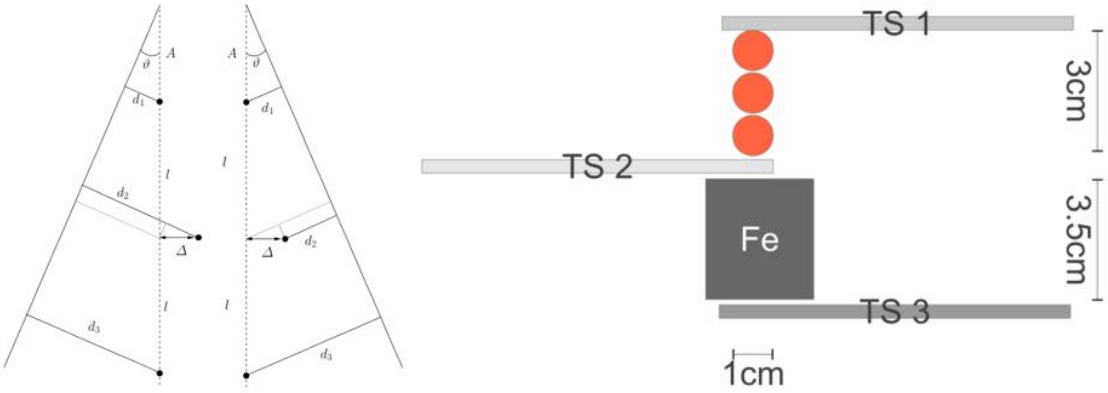

Figure 3.4: The distances between a normal-incident cosmic ray and the sense wires together with a scheme of the 3-tubes experimental set-up.

The expectation value for b_i is given by the measured drift distance d_i ($\langle d_i \rangle \approx b_i$). For almost vertical tracks (with small impinging angles θ) traversing all three cells and not passing in between the sense wires, the combination of the three drift distances gives the displacement estimator $\mathcal{S}$ of the central sense wire.

$$(\pm)\Delta \cos\theta = \frac{d_1 + d_3}{2} - d_2 \quad \rightarrow \quad (\pm)\Delta \approx \frac{d_1 + d_3}{2} - d_2 \equiv \mathcal{S} \tag{3.3}$$

As expected from Equation 3.3, the measured distribution of $\mathcal{S}$ is bimodal (Figure 3.5) and well described by the sum of three Gaussian functions. Two have means $\mu^{\pm}$ centered

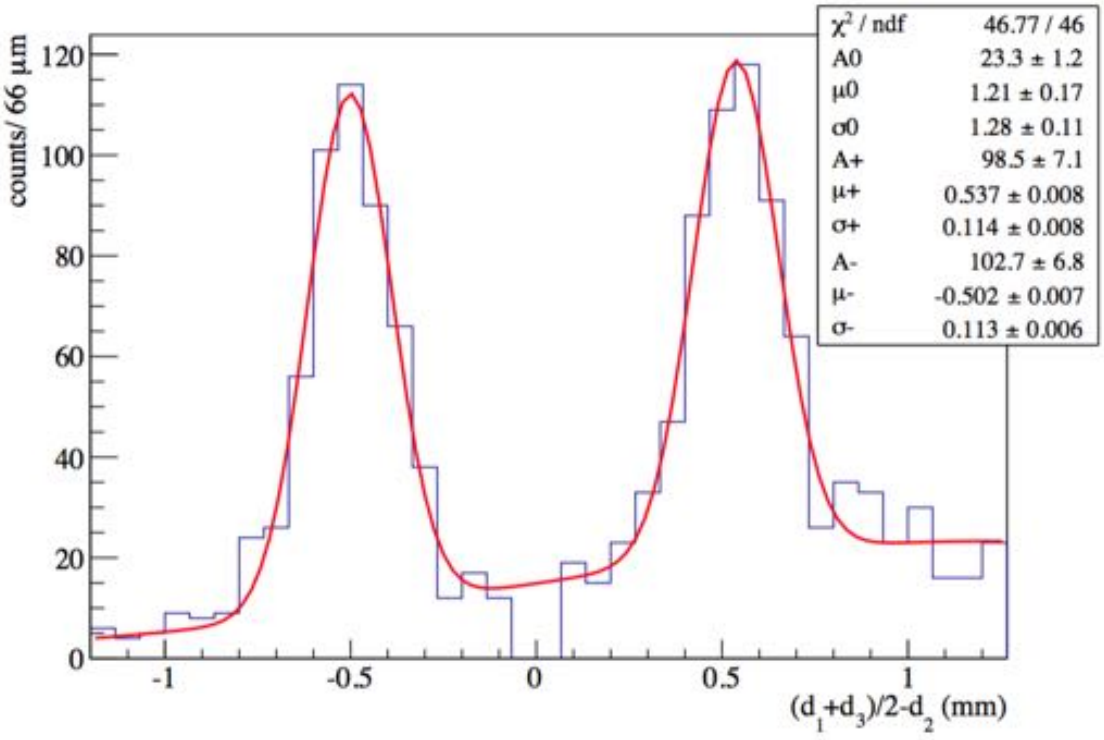

Figure 3.5: Distribution of the measured $\mathcal{S}$ with a triple-Gaussian fit.

at about $\pm\Delta$ and the third takes into account wrong track reconstructions. In fact the approximation of Equation 3.3 does not hold for tracks crossing the zone between the sense wires. Moreover, the resolution worsens for tracks passing in the proximity of the wires. The single hit resolution σ_{HIT} must be smaller than the stagger Δ since otherwise the left-right ambiguity can not be resolved. The average value of the fitted peaks positions $(|\mu^+| + |\mu^-|)/2 \approx 520$ μm, gives a result in agreement with the displacement Δ of the central sense wire, taking into account the uncertainties on the positioning of the anodes. By assuming an equal average resolution for the three drift tubes ($\sigma_{d_1} = \sigma_{d_2} = \sigma_{d_3} = \sigma_d$) and taking the variance of $\mathcal{S}$ from Equation 3.3, an estimate of σ_{HIT} is obtained from the average width of the two peaks of Figure 3.5 $(\sigma^+ + \sigma^-)/2 = \sigma_{\mathcal{S}}$:

$$\sigma^2_{\mathcal{S}} = \sum_{i=1}^{3} \left(\left| \frac{\partial \mathcal{S}}{\partial d_i} \right|^2 \sigma^2_{d_i} \right) \quad \rightarrow \quad \sigma_{\mathcal{S}} \approx \sqrt{\frac{3}{2}}\, \sigma_d \quad \rightarrow \quad \sigma_{HIT} \approx \sigma_d \approx \sqrt{\frac{2}{3}}\, \sigma_{\mathcal{S}} \tag{3.4}$$

The measurement has been repeated with different Helium-Isobutane mixtures. The results are shown in Table 3.1.

He:Isobutane Mixture	σ_{TOT} (μm)
50:50	71 ± 2
75:25	80 ± 4
80:20	90 ± 4
85:15	93 ± 5
90:10	107 ± 7
95:5	115 ± 15

Table 3.1: Measured spatial resolution with different Helium-Isobutane gas mixtures.

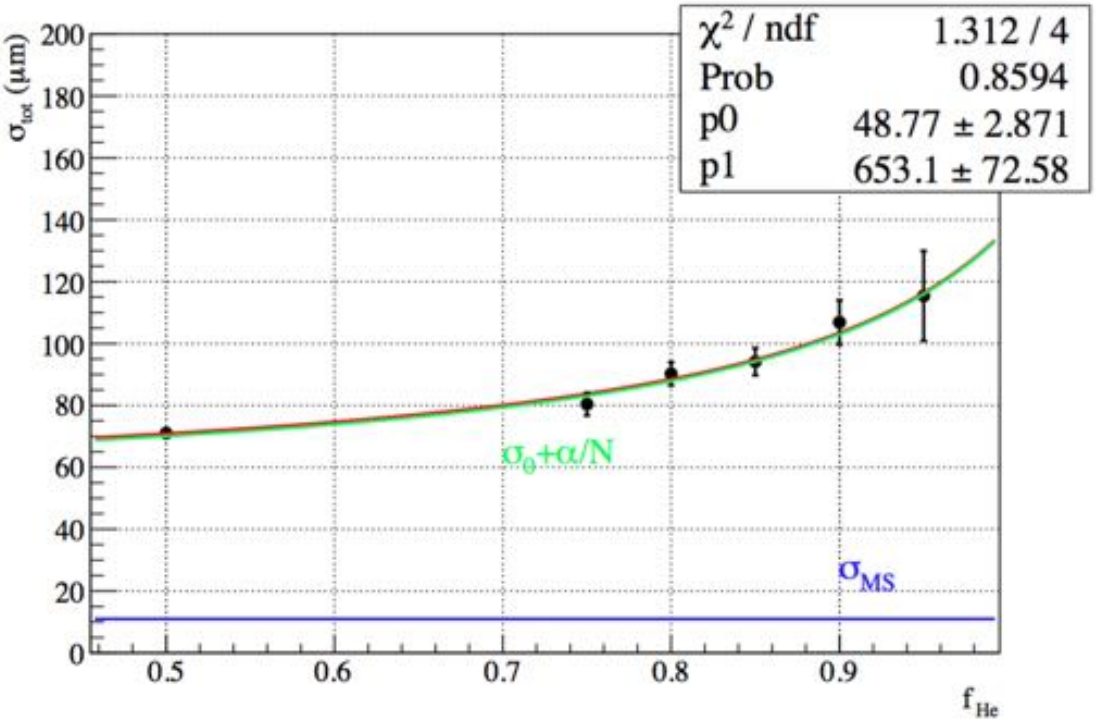

Figure 3.6: The trend of the spatial resolution σ_{TOT} as a function of the He fraction in the gas mixture.

The spatial resolution as a function of the He fraction is reported in Figure 3.6. The experimental points are fitted with the function:

$$\sigma_{TOT} = \sqrt{\sigma_{MCS}^2 + \sigma_d^2} \tag{3.5}$$

where $\sigma_{MCS} \approx 10$ μm is the constant contribution due to MCS of cosmic rays in the

copper walls, added in quadrature to the spatial resolution of the single drift tube σ_d. The gas contribution is modelled as:

$$\sigma_d = \sigma_0 + \frac{\alpha}{N} \tag{3.6}$$

where N is the average number of ionization clusters and σ_0 and α are free parameters. For a given He fraction f_{He}, one has $N = f_{\mathrm{He}} N_{\mathrm{He}} + (1 - f_{\mathrm{He}}) N_{\mathrm{Isobutane}}$, with the average cluster densities $N_{\mathrm{He}} = 7.4/\mathrm{cm}$ and $N_{\mathrm{Isobutane}} = 54/\mathrm{cm}$.

CYLDCH will run with a low-Z counting gas mixture of Helium-Isobutane (He:iC_4H_{10}) in the fraction 85:15, which is the best compromise between track resolution and minimization of MCS. This latter is a critical issue with a large fraction of Isobutane, whose density is 15 times that of Helium (2.59×10^{-3} g/cm^3 versus 0.178×10^{-3} g/cm^3). By comparing the radiation length X_0 of Helium (745 m) and Isobutane (169 m) [19] and by using Equation 4.10, the resulting MCS contribution of Isobutane is twice that of Helium. The single-hit resolution is measured to be 93 ± 5 μm with the 3-tubes prototype filled with the chosen gas mixture. Extended resolution studies with several prototypes are reported in [53]. The combined results of all the tests on prototypes lead to an expected single-hit resolution for CYLDCH of about 110 μm. For the prototypes measurements only the information from the first ionization cluster is used. In the final chamber further improvements are expected with the implementation of a front-end electronics with a wider bandwidth which will allow to exploit the *Cluster Timing* technique (see Section 3.2.3).

3.2.2 Ageing Tests on Prototypes

There is experimental evidence of a deterioration in performances of drift chambers after they have been used for some time. Once the total charge collected on the anode wires during their lifetime exceeds some values between 10^{-4} and 1 C per cm of wire length, a loss of gain and excessive dark currents are observed. One quantifies the lifetime of a wire by adding up the charge that it has collected during its lifetime. This dose is calculated as the product of the total charge which has drifted towards it times the avalanche gain factor. The limit of observable deteriorations depends very much on the gas composition and on the electric field on the electrode surfaces, but also on the material properties of the anodes and cathodes as well as their size. Secondary electrons can be extracted from a thin insulating superficial film formed by material deposits on the cathodes surface by the positive ions that are produced in the avalanches and drift to the cathodes. The surface charge density depends on the balance between the neutralisation rate and the

ion collection rate, the latter being proportional to the rate of charge multiplication on the anode. If the surface charge density increases above some critical value, secondary electron emission from the cathode into the gas becomes possible. This is the so-called Malter effect [58]. The secondary electrons reach the anode and produce avalanches, thus increasing the positive-ion production rate. If the secondary-electron emission rate is sufficiently high, the process becomes self-sustaining and the dark current remains, even if the source of the primary radiation is removed from the chamber. The only way to stop the process is by turning down the anode voltage. An efficient way of preventing the development of cathode deposits is to keep the electric field at the cathode surfaces low. Another cause of standing currents and of the breakdown of chambers is the so-called whiskers: fine strands of material growing on the cathode or the anode. Glow discharges may appear due to the large fields they create. The growth of whiskers is primarily related to the gas composition.

During the entire acquisition time of the upgraded MEG experiment (MEG-II) the total charge collected by the innermost cells of the new CYLDCH is evaluated to be ≤ 0.4 C/cm for a gain of 10^5 and a muon stopping rate of 7×10^7 Hz. This represents a huge amount of charge collected on anodes and cathodes and therefore a study of the CYLDCH ageing is mandatory. The drift chambers ageing induces gain loss, excessive chamber current, self-sustained discharges, sparking and high voltage instability. This is predominantly caused by the free radical polymerization.

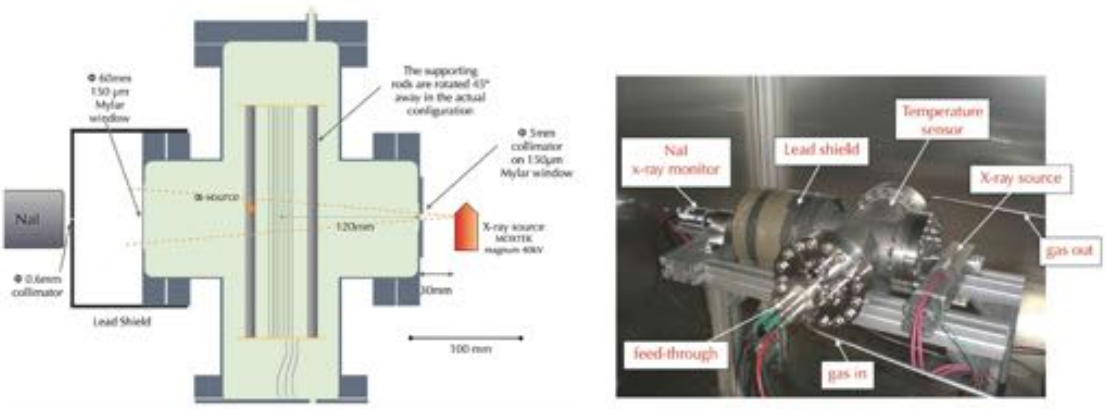

Figure 3.7: Experimental set-up for the ageing test on the drift cell prototype.

During a test, a CYLDCH cell prototype was irradiated with a ^{241}Am α-source with an activity of about 1 Bq, since with the help of intense radioactive sources the ageing process occurs within shorter periods of time. The chamber gain was monitored as

a function of the total integrated charge. The ageing test was performed on a 7×7 mm^2 cell prototype of 20 cm length surrounded by field shaping wires mimicing the presence of all the other cells. The gas mixture was He:iC_4H_{10} 90:10. All wires were in gold-plated tungsten: the central sense wire had a diameter of 20 μm, while the field and shaping wires had a diameter of 80 μm. The high-intensity α-source was placed on the cell support structure to provide large ionization signals. These are clearly visible on the oscilloscope with no need of preamplification. The prototype was placed inside a stainless steel chamber with a volume of 3500 cc made of standard CF100 high vacuum components and equipped with HV and signal feedthroughs. It had two 150 μm-thick windows in order to let ionizing radiation through. The wires were soldered on a FR4 PCB and all the other internal connections were made with polytetrafluoroethylene (PTFE)-coated coaxial cables. The test HV configuration was opposite with respect to the final CYLDCH, i.e. negative HV was applied to the field wires while the sense wire was grounded through a Keithley 2635 picoammeter in order to read out the DC current. The entire set-up (Figure 3.7) was placed inside a lead/aluminum box for radiation safety. A commercial MKS gas system was assembled to deliver the gas from bottles containing the mixture to the test chamber. The gas was sampled by a Residual Gas Analyzer (RGA) to monitor the gas composition at the percent level. Gas was flushed at 50 cc/min to provide a complete volume exchange in one hour. A 2.5 cm long-portion of the sense wire was irradiated with a MOXTEK Magnum 40 keV reflection source X-ray gun able to provide $\geq 10^{11}\gamma/(\text{s} \times \text{sterad})$. The stability of the source was monitored by means of a NaI X-ray detector preceded by a lead collimator with a diameter of 600 μm. The rate was measured to be linear with the X-ray source current. Due to the lightness of the gas mixture most of the photons are not stopped inside the sensitive volume. A fraction of photons ionized the gas in the cell region and contributed to the DC current. The test DC current was 20 times the maximum current foreseen in a normal experimental conditions, i.e. 120 nA/cm. The ageing acceleration factor is 20: in ten days an amount of charge equivalent to one full running year is collected. The HV is set to -1250 V for a gain of about 10^4. Even the gain-density relation is measured by modifying the system pressure in order to take into account the daily oscillations induced by the temperature and the corresponding correction factor is applied. Variations of the X-ray source are measured to be well below 1% and daily checks for possible sparks and discharges are done. The cell prototype is irradiated for 15 days continuously and a gain loss as a function of time is observed. The tests shows that a yearly gain drop $< 25\%$ is expected at the hottest spot of the innermost CYLDCH drift cell. The largest fraction of CYLDCH is subject to a gain drop $< 10\%$ per year (Figure 3.8).

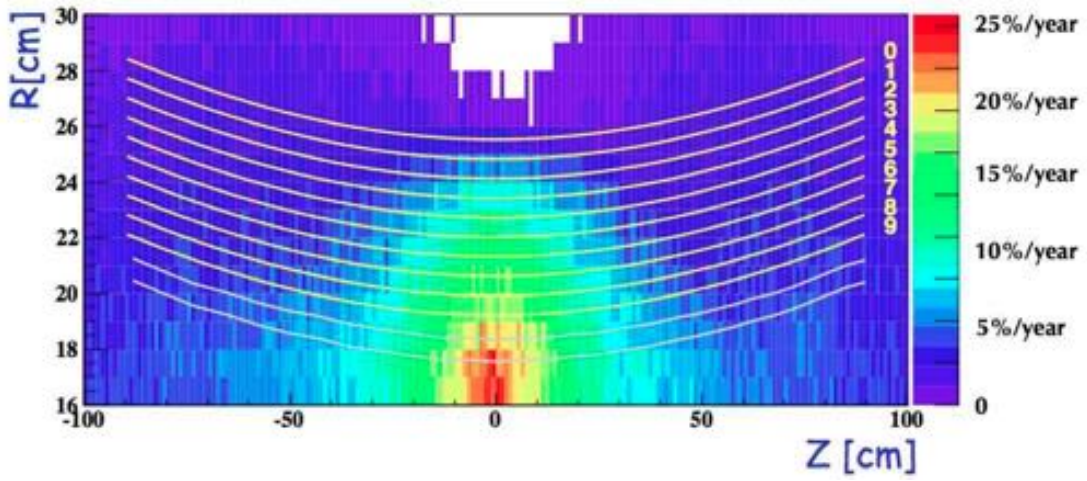

Figure 3.8: Gain drop in one year of DAQ time at 7×10^7 μ^+/s.

3.2.3 Fast Read-Out and Cluster Timing Technique

The use of a low-Z gas mixture such as He:iC_4H_{10} 85:15 is essential for minimizing the effects of Multiple Coulomb Scattering (MCS). The average number of ionization clusters produced by the passage of a 52.8 MeV positron in the counting gas is lower than in the previous MEG Drift Chambers (DC): about 14/cm instead of about 30/cm. This lead to a bias in the measurement of the distance of closest approach, i.e. the impact parameter, of a particle from the anode wire. In Figure 3.9 the single hit resolution as a function of the impact parameter, as measured by the KLOE experiment with a gas mixture of He:iC_4H_{10} 90:10, is shown. In the range of interest of the MEG-II CYLDCH, below 3.5 mm, the contribution of primary ionization dominates.

When a charged particle traverses the gas of a drift chamber, it leaves a track of ionization along its trajectory. The encounters with the gas atoms are purely random and are characterized by a mean free flight path λ given by the ionization cross section per electron σ_I and the density n of electrons:

$$\lambda = \frac{1}{n\sigma_I} \tag{3.7}$$

The probability of having zero interactions along the track length L is:

$$P(\bar{N}, 0) = e^{-\bar{N}} \tag{3.8}$$

where $\bar{N} = L/\lambda$ is the mean number of interactions in the length L. This equation

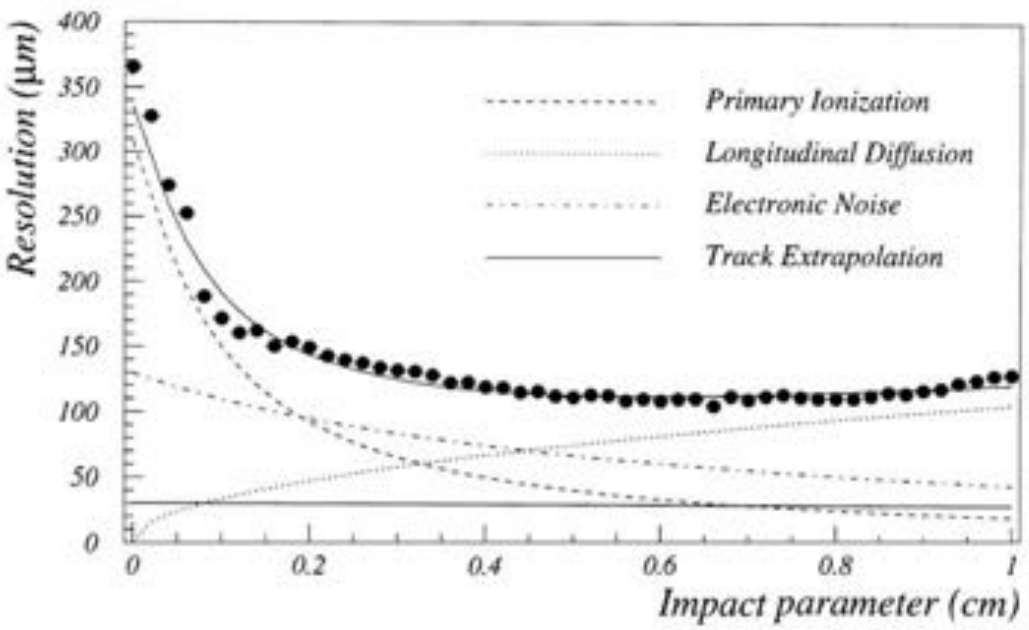

Figure 3.9: Resolution on the drift measurement as a function of the impact parameter as measured by the KLOE experiment. The estimated individual contributions to the final measured values are also shown.

provides a method for measuring λ. If a gas counter with sensitive length L is set up so that the presence of even a single electron in L will always give a signal (ideal detector), then its inefficiency may be identified with Equation 3.8. An estimate of the bias on the impact parameter can be provided by the expectation value of the distance L covered by the particle in the tracker gas. Following Equation 3.8 one obtains:

$$P\left(\frac{2L}{\lambda}, 0\right) = e^{-2L/\lambda} \quad \rightarrow \quad \langle L \rangle = \frac{\lambda}{2} \tag{3.9}$$

For CYLDCH, given the gas mixture He:iC_4H_{10} 85:15, the mean free flight path $\lambda \approx 700$ μm and thus the estimate on $\langle L \rangle$ is about 350 μm. The MEG collaboration proposed to use the **Cluster Timing** technique to eliminate the bias on the positron impact parameter to the sense wire and aim at reaching a single hit resolutions, i.e. the accuracy on the e^+ impact parameter, $\sigma < 120$ μm. This technique, as opposed to the traditional determination of the impact parameter which uses only the arrival time of the first cluster, consists in measuring the time of all the individual clusters and produces a bias-free estimator.

The Cluster Timing technique needs very fast front-end electronics for signal acqui-

sition, the temporal separation between signals produced by different ionization clusters being a few nanoseconds. A new multistage low-noise and low-distortion front-end electronics with a large bandwidth, of the order of 1 GHz, was developed. By employing commercial components, a very compact version of PCB for the front-end has been designed, assembled and successfully tested using both signals from a pulse generator and from the 3-tubes prototype (see Section 3.2.1 and [1]) and the 3-cell prototype (see [53]). With a high voltage power supply of 1.5 kV and a gas mixture He:iC_4H_{10} 90:10 as working conditions, the acquired signal showed a total drift time of about $200 \div 250$ ns and a number of clusters per pulse of about 10, both compatible with what expected.

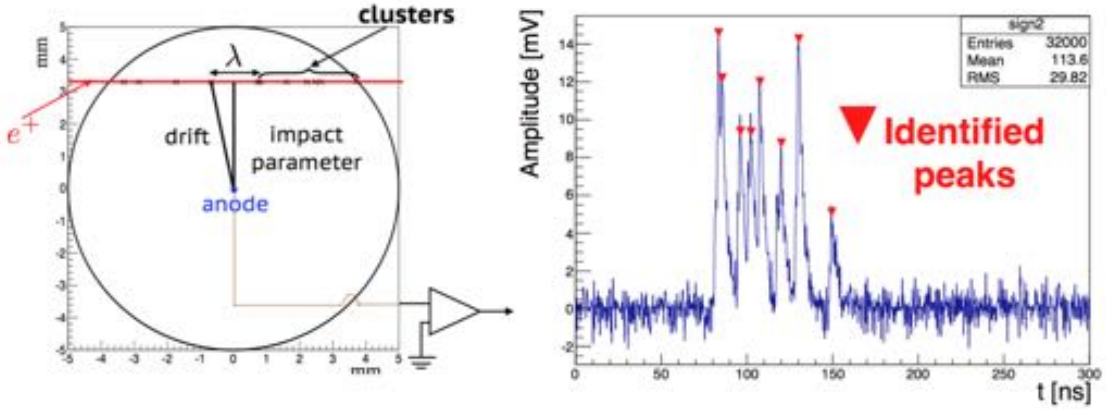

Figure 3.10: Left: distribution of ionization clusters when a e^+ passes through a drift cell and the resulting bias on the measured impact parameters. Right: example of identified peaks in the signal waveform corresponding to the individual ionization clusters. The *Cluster Timing* algorithm exploits this information to reduce the bias and improve the single-hit resolution.

The DRS4 digitizer developed for MEG can work at sampling frequencies up to 2.3 GHz and will be used for digitizing the analog signals from CYLDCH. The implementation of new electronic boards is necessary in order to increase the imput bandwidth, as requested by the Cluster Timing technique and to cope with the increased number of channels needed by the MEG upgrade. In Figure 3.10 (on the left) the distribution of ionization clusters when a e^+ passes through a drift cell and the resulting bias on the measured impact parameters are shown. On the right an example of the identified peaks in the signal waveform corresponding to the individual ionization clusters is shown shown. The *Cluster Timing* algorithm exploits this information to reduce the bias and improve the single-hit resolution.

3.3 The MEG-II Timing Counter

The MEG Timing Counter (TC) experienced a worsening of the intrinsic time resolution during the running phase of the experiment up to 65 ps compared to the excellent time resolution of 40 ps shown during the preliminary beam tests before the experiment. There are several reasons for this:

- the high intensity magnetic field provided by the COBRA magnet causes a gain lowering of the PhotoMultiplier Tubes (PMT) amplification stage up to a factor of 30 and an increase of $\approx 5\%$ in the Transit Time Spread (TTS), leading to a larger time-walk contribution on the time resolution, up to ≈ 20 ps;
- a positrons sometimes can leave double hits in a single TC bar. The scintillation pulse width is increased by the large z projection of the tracks which produces a tail component in the time response function. This gives an further time spread of ≈ 20 ps;
- the contribution of the electronic time-jitter alone is ≈ 40 ps.

Furthermore, the PMTs occupancy of ≈ 1 MHz/PMT is at the edge of their working point. The foreseen increment of the muon decay rate for MEG-II, up to a factor of three, requires a segmentation of the detector. All these issues lead the MEG collaboration to design and build a new highly segmented, fast TC array.

The new pixelated TC is composed of two sets of semi-cylindrical shape scintillation detectors similarly to the MEG TC, but each detector hosts many ultra-fast plastic scintillator tiles coupled to two Silicon PhotoMultipliers (SiPMs) connected in series at each side for the light collection. The positron impact time for the single pixel is obtained by averaging the times measured at both sides. The pixel dimensions are $30 \times 90 \times 5$ mm^3. The SiPMs (Figure 3.11) are interesting because of their compact size, low power consumption, excellent time resolution (< 100 ps for a single photo-electron), high photon detection efficiency peaked at ≈ 450 nm and sensitiveness to single photon, high internal gain ($10^{5 \div 6}$), low bias voltage (< 100 V) and no avalanche fluctuation (excess noise factor $\approx 1 \div 1.5$). The detector is operational in the COBRA bore filled with He gas and the SiPMs are insensitive to the magnetic field. The analog signals from the semiconductor sensors are directly send to the DAQ board and digitized at 2 GHz. The issue of double hits in the same scintillator is avoided by the new pixelated TC. The flexibility of the new timing detector is granted since the position and angle of each pixel module can be adjusted individually in order to maximize the geometric acceptance (Figure 3.11). The

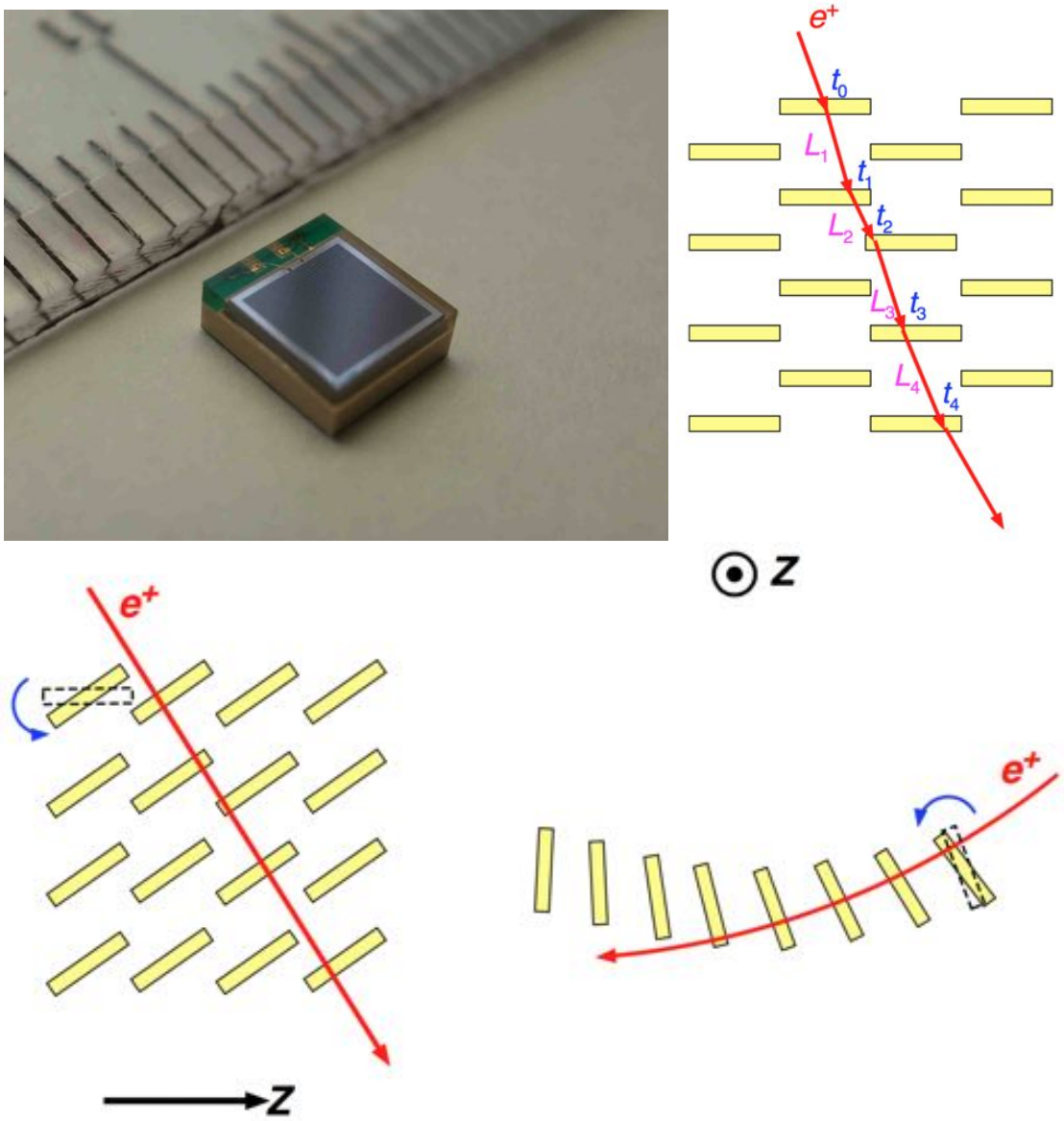

Figure 3.11: Above: on the left a picture of the AdvanSiD SiPM [50] chosen for the MEG-II TC is shown. On the right a schematic view of a positron passing through more than one scintillating tiles is presented with the inter-pixel path and TOF. Below: rotations of the pixel modules in the z-ϕ and r-ϕ planes respectively, in order to maximize the geometric acceptance.

new detector can withstand the increased e^+ rate (7×10^7, see Section 3.1) and allows improved time resolution capabilities in order to minimize the number of background events entering the signal time window. At the MEG-II μ stopping rate, the hit rate at each tile is lower than 1 kHz, thus the pile-up probability is quite low. The segmentation brings an intrinsic improvement in the positron time resolution since ambiguity in the e^+ path length inside the pixel and also in the scintillation light propagation time to the photosensor is small. Moreover, most of the signal e^+'s pass through more than one pixel, thus one can exploit the multiple hit tiles to average the positron time. During the offline analysis it is possible to take into account the e^+ inter-pixels Time-Of-Flight (TOF) by exploiting the positron path length between the hit pixels estimated by the reconstructed track by the CYLDCH and extrapolated to the TC (Figure 3.11). The multiple pixel hits can provide additional track information. In fact, the new improved e^+ tracking procedure follows the positron trajectory up to the entrance of timing detector and measures the position of the impact point on it by exploiting the new tracker and TC layouts.

The uncertainty in the extrapolation of the track to the TC should be small. The accuracy of the estimation of the path length between the pixels is degraded by Multiple Coulomb Scattering (MCS) in the hit pixels. The overall time resolution σ_{TOT} for a given number of hit pixels N_{HIT} can be expressed as:

$$\sigma_{TOT} = \sqrt{\frac{\sigma^2_{SINGLE}}{N_{HIT}} + \frac{\sigma^2_{INTER}}{N_{HIT}} + \sigma^2_{MCS}(N_{HIT})} \tag{3.10}$$

where σ_{SINGLE} is the time resolution of the single pixel, σ_{INTER} is the contribution from misalignment in time or time-jitter between pixels, which is estimated to be $\leq 30 \div 40$ ps for the planned electronics and σ_{MCS} is the contribution from MCS. The first two terms are reduced as N_{HIT} increases. The latter quantity gets worse as N_{HIT} increases. The MCS makes the actual e^+ track deviate from the reconstructed one. The angular spread is estimated to be ≈ 35 mrad for each scintillating tile which corresponds to ≈ 5 ps uncertainty in the inter-pixel TOF correction. The improvement of the overall time resolution gets saturated for large N_{HIT}.

Monte Carlo (MC) simulation studies show a resolution of about ≈ 55 ps for a single pixel hit, even going down to $\approx 20 \div 30$ ps for multiple pixel hits (Figure 3.12). The time calibration can exploit both Michel positrons and a picosecond laser whose light is deliverd to each pixel module through optical fibers. Two things to keep under control are the modest radiation hardness and the temperature stability of the SiPMs in the experimental environment.

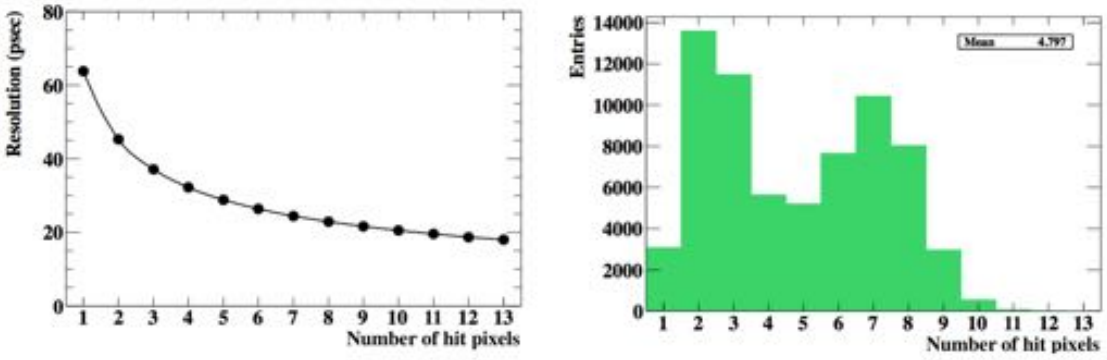

Figure 3.12: Left: time resolution of the new TC as a function of the number of hit scintillating tiles. Right: distribution of the number of hit pixels for signal positrons.

Half of the downstream module of the new TC has just been installed in the experimental area and the first data has been taken during the last engineering run with Michel e^+ at PSI. Figure 3.13 shows the insertion of the partial section of the TC inside the COBRA bore under the new CYLDCH mechanical mock-up (see Section 4.2.3), together with an example of event display with the hit tiles and the related waveforms and a simulated signal positron as seen by the whole timing detector.

3.4 The MEG-II Calorimeter

The LXe calorimeter is a key ingredient of the MEG experiment to suppress the background in $\mu^+ \to e^+\gamma$ decay search. Therefore, substantial improvements of the detector performances, geometric acceptance and energy, position and time resolutions, are crucial for the upgrade of the experiment (MEG-II). The calorimeter energy resolution is dependent on the depth of the γ-conversion: reconstruction capabilities are worse for photons converting close to the inner face and at the edge of the acceptance. The non complete coverage of the entrance face by the 2" PMTs introduces a strong photo-detection non-uniformity, and close to the lateral faces the PMTs arrangement causes loss of acceptance. The left picture of Figure 3.14 shows the scintillation light collection efficiency of the MEG-I LXe calorimeter as a function of the depth of the first interaction for signal γ's. The Photon Collection Effciency (PCE) strongly depends on the incident position. The non-uniform response is partly corrected in the offine analysis, but it still deteriorates the energy and position resolutions due to the event-by-event fluctuations of the shower shape, especially for events with a shallow γ conversion point, at a distance ≤ 2 cm from the entrance LXe face (shallow events). Events with γ conversion points at a

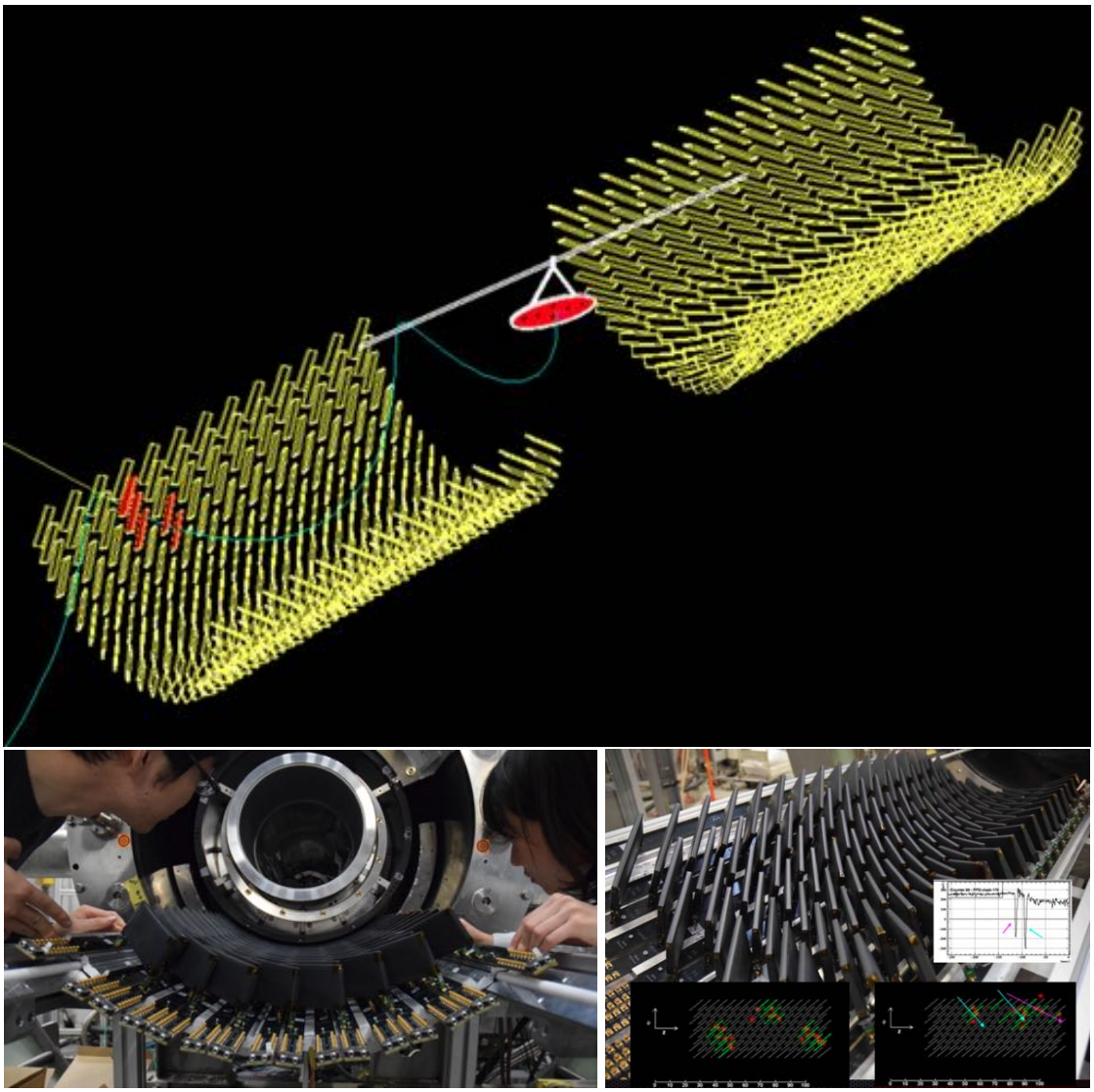

Figure 3.13: Above: simulated signal positron as seen by the new pixelated TC. Below: insertion of half of the downstream section of the TC inside the COBRA bore under the new CYLDCH mechanical mock-up, together with an example of event display with the hit tiles and the related waveforms taken during the last engineering run at PSI.

distance > 2 cm from the entrance LXe face are considered as deep events.

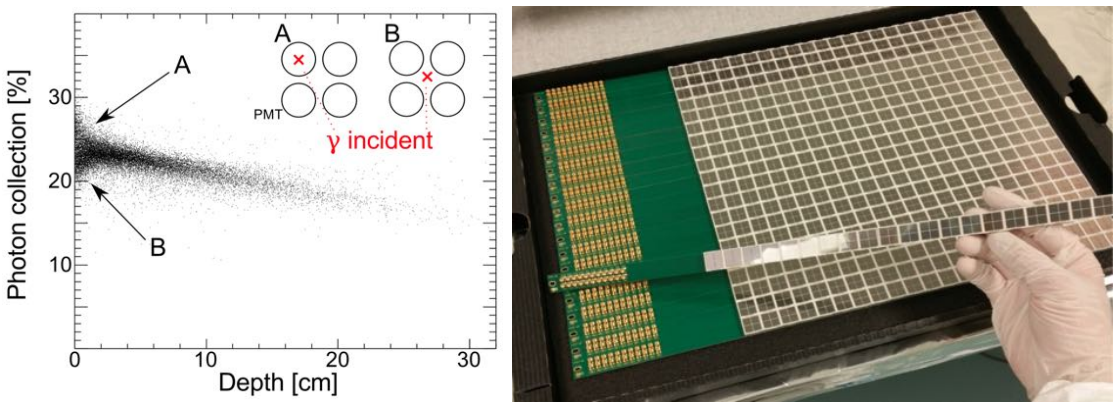

Figure 3.14: Left: PCE of the MEG-I LXe calorimeter as a function of the depth of the first interaction for signal γ's. Right: VUV-sensitive Hamamatsu MPPCs (Multi-Pixel Photon Counter) mounted on PCB strips.

The MEG-II improvements consist in increasing the granularity at the incident face by replacing the PMTs with a larger number of smaller photosensors and optimizing the photosensor geometry on the lateral faces (Figure 3.15).

VUV-sensitive Multi-Pixel Photon Counters (MPPC) with an area of 1×1 cm^2 will be adopted (Figure 3.14 on the right), leading to better spatial (< 3 mm) and time resolutions (≈ 85 ps). The MPPC is a new type of photon counting device developed by Hamamatsu Photonics[1] and is part of the SiPM family. Both the PMTs and MPPCs signals will be readout by the DRS4 boards [26] [27]. The current cryostat (Figure 2.13) will be re-used for the LXe detector upgrade. In order to cover the increase of the external heat inflow due to ≈ 4000 signal cables for the MPPCs, the cooling power of the refrigerator has to be increased either by installing more powerful pulse tube cryocooler or by adding another cryocooler of the same type as the current one.

Improved energy resolutions both for shallow and deep photon conversions have been shown by MC simulations thanks to a more uniform light collection efficiency. Figure 3.16 shows a MC simulation of the energy response of the LXe calorimeter for the MEG experiment (above) and for MEG-II (below) for events with shallow (on the left) and deep (on the right) conversion points respectively. The expected energy resolutions are obtained from the fit to the corresponding distributions (bottom histograms). The fit has been performed with a Crystal Ball function, consisting of a Gaussian core portion and a power-law low-end tail. The σ's of the Gaussian core provide an energy resolution

[1] http://www.hamamatsu.com/eu/en/index.html.

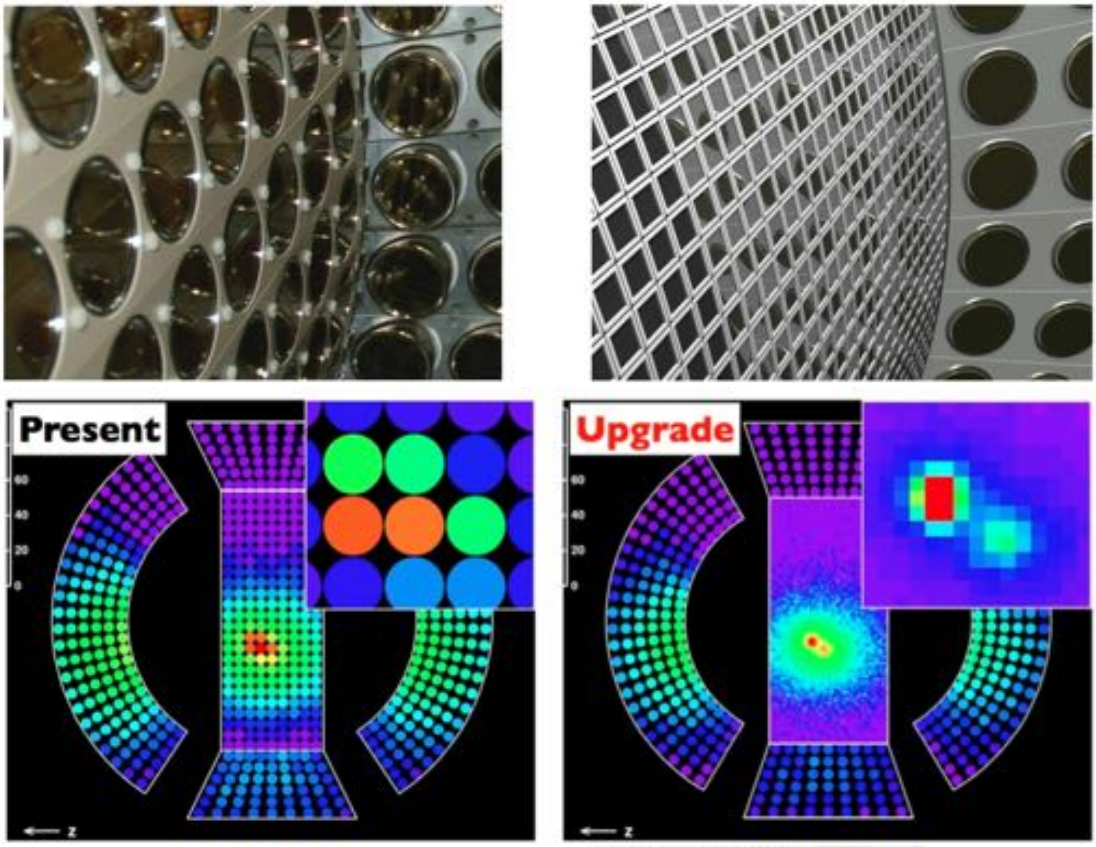

Figure 3.15: Above: interior view of the LXe calorimeter before (on the left) and after the detector upgrade (on the right) for MEG-II. Below: example of scintillation light distribution as seen by the MEG LXe calorimeter equipped with PMTs on the entrance face (on the left) and by the upgraded LXe detector with the smaller MPPC photosensors (on the right).

of 1.0% and 1.1% for deep (right plot) and shallow (left plot) events respectively. The signal photon traverses the photosensors on the entrance face. The material in front of the active LXe volume can be substantially reduced in case of using MPPCs which are much thinner than PMTs. The Photon Detection Efficiency (PDE) is estimated to be improved by $\approx 9\%$. The modification of the PMTs layout on the lateral faces extends the LXe calorimeter acceptance by $\approx 10\%$ on each side. The PMTs are tilted such that all the photocathodes lie on the same plane. This operation minimizes the effect due to electromagnetic shower fluctuations for events near the lateral walls.

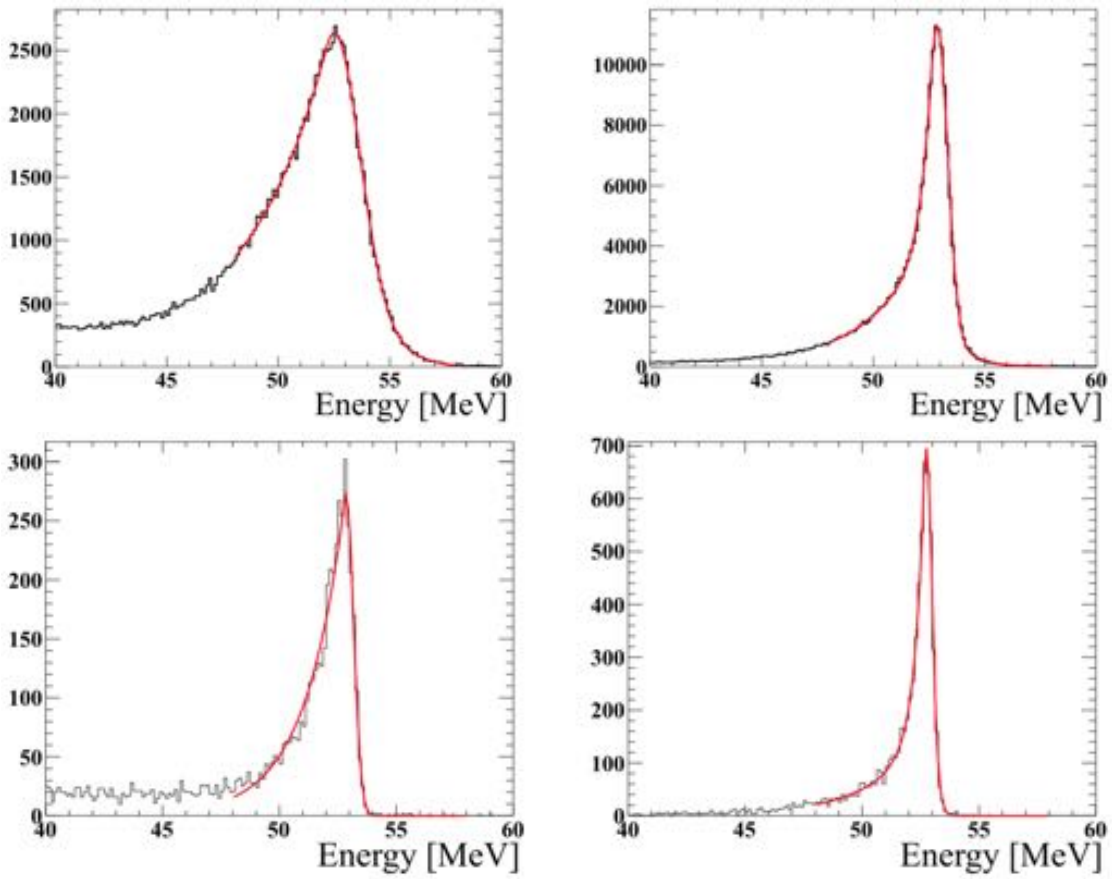

Figure 3.16: MC simulation of the energy response of the LXe calorimeter for the MEG experiment (above) and for MEG-II (below) for events with shallow and deep γ conversion points, respectively at a distance < 2 cm from the entrance LXe face (on the left) and > 2 cm (on the right).

3.5 The MEG-II Front-End Electronics

The stringent requirements of an increased number of readout channels due to the higher granularity of the MEG-II detectors will be handled by a new DAQ scheme involving the implementation of a new combined readout board, called WaveDREAM, capable of integrating the various functions of waveform digitizing, through the DRS4 chip, trigger capability and splitter functionality into one condensed unit, while maintaining a high bandwidth.

3.5.1 DAQ

The new mixed trigger/digitizer DAQ board is very compact given the limited space around the detector. The entire front-end has been optimized to give an overall bandwidth of the order of 1 GHz. This will be granted by an analog front-end with two switchable gain stages which can be combined to obtain a post-amplification by a factor one to about 70. This feature can be used to increase the signal amplitude coming from the CYLDCH and the SiPM pre-amplifiers, which are typical $\sim$ few tenths of mV. More accurate charge measurements is allowed by increasing the amplitude to $\sim$ few hundred of mV, such that the Signal-to-Noise Ratio (SNR) inside the DRS4 chip is improved. New DRS4 timing calibration methods can bring an overall improvement of almost 40 ps compared to the resolution on the relative e^+ and γ times ($\delta t_{e\gamma}$) obtained during the first phase of the MEG experiment: from 120 ps down to 85 ps (see Table 3.2). Furthermore, each channel will have a dedicated comparator which can be used to implement a rate counter or trigger. For the initial tests, the new DAQ board is designed to work in a standalone mode with a Gigabit Ethernet interface for data transfer to a PC. For the final full system, the DAQ boards will be housed in a dedicated custom crate, which can bring a cost-saving factor of three with respect to a standard VME system. The crate can hold up to 16 boards with a total of 256 channels plus a DAQ concentrator board which collects and combines the data before sending them to a PC. The new electronics will exploit the computing power and programming flexibility of modern FPGAs to adapt to the MEG-II requirements, even if they will change during the operation. A simplified schematics of the new DAQ board is presented in Figure 3.17.

3.5.2 Trigger

The functionality of the MEG trigger system will be integrated into the new DAQ boards. The DRS4 chips operate in the so-called *transparent mode* where their input appears directly to the output, where the ADCs can continuously digitize the signals and provide data to the trigger system. The ADC sampling frequency is 80 MSPS with a resolution of 12 bits. For the first phase of the MEG experiment the frequency was 100 MSPS, but no worsening of the photon energy resolution is expected. In fact the potentially poorer determination of the pulse amplitude which is relevant for the γ's energy reconstruction is eventually compensated by the increased ADC resolution, from 10 to 12 bits. The wider dynamic range is crucial to fully exploit the improved single photoelectron response of the new LXe photosensors. As described above, for trigger purposes one can benefit from using the comparators implemented in each input channel, both for TC and LXe for the

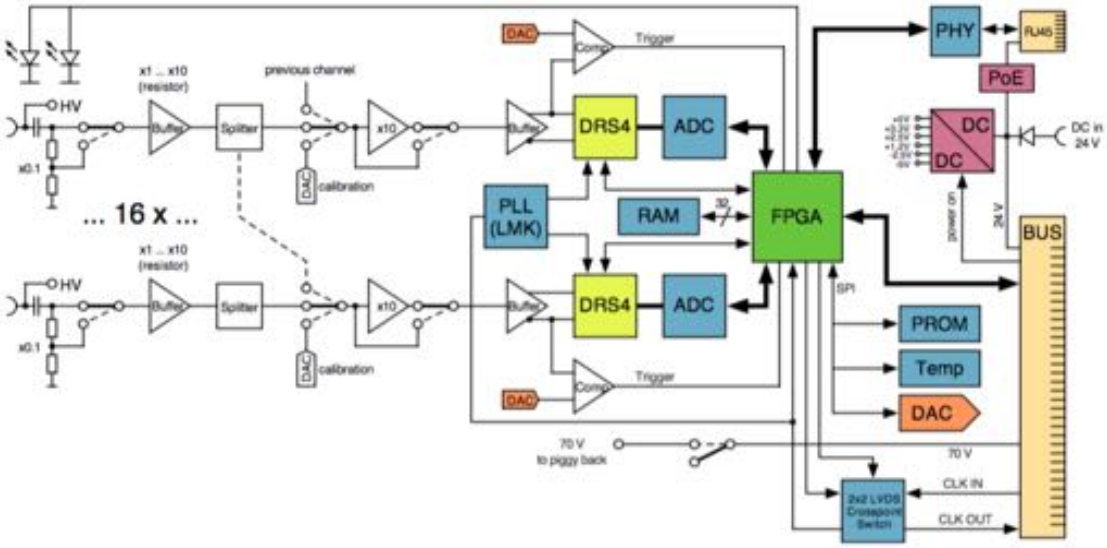

Figure 3.17: Simplified schematics of the MEG-II DAQ board.

determination of the relative e^+-γ time. An overall improvement in time resolution up to 1 ns is expected, even thanks to further refinements to correct for time-walk effects, based on the implementation of look-up tables inside the FPGA. Each board can run a digital algorithm which operates the sum of all 16 inputs and the determination of the maximum pulse amplitude with the related index and the pulse time. This provides the coarse determination of the γ energy, direction and time for trigger purposes, together with the e^+ time from the TC. All values are arranged in a 48-bit bus and passed to proper Trigger Concentrator Board (TCB) through LVDS serializers. The TCBs are designed to receive and combine all the pieces of information from the DAQ boards and are housed at the side of each crate next to the DAQ concentrator boards. Concerning the data storage in view of the data throughput increase, an online zero suppression will be performed.

3.6 Radiative Decay Counter (RDC)

A Radiative muon Decay veto Counter (RDC) will be used for background suppression purposes, basically by tagging low-energy positrons associated with high-energy γ's in the signal region in order to exclude these photons from the signal candidate sample. The dominant source of γ-rays from accidental background events in the MEG analysis window is the Radiative Muon Decays (RMD).

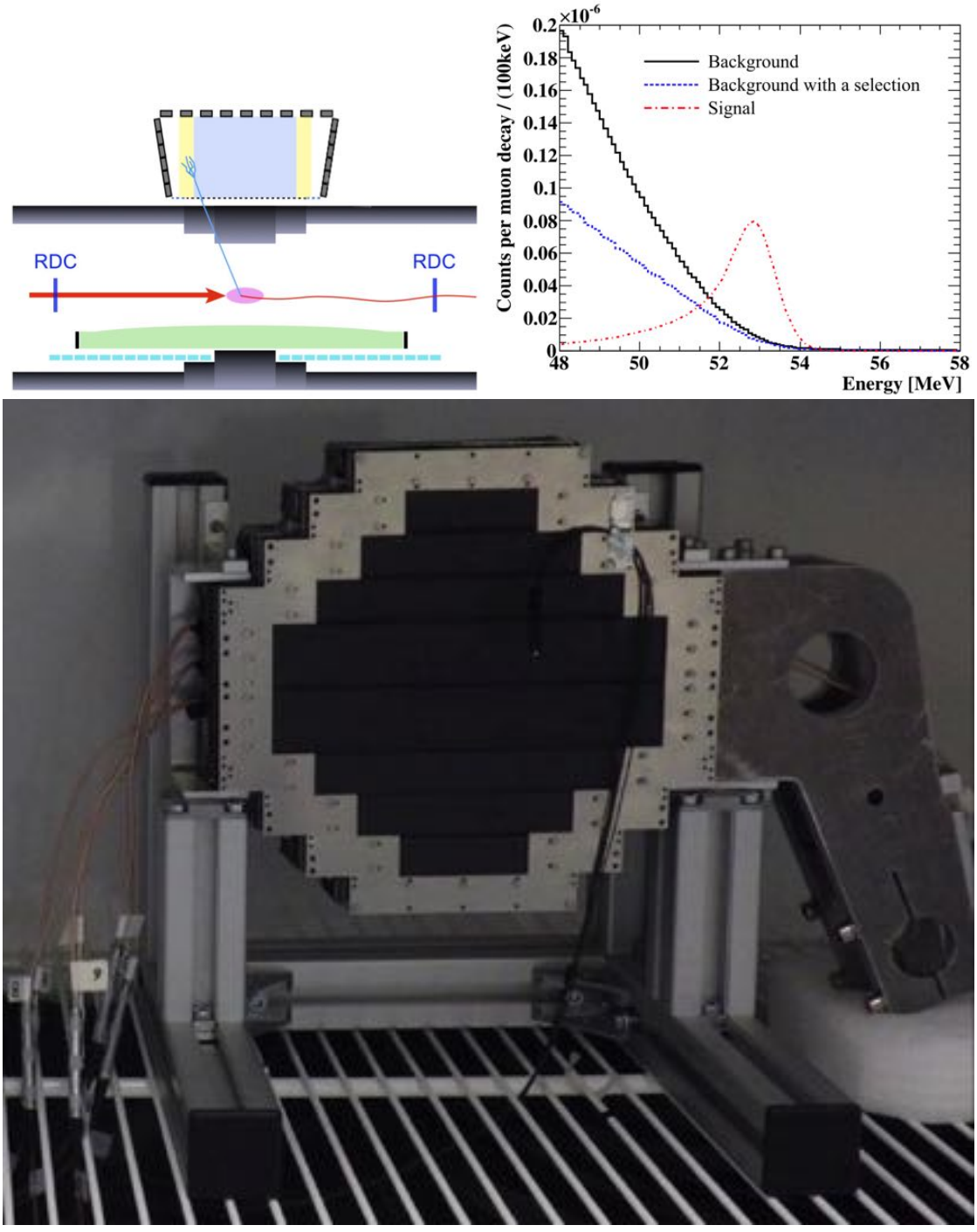

Figure 3.18: Top left: position of the two RDC modules inside the MEG-II detector (the upstream one is not approved yet). Top right: spectrum of background photons detected by the upgraded LXe calorimeter (black histogram) and the same after the rejection of RMD events identified by the RDC (blue histogram). The signal spectrum (red histogram) is arbitrary scaled. Bottom: the downstream RDC module.

For MEG-I, 53% of γ-rays above 48 MeV were from RMDs and the fraction is more for MEG-II because of the reduced background photons thanks to the new CYLDCH. The bending radii of low momentum positrons, say ≤ 2 MeV, are typically smaller than 4 cm and 9 cm at the center and at the end of the magnet respectively. Therefore the RDC has to be mounted on the muon beam axis. The position is far from the center of the magnet and outside the tracking volume, thus neither a significant increase of background γ-rays, nor the reduction of the signal detection efficiency is expected. The detection of the low-momentum positrons will be done using plastic scintillators of about 250 μm thickness and an array of LYSO[2] counters, read-out by Silicon PhotoMultipliers (SiPM). Through Monte Carlo (MC) simulation studies, the tagging efficiency of RMDs is evaluated to be $\approx$ 70% for radiative decays with a photon energy higher than 48 MeV, when the coincidence time window between the RDC and the LXe calorimeter is chosen to be 8 ns. Two RDC modules are foreseen: one in the upstream side and one in the downstream side along the z axis (top left picture of Figure 3.18). The first is not approved yet. The top right picture of Figure 3.18 shows the spectrum of background photons detected by the upgraded LXe calorimeter (black histogram) and the same after the rejection of RMD events identified by the RDC (blue histogram). The signal spectrum (red histogram) is arbitrary scaled. The downstream RDC module is shown in the bottom picture of Figure 3.18.

3.7 Expected Performance

Variable	Design MEG	Obtained MEG	Foreseen MEG-II
δE_e (keV)	200	380	130
$\delta\theta_e, \delta\phi_e$ (mrad)	5,5	9,11	5,4
Efficiency$_e$ (%)	90	40	90
δE_γ (%)	1.2	1.6	1.0
δPosition$_\gamma$ (mm)	4	5	< 3
$\delta t_{e\gamma}$ (ps)	65	120	85
Efficiency$_\gamma$ (%)	> 40	60	70

Table 3.2: Expected performaces of the MEG experiment upgrade (MEG-II) compared to the design and obtained detectors resolutions and efficiencies for MEG-I.

[2]Lutetium-Yttrium orthoSilicate Oxyde: an inorganic chemical compound with main use as a scintillator crystal.

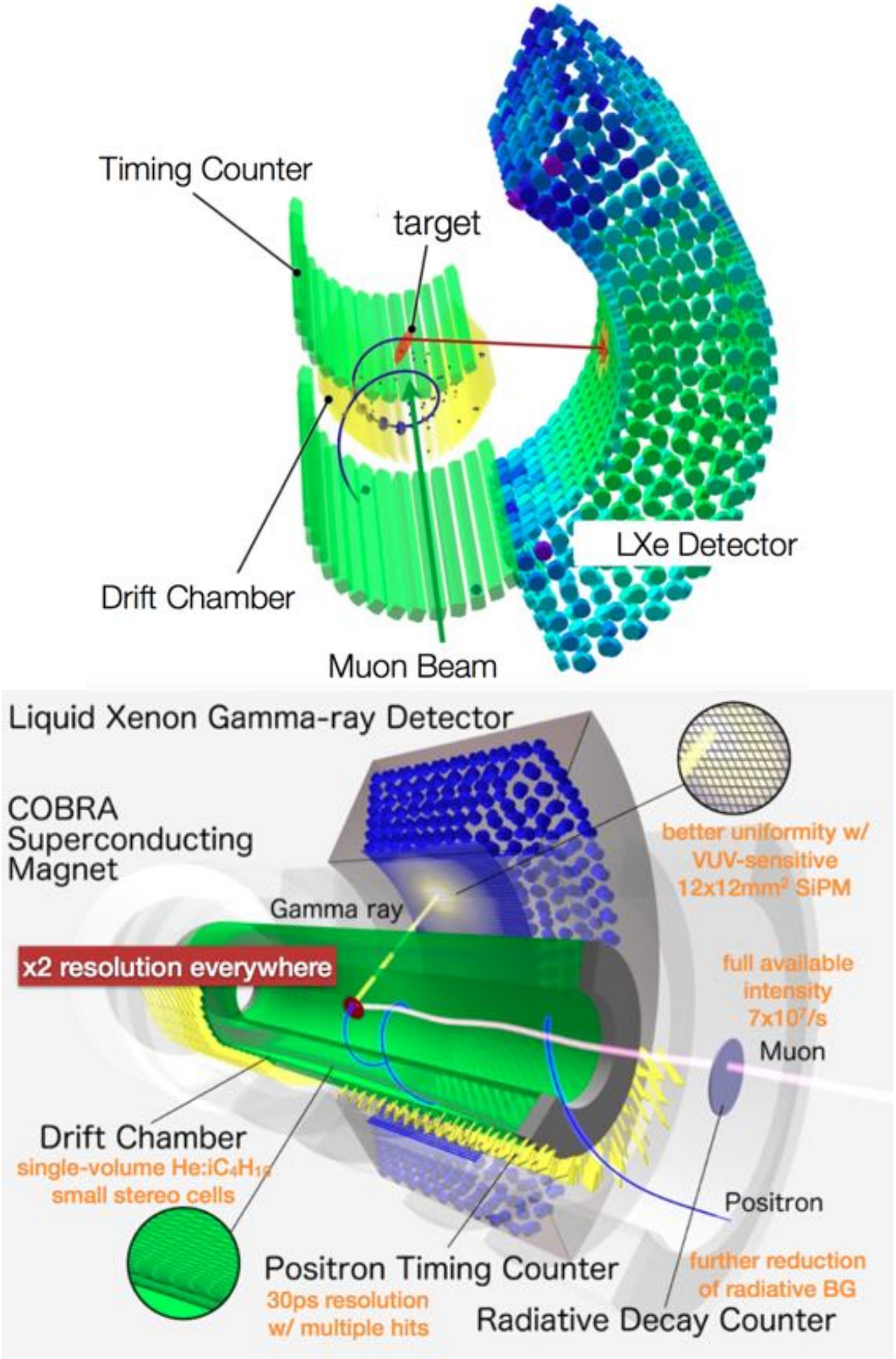

Figure 3.19: 3D schematic view of a signal event as seen by the previous experimental apparatus used during the first phase of the MEG experiment (above) and by the new MEG-II upgraded detector (below). The overall improvements are summarized in the bottom picture.

A summary of the resolutions and efficiencies expected for MEG-II is shown in Table 3.2. The expected trigger efficiency is $\approx 99\%$. The planned improvements in detectors resolutions allow for a larger muon stopping rate up to 7×10^7 Hz, more than twice the previous muon flux on the stopping target, without being overcrowded by the backgrounds (see Section 2.1). From the aforementioned discussion of Chapter 2, it is clear that the accidental background will still be the dominant one, since the expected sensitivity is at the level of 4×10^{-14}. In fact, with detectors resolutions of $\approx 1\%$ on both photon and positron kinematic variables, the Radiative Muon Decay (RMD) rate is expected to be limited at the level of $\approx 10^{-15}$. Figure 3.19 shows a 3D schematic view of a signal event with the previous experimental apparatus used during the first phase of the MEG experiment (top) and with the new MEG-II upgraded detector (bottom). The overall improvements are summarized in the bottom picture.

Chapter 4

The new MEG-II CYLindrical Drift CHamber (CYLDCH)

The MEG-II positron spectrometer consists in a unique volume low-mass CYLindrical Drift CHamber (CYLDCH) with a high granularity and a stereo wires configuration, followed by the multi-tile scintillation Timing Counter (TC) for a precise measurement of the decay e^+ momentum and time respectively. Both detectors are placed inside the COBRA superconducting gradient field magnet designed specifically for the MEG experiment (see Section 2.2.2). In the new configuration the amount of material crossed by the particles along their helix trajectories is extremely reduced, allowing a more accurate determination of the decay positrons kinematic variables and an enhanced capability of matching the information reconstructed by the two detectors. In fact, a new improved e^+ tracking procedure will be used in MEG-II. As shown in Figure 3.1, it consists in following the positron trajectory up to the entrance of the TC and measuring the position of the impact point on it by exploiting the new CYLDCH and TC layouts.

The preparation of the new drift chamber involves the common effort of four working groups within the MEG collaboration. The Pisa group is responsible for the mechanical support and integration, but also for the design and production of the the final end-plates and PCBs where wires are soldered (wire-PCBs). The Lecce group is responsible for the wires procurement and tests, the wiring machine with which the wires are soldered to the PCBs and the front-end electronics. The Roma group is responsible for the gas and HV systems, together with the wires strength measurements. A PSI group is responsible for the final integration of CYLDCH in the MEG-II experimental apparatus.

4.1 CYLDCH Geometry

The MEG-II positron tracker is inspired by the one used in the KLOE experiment [36]. It presents a cylindrical symmetry along the z axis, parallel to the muon beam. It covers the whole azimuthal angle ϕ divided by 12 30°-sectors (conventionally numbered from 0 to 11). The stereo wires layout gives a hyperbolic shape to the active volume which extends radially from about 170 mm to 246 mm at the detector center ($z = 0$) and from about 196.5 mm to 284 mm in proximity of the endcaps, at $z = \pm 956$ mm. In fact, the wires starting in sector i in one end-plate arrive in sector $i \pm 2$ in the other endplate ($\Delta\phi = 60°$). The entire length of the sensitive volume, formed by ten layers of drift cells, is 1912 mm. A scaled 3D schematic view of the CYLDCH is shown in Figure 4.1.

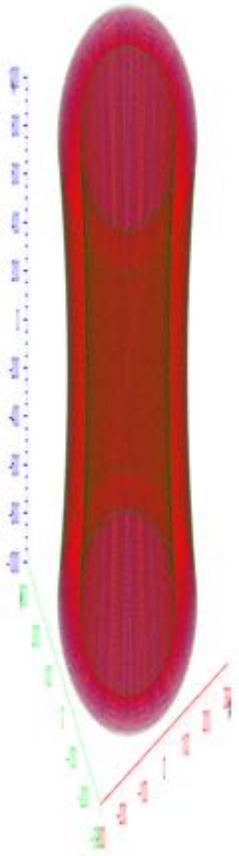

Figure 4.1: Scaled 3D schematic view of the new MEG-II CYLindrical Drift CHamber (CYLDCH).

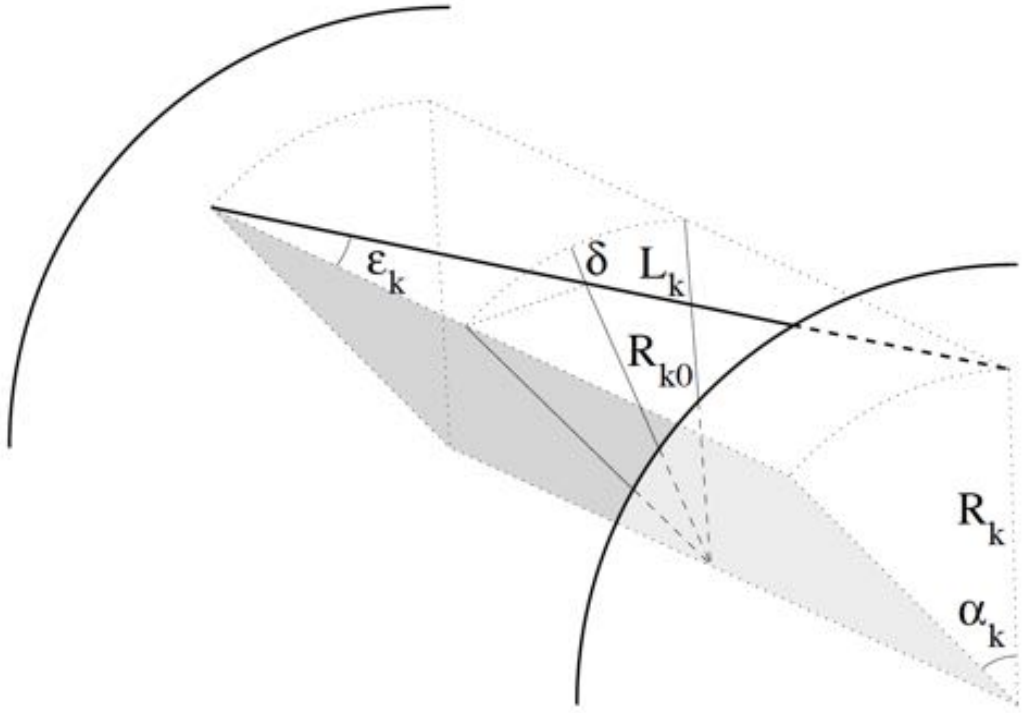

Figure 4.2: Schematic view of the stereo configuration for one wire of length L_k and stereo angle ϵ_k: R_k and $R_{k0} = R_k \cos(\alpha_k/2)$ are wire radius at the endplates and at the chamber center respectively, with $\delta = R_k - R_{k0}$; α_k is the azimuthal shift of one wire end with respect to the other end.

The external radius of the chamber is constrained by the available space inside the COBRA magnet, while its length is dictated by the necessity of tracking the positrons trajectories until they hit the pixelated TC. This reduces any passive material along the positrons path to the TC, minimizing the contribution of the track length measurement to the positron time resolution and increasing the positron reconstruction efficiency, i.e. tracks reconstructed in the drift chamber with a corresponding hit on the TC. The internal radius is large so that low energy positrons are swept out of the magnet by the gradient field without crossing the sensitive volume. On the other hand, positrons with momentum larger than $\approx$ 45 MeV/c are tracked until they reach the TC scintillation tiles crossing a minimum amount of passive material. Read-out preamplifiers, cables and the structure supporting the wires are placed in regions which are off the positron paths. MC simulation studies show that the expected positron reconstruction efficiency is larger than 85% due to the new chamber's ability to track the positrons up to the CYLDCH-TC interface. The efficiency is more than twice the one of the MEG e^+ spectrometer (40%).

The wires are not parallel to the chamber axis but form with z a stereo angle which varies from about 6° in the innermost layer to about 8.5° in the outermost one. In Figure 4.2 a schematic view of the stereo configuration for one wire is shown. The wire length is L_k and stereo angle is ϵ_k. The wire radii at the endplates and at the chamber center respectively are R_k and $R_{k0} = R_k \cos(\alpha_k/2)$, with $\delta = R_k - R_{k0}$. The azimuthal shift of one wire end with respect to the other end is α_k. In this way the drift chamber takes the shape of a rotation hyperboloyd whose surface is given by the envelope of the wires planes. The sign of the stereo angle is both positive and negative, depending on the wires layer. Thus one can define two directions along the wires, corresponding to the positive and negative stereo angle, the U direction ($\hat{U}$) and the V direction ($\hat{V}$) respectively. These two axes define two projective views, the U-view and the V-view respectively, in which the line of sight is parallel to all wires with the same sign of the stereo angle.

In CYLDCH three kinds of wires are used (the wires choice will be treated in detail in Section 4.3):

1. the **Guard wires** have a shaping and closing function of the electric field lines near the edge of the active volume both internally near the beam axis and externally near the COBRA magnet coils. The guards consist in silver-plated aluminum wires with a diameter of 50 μm;

2. the **Cathode field wires** create the ground mesh and define the drift cells of the chamber. The cathodes consist in silver-plated aluminum wires with a diameter of 40 and 50 μm;

3. the **Anode sense wires** collect the charge induced by the positrons crossing which produces the ionization of the gas filling the sensitive volume of the drift chamber. The anodes consist in gold-plated tungsten wires with a diameter of 20 μm.

As shown in Figure 4.3, the innermost and the outermost wires planes are made of guard wires which enclose the whole drift chamber volume. In order to guarantee the guard mesh, a double layer of wires each characterised by a positive and negative stereo angle is placed at the same radius. Between the two guard planes, eleven cathode planes and ten anode planes alternate. Like the guards, also the cathode planes are common to the $\pm$ stereo views and are stringed in both U and V directions, creating the ground mesh between the anode planes. CYLDCH is composed of ten criss-crossing sense wires planes in order to measure the z coordinate of the reconstructed hits along the beam axis by combining the information of adjacent planes. In fact, unlike cathodes and guards, each

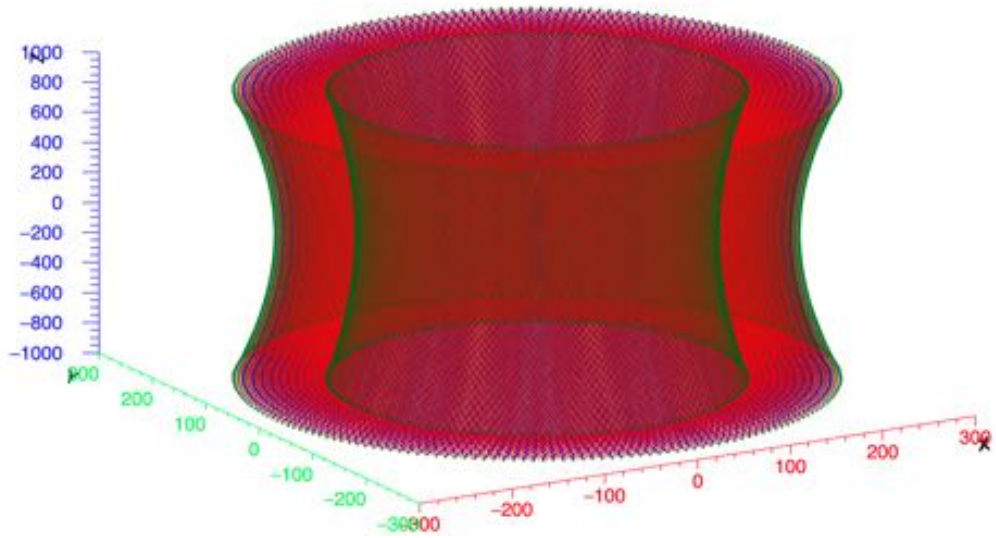

Figure 4.3: Not Scaled 3D schematic view of CYLDCH to highlight the wires configuration and magnify the rotation hyperboloyd shape given by the envelope of the stereo wires planes. The guards are in green, the cathodes in red and the anodes in blue.

anode plane is a single layer of wires with alternating sign of the stereo angle. Within the anode plane, sense and field wires alternate in order to form a drift cell together with the field wires of the upper and lower cathode planes. Each drift cell has an almost square shape with eight field wires surrounding the central sense wire. Figure 4.4 shows the drift cells configuration for one 30°-sector.

The diameter of the field wires within the cathode and anode planes is 40 μm and 50 μm respectively. In fact the cathodes between anodes are in common between two consecutive cells of the same layer and must withstand a higher electric field avoiding the ions multiplication near the wires and consequently the accelerated wires ageing (see Section 3.2.2). The cells dimensions increase linearly with the radius of the layer and, beacause of the stereo configuration, also slightly vary with the position along the CYLDCH axis (z axis). In particular, the width varies from about 6.7 mm for the innermost cells to about 9 mm for the outermost ones in order to guarantee a tolerable occupancy of the innermost sense wires. These are placed at 177.4 mm from the beam axis where the rate is ≈ 1 MHz for the muon stopping rate foreseen for MEG-II of 7×10^7 Hz. With a maximum drift time of ≈ 250 ns and a high transparency gas mixture, this corresponds to a $\approx 25\%$ occupancy.

Because of pile-up, pattern recognition algorithms are supported by an additional

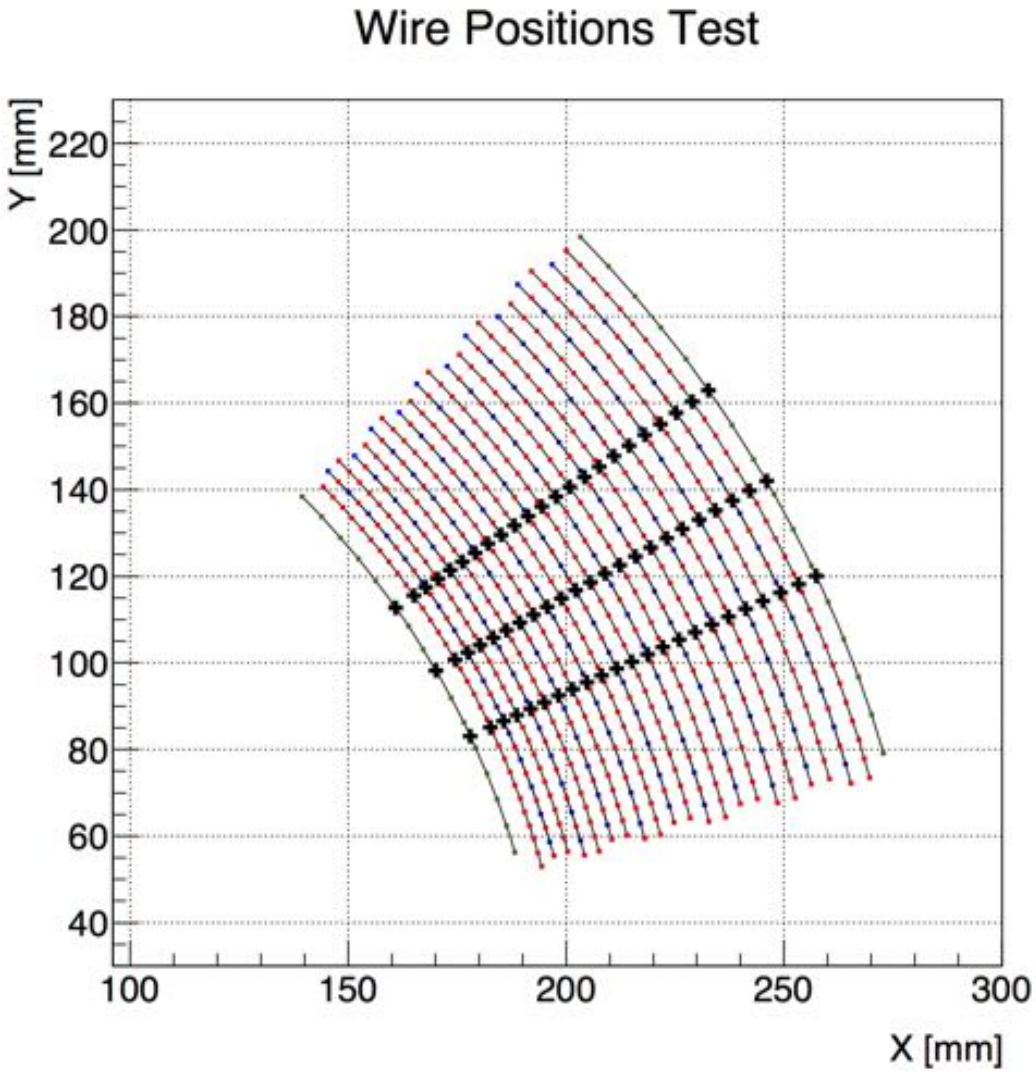

Figure 4.4: Drift cells configuration for one 30°-sector. The guards are in green, the cathodes in red and the anodes in blue. The black crosses are in correspondence of reference markers on the wire-PCBs.

coarse method of determining the z coordinate of the hit. In MEG-I this was performed through the charge division method, but for MEG-II this is not feasible because the sense wires of the new positron tracker have very low resistivity ($\approx$ 170 Ω/m). For MEG-II the determination of the z coordinate with an uncertainty of the order of 10 cm or even better will be achieved by the measurement of the difference in the arrival times of the signal at the two ends of the sense wire. After the passage of a charged particle through the sensitive gas volume, the electrons produced in the ionization process along a trajectory segment drift toward the sense wire, where they are collected and amplified in avalanches. The position of particles is obtained by measuring the drift time: using the known drift velocity of ionization electrons, this determines the distance along their drift trajectory between the sense wire and the tracks. Simulation studies have shown that a single-hit resolution < 120 μm with a gas mixture He:iC_4H_{10} 85:15 is expected (see Section 3.2.1). Comparing the two methods, both based on a measurement of time, the difference in the achievable resolution is immediately explained since the response, i.e. the change in measured time per unit length of coordinate displacement, is inversely proportional to the velocity involved, this being the drift velocity v_D in the gas and the signal propagation velocity v_S along the sense wire. This latter is a good fraction of the speed of the light, resulting in a better response of the drift time measurement by the order of magnitude of the ratio v_S/v_D, which has typical values of 10^3 to 10^4 ($\sim$ 100 μm against $\sim$ 10 cm). For a 140 μm thick target placed at 15° with respect to the beam axis, the estimated momentum resolution is $\approx$ 130 keV/c and the angular resolutions are $\delta\phi_e \approx 4$ mrad and $\delta\theta_e \approx 5$ mrad (see Table 3.2).

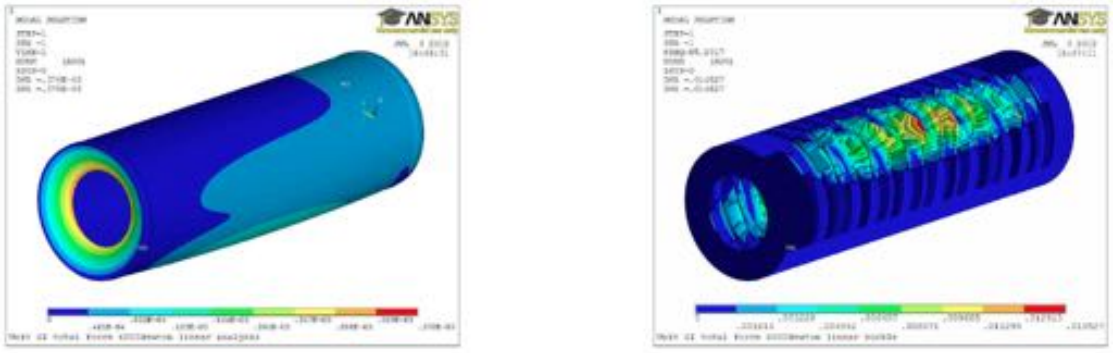

Figure 4.5: Finite Elements Analysis (FEA) simulation results with the end-plates loaded with a total wires pressure of 6000 N, uniformly distributed over 300° in ϕ. The end-plates deflection and the cylinder linear buckling are shown on the left and on the right respectively.

An evaluation of the mechanical feasibility of the new CYLDCH was done simulating, through a commercial Finite Elements Analysis (FEA) program, a model composed of two circular aluminum end-plates kept in position by a 180 cm long external carbon-fiber cylinder. It is made of sixteen intermediate high-module pre-preg layers with a thickness of 2 mm. Each end-plate have an equivalent thickness of 20 mm which corresponds to a 30 mm thick end-plate with slots for PCB cards. The simulation results are shown in Figure 4.5 with the end-plates loaded with a total wires pressure of 6000 N, uniformly distributed over 300° in ϕ. The maximum deflection is 370 μm which is tolerable given the stretching of the wires at the proposed mechanical tension (see Table 4.5). The linear buckling of the carbon-fiber cylinder happens at about 85 times the nominal tension, indicating that distorsions are kept within good safety margins. The total load for CYLDCH is about 3530 N by summing the contribution of all the wires and the total torque due to the stereo wires configuration is almost balanced, resulting in about 1 N·m.

The final CYLDCH end-plates consist in a gold-plated aluminum wheel with a thickness of 30 mm (Figure 4.6). The measured concentricity is better than 14 μm, while the roundness and the planarity are within 40 and 30 μm respectively. The nominal distance between the internal faces of the two end-plates is 1932 mm. The wheel presents a central hole with a radius of 161.500 mm and twelve radial spokes which divide the azimuthal angle ϕ in twelve sectors. The entire structure seems like a ship rudder. The external and internal radii are 285.350 mm and 195.687 mm respectively. Each sector spans an angle ϕ of 30° and acts as housing for the FR4[1] PCB cards where wires are soldered (wire-PCB). The FR4 board thickness is 400 μm and the gold tracks of the circuit, whose thickness is 35 μm, are printed on both surfaces. Each wire-PCB is placed at the proper radius through PEEK[2] spacers (Figure 4.7) whose radial thickness is adjusted in order to have the correct radial dimensions for the drift cells. The side perimeter is contoured to fit with the complementary shape of the end-plates spokes. The first wire-PCB layer at the innermost radius is electrically insulated from the end-plates through a 400 μm-thick FR4 insulator.

[1]Composite material composed of woven fiberglass cloth with an epoxy resin binder. “FR” stands for Flame Retardant.

[2]PolyEther Ether Ketone, a colourless organic thermoplastic polymer.

Figure 4.6: The final CYLDCH end-plates.

Figure 4.7: The PEEK spacers. The side perimeter is contoured to fit with the complementary shape of the end-plates spokes.

Each single wires plane contains a fixed number of wires depending on the plane type: guard plane, cathode plane or anode plane. The wires within one plane are equally

spaced and the mutual distance varies according to the radius. Each single guard plane contains 192 wires, 16 for each sector/wire-PCB. The distance between wires varies from 6.429 mm to 9.295 mm for the innermost and the outermost layer respectively. There are two double layers of guards (U-view and V-view) for a total of 768 wires in 4 planes. Each single cathode plane contains 384 wires, 32 for each sector/wire-PCB. The distance between wires varies from 3.297 mm to 4.573 mm for the innermost and the outermost layer respectively. There are 11 double layers of cathodes (U-view and V-view) for a total of 8448 wires in 22 planes. There are 10 single anode plane (5 in the $\hat{U}$ direction and 5 in the $\hat{V}$ direction) each containing 384 wires, 32 for each sector/wire-PCB in which 16 sense wires and 16 field wires alternate for a total number of 3840 wires, including 1920 sense wires. The distance between wires varies from 3.352 mm to 4.500 mm for the innermost and the outermost layer respectively. The total number of wires in CYLDCH amounts to 13056 in 36 single wires planes. The total number of drift cells is 1920, divided in ten layers each containing 192 cells. A schematic view of the DownStream (DS) and UpStream (US) endplates with all the wires is shown in Figure 4.8.

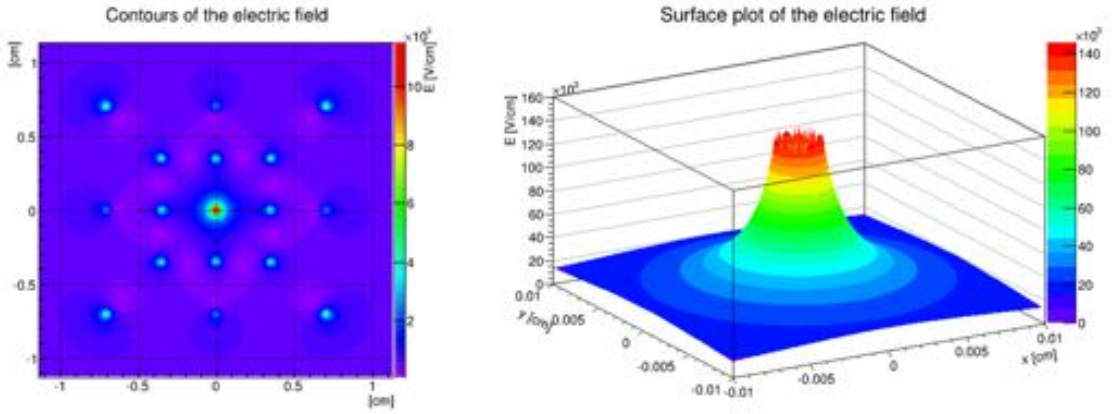

Figure 4.9: Map of the electric field in a drift cell (on the left) and close to the anode wire (on the right).

A positive HV of about 1.5 kV will be applied to the anode wires, while the cathodes are grounded. The HV applied to the guard wires for shaping the electric field at the edge of the sensitive volume will be smaller. The average electric field within the drift cells is approximately (1.5 kV)/(0.5 cm) = 3 kV/cm. The electric field near the cathodes at the cell boundary is $\leq$ 20 kV/cm in order to limit the ions multiplication and an accelerated drift chamber ageing (see Section 3.2.2). The value of the electric field between the cathodes and the anodes is smaller and then reaches the value of $\approx$ 150 kV/cm near

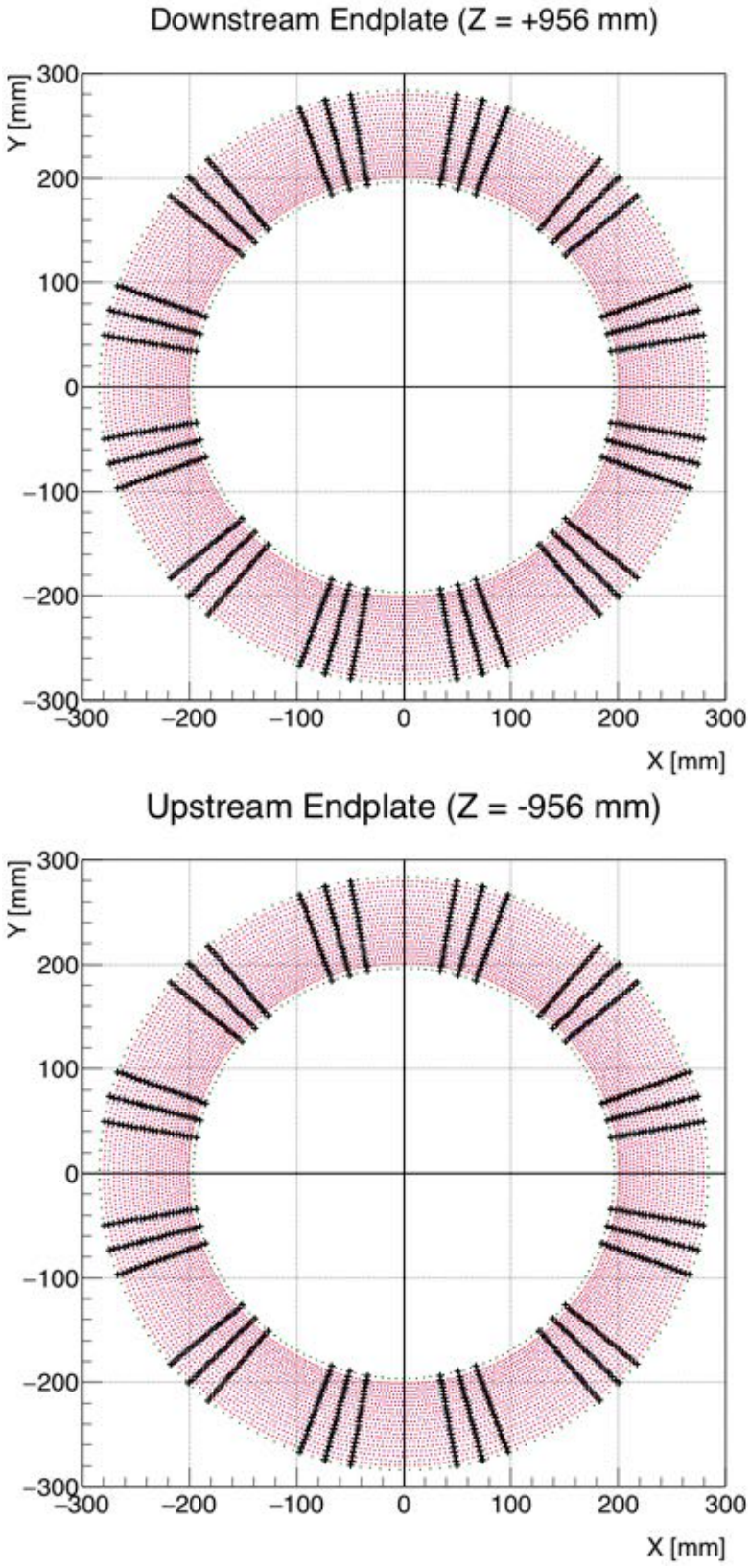

Figure 4.8: Schematic view of the DownStream (DS) and UpStream (US) endplates with all the wires. The guards are in green, the cathodes in red and the anodes in blue. The black crosses are in correspondence of reference markers on the wire-PCBs.

the anodes to guarantee the e^- multiplication before the charge is collected by the sense wires. Simulations of the electric field have been performed (Figure 4.9) by means of the Garfield toolkit for the detailed simulation of particle detectors that use gas and semi-conductors as sensitive medium [60].

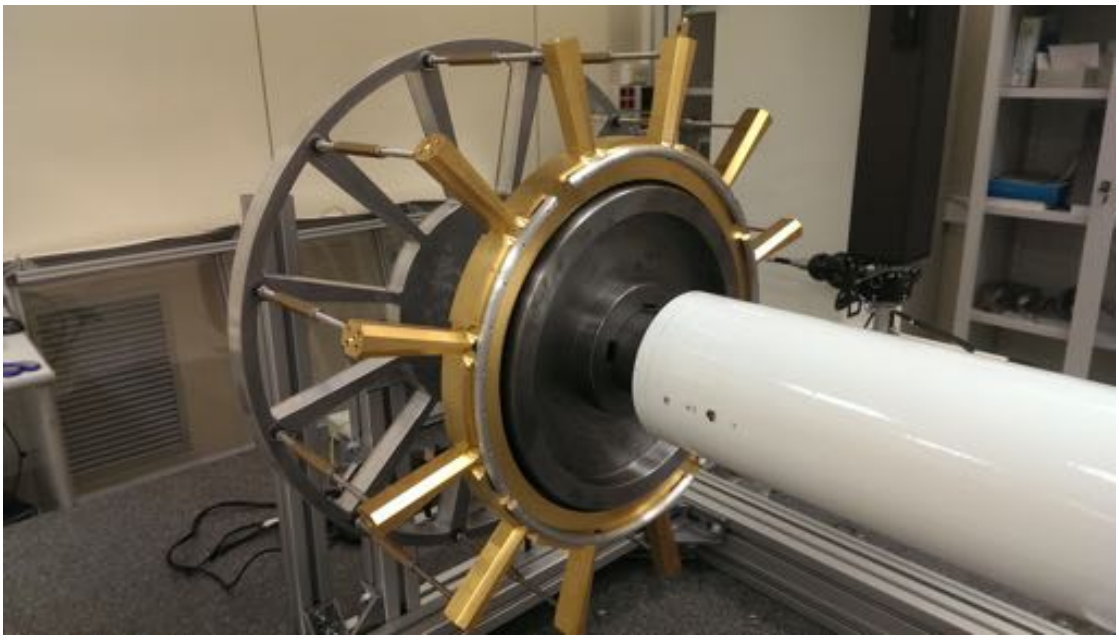

Figure 4.10: The system of four perforated pipes covering the whole azimuthal angle for the flushing of the gas mixture inside the sensitive volume of the drift chamber.

On both internal faces of the end-plates ring a system of four perforated pipes covering the whole azimuthal angle allows the proper flushing of the gas mixture inside the sensitive volume of the drift chamber (Figure 4.10). The gas volume is ≈ 380 liters and the total gas exchange is completed approximately in 12 hours at a flow rate of about 500 cc/minute. On the external faces of each spoke three threaded holes allow the fixing of structural extensions housing the support structures for the HV and readout electronics boards and for the gas distribution system. A schematic view of the electronics board prototype is shown in Figure 4.11 with the input and output connectors highlighted together with the HV and read-out gain stages. On both external faces of the end-plates ring, four feedthroughs each spaced by 90° in ϕ guarantee the gas mixture flow to the inner flushing system. The electronics components are extremely close and the generated heat (≈ 500 Watt/end-plate) must be carried away. A number of sensors will be placed in each end-plate sector in order to monitor the temperature near the hot electronics. The cooling power and temperature stability will be guaranteed by a cryostat. In addition a

system of perforated pipes glued to the external faces of the end-plates flushing nitrogen or fresh dry air is planned in order to uniform the extensions temperature and avoid the formation of dangerous temperature gradients.

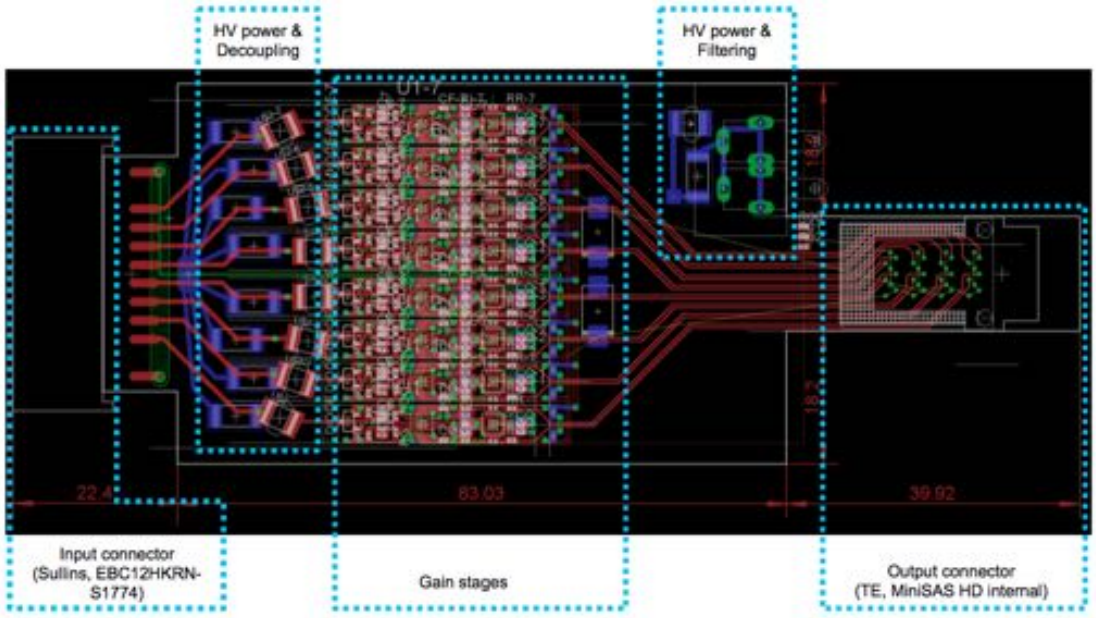

Figure 4.11: Schematic view of the electronics board prototype.

4.1.1 Wire-PCBs Design

The new MEG-II CYLDCH nominal geometry is generated by a C++ macro which produces in output a series of text files with all the geometry information encoded. The generation starts from the position vector of a wire at $z = 0$ and $\phi = 0$, then the wire vector is created taking into account the tilt angle due to the corresponding stereo angle θ_i. The wire vector length is defined by the half length of the sensitive volume as: (956 mm)/$\cos\theta_i$ (the wire length is twice this value). In this way the intersection of the wire vector with the planes placed at $\pm$956 mm defines the nominal position of both wires ends at the end-plates. The spacing $R_i\delta\phi_i$ between consecutives wires in the same layer is obtained by taking into account the nominal radius and the number of cells (16) in one end-plate sector (30°). The procedure is iterated for each layer radius, rotating the initial position vector of the wire at the drift chamber center by the nominal angle $\delta\phi_i$ until the whole azimuthal angle is covered.

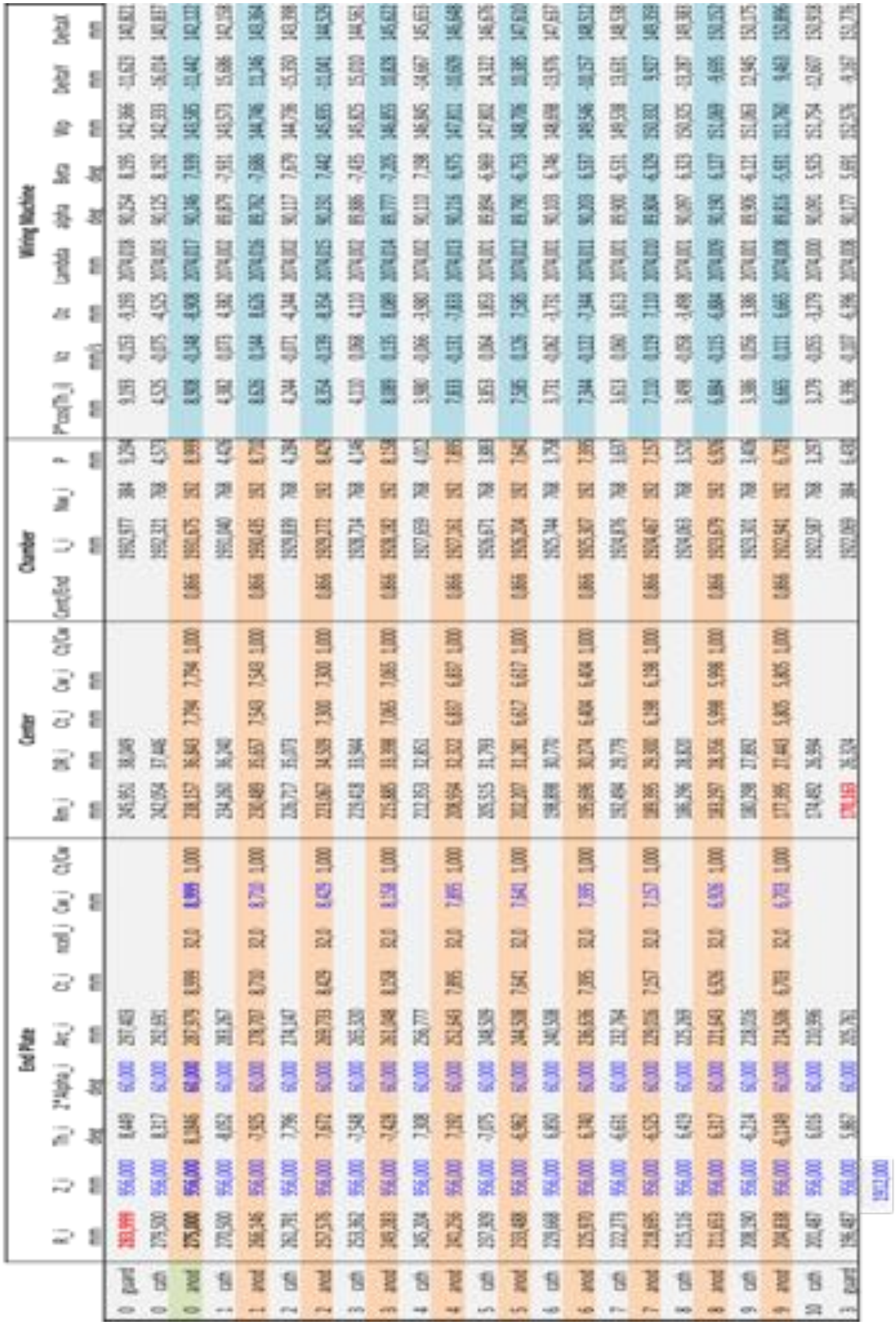

Figure 4.12: Summary of some geometric parameters for the three wires types (anodes, cathodes and guards) as a function of the nominal radius.

The geometry parameters in the output text files include, besides the components of the wire vectors descibed above, the radii R_i and R_i^m of each wires layer at the end-plates ($z = \pm 956$ mm) and at the drift chamber center ($z = 0$) respectively, the stereo angle θ_i, the cells width as a function of the wires layer at the end-plates and at $z = 0$, the wires length as a function of the radius. Moreover they include the values of the wiring machine parameters, defined in Section 4.1.2, depending on the wires layer and the information for the design and construction of the wire-PCBs. A summary of some geometric parameters is reported in Figure 4.12 for the three wires types (anodes, cathodes and guards) as a function of the nominal radius.

The output files are also used by the MEG software package (see Section 5.1) for simulation and analysis purposes. For instance the new CYLDCH geometry can be loaded by the MEG Monte Carlo (MC) code which reads the text files. A modification of the software allows to read and load the same parameters from an online database, which contains all the information related to the new geometry, through proper queries. A test database has been implemented into the MEG software and several tests have been conducted successfully.

The correct design of the wire-PCBs is crucial for the proper operation of CYLDCH. Several PCB versions have been designed until the final one has been chosen. The FR4 PCB cards have a nominal thickness of 400 μm and present 35 μm-thick gold tracks printed on both surfaces. During the design phase, the tracks must comply with some criteria, like a minimum bend angle, a minimum mutual distance and a minimum separation from the PCB edges. Five holes, two fixed and three variable depending on the wires layer, are made in PCBs for handling and holding purposes. The thicknesses have been measured on a wire-PCBs sample by means of a micrometer in different positions of the surface, including the single and double metallization. The agreement with respect to the nominal thickness is within 10 μm. The tracks are independent in the anode PCBs for the signal read-out, while they are connected together in the cathode PCBs since these wires are grounded, as they are in the guard PCBs. Only two tracks at both PCB ends are independent for test purposes. On both wire-PCB surfaces three reference markers are printed, together with some information like the wire-PCB type, the value of the stereo angle and the nominal mounting radius. The reference markers are used for the optical surveys with the measuring machine in order to monitor each wire-PCB position once it is mounted on the CYLDCH and for wires test purposes. The wire-PCB perimeter has a complementary design with respect to the shape of the end-plates spokes in order to fit into the proper slot in each sector. The PCB side facing inwards the sensitive volume is equipped with a number of pads where wires are soldered. The

connectors for the HV and read-out are on the opposite side. The anode PCB have two connectors. The number of soldering pads is 16 for the guard PCBs and 32 for the anode and cathode PCBs. The pitch between the soldering pads varies as a function of the radius.

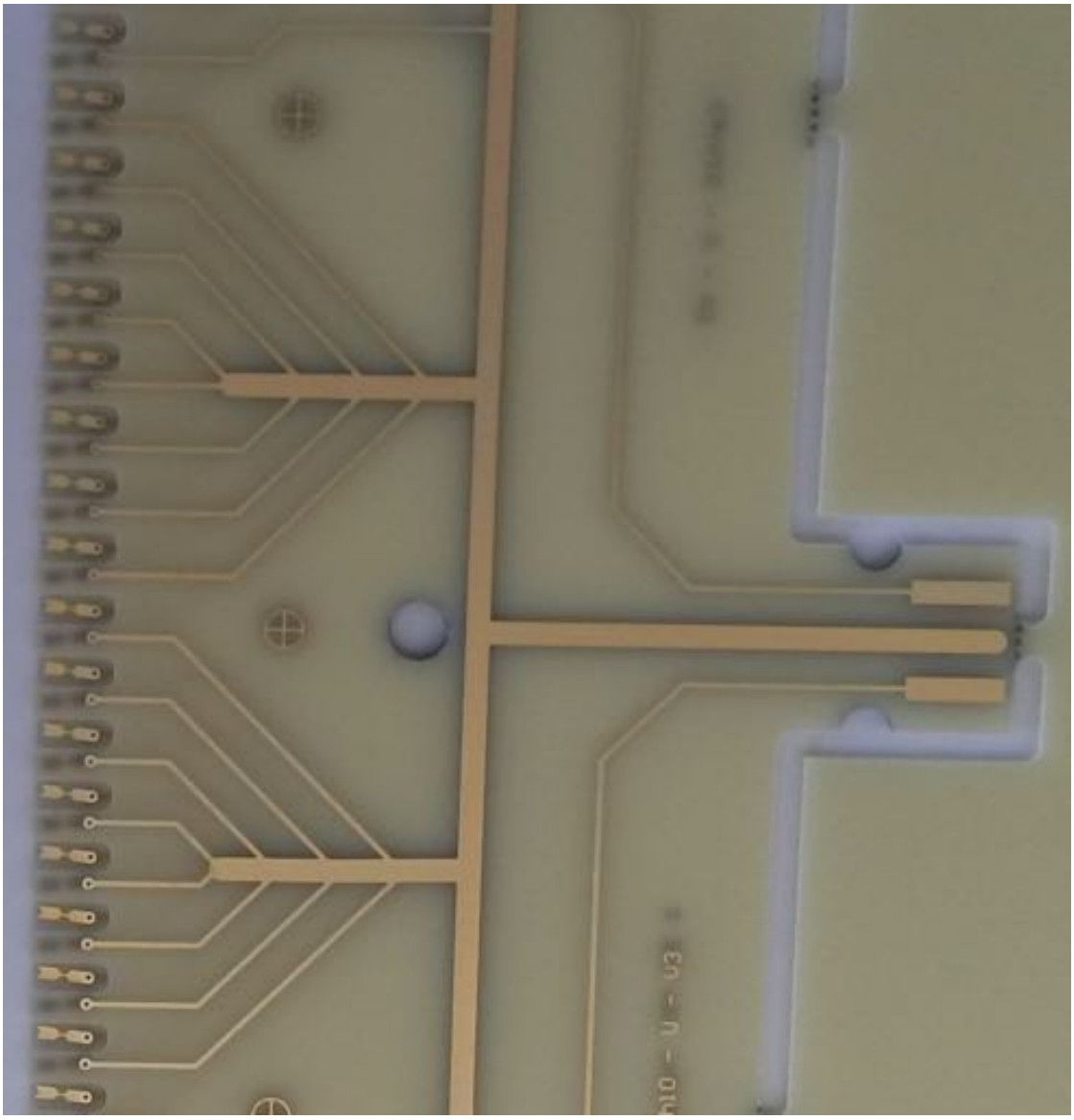

Figure 4.13: A picture of two overlaid wire-PCBs. Once flipped, the soldering pads of the upper PCB do not overlap with the ones of the lower PCB, since otherwise the soldering thickness would deform the wire-PCB pads, affecting the wires position and leading to unwanted wires stress.

Moreover, the pad positions is also different within the same wires layer depending on whether the wire-PCB has to be mounted on the downstream or upstream end-plate. Thus, two PCB versions have to be designed for each radius, the US and the DS one. In fact the guard and cathode wires planes are double layers in order to create the optimal shaping and ground meshes. Here the wire-PCBs have to be mounted one over the other, with the upper one flipped in order to have the wires at the same radius. Once flipped, the soldering pads of the two wire-PCBs in contact must not overlap since otherwise the soldering thickness would deform the wire-PCB pads, affecting the wires position and leading to unwanted wires stress (Figure 4.13 and Figure 4.17). Great attention has been put on this issue by modifying and tuning each pads position and width.

The wire-PCBs have been designed following the dedicated output text file by means of the *Altium Designer* electronic design automation software package for printed circuit board, FPGA and embedded software design. In Figure 4.15 and Figure 4.16 the wire-PCBs for one of the guard, cathode and anode wires layer are shown, together with the design scheme produced with the Altium software. All the wire-PCB projects are sent to the company[3] for the construction. Two wire-PCBs are connected in a single FR4 PCB (Figure 4.14) to facilitate the positioning for the wiring procedure and the following separation. This PCB is provided with a big central metallization for manual soldering.

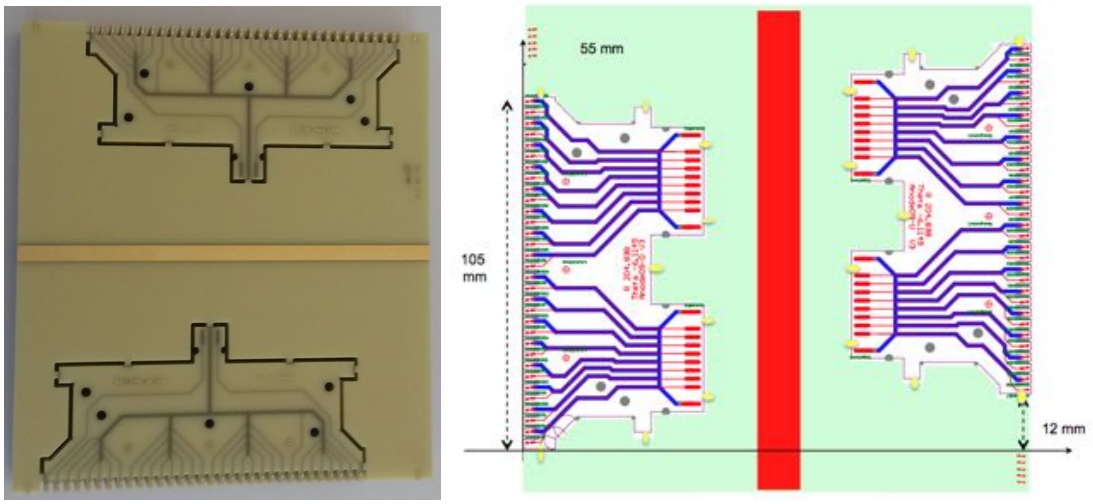

Figure 4.14: The single FR4 PCB connecting two wire-PCBs to facilitate the positioning for the wiring procedure and the successive separation. The big central metallization is used for the manual soldering.

[3]ARTEL Master & Circuiti Stampati Srl.

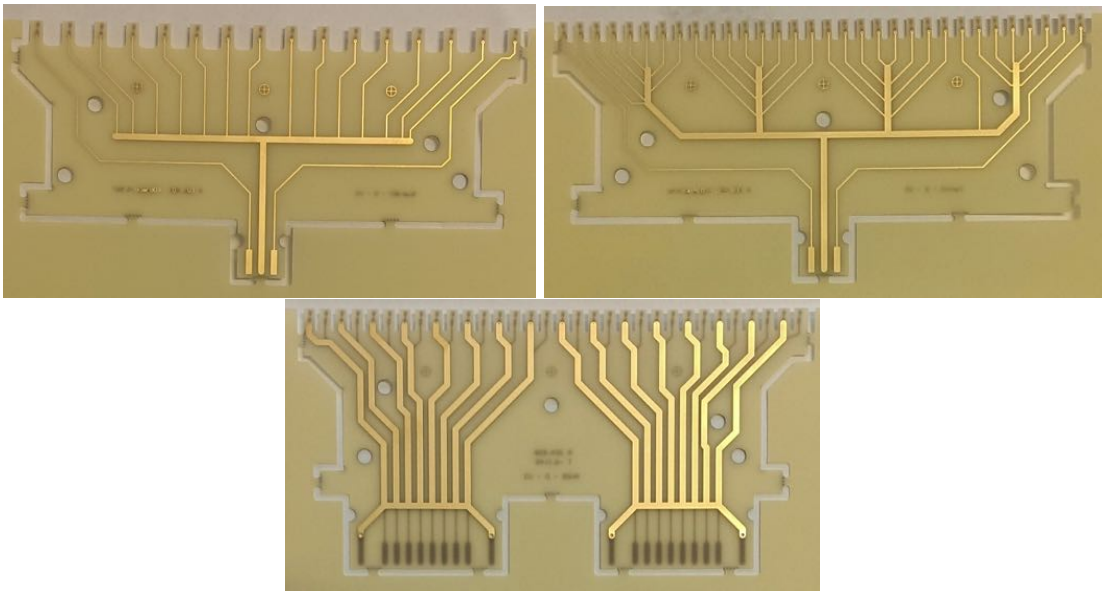

Figure 4.15: Wire-PCBs pictures for one of the guard, cathode and anode wires layer.

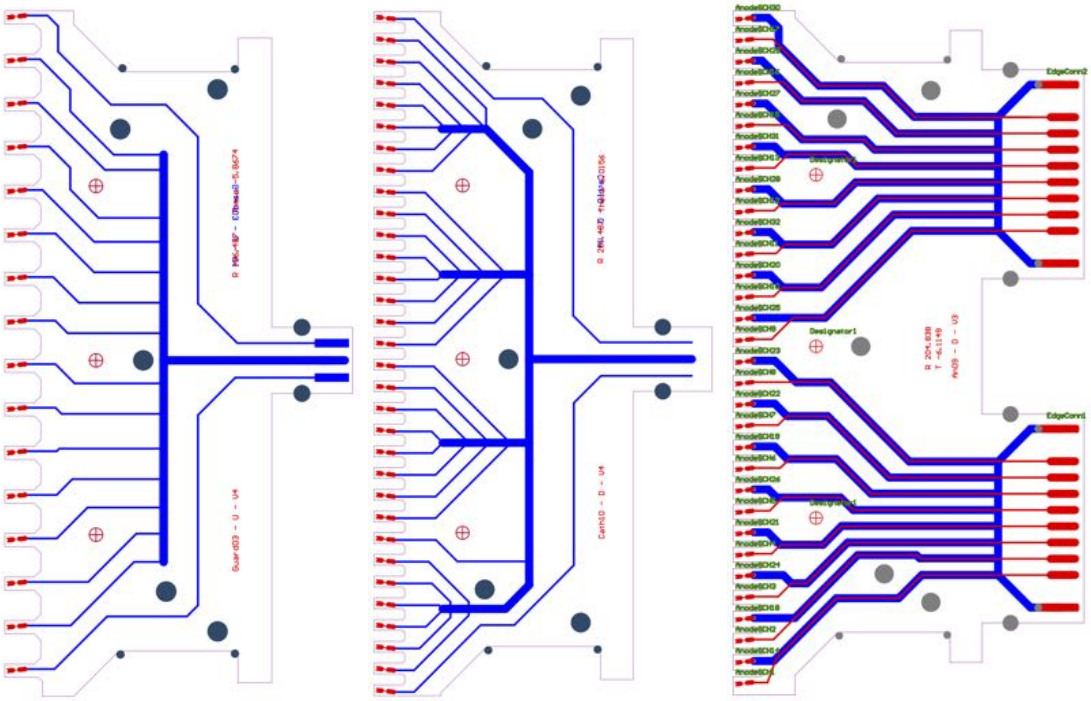

Figure 4.16: Design scheme for one of the guard, cathode and anode wire-PCBs as produced by the Altium Designer software package.

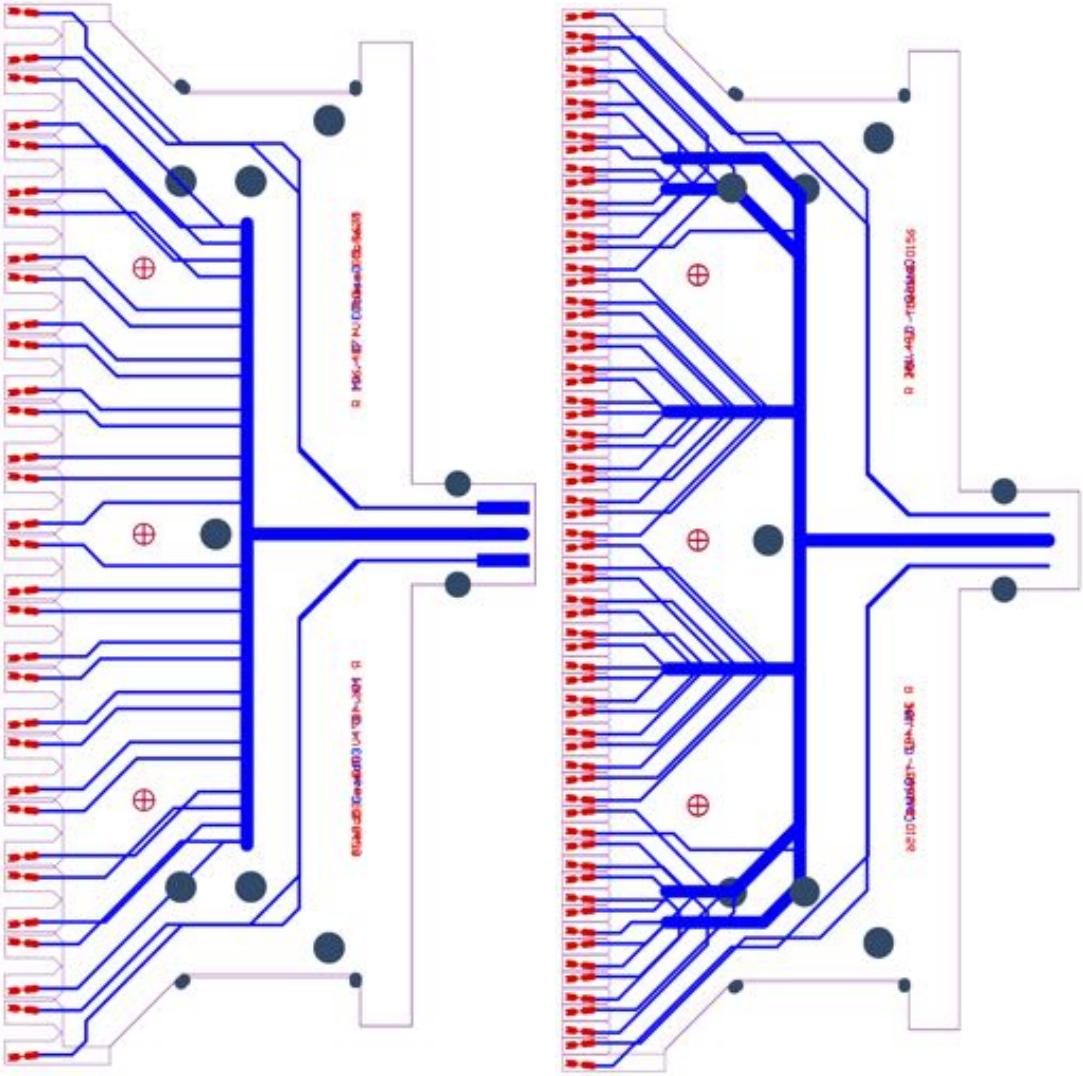

Figure 4.17: Flip test of two overlaid guard and cathode wire-PCBs.

4.1.2 Wiring Procedure

The wires of CYLDCH are not strung directly on the final chamber, but they are soldered at both ends on the pads of two wire-PCBs. The wire-PCBs are then mounted in the proper slots of the end-plates. The wires soldering to the PCBs is performed at the INFN Lecce facility inside a class 10000 cleanroom by means of a computer-controlled wiring machine (Figure 4.18) which is formed by many parts. A digital camera is used to monitor the correct wire soldering on the pads of the wire-PCBs. A laser, whose power is adjusted not to break the wires, is used for soldering since its light spot has approximately the

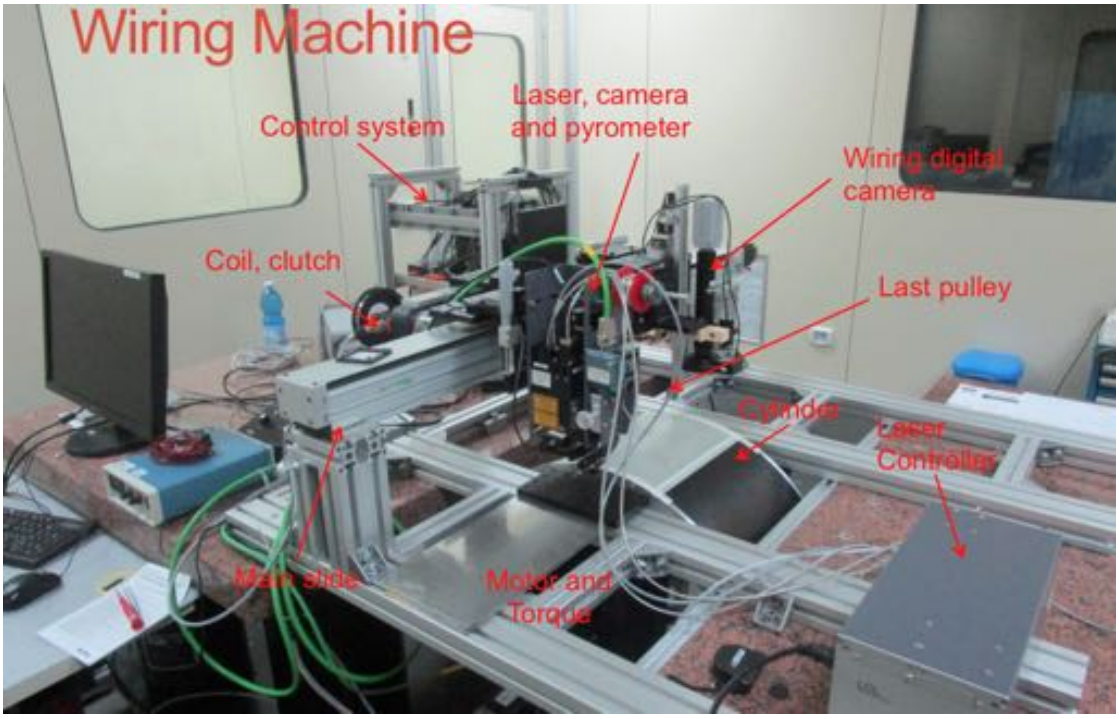

Figure 4.18: Picture of the wiring machine in the INFN Lecce facility.

same dimensions of the wire-PCB pads. A laser pulse melts a small portion of a tin wire placed over the soldering pad, and the resulting tin drop is deposited on the pad, together with the solder flux. A cylindrical wiring drum is made to rotate by an electric motor and the soldering arm can move horizontally and vertically for wiring. A board template ensures the correct positioning of the single FR4 PCB connecting the two wire-PCBs on the wiring drum whose radius is tuned to guarantee the correct wires length. The mutual distance between the soldering pads varies depending on the CYLDCH wires layer, thus even the sliding velocity of the soldering arm is adjustable. A single wire is strung in a helix such that it passes over all the wire-PCB pads (Figure 4.19). The soldering procedure is done for each pad and the excess wire is cut away. At this point the right number of wires are strung from one soldering pad in one wire-PCB to the corresponding one in the other. Then the two wired PCBs are separated from the single FR4 PCB connecting them. At the end an extraction system uses a dedicated arm equipped with a number of vacuum suckers (Figure 4.20) to remove the wire-PCB and the soldered wires from the wiring machine.

The wiring procedure is semi-automatic with only the most delicate operations made by hand. These include the positioning and fixing of the PCB on the wiring drum inside

Figure 4.19: Wiring procedure: a single wire is strung in a helix such that it passes over all the wire-PCB pads. The single big FR4 PCB connecting two wire-PCBs is correctly positioned and fixed into the board template on the wiring drum.

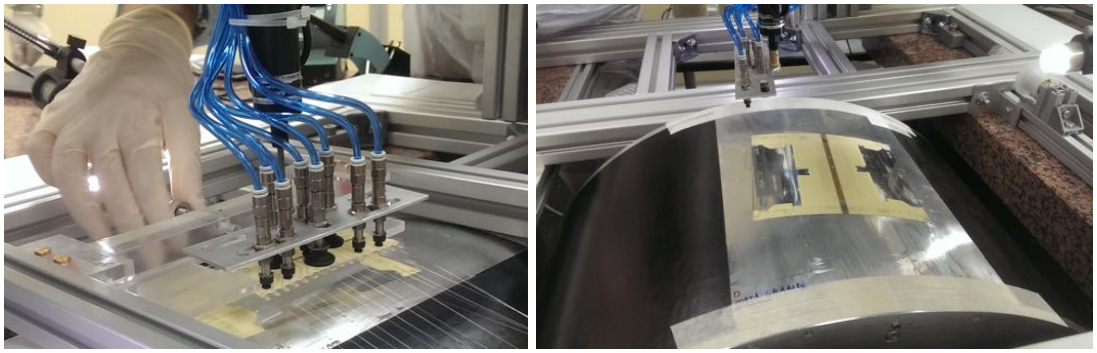

Figure 4.20: The extraction system based on vacuum suckers and the resulting empty big PCB connecting two wire-PCBs.

the board template, the cut of the excess wire, the separation of the two wire-PCBs from the single FR4 PCB which connects them and finally the fixing of the wire-PCBs with the soldered wires on the transport trays. These consist in a simple rectangular frame made of aluminum profiles. Two plexiglass structures are dedicated to hold the wire-PCBs at the correct stereo angle by means of teflon screws put inside the PCB holes. One side is fixed, while at the other side the movable support structure, sliding in the tray rails, allows to adjust the mutual distance between the two PCBs and thus the wires length by means of a longitudinal threaded rod. The transport trays are stored inside the cleanroom at Lecce until they are shipped to Pisa by means of a truck for the CYLDCH assembly, enclosed in a tight wrapping. A dedicated damping support structure (Figure 4.21) made of aluminum profiles anchored to the truck body has been constructed in order to absorb the travel shocks. A set of accelerometers joint to the transport structure and truck are used to record and monitor the wires stress during the Lecce-Pisa travel. The tight wrapping is then opened only in the Pisa cleanroom.

Wiring parameters

The wiring procedure is based on several parameters which are indicated in Figure 4.22 for a positive stereo angle and reported in Figure 4.12 for the three wires types (anodes, cathodes and guards) as a function of the nominal radius. The case of negative stereo angle is similar.

Wire-PCBs geometry parameters:

- P: distance between wire pads on PCB;
- θ: stereo angle (the sign convention is shown);

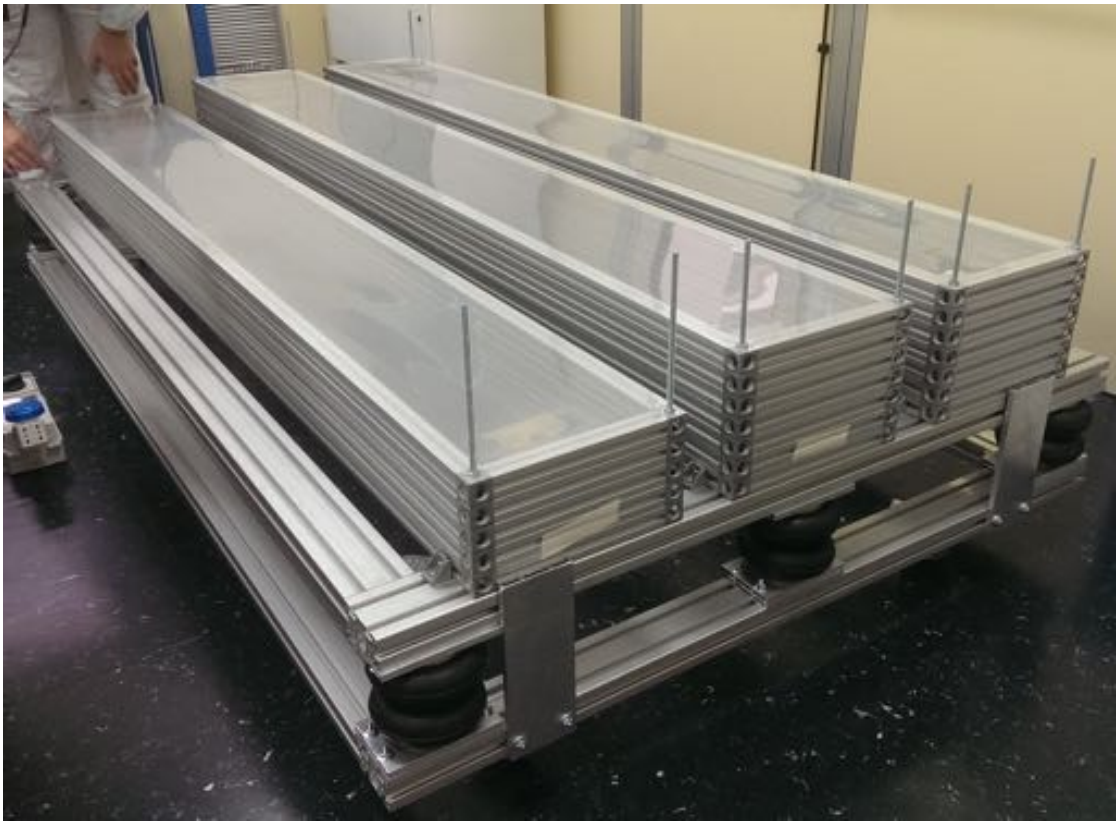

Figure 4.21: The dumping support structure. It is anchored to the truck body. In the picture the transport trays with the wired PCBs have not been enclosed in the tight wrapping yet.

- L: wire length (stretched).

Wiring machine parameters:

- R: drums radius;
- ω: angular velocity;
- v_z: linear velocity along the drum axis z.

Intermediate parameters:

- α: angle between wire and drum axis;
- Δz: helix increment;

- Δ: distance between wires;
- λ: helix spire length;
- W_P: wire length between pads.

Placing parameters:

- β: angle between PCB and drum axis;
- ΔX: distance between the soldering pads of the two wire-PCBs connected to the PCB template;
- ΔY: relative shift between the soldering pads of the two wire-PCBs connected to the PCB template.

The sliding velocity of the soldering arm along the wiring drum axis z is a wire-PCB dependent variable. In fact, if $\theta > 0$, v_z and ω have the same sign ($v_z < 0$), while, if $\theta < 0$, v_z and ω have the opposite sign ($v_z > 0$). The following equalities define v_z:

$$\begin{cases} \Delta z = 2\pi \frac{v_z}{|\omega|} \\ P\cos\theta = |\Delta z|\sin\alpha = \Delta \\ \tan\alpha = \frac{|\omega|R}{v_z} \quad ; \quad \sin\alpha = 2\pi\frac{R}{\lambda} = \sqrt{1-\left(\frac{P\cos\theta}{2\pi R}\right)^2} \end{cases} \tag{4.1}$$

where:

$$\lambda = 2\pi\sqrt{R^2 + \left(\frac{v_z}{\omega}\right)^2} \tag{4.2}$$

leading to:

$$v_z = \pm\sqrt{\frac{(P\cos\theta)^2}{(2\pi R)^2 - (P\cos\theta)^2}}R|\omega| \tag{4.3}$$

The v_z sign follows the sign of the stereo angle θ. The angle $\beta = \pi/2 - \alpha + \theta$. If $\theta > 0$, then $\alpha > \pi/2$ and $\beta > 0$, while, if $\theta < 0$, then $\alpha < \pi/2$ and $\beta < 0$. The segments in Figure 4.22 are defined as follows: $AD = \lambda$, $AB = P$, $BC = P|\sin\beta|$, $BD = BC/\sin\alpha$, $AE = \lambda - L + BD = W_P$.

$$\begin{cases} \Delta X = W_P\cos\theta = \left(\lambda - L + P\frac{|\sin\beta|}{\sin\alpha}\right)\cos\theta \\ \Delta Y = \pm(P - W_P|\sin\theta|) \end{cases} \tag{4.4}$$

The ΔY sign follows the sign of the stereo angle θ.

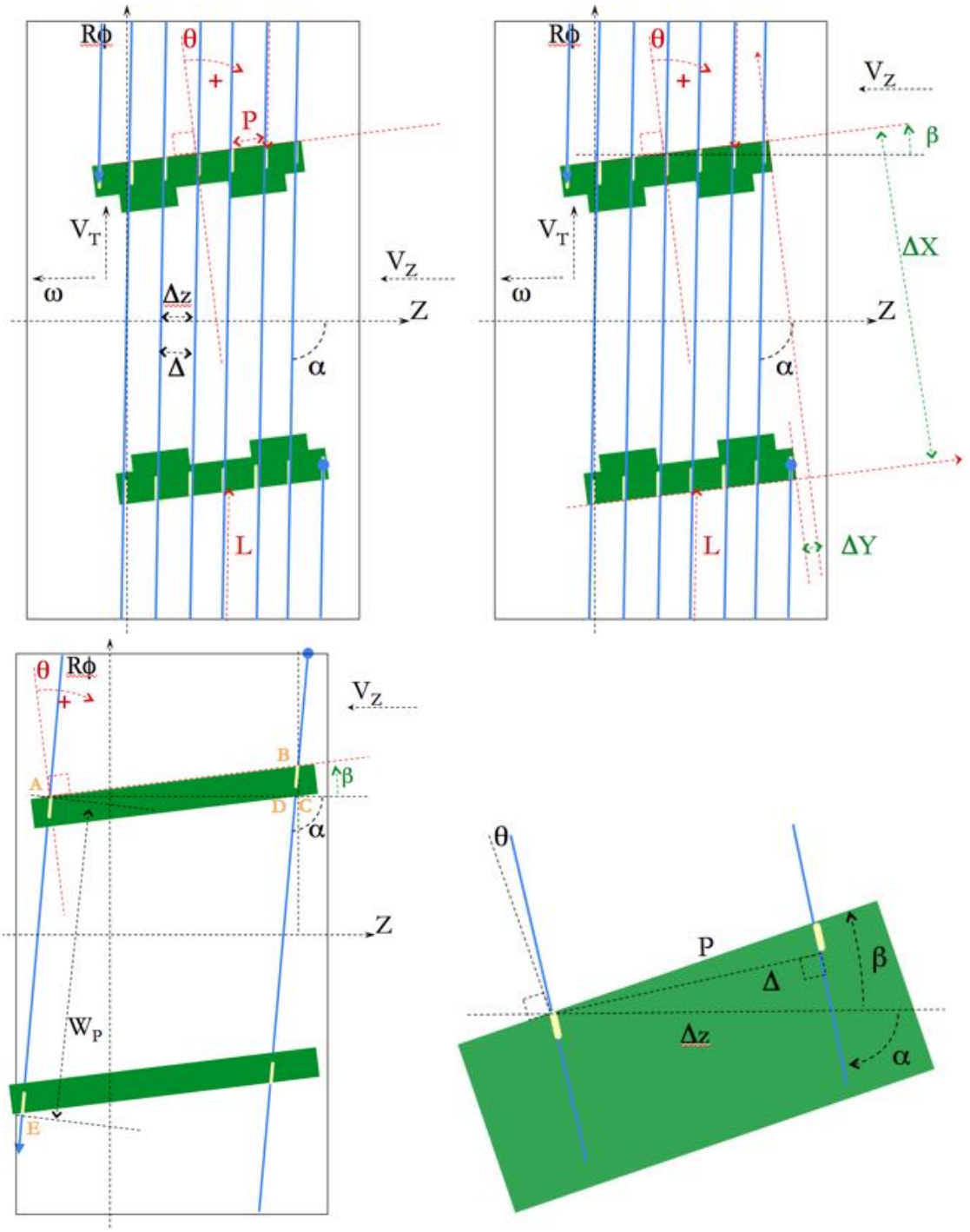

Figure 4.22: Schematic view of the wiring parameters.The sliding velocity of the soldering arm along the wiring drum axis.

4.2 Drift Chamber Construction

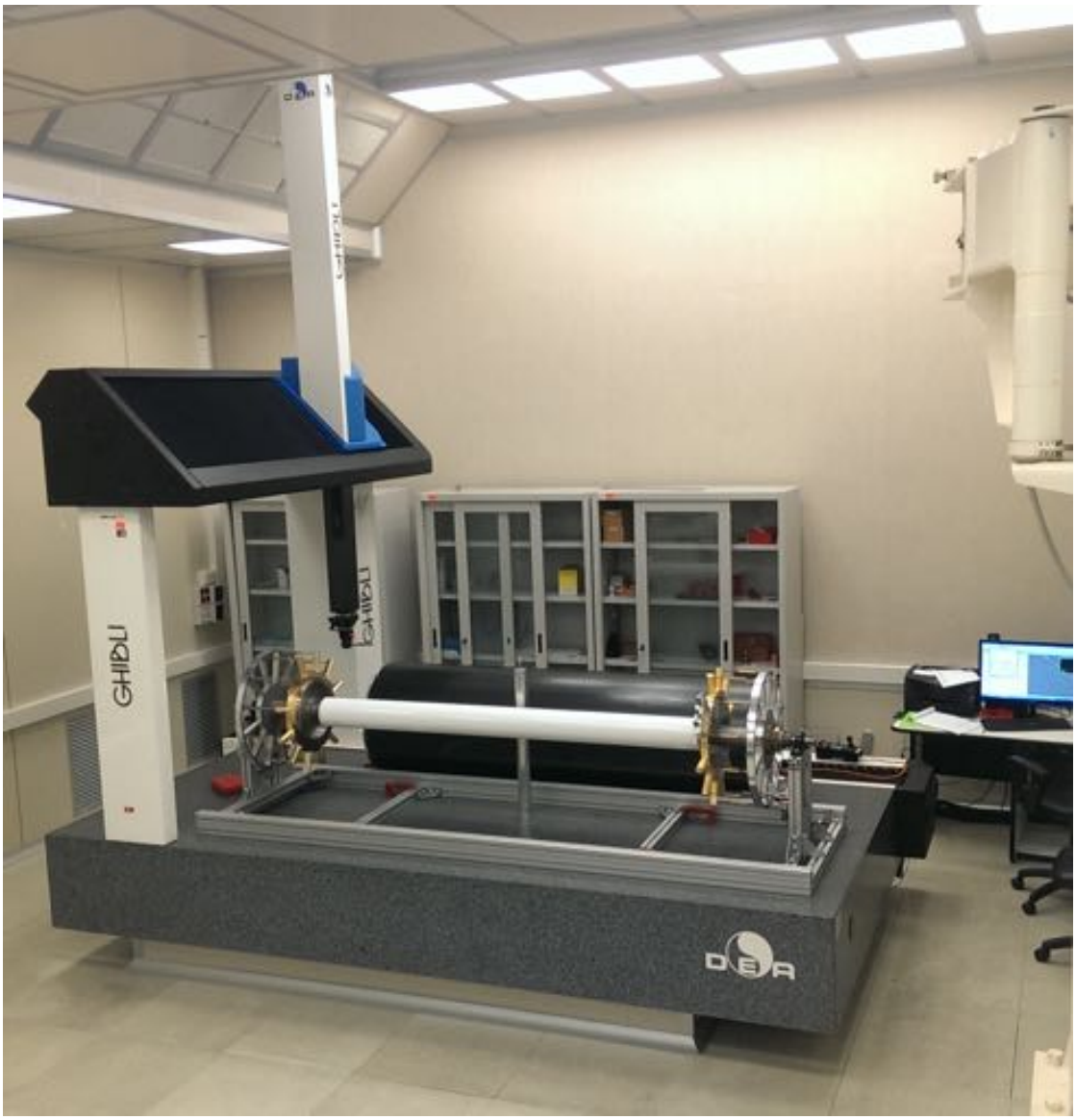

Figure 4.23: The *Brown & Sharpe DEA GHIBLI* 3D Coordinate Measuring Machine (CMM) used for the geometrical monitoring of the CYLDCH assembly, together with the granite work table used to minimize the vibrations during construction.

The new MEG-II CYLDCH is assembled at the San Piero a Grado (Pisa) facility of INFN Pisa, inside a class 100000 cleanroom. The mounting workstation is placed on a granite work table with dimentions $170 \times 360 \times 45$ (W-L-H) cm^3 to guarantee the

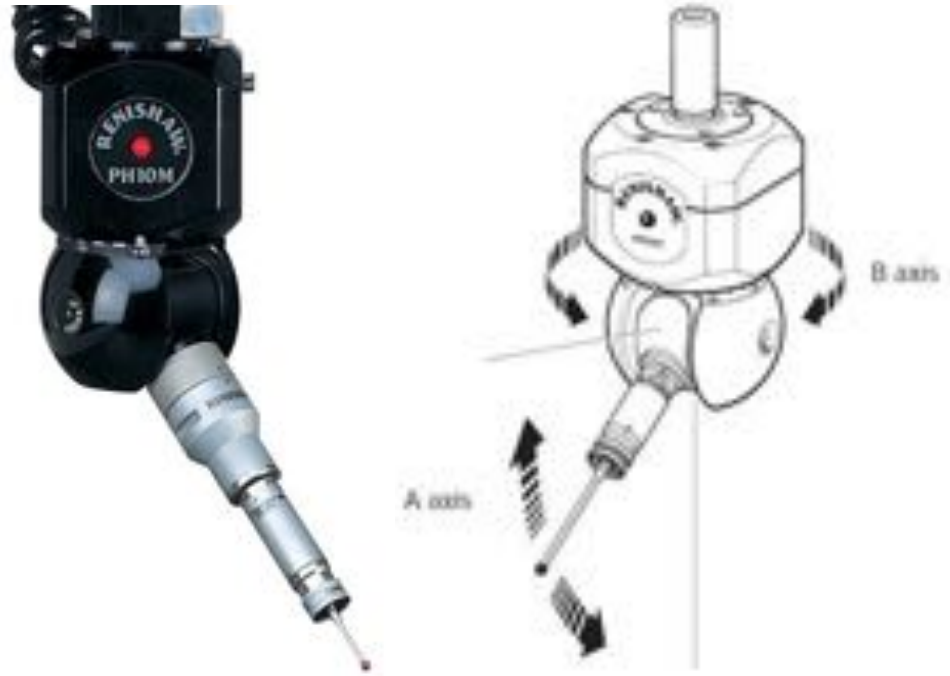

Figure 4.24: The *Renishaw* motorized touch-trigger probe system with the two motion axes highlighted.

minimum amount of vibrations during construction. A *Brown & Sharpe DEA GHIBLI* three-dimensional CNC (Computer Numerical Control) Coordinate Measuring Machine (CMM) is used for the geometrical monitoring of the CYLDCH assembly. The CMM features a unique slant bridge and the measuring volume is approximately $150 \times 300 \times 125$ (W-L-H) cm^3 (Figure 4.23).

The CMM is Direct Computer Controlled (DCC) and runs using the PC DMIS software. A hydraulic system operating by compressed air ensures the measuring machine movements. The CMM uses a *Renishaw*[4] flexible measuring system (Figure 4.24) that support precision, single-point probing for inspection of simple geometric dimensions. Once programmed the CMM, a high-speed open loop technique can be used to measure predefined surfaces. In scanning mode the CMM guarantees an accuracy of approximately 2 μm/m. The measuring machine calibration, required before using the high-speed scanning mode, is done by touching a calibration ceramic sphere with a mechanical probe. Several points of its surface are recorded approaching the sphere at the maximum scanning velocity from different directions and predefined probe configuration.

[4]Renishaw web-site: http://www.renishaw.com/en/cmm-probes-software-and-retrofits--6329.

After the calibration procedure the flexible head of the probe guarantees the highest accuracy. The same ceramic sphere is used as reference point for the measurement of the azimuthal tilt angle between the two CYLDCH end-plates. This procedure is described below in this Section. The mechanical probe can be removed and an optical probing system (Figure 4.27) can be mounted on the CMM arm in order to perform position measurements. The system consists in a digital camera with an interchangeable eyepiece to adjust the magnification power depending on the circumstances. The live video is send to the control PC. Once the CMM is in the optical probing mode, it is manually controlled by means of a joystick. The accuracy of the optical measurement is related to the conductor ability, however in the plane perpendicular to the optical axis a precision < 20 μm is achievable. The vertical accuracy depends on the manual image focusing on the PC screen and reaches a precision of the order of ± 30 μm.

During the mounting period two end-flanges are placed in the central hole of the end-plates and kept in a fixed position by means of two through pins. The two end-flanges are connected by an iron shaft (see Figure 4.25). The reference end-flange, at the upstream side, is kept in a fixed z position, while at the downstream side, the end portion of the structural shaft is threaded in order to make the distance between the two end-plates tunable by turning a big screw. The pitch of the screw is made such that one full turn shifts the sliding end-plate by 2 mm. In order to lower the friction and ensure a better slipping, a teflon film is coated on the threaded surface of the iron shaft. Externally, two additional end-plates are placed on the shaft. Both the external end-plates have twelve spokes connected to the CYLDCH ones by means of twelve turnbuckles. In Figure 4.25 the final CYLDCH end-plates, end-flanges and external end-plates are shown together with the central structural iron shaft. The shaft is kept elevated by means of a support structure anchored to the granite work table by means of fixing clamps. A plexiglas cover provides the CYLDCH protection against accidents and residual dust in the cleanroom during assembly. All the mechanical parts are cleaned by means of acetone and isopropyl alcohol before the mounting procedure.

A critical feature for the CYLDCH performances is the accuracy in the **mechanical alignment** of the end-plates. The *planarity*, the *parallelism* and the *azimuthal tilt angle* are periodically monitored during assembly by means of the measuring machine. A fine-tuning of the mechanical alignment can be performed at the end of the drift chamber assembly adjusting the positions of all the spokes individually by acting on the 24 turnbuckles, until the correct planarity and parallelism between the two CYLDCH endplates are reached. The alignment procedure exploits the mechanical probe muonted on the CMM arm. The measuring machine is programmed to touch the external faces of the

spokes of the two end-plates by means of its flexible head. The recorded 3D positions are used to obtain the planarity of the two endplates: ≈ 27 μm for the reference end-plate (the upstream one) and ≈ 103 μm for the other end-plate (the downstream one).

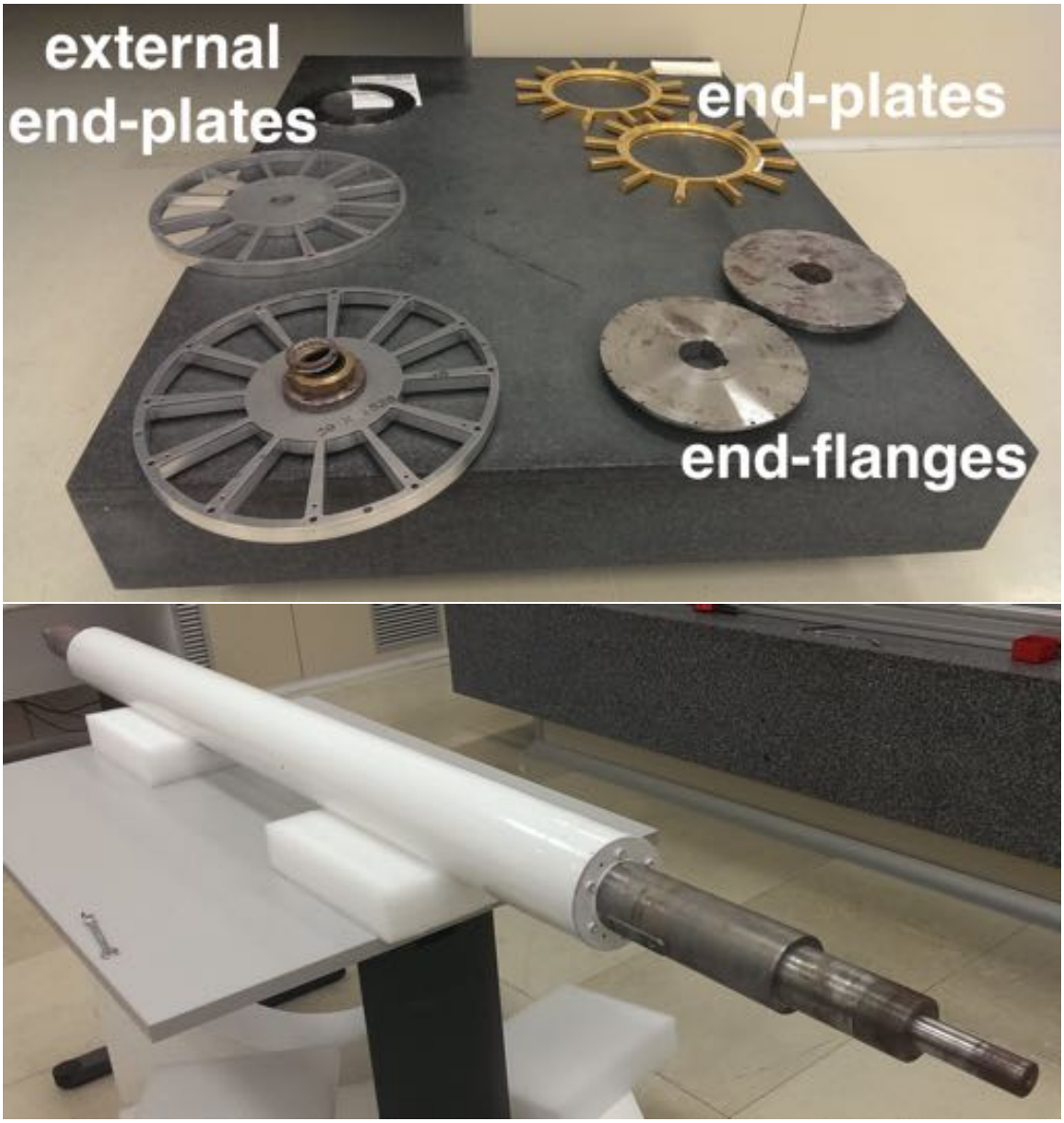

Figure 4.25: The final CYLDCH end-plates, end-flanges and external end-plates together with the central structural iron shaft.

The planarity tolerance defines a tridimensional zone limited by two parallel virtual planes with a mutual distance equal to the value of the specified tolerance. All the

measured points are within the two virtual planes. The average reference plane is defined by the reference end-plate. The probe touches also the spokes summit. These measured points are projected on the reference plane in order to measure the end-plates radii and centers by means of a bidimensional circle fit. The center of the reference end-plate defines the origin of the CYLDCH reference system during assembly. The z axis points to the direction of the other end-plate. The y axis points to the measured position of the reference sphere mounted on top of the vertical spoke of the upstream end-plate. The x axis completes the reference system. In this reference system the measured center of the downstream end-plate is located at $x \approx -136$ μm and $y = 304$ μm. This defines the concentricity of the two end-plates. The parallelism is within ≈ 301 μm. The distance between the two reference spheres mounted on top of the vertical spokes of the two end-plates, projected on the reference plane, is measured to be ≈ 52 μm (azimuthal tilt angle). The alignment procedure was repeated also with the chamber loaded with ≈ 800 kg. The parallelism between the two end-plates became within ≈ 963 μm with a planarity of the reference one of ≈ 305 μm.

At the end of the CYLDCH assembly, the two endplates will be kept in the correct position by a 1962 mm long external carbon-fiber cylinder screwed at the spokes summit. The central structural iron shaft used during assembly will be removed, including the two end-flanges. A test of the shaft extraction procedure has been successfully performed in Pisa. The carbon-fiber cylinder is made of two halves which are interlocked to enclose the whole CYLDCH internal volume. It is made of sixteen intermediate high-module pre-preg layers with a thickness of 2 mm. The external carbon-fiber cylinder, besides a structural function, ensures also the tracker gas mixture tightness, together with a kapton foil glued to the inner radius of the end-plates and locked by structural aluminum rings at both ends to guarantee the correct cylindrical shape. The carbon-fiber covers even the extensions on both sides of the drift chamber by means of two shorter cylinders. A replica of the two aluminum end-plates, kept in position by an aluminum shaft (Figure 4.26), is used by the company[5] in order to build the carbon-fiber semi-cylinders with sufficient precision. The alignment of this structure is performed using the same method explained above. The entire structure required for the construction of the carbon-fiber cylinder was delivered to the company in June 2016.

[5]Loson Compositi Srl.

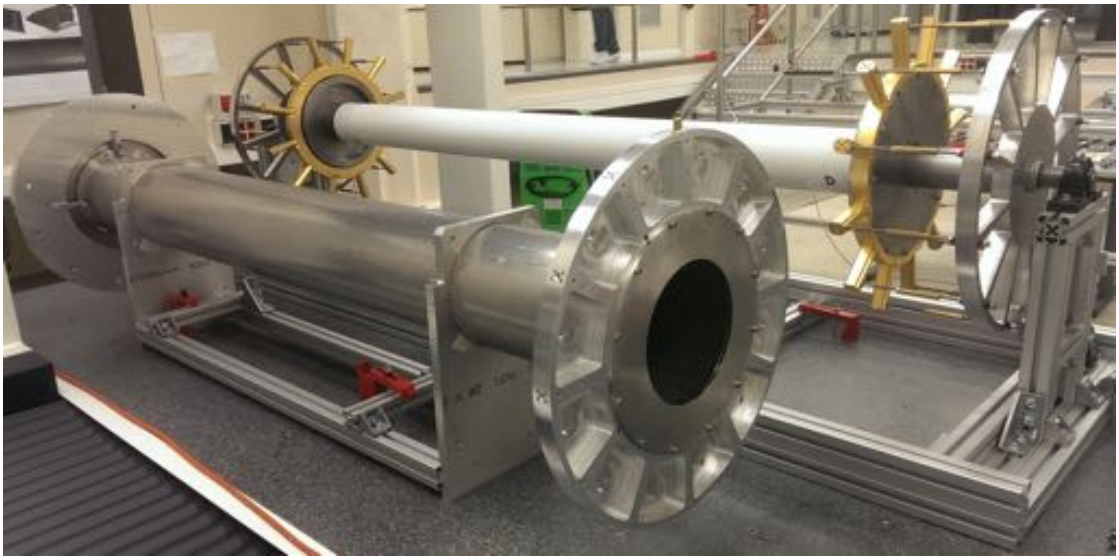

Figure 4.26: The replica of the two aluminum end-plates hold at their final relative distance by an aluminum shaft. Once aligned, this structure is provided to the company for the construction of the carbon-fiber structural cylinder.

4.2.1 Wires Acceptance Test

Once the transport trays are delivered to Pisa, a number of tests before mounting the wires on CYLDCH is performed. The first check is done in order to verify the correspondence between the trays and wire-PCBs IDs in Pisa with the Lecce wiring database. Then a visual inspection is performed, concerning the parallelism between the plexiglass PCB holders, the correct positioning and good appearance of the wire-PCBs. The solderings on the pads are also checked. The inspection continues with a careful monitoring of the wires in order to verify the oxydation state and the presence of any defects or soldering residuals.

Before considering a wires tray suitable to be mounted on the drift chamber end-plates, a mechanical elongation test is performed. The wires are over-stretched beyond the nominal length, within their elastic range, in order to verify the design mechanical properties. The nominal wires length L_{NOM} is settled at 50% of the elastic limit. The elastic range extends from $L_{NOM} - 4$ mm to $L_{NOM} + 4$ mm where the break point is reached. Hence the elastic range is about 8 mm long. The wires are slightly under-stretched compared to L_{NOM} during the Lecce-Pisa travel. The test is performed in two steps. Firstly, by acting on the longitudinal threaded rod of the transport trays, the distance between the two wire-PCBs is set so that the wires length corresponds to

L_{NOM}, and the parallelism between the two wire-PCBs is measured. Then the procedure is repeated for a wire-PCBs distance corresponding to a wires length of $L_{NOM} + 1$ mm. Sometimes the wires have been stretched to $L_{NOM} + 2$ mm. These two values correspond to 62.5% and 75% of the elastic limit. No wire broke during the mechanical extra elongation, otherwise the entire wires tray would have been discarded.

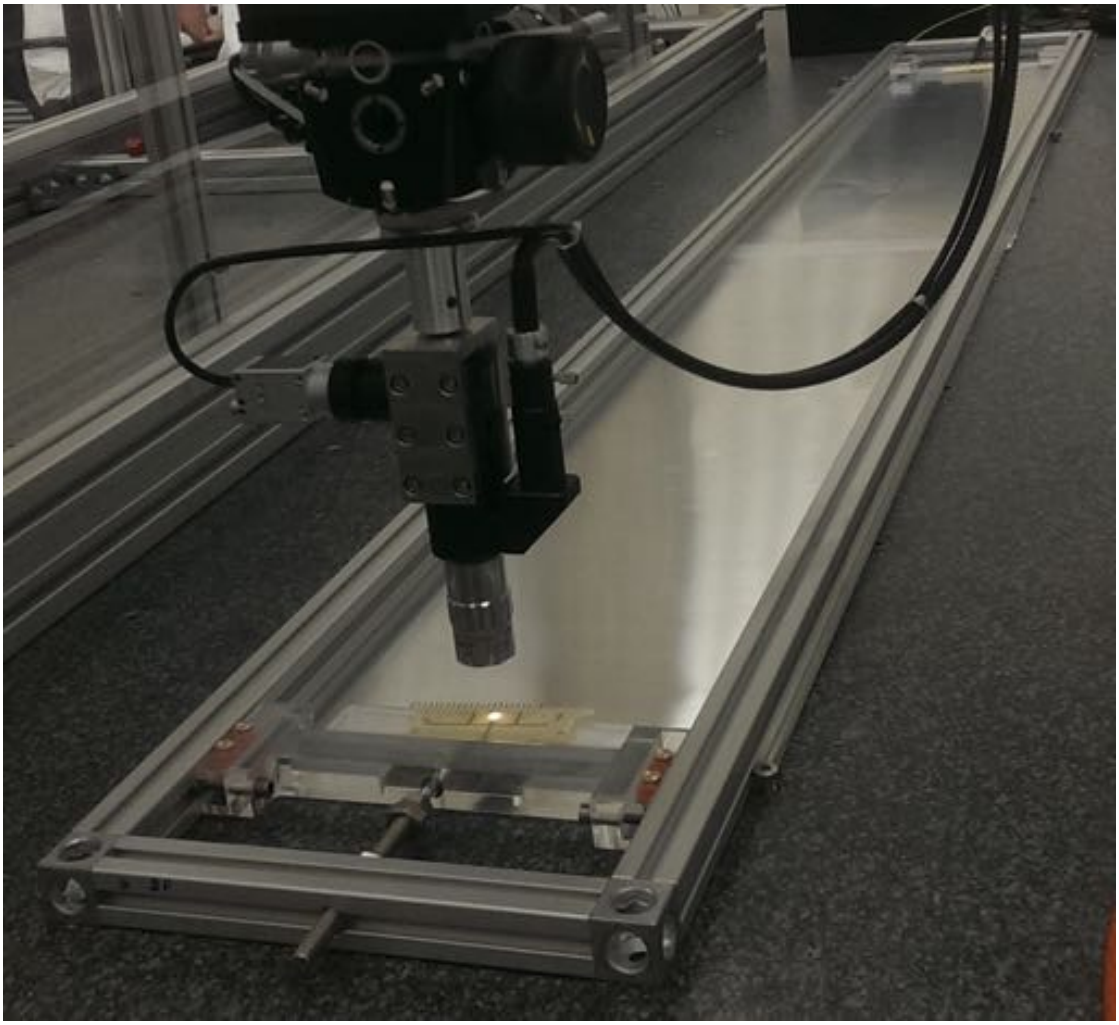

Figure 4.27: A tested wires tray aligned along the z axis of the measuring machine for the mechanical extra-elongation stress test.

The wires length is obtained indirectly by measuring the position of the three reference markers on the wire-PCBs surface by means of the measuring machine with the optical probing system. The tested tray is laid on the granite work table (Figure 4.27) and aligned with the longitudinal side along the z axis of the measuring machine.

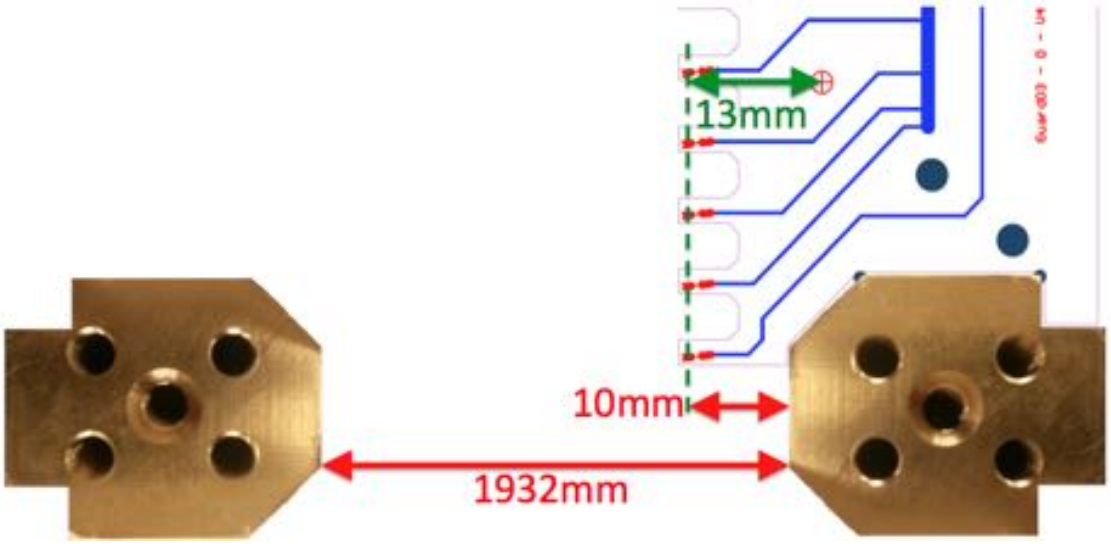

Figure 4.28: Given the nominal distance of 1932 mm among the internal faces of the two end-plates in the nominal position, the wires length along the z axis of the drift chamber 1912 mm, since the soldering pads protrude 1 mm inside the chamber volume with respect to the end-plates. The distance between the z position of the reference markers and the soldering pads is 13 mm. The wire-PCBs perimeter fits exactly the complementary shape of the end-plate spokes.

Once the wires tray are mounted on CYLDCH, with the nominal distance between the internal faces of the end-plates of 1932 mm, the wires length along the z axis of the drift chamber is 1912 mm, since the soldering pads extend for 1 mm inside the chamber volume with respect to the end-plates (Figure 4.28). Thus, the nominal wires length is given by (1912 mm)/$\cos\theta_i$ where θ_i is the stereo angle. The distance between the z position of the reference markers and the soldering pads is 13 mm. One can reproduce this situation with the wire-PCBs in the transport trays with the procedure shown in Figure 4.29 for the nominal position. From the distance between the reference markers one can trace back the wires length. The procedure is the same for the extra elongation. The parallelism among the two wire-PCBs on the benchtop is checked by means of the misalignment angle α between the two straight lines resulting from a 2D fit of the measured positions of the three reference markers. The wires tray is accepted only if $|\alpha| < 0.3°$.

The wire-PCBs misalignment is due to two factors. The PCBs are fixed to the plexiglass support structures of the transport trays by means of teflon screws. The PCBs can still slightly move within the holes for the screws. Moreover a certain sliding difficulty of the movable wire-PCBs support structure in the tray rails has been noted, leading to

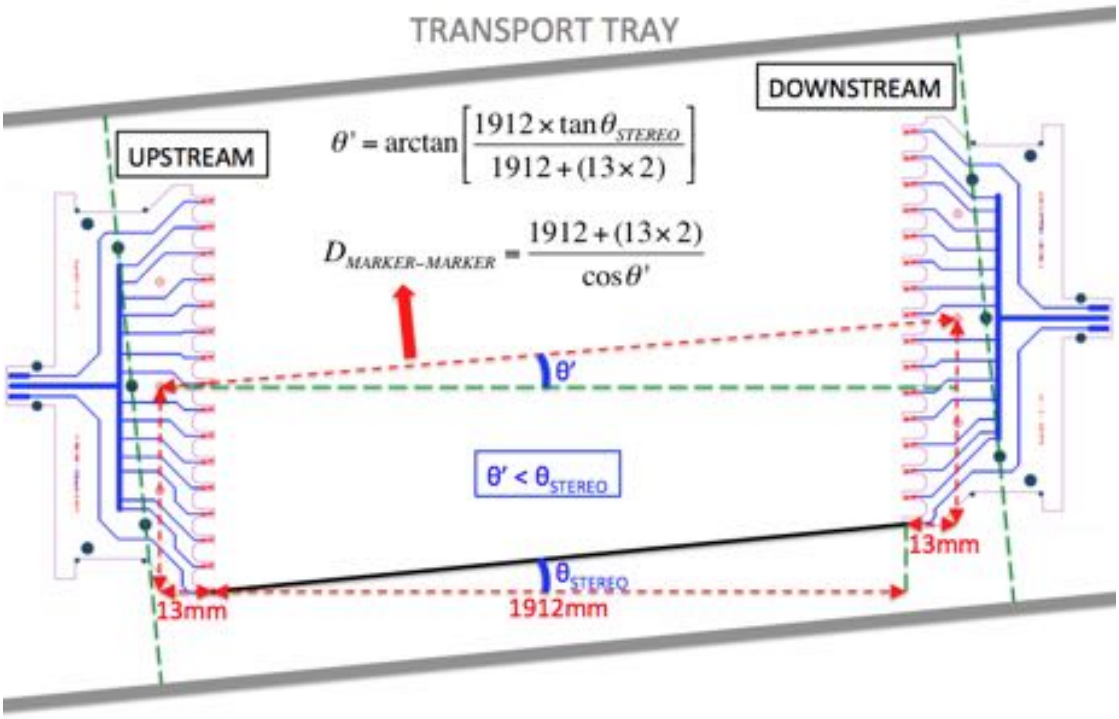

Figure 4.29: Indirect measurement of the wires length starting from the distance between the reference markers printed on the wire-PCBs surface.

a misalignment among the two plexiglass PCB holders of the same tray. Attempts to reduce the two misalignment sources have been done before the measurements. The wire-PCBs misalignment clearly leads to different relative distances among the three corresponding reference markers. Consequently even the wires length slightly varies, but the misalignment is kept under control. The maximum spread between the measured values is within ± 150 μm ($|\alpha| < 0.3°$), leading to ≈ 50 μm/0.1°.

4.2.2 Mounting Procedure

After the mechanical stretch test is positively passed, a wires tray is ready to be mounted on CYLDCH. A simplified description of the new drift chamber assembly procedure is given below. After an initial training phase, an operative manual has been written in order to ensure a safe operation and minimize the failure probability. During the mounting phase the end-plates are moved closer with respect to the nominal position down to 1926 mm in order to not stress the wires during assembly.

Figure 4.30: Above: support structure where the wires tray are anchored to the mounting arm. Below: the flipping tray used to mount wire-PCBs on the flipped wires layer.

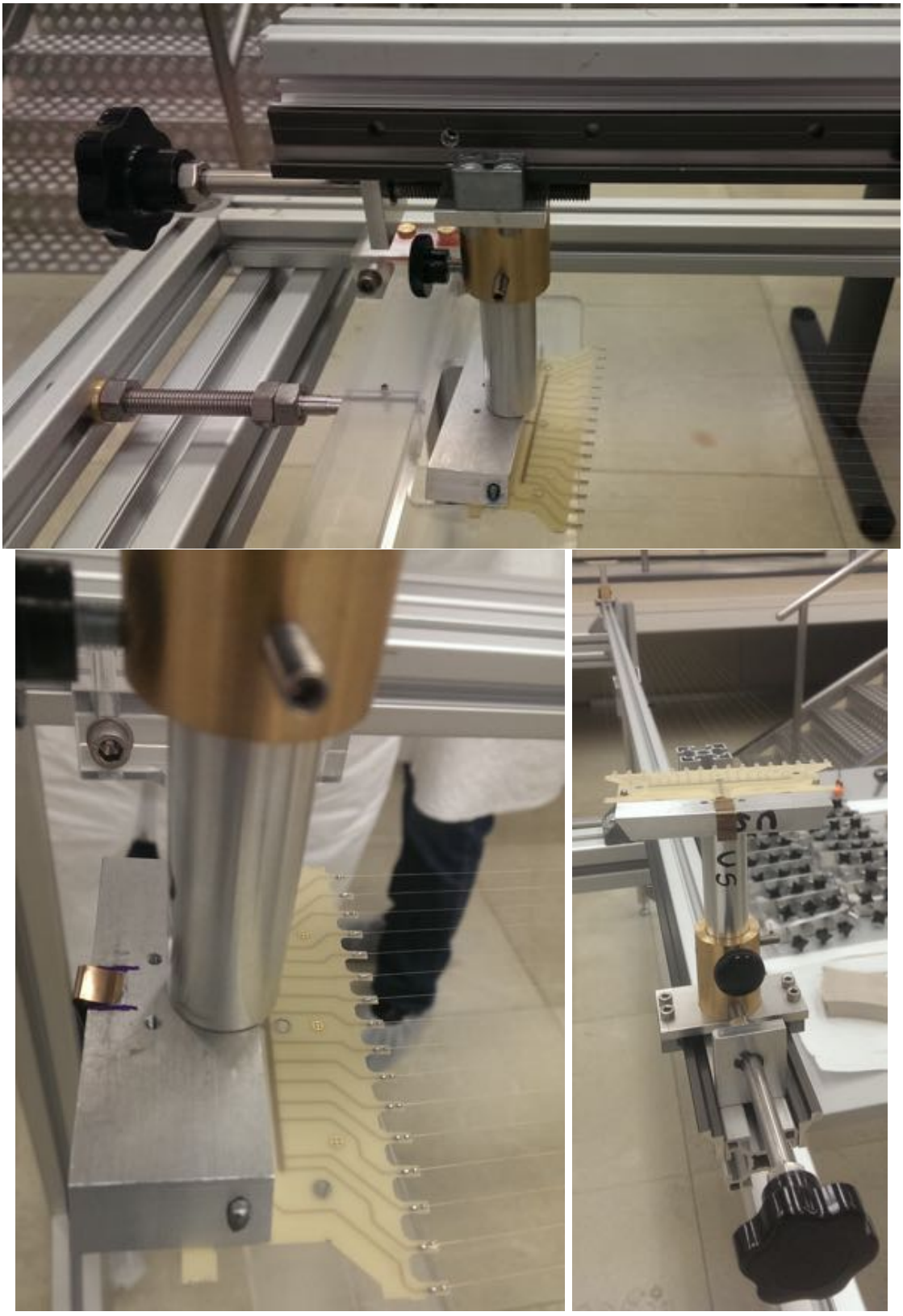

Figure 4.31: The anchoring procedure and the hang wires ready to be mounted on CYLDCH.

The mounting procedure is performed with a dedicated anchoring arm (Figure 4.30). Two aluminum blocks are fixed in an aluminum bar. Their relative distance can be adjusted through a knob in order to match the variable wire-PCBs distance. Even their angle can be adjusted depending on the stereo angle by means of two pins under the aluminum blocks which are dedicated to match the position of the two fixed holes in the wire-PCBs. The transport tray is laid on a support structure and, after a further visual inspection, the wire-PCBs are anchored to the mounting arm. A clip is applied to the wire-PCBs tails and the teflon screws are removed (Figure 4.31). In this way a safe separation and lift of the wires tray is ensured. If in the current wires layer the wire-PCBs have to be mounted flipped, an intermediate step is done. This happens for all the cathode and guard planes since they feature a double layer of wires at the same mounting radius. A dedicated flipping tray (Figure 4.30), featuring the same characteristics of the mounting arm, holds the wires tray before using the anchoring arm. Afterwards the mounting arm with the hang wires (Figure 4.31) is driven to one side of CYLDCH for the engagement procedure.

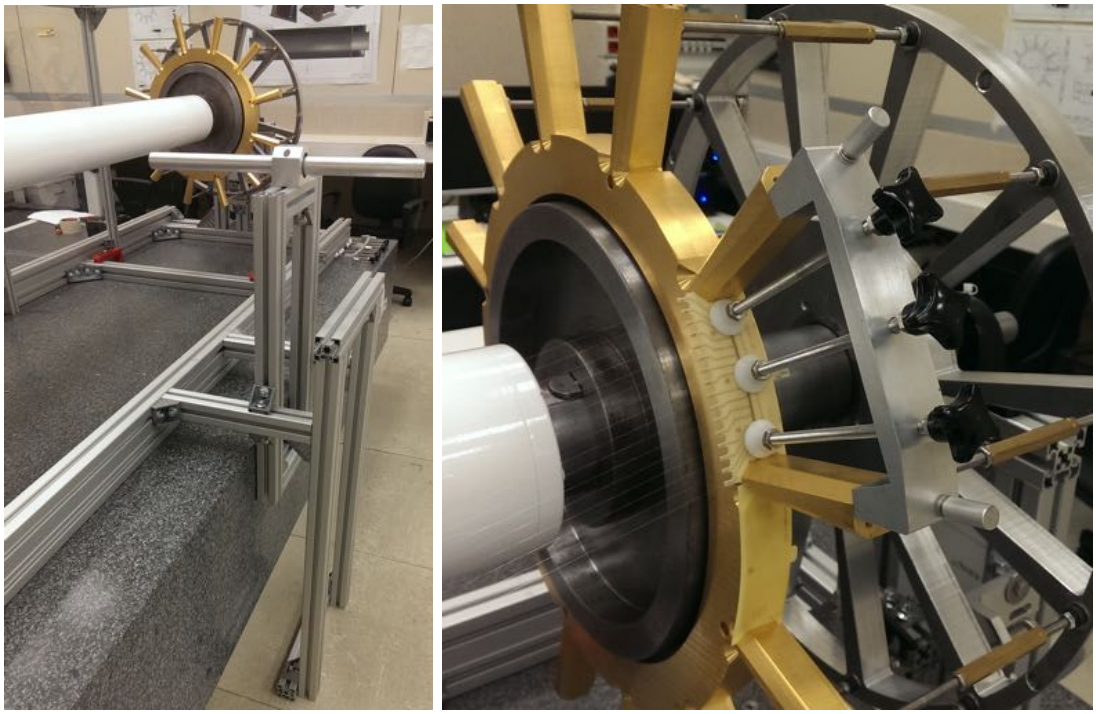

Figure 4.32: Left: support structure used for assembly with the aluminum rod which keeps the mounting arm at the correct level. Right: aluminum holder to keep pressed the wire-PCBs just mounted on CYLDCH.

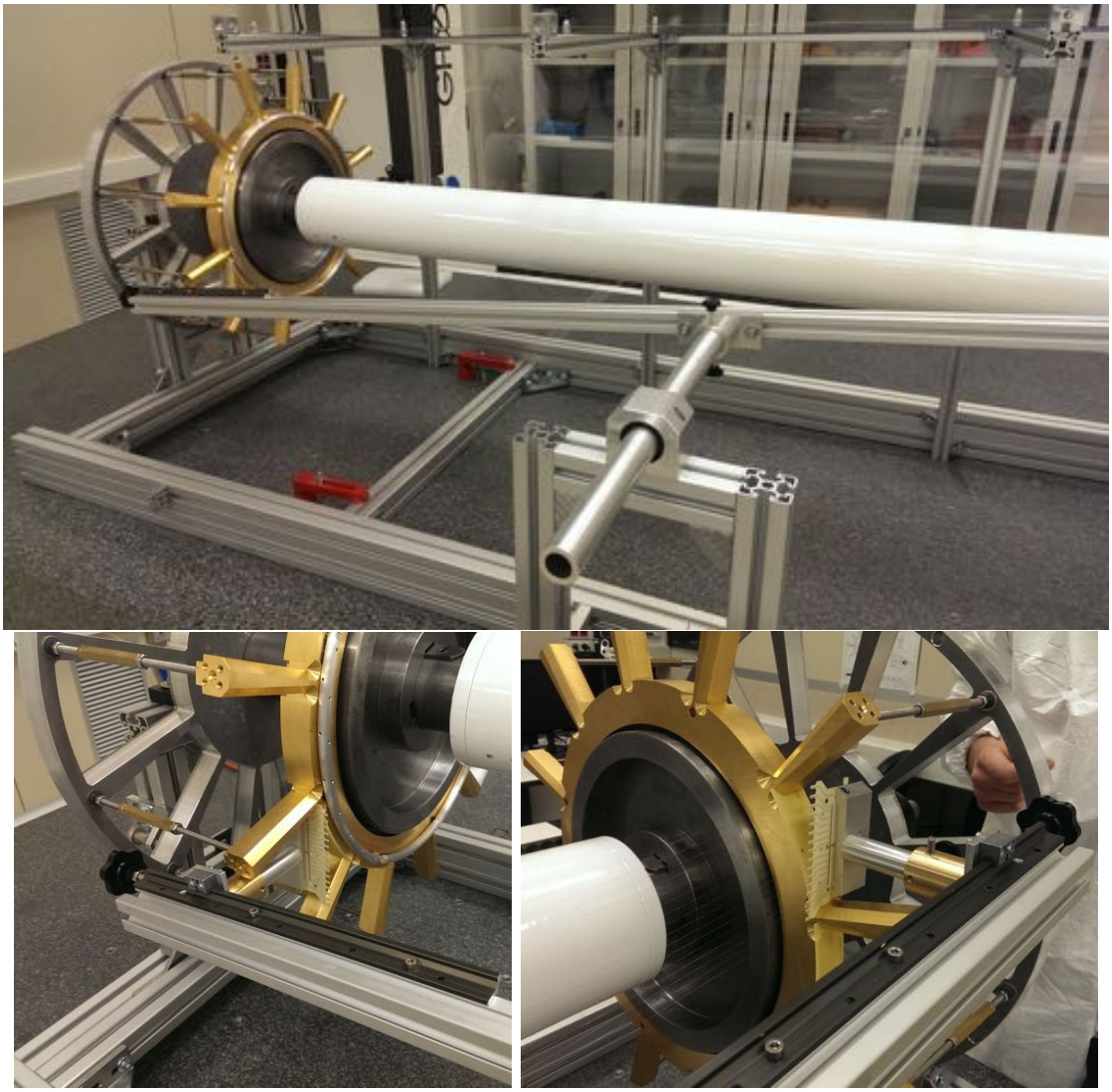

Figure 4.33: The wires tray approach to the proper slots on the CYLDCH end-plates.

The safe wire-PCBs approach to the slots in the end-plate sectors is ensured by another structure which holds an aluminum rod used to keep the mounting arm at a correct level (Figure 4.32). The distance between the wires tray and the chamber is adjustable since the rod can slide with respect to the support structure perpendicularly to the drift chamber axis, being connected to the mounting arm through a joint placed approximately in the middle of it. The wire-PCBs are positioned in this way very close to their final position on the chamber (Figure 4.33). The last few centimeters are driven by hand through dedicated nippers. The wire-PCBs perimeter fits exactly the complementary

shape of the end-plate spokes (Figure 4.28). The wire-PCBs are kept in the correct position by means of a 3M[6] double-sided tape previously applied on the lower PCBs layer. Dedicated aluminum holders (Figure 4.32) keep the wire-PCBs slightly pressed for about a day and are then removed. The holders are screwed on the spokes summit and possess three threaded rods with a knob on top and a teflon presser in order to better distribute a uniform pressure on the PCBs surface. The same procedure is repeated for all the sectors and wires layer. When an entire wires layer is assembled, the end-plates are moved to the nominal distance and the alignment procedure is performed again.

Wire-PCBs Position Survey

Before assembly of the successive wires layer, a survey is performed by means of the measuring machine in order to measure the actual position of the wire-PCBs mounted on CYLDCH. In fact, possible deviations from the nominal radial position can happen mainly due to the unknown actual thickness of the double-sided tape. Its nominal thickness is 50 μm, but being a soft material, it can assume different values once pressed. Moreover even its behaviour with the 35 μm-thick gold tracks on the wire-PCBs surfaces is unpredictable. However, a fine-tuning of the thickness of the PEEK spacers put between the several wires layers can compensate and reduce the discrepancy.

A survey consists in measuring the position of the three reference markers on the wire-PCBs surface by means of the optical probing system of the CMM. The measurement is done on both end-plates with the tested sector in the upper position, thus in one layer the endplates are rotated 12 times by 30°. In order to link all the measurements, a local reference system is created by measuring three points, spaced as much as possible, on the edges of the two spokes delimiting each sector. Thus, the markers positions are relative to the average point on the spokes edges. Summarizing, a total of 9 points are recorded for each sector. These points are then azimuthally shifted in order to build a virtual end-plate (Figure 4.35). The distribution of the measured points (front, top and side views) is shown in Figure 4.34 for the DS and US end-plates of one guard layer, as example. A 2D circle fit of the virtual end-plate is then performed to obtain the actual mean radial position R_{FIT} of the wire-PCBs mounted on the drift chamber (Figure 4.35). The plots refer to the double wires layer (U- and V-view) of the first guard plane. The deviation with respect to the nominal radius is $-(200 \div 250)$ μm depending on the wires layer. The radial distribution around R_{FIT} of the three reference markers is also shown.

[6] 3M web-site: http://www.3mshop.it

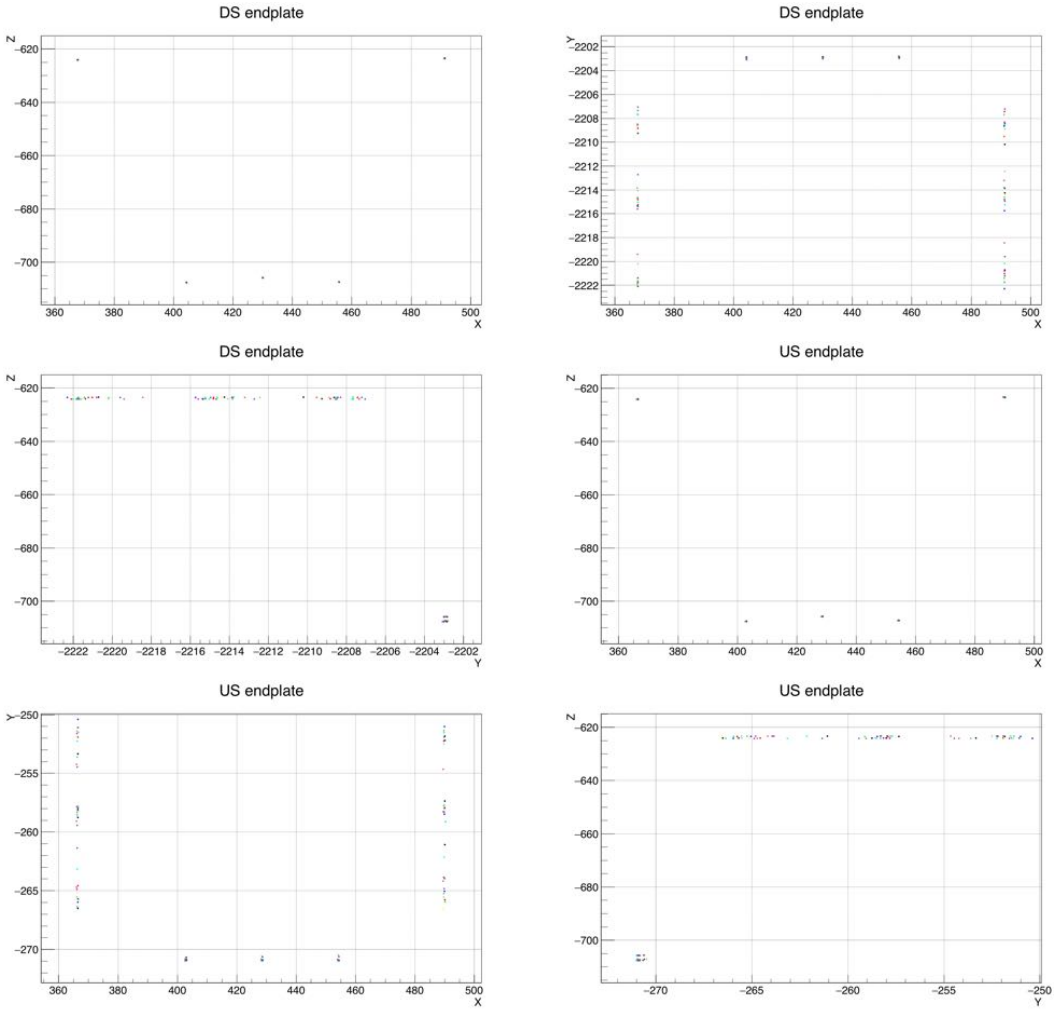

Figure 4.34: Distribution of the optically measured points (front, top and side views) for the DS and US end-plates of one guard layer as example. The axes are in millimeters and the values are in the default global reference system of the CMM. Each sector $(0 \div 11)$ has a different color.

In addition to the optical survey, in order to further verify the radius of the mounted wire-PCBs, a more accurate measurement with the CMM mechanical touching probe have been also performed. With the end-plates kept in a fixed postion, the measuring machine has been programmed to touch the upper surfaces of the wire-PCBs in three points spaced as much as possible. The resulting circle fit of the acquired points gives a measured radius which is in agreement with respect to the nominal one within $\pm(50 \div 100)$ μm depending on the wires layer.

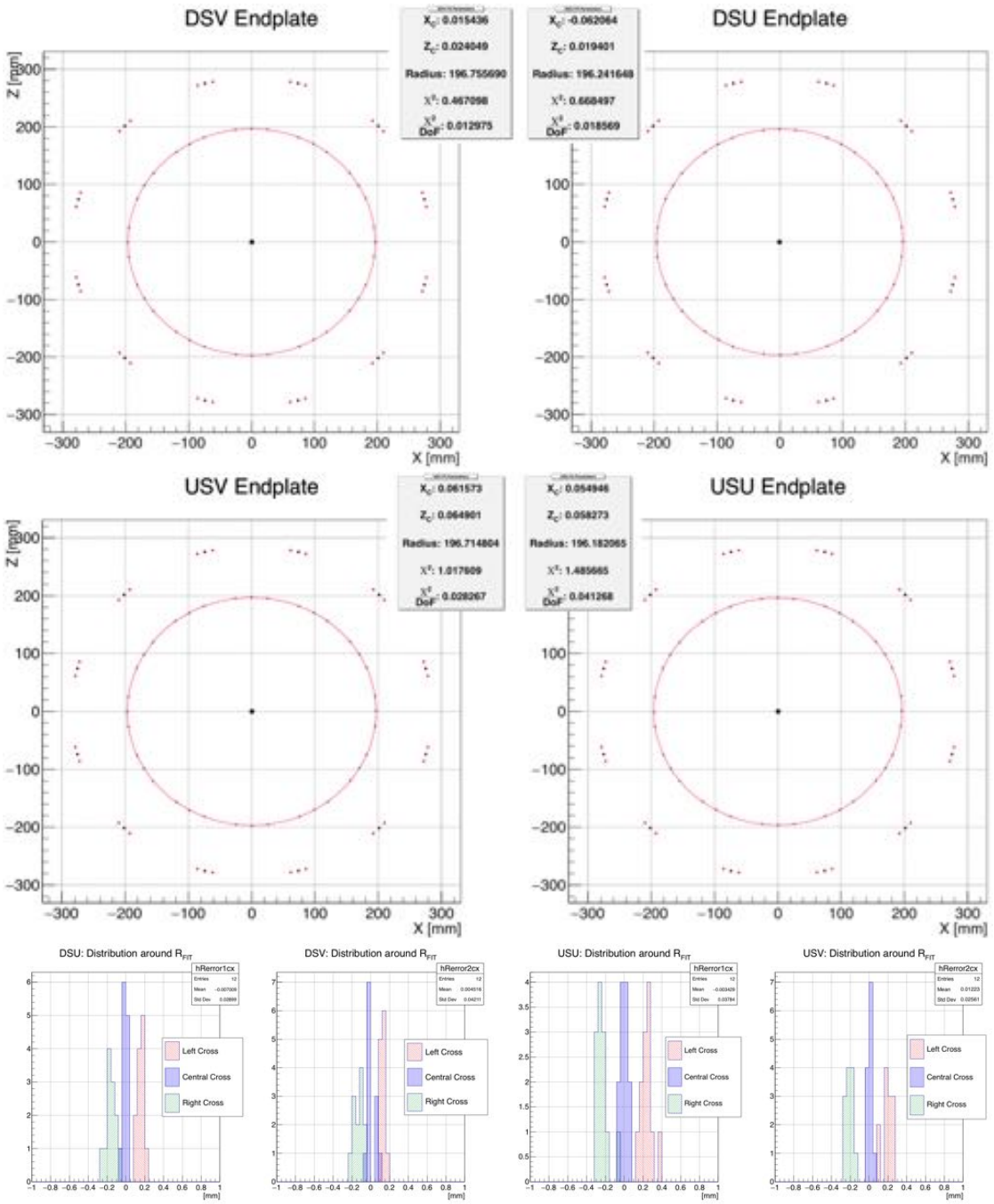

Figure 4.35: 2D circle fit of the measured reference markers (blue dots) to obtain the average radial position R_{FIT} of the wire-PCBs mounted on the drift chamber. The plots refer to the double wires layer (U- and V-view) of the first guard plane. The red dots are the mean positions of the measured spokes edges, while the black dots are the nominal spokes centers. The mean spokes edges are used to build a local reference system for each sector. In this way the measured reference markers can be azimuthally shifted to build a virtual end-plate. The radial distribution around R_{FIT} of the three reference markers is also shown.

4.2.3 Mock-up and Final Chambers

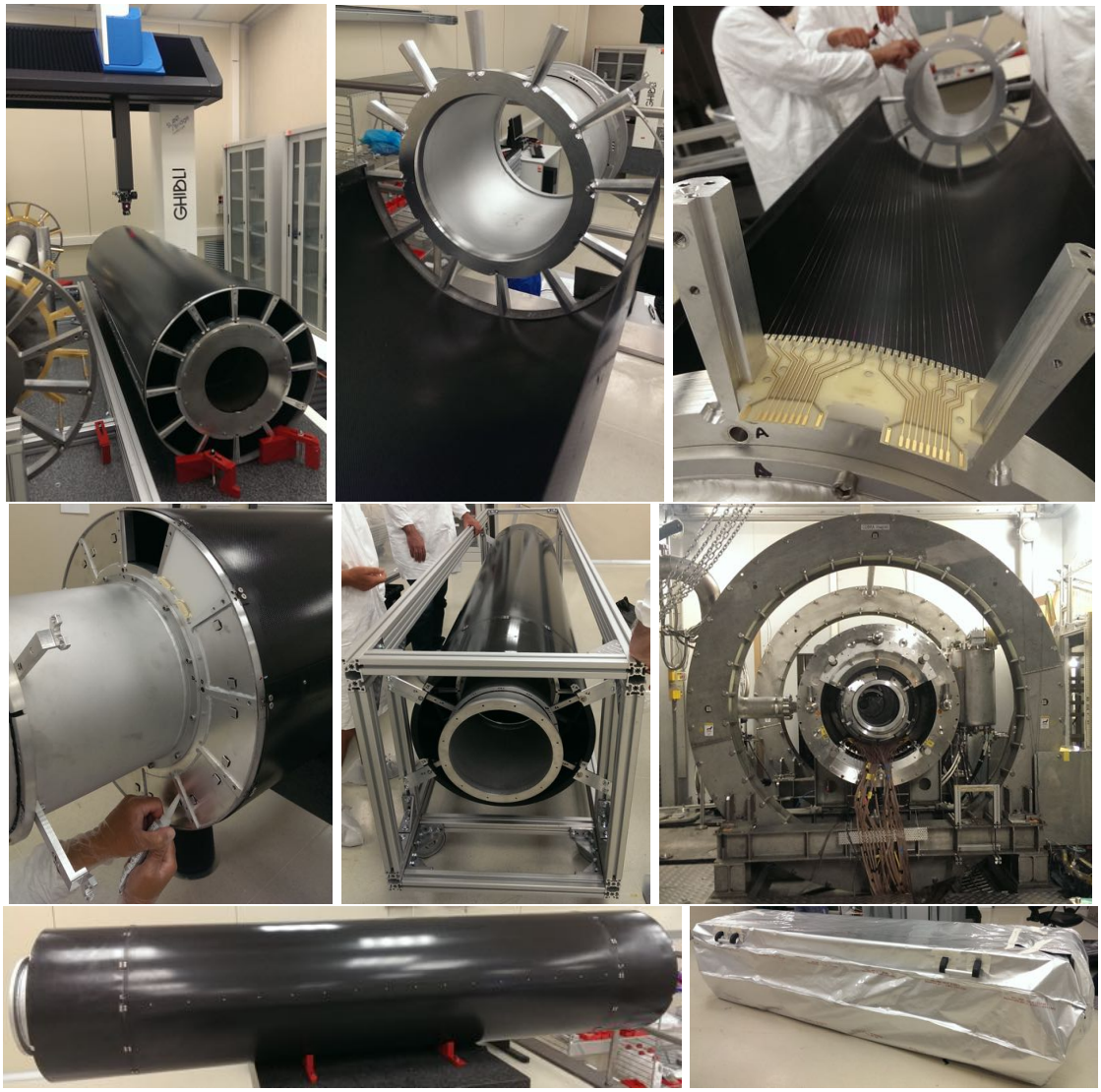

Figure 4.36: Some pictures of the mock-up chamber assembly. From top left: the mock-up chamber with the structural carbon-fiber cylinder mounted alongside CYLDCH for the alignment procedure with the CMM; one aluminum end-plate with half carbon-fiber cylinder applied and the extension connected to the ring; the anode wires strung in one sector with the wire-PCBs kept at the nominal radius thanks to proper spacers; the sealing of the empty sectors (the two connectors of an anode wire-PCB are visible); the support structure used for the Pisa-PSI travel; the mock-up chamber inserted into COBRA; the whole mock-up chamber with the carbon-fiber applied also to the extensions; the tight wrapping used to enclose the mock-up chamber during the transport.

A mechanical mock-up (Figure 4.36) of the final CYLDCH was assembled at the San Piero a Grado (Pisa) facility of INFN. The mock-up features the same size and mechanical characteristics of the final MEG-II CYLDCH. The anode wires were strung only in one plane and in one sector of the aluminum end-plates in the correct radial position by means of a proper spacer. The remaining 22 empty sectors were sealed by means of aluminum annulus-shaped caps glued to the external faces of the end-plates. Even the extensions on both sides of the chamber were mounted. The two halves of the structural carbon-fiber cylinder were interlocked in the correct final position, together with the shorter cylinders covering the two extensions. The mechanical mock-up chamber was delivered at PSI on August 2015. Mechanical insertion inside the COBRA magnet and gas leak tests were successfully performed, together with electrical tests on the mounted wires in order to measure the noise level in the MEG experimental area. The mock-up chamber was of fundamental importance for tuning the insertion of the new MEG-II pixelated Timing Counter (TC) inside COBRA (Figure 3.13) in view of the pre-engineering Michel run foreseen in winter 2015.

Regarding the final CYLDCH assembly in Pisa, some pictures of the wire-PCBs and PEEK spacers stack with the wires strung at their stereo angle on CYLDCH are shown in Figure 4.37. Finally, a picture of the final drift chamber with the first two double layers of guard and cathode wires is shown in Figure 4.38.

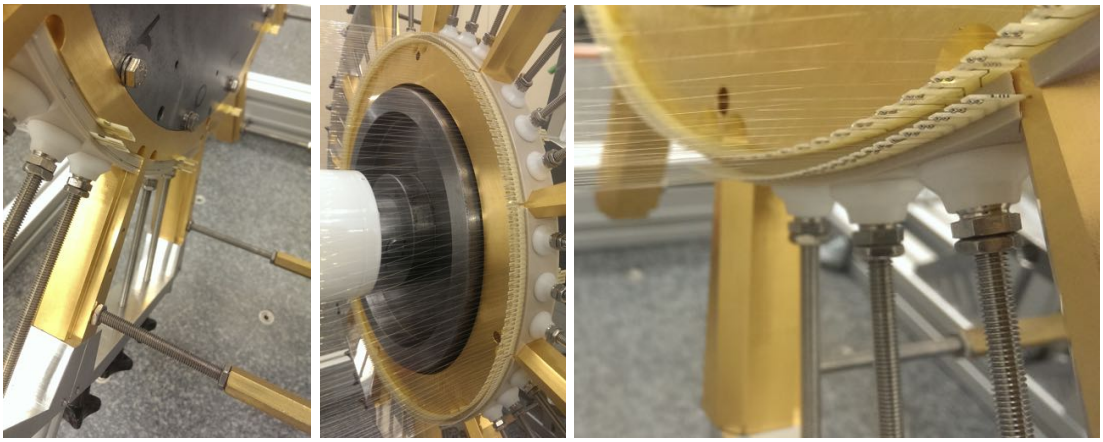

Figure 4.37: The wire-PCB and PEEK spacers stack during assembly with the wires strung at their stereo angle on CYLDCH. Also the connectors and the spacing between the first double layer of guard wires and the cathode plane are visible. As planned, the soldering pads of the flipped guard wire-PCBs do not overlap the lower ones.

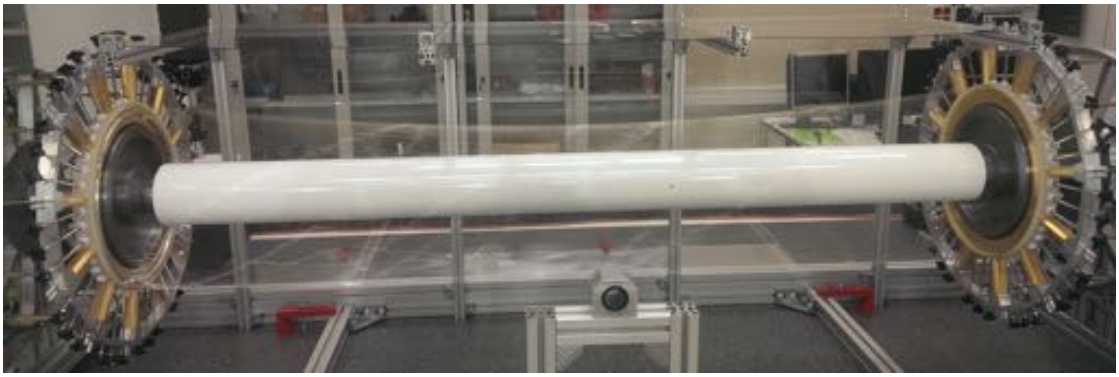

Figure 4.38: The final MEG-II CYLDCH assembled in Pisa with the first two double layers of guard and cathode wires.

4.3 Wires Choice

Several wires candidates from different companies[7] were taken into account in the design and R&D period. Given the high granularity of the new drift chamber covering the whole azimuthal angle ϕ in a unique volume, its transparency is a crucial feature in order to keep at a minimum the Multiple Coulomb Scattering (MCS) for positrons whose energy is of the order of 50 MeV. Moreover minimization of the background photons rate in the LXe calorimeter from bremsstrahlung and e^+ Annihilation-In-Flight (AIF) with the electrons of the traversed materials is of crucial importance. The radiation length X_0 in a mixture or compound can be approximated by [20]:

$$\frac{1}{\mathrm{X}_0} = \sum_i \frac{w_i}{\mathrm{X}_i} \tag{4.5}$$

where w_i and X_i are the fraction by weight and the radiation length for the i^{th} element respectively. In Table 4.1 a summary of the characteristics of the possible types of field and guard wires is shown. In particular, the radiation length X_0, the thickness $\langle X \rangle$ and the angular deflection θ_{MCS} due to MCS are reported. The contributions due to the wires only and all the crossed materials are highlighted. For the calculation of the materials thickness and MCS contribution see Section 4.4.

[7]California Fine Wire (CFW) Company, Alloy Wire International (AWI), Luma Metall Fine Wire Products.

Type	X_0 (mm)	$\langle X \rangle^{wires}$ (10^{-3} X_0)	$\langle X \rangle^{tot}$ (10^{-3} X_0)	θ^{wires}_{MCS} (mrad)	θ^{tot}_{MCS} (mrad)
Al (5056)	89	0.72	1.5	5	7.6
Ti	36	1.26	2.1	6.8	9
CuBe	14.7	2.58	3.4	10.1	11.7
Stainless Steel (302)	17.8	2.2	3	9.3	11

Table 4.1: Summary of the possible candidates considered for field and guard wires of CYLDCH.

Type	Resistivity (Ω/m)	Composition	X^i_0 (g/cm^2)	ρ^i (g/cm^3)	X^i_0 (cm)
Ti	200	Ti	16.16	4.51	3.60
CuBe	25	0.981 Cu	12.86	8.93	1.44
		0.019 Be	64.13	1.85	34.66
Stainless Steel (302)	200	0.720 Fe	13.84	7.87	1.76
		0.090 Ni	12.68	8.91	1.42
		0.180 Cr	14.94	7.14	2.1
		0.010 Mn	14.64	7.47	1.96

Table 4.2: Detailed composition of the possible candidates considered for field and guard wires material.

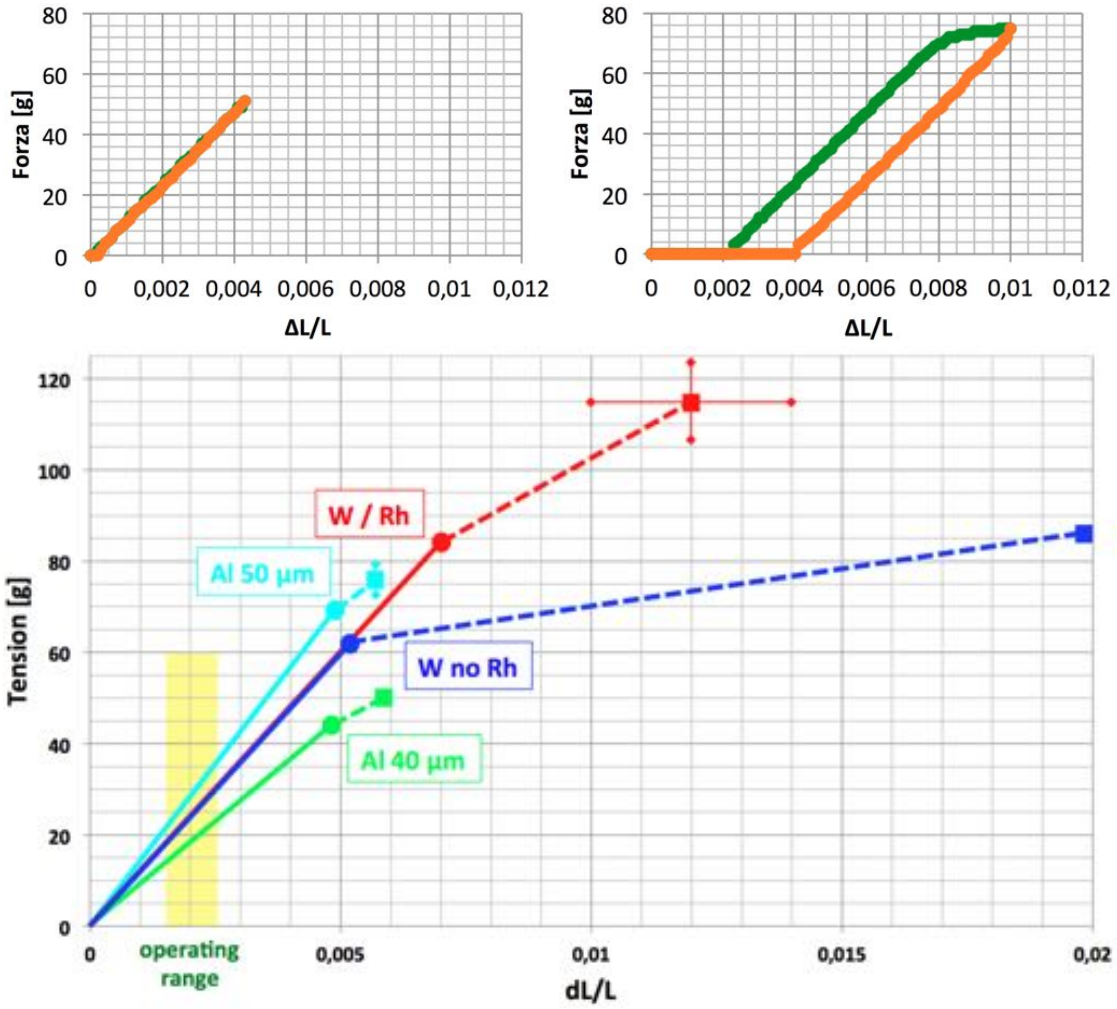

Figure 4.39: Above: example of hysteresis studies on the pure-W wires. Below: the operating range of all wires.

In Table 4.2 the detailed composition of the wires material are shown. For the aforementioned reasons, the 5056 aluminum alloy from the CFW company has been chosen for the field and guard wires of CYLDCH with diameters of 40 μm and 50 μm. This alloy is composed by: 94.6% Al, 5.2% Mg, 0.1% Cr, 0.1% Mn. The density is $\rho = 2.7$ g/cm^3 and the resistivity is ≈ 20 Ω/m. The wires are further silver-plated. The coating thickness is a fraction of micron and the density ρ becomes approximately 3 g/cm^3. The same wires, but with a diameter of 80 μm, were used by the KLOE collaboration for the drift chamber [36].

Two options have been considered for the anodes: pure-tungsten or tungsten with the addition of $\approx 3\%$ of Rhenium. The W-Re wires have a larger elastic limit but this is not important for the MEG upgrade once the working point is defined. Conversely, after R&D studies, they presented a higher non-uniformity, a shorter elongation at break point and a larger resistivity: 290 Ω/m vs. 170 Ω/m of pure-tungsten wires which implies a narrower bandwidth due to larger noise and smaller gain. Since this is a critical feature for the *Cluster Timing* technique (described in Section 3.2.3) the choice fell on 20 μm-thick pure-W wires, gold plated for a final density of $\rho \approx 19.25$ g/cm^3.

An example of hysteresis studies on the pure-W wires, together with the operating range of all wires are shown in Figure 4.39. The mechanical features of the silver-plated aluminum and gold-plated tungsten wires chosen for CYLDCH are summarized in Table 4.3.

Type	Break Point
Al (40 μm)	50 ± 3 g @ 5.8 ± 0.3 mm/m
Al (50 μm)	75 ± 4 g @ 5.6 ± 0.3 mm/m
W (20 μm)	86 ± 3 g @ 19.7 ± 0.3 mm/m
Type	Elastic Limit
Al (40 μm)	44.3 ± 0.8 g @ 4.8 ± 0.1 mm/m
Al (50 μm)	69.5 ± 0.5 g @ 4.90 ± 0.04 mm/m
W (20 μm)	62.0 ± 0.7 g @ 5.30 ± 0.05 mm/m
Type	Elastic Modulus
Al (40 μm)	9.2 ± 0.1 g/mm/m
Al (50 μm)	14.2 ± 0.2 g/mm/m
W (20 μm)	11.71 ± 0.03 g/mm/m

Table 4.3: Mechanical features of the wires used for the new MEG-II CYLDCH.

4.4 Material Budget Estimation

In order to get an estimate of the mean amount of material crossed by the positrons in one full turn in CYLDCH the following procedure can be used. A schematic representation of a wires layer (red dots) is shown in Figure 4.40 on the left. The wire diameter is d_W, the radius of the wires layer is ρ, while the mutual distance between the wires within the same layer is $C_W/2$. The total discrete area covered by the n wires in one layer can be written as:

$$A = n\pi \left(\frac{d_W}{2}\right)^2 = n\left(\frac{C_W}{2}\right)\langle\delta\rangle \quad \rightarrow \quad \langle\delta\rangle = \frac{2\pi(d_W/2)^2}{C_W} \tag{4.6}$$

which is equivalent to a rectangle of height $\langle\delta\rangle$ and basis $n(C_W/2)$ (Figure 4.40 in the middle).

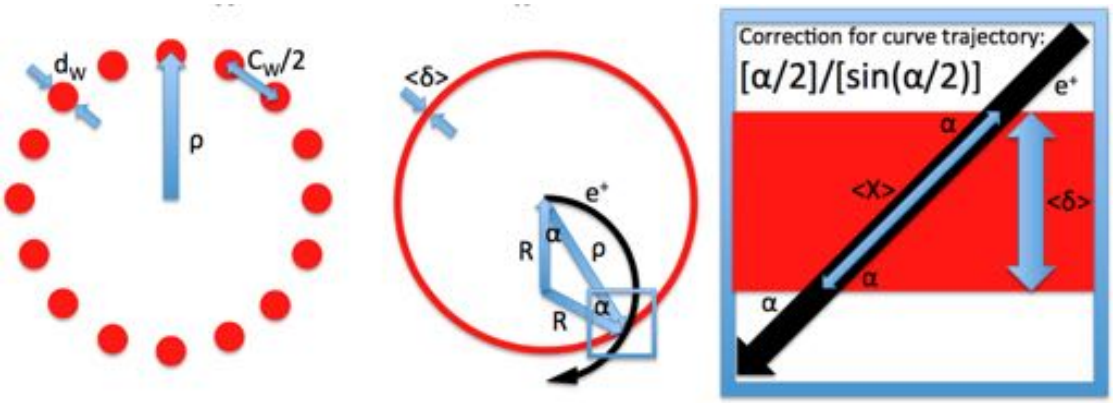

Figure 4.40: Estimation of the mean amount of material crossed by the positrons in one full turn through CYLDCH.

The average crossed width $\langle X\rangle$ in one full turn can be written as (Figure 4.40 on the right):

$$\langle X\rangle = \frac{\langle\delta\rangle}{\sin\alpha} \tag{4.7}$$

The angle α can be written in terms of the radius R of the positron trajectory:

$$\cos\alpha = \frac{\rho}{2R} \quad \rightarrow \quad \frac{1}{\sin\alpha} = \frac{1}{\sqrt{1-\left(\frac{\rho}{2R}\right)^2}} \tag{4.8}$$

leading to:

$$\langle X \rangle = \frac{2\pi(d_W/2)^2 2R}{C_W\sqrt{2R^2-\rho^2}} \tag{4.9}$$

By summing over all the crossed wires layers and considering all the traversed materials, except the polyethylene stopping target and including kapton foils, He inner gas and He:iC_4H_{10} tracker gas, the average thickness due to all traversed materials seen by a positron after one full turn is expected to be about 1.5×10^{-3} X_0, which is smaller than 1.7×10^{-3} X_0 of the previous MEG spectrometer, despite the high granularity unique volume covering the whole azimuthal angle of CYLDCH. This is crucial to keep at minimum level the Multiple Coulomb Scattering (MCS) contribution to the positron momentum and angular resolutions and also the rate of background photons in the LXe calorimeter generated by bremsstrahlung and the positron Annihilation-In-Flight (AIF) with electrons of the crossed materials.

4.4.1 Multiple Coulomb Scattering (MCS) Contribution

The minimization of the MCS contribution is crucial in order to achieve optimal momentum and angular resolutions of positrons. When a charged particle traverses a medium, it is deflected by many small-angle scatters. Most of this deflection is due to Coulomb scattering from nuclei and hence this effect is called Multiple Coulomb Scattering (MCS). The scattering distribution is well described by the theory of Molière [56] [55] and, for small deflection angles, it is roughly Gaussian with a σ given by:

$$\theta_0 = \frac{13.6 \text{ MeV}}{\beta cp} z\sqrt{\frac{x}{X_0}}\left[1 + 0.038 \ln\left(\frac{x}{X_0}\right)\right] \tag{4.10}$$

where p, βc and z are the momentum, velocity and charge number of the incident particle respectively, x is the thickness of the scattering medium and X_0 is its radiation length. This value is a projected angular distribution on a plane, while the expected width of the angular distribution in space is $\theta_{space} = \sqrt{2}\theta_0$. This value of θ_0 is derived from a fit to the Molière distribution for singly charged particles with $\beta = 1$ for all Z and it is accurate to 11% or better for $10^{-3} < x/X_0 < 100$. For deflection angles greater than a few θ_0 the MCS distribution behaves like a Rutherford scattering ($\sim 1/\sin^4(\theta/2)$), resulting in larger tails compared to a pure Gaussian distribution. For many applications it is sufficient to use the Gaussian approximation for the central 98% of the projected angular distribution.

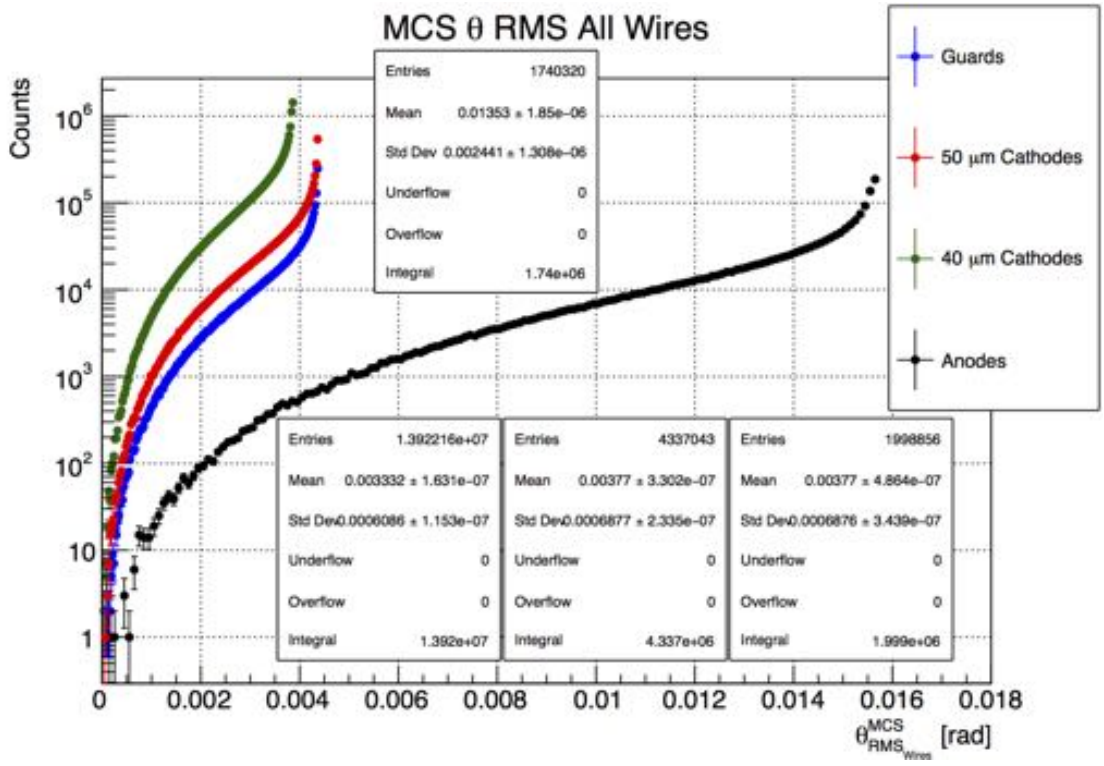

Figure 4.41: Values of θ_0 for the wires materials crossed by positrons along their trajectories through CYLDCH. The variable position of the impact point on the wires has been taken into account, resulting in a variable thickness traversed by the positrons.

When a positron passes through the CYLDCH volume, it can hit one wire or even more (sense, field or guard wires) and can be deviated from its original path. An important contribution to the MCS is precisely the collision with the wires which can limit the maximum achievable resolution on the positrons kinematic variables. A rough estimate of the probability for a e^+ of hitting a wire within one drift cell can be deduced in a geometrical way by considering the ratio between the sum of the wires dimensions within one drift cell and the dimension of the cell itself. For this value one can consider the diagonal of an almost square drift cell with an average side length. The drift cells width varies from 6.7 mm to 9 mm, therefore an average dimension of 7.9 mm is considered. Then for a single cell layer, the hit probability is:

$$P_{HIT} = \frac{4 \times 40\ \mu\text{m} + 50\ \mu\text{m} + 20\ \mu\text{m}}{\sqrt{2} \times 7900\ \mu\text{m}} \approx 2\% \tag{4.11}$$

Thus the probability of no hit within one cell layer is $P_{NO\text{-}HIT} = 1 - P_{HIT} \approx 98\%$. The hit probabilities are independent for different cell layers, so one can take the product

$P_{NO\text{-}10} = (P_{NO\text{-}HIT})^{10} \approx 80\%$. In conclusion, a rough estimate of the probability for a e^+ of hitting at least one wire along its path through the 10 drift cells planes of CYLDCH is $P_{\geq 1\text{-}HIT} = 1 - P_{NO\text{-}10} \approx 20\%$.

A toy Monte Carlo (toy-MC) simulation has been used in order to evaluate the e^+ angular deviation due to the MCS given by all the traversed materials in one half turn from the polyethylene stopping target to the the last wires plane, including the He gas, the He:iC_4H_{10} 85:15 tracker gas and the kapton foil which separates the inner volume from the sensitive volume. The number of generated signal positrons is 10^8 with a bending radius of their trajectory of 14 cm, corresponding to a e^+ momentum of about 52.8 MeV. The polyethylene stopping target has a radiation length $X_0 = 503$ mm and a thickness of 140 μm. The kapton foil has a radiation length $X_0 = 286$ mm and a thickness of 25 μm. The He inner gas has a radiation length $X_0 = 5.70 \times 10^6$ mm, while the tracker gas mixture has $X_0 = 1.03 \times 10^6$ mm. The 20 μm-thick gold-plated tungsten sense wires have $X_0 = 3.5$ mm, while the 40 and 50 μm-thick silver-plated aluminum field and guard wires have a radiation length $X_0 = 89$ mm.

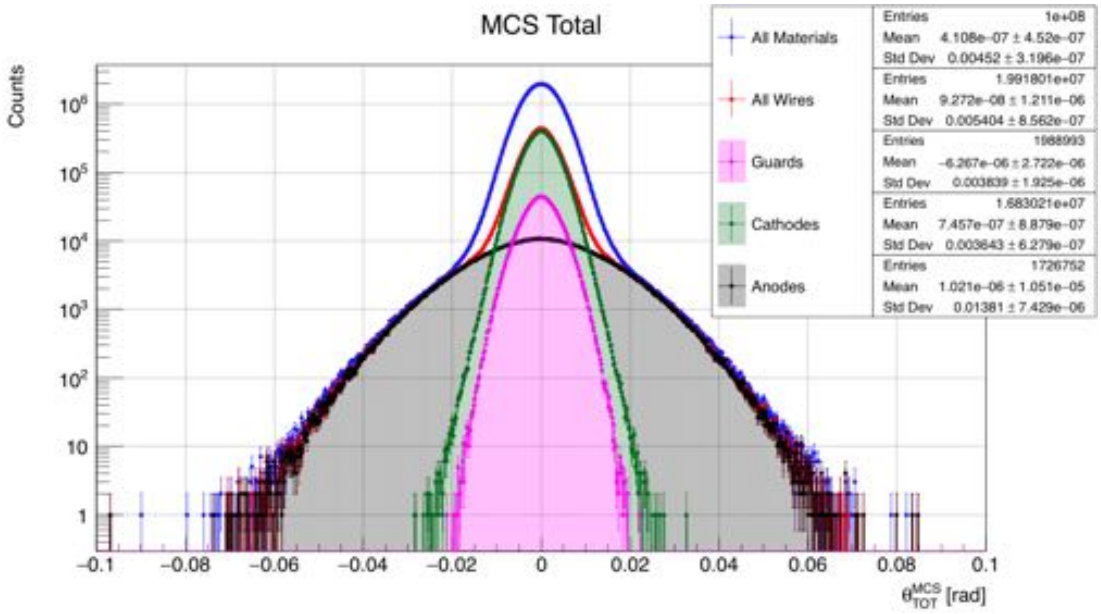

Figure 4.42: Distribution of the MCS angular deflection with the single contributions due to the different traversed materials highlighted with different colors.

The single values of θ_0 for all the traversed materials except the CYLDCH wires are: $\sigma_{IN\text{-}GAS} \approx 0.8$ mrad, $\sigma_{TRK\text{-}GAS} \approx 0.5$ mrad, $\sigma_{KAPTON} \approx 1.6$ mrad, $\sigma_{TARGET} \approx 3$ mrad. The total for these materials amounts to $\sigma_{MAT} \approx 3.8$ mrad.

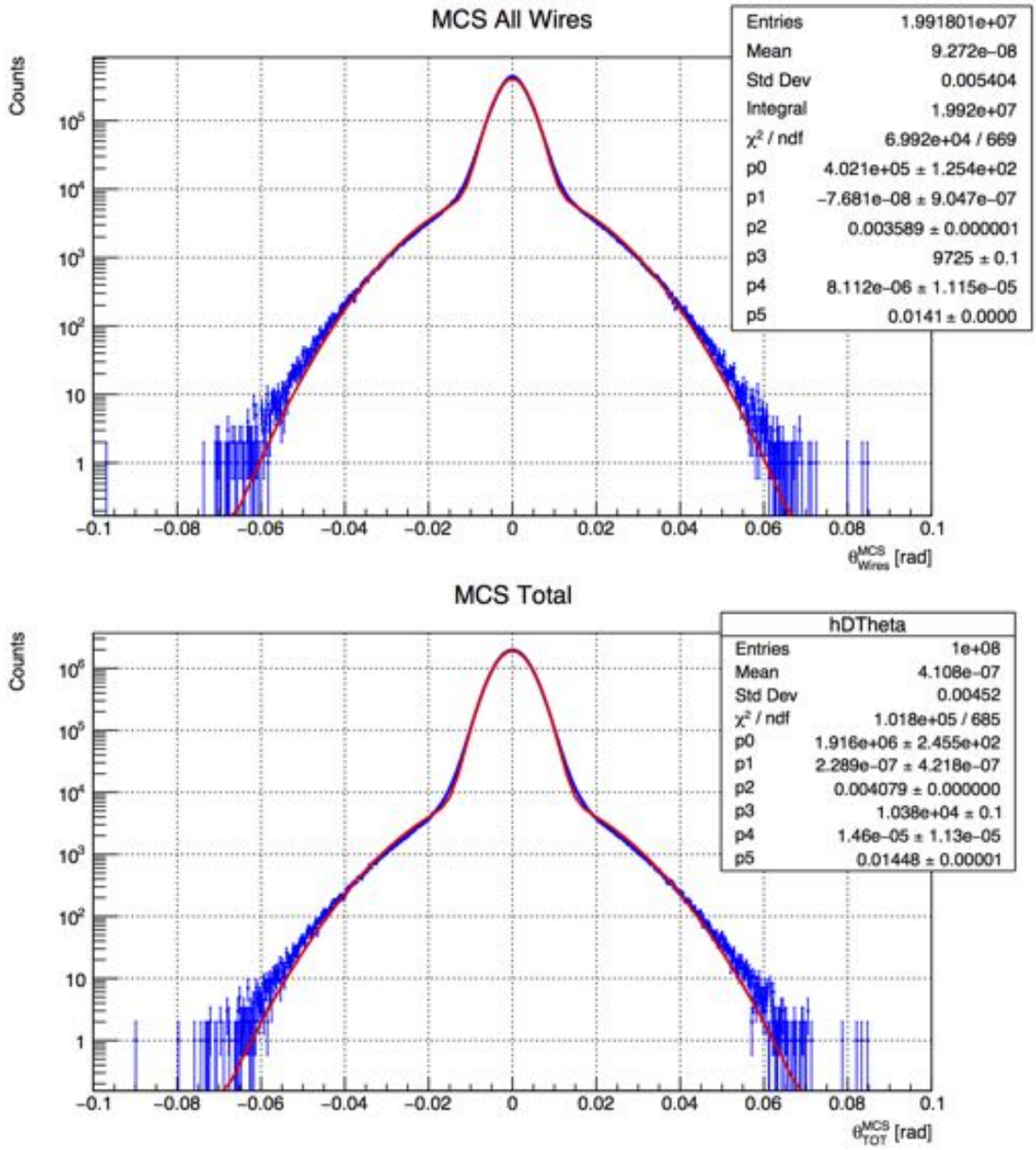

Figure 4.43: Double-Gaussian fit of the two distributions of the angular deflection given by the wires only (above) and all the materials (below).

Figure 4.41 shows the values of θ_0 for the wires materials crossed by positrons along their trajectories through CYLDCH. The variable position of the e^+ impact point on the wires has been taken into account by extracting it from a uniform distribution within the different wires diameter. This results in a variable size of the wires thickness crossed by positrons. Figure 4.42 shows the distribution of the MCS angular deflection with the

single contributions due to the different traversed materials highlighted with different colors.

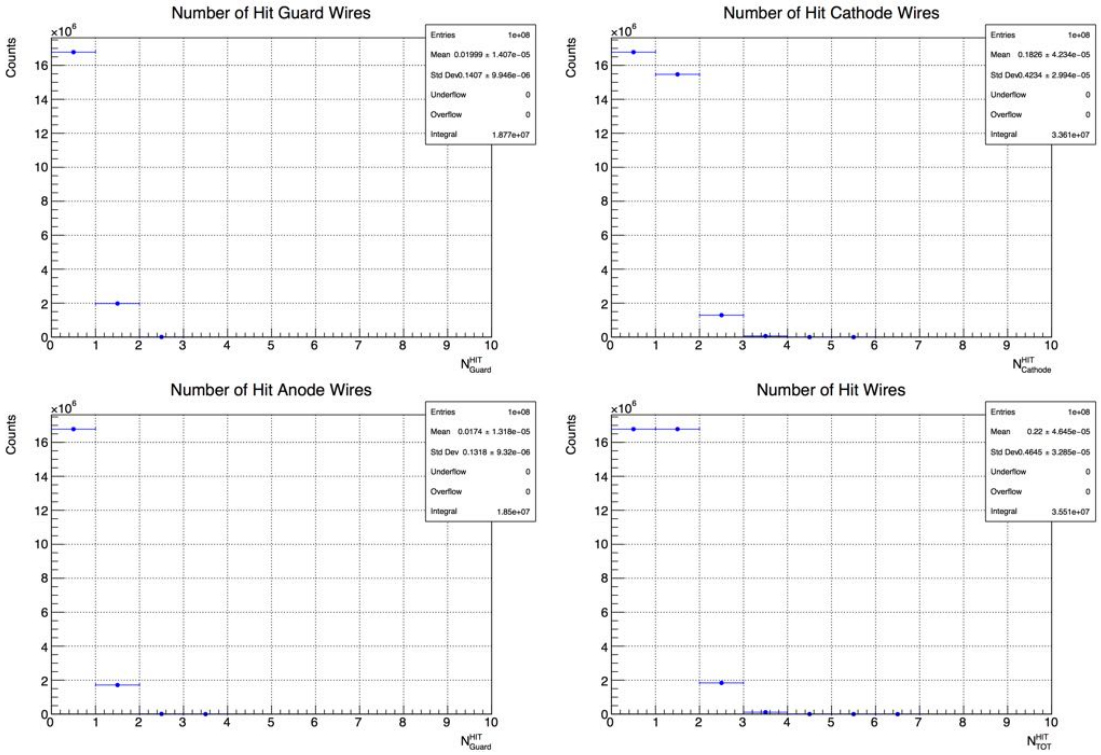

Figure 4.44: Distributions of the number of the hit wires for the anodes, cathodes and guards separately, and for their sum. The probabilities of hitting a wire are respectively $P_{anode} \approx 1.7\%$, $P_{cathode} \approx 18.3\%$ (14% for the 40 μm-thick wires and 4.3% for the 50 μm-thick wires) and $P_{guard} \approx 2\%$. Hence the total probability is $P_{hit} \approx 22\%$.

The two distributions for the wires only and for all the materials respectively have been fitted with the sum of two Gaussian functions (Figure 4.43) in order to take into account the contribution due to the gold-plated tungsten anode wires which enlarges the distribution by a factor of ≈ 3.5, as one can see from Figure 4.41 and Figure 4.42. In fact, the σ's from the fit are respectively: $\sigma_{core}^{wires} \approx 3.6$ mrad, $\sigma_{tail}^{wires} \approx 14.1$ mrad, $\sigma_{core}^{all} \approx 4.1$ mrad, $\sigma_{tail}^{all} \approx 14.5$ mrad. In the distribution core the contribution of the traversed wires to the width is $\approx 88\%$, while in the tails this value increases to $\approx 97.5\%$. The fraction of events falling in the region $|\theta_{TOT}^{MCS}| > 15$ mrad is 6‰, while in the region $|\theta_{TOT}^{MCS}| > 10$ mrad is 2.5%. For this fraction of events the achievable angular resolution would be worse than expected, mainly due to the MCS in wires materials, in particular the gold-plated tungsten anodes.

The distributions of the number of the hit wires are reported in Figure 4.44 for the anodes, cathodes and guards separately and for the sum of all the wires. The mean values are related to the probabilities of hitting a wire and are respectively $P_{anode} \approx 1.7\%$, $P_{cathode} \approx 18.3\%$ (14% for the 40 μm-thick wires and 4.3% for the 50 μm-thick wires) and $P_{guard} \approx 2\%$. Hence the total probability is $P_{hit} \approx 22\%$, in agreement with the rough estimate given above.

The expected resolutions on the positron emission angle foreseen for the MEG-II upgraded detector are $\delta\theta_e \approx \delta\phi_e \approx 5$ mrad (Table 3.2), but any e^+ collision with a sense wire will result in a worsening of the angular resolution due to the MCS.

4.5 Wires Sagitta

In drift chambers the main reason for wire displacement with respect to a straight line is the weight w of the wire itself. Even when strung with a pulling force T close to the breaking limit, wires with a length L of the order of one meter will experience a gravitational sagitta that is large in comparison with the achievable accuracy in drift chambers.

4.5.1 Gravitational Sagitta

Let's define the coordinates y (downwards) and z (horizontal). The wire displacement as a function of z is (see Appendix A):

$$y(z) = \left(\frac{\rho g \sigma}{2T}\right)\left(\frac{L^2}{4} - z^2\right) \tag{4.12}$$

where ρ and σ are the density and the cross sectional area of the wire respectively and $g = 981$ cm/s^2 is the gravitational acceleration. Actually, uniform density wires tensioned in a uniform gravity field hang in the form of a *catenary* with vertical deflection:

$$y(z) = \frac{T}{\rho g \sigma}\left[\cosh\left(\frac{\rho g \sigma L}{2T}\right) - \cosh\frac{\rho g \sigma}{T}\left(\frac{L}{2} - z\right)\right] \tag{4.13}$$

where T is the horizontal component of the pulling force which is uniform from one end of the wire of length L to the other. The weight of the wire per unit length $\rho g \sigma$ is also assumed uniform along the wire. For highly tensioned wires, the substitution of the first two terms of the power series expansion for $\cosh(u) = 1 + (u^2/2!) + (u^4/4!) + ...$ gives the simple parabolic approximation of Equation A.5.

For wires strung horizontally the point of maximum displacement is the sagitta s in the middle of the wire:

$$s = y(0) = \frac{\rho g \sigma L^2}{8T} \tag{4.14}$$

The wire sag s is proportional to the inverse of the mechanical tension. If T is increased, s is reduced, but the tension can not be arbitrarily increased since non-elastic deformations take place. The maximum pulling force T_{MAX} that can be applied to a wire is proportional to its cross section and the ratio T_{MAX}/σ is constant (except for very thin wires). The minimum achievable sagitta of a wire of given length is independent of the wire cross section. Usually the wires are strung to a tension close to the critical one in order to reduce the sagging. The values of the critical tension and the corresponding sagittas for 1-m-long wires of typical materials are shown in Table 4.4.

Material	T_{MAX}/σ (kg/mm^2)	s (μm) @ T_{MAX}
Al	$4 \div 16$	$21 \div 84$
Cu	$21 \div 37$	$30 \div 53$
Fe	$18 \div 25$	$39 \div 54$
W	$180 \div 410$	$6 \div 13$

Table 4.4: Critical tension and corresponding sagittas for 1-m-long wires of typical materials.

By inspecting Table 4.4, one notices that among the various materials, tungsten is the one that allows the smallest sagittas but at the expense of quite a large tension for a given diameter of the wire. Since the tension of the wires is held by the end-plates of the drift chamber, a large tension requires stiff ones. In the design of a drift chamber one usually compromises between these two parameters.

In the case of CYLDCH, the expected values of the gravitational sagitta at half of the wires length, given by Equation 4.14, are reported in Table 4.5 for the different types of wires and the nominal wiring tension used. Because of the stereo design of the new drift chamber the wires length varies according to the radius and it is maximum for the outermost wires. The calculation is done for the wires with the maximum length (strung at the maximum radius) in order to show the maximum sag displacement.

A practical way of obtaining the sag size consists in measuring the oscillation frequency of a wire. The frequency f_n of the n^{th} mode of the elastic string is:

$$f_n = \frac{v}{\lambda_n} \tag{4.15}$$

Type	L_{MAX} (R_{MAX}) (mm)	T (grams)	s (μm)
W 20 um (sense wires)	1931.675 (275)	24.50	115
Al 40 μm (field wires)	1932.321 (279.5)	19.25	91
Al 50 μm (field wires)	1931.675 (275)	29.64	92
Al 50 μm (guard wires)	1932.977 (284)	29.64	93

Table 4.5: Expected values of the gravitational sagitta at half of the wires length s for the different types of wires and the nominal wiring tension T used for MEG-II.

where v is the perturbation velocity on the wire and λ_n is the n^{th}-mode wavelength:

$$v = \sqrt{\frac{T}{\rho g \sigma}} \quad ; \quad \lambda_n = \frac{2L}{n} \tag{4.16}$$

By taking $n = 1$ for the lowest mode, one obtains:

$$f_1 = \frac{v}{\lambda_1} = \frac{\sqrt{T/(\rho g \sigma)}}{2L} \tag{4.17}$$

One can express the frequency f_1 as a function of the sagitta s leading to the following simple relation:

$$f_1^2 = \frac{g}{32s} \tag{4.18}$$

By using Equation 4.18 and measuring the characteristic oscillation frequencies of the wires once mounted on CYLDCH, one can indirectly trace back to the wires sag displacement. Measurements on CYLDCH have not been done yet, however some measurements of the oscillation frequencies of the wires in the transport trays have been performed in order to obtain an indirect measurement of the wires pulling force through Equation 4.17 (see Section 4.6). A frequency of 60 Hz leads to a sagitta of ≈ 85 μm, a frequency of 55 Hz leads to a sagitta of ≈ 100 μm, while a frequency of 45 Hz leads to a sagitta of ≈ 150 μm.

4.5.2 Electrostatic Force on Sagged Wire

The displacement s of the central wire of a drift cell creates an average extra electric field on the wire surface as large as the field perturbation throughout the sensitive volume [10]:

$$\overline{E(a)_y} = -\frac{V}{\ln(b/a)} \frac{s}{b^2} \tag{4.19}$$

where a and b are the dimensions of the wire and the drift cell respectively and V

is the potential. This average extra electric field acts on the electric charge of the wire and produces a force which tends to increase the displacement, i.e. the electrostatic force acts in the direction of gravity. In order to take into account this effect, one can add to the differential Equation A.3 a term proportional to the displacement which represents the electrostatic force per unit wire length:

$$\lambda \overline{E(a)_y} \tag{4.20}$$

where λ is the linear charge density on the wire given by:

$$E(r) = \frac{\lambda}{2\pi\epsilon_0}\frac{1}{r} \tag{4.21}$$

The differential Equation A.3 becomes:

$$y'' + k^2 y + \frac{\rho g \sigma}{T} = 0 \tag{4.22}$$

with $k^2 = 2\pi\epsilon_0 E^2(b)/T$, where $E(b)$ is the electric field at the drift cell boundary. The general solution is:

$$y_E(z) = C_1 \cos(kz) + C_2 \sin(kz) - \frac{\rho g \sigma}{k^2 T} \tag{4.23}$$

where the constants C_1 and C_2 are determined by the bound condition: $y = 0$ at $z = \pm L/2$, leading to:

$$y_E(z) = \frac{\rho g \sigma}{k^2 T}\left(\frac{1}{\cos(kL/2)}\cos(kz) - 1\right) \tag{4.24}$$

The electrostatic force has changed the form of the wire from the parabola A.5 to the cosine function 4.24. The new sagitta s_E becomes:

$$s_E = y_E(0) = \frac{\rho g \sigma}{k^2 T}\left(\frac{1}{\cos(kL/2)} - 1\right) \tag{4.25}$$

which reduces to the result of Equation 4.14 without the field perturbation in the case $kL \ll 1$. Therefore the electrostatic force increases the sagitta by the factor:

$$\frac{s_E}{s} = \frac{2}{(kL/2)^2}\left(\frac{1}{\cos(kL/2)} - 1\right) \tag{4.26}$$

As the product kL approaches the value π, the excursion diverges and the wire is no longer in a stable position (Figure 4.45 on the left). Figure 4.45 (on the right) shows also the values of the constant k in Equation 4.22 relevant for the electrostatic amplification

of the gravitational sag, as a function of the electric field $E(b)$ at the drift cell boundary, for various wire pulling forces T.

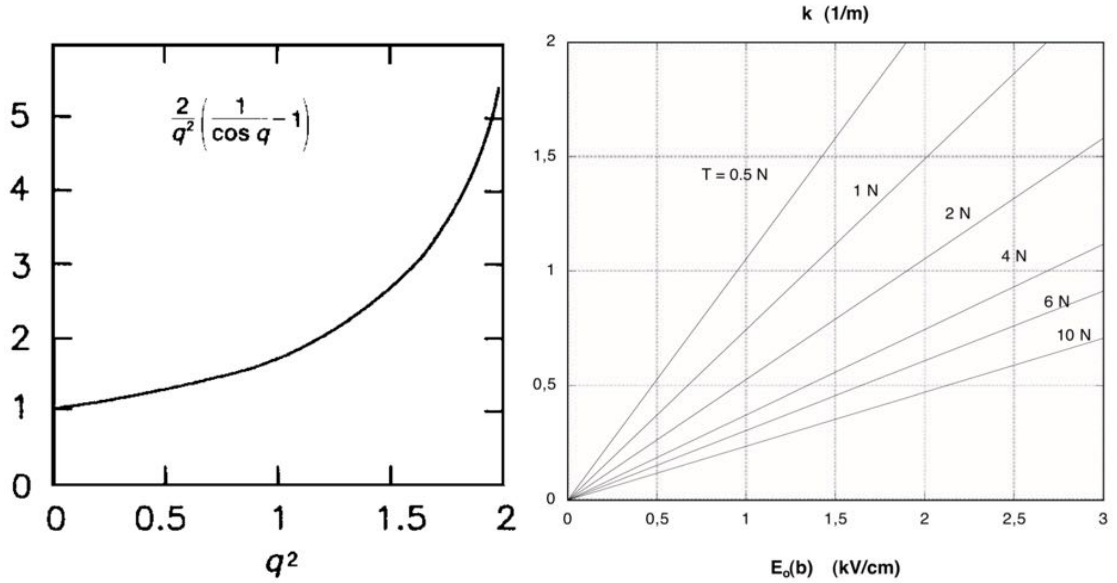

Figure 4.45: On the left: amplification factor of the gravitational sag given by Equation 4.26 as a function of $q^2 = [(kL)/2]^2$. On the right: values of the constant k in Equation 4.22 relevant for the electrostatic amplification of the gravitational sag, as a function of the electric field $E(b)$ at the drift cell boundary, for various wire pulling forces T.

A simple calculation can provide this value in the case of the sense wires of CYLDCH. By putting the values of the electric field $E(b) \approx 1$ kV/cm and the pulling force $T = 24.5$ g ≈ 0.24 N for the computation of $k \approx 0.5$ m^{-1} and a length $L \approx 1.932$ m of the anode wires, the factor $s_E/s \approx 1.1$, resulting in an increase of $\approx 10\%$ of the sag displacement.

4.6 Measurement of Wire Tension

The mechanical tension applied to the wires is monitored during the wiring procedure in Lecce. However, when the wire-PCBs are delivered to Pisa and are still in the transport trays before assembly or even once the wires are mounted on CYLDCH, the indirect method of measuring the characteristic oscillation frequency of the wires induced by an external known perturbation is used to verify the mechanical stringing tension.

For CYLDCH two perturbation methods are used. One consists in inducing a mechanical oscillations of a wire by applying a periodic high voltage. This method was

used by the Lecce group. The other consists in exploiting the bass sound waves from a subwoofer placed in front of CYLDCH or the transport tray. This method was proposed by the Roma group and used in Pisa. In the first case the periodic high voltage and the ground are applied through an electronic board connected to the wire-PCBs. The resulting electrostatic force induces the chamber wire to oscillate. The readout is provided by the same board. In the second case an electronic read-out board is connected to the wire-PCBs, while the wires surrounding the tested one are grounded manually. The board is connected to a computer for the configuration procedure and provides also the constant high voltage to the wires. For the measurement on the trasport tray the ground is provided through an aluminized plane placed under the wires tray (Figure 4.46 on the left). The resonance frequency f_1 is found as the value of the external perturbation frequency which maximizes the wire oscillation amplitude.

The working principle of the indirect methods of measuring the mechanical stringing tension is explained in the following. The oscillation of the tested wire results in a periodical variation of the capacitance C^* between the tested wire and a reference (another wire or the metalized plane, both grounded). The amplitude of this variation is measured by a digital system as a function of the external perturbation frequency f. The measurement of the capacitance C^* is realized by coupling it to a LC circuit of a high frequency oscillator f_0. Considering that $C^* \ll C$ the oscillator frequency is:

$$f_0 = \frac{1}{2\pi\sqrt{L(C+C^*)}} \approx \frac{1}{2\pi\sqrt{LC}}\left(1 - \frac{C^*}{2C}\right) \tag{4.27}$$

When the wire is oscillating at a frequency f, the capacitance C^* and therefore the high frequency f_0 vary periodically in time with a period $T = 1/f$. The amplitude Δf of the high frequency variation is maximum at the resonance frequency f_1. In order to evaluate this amplitude, two values of f are recorded at different phases with respect to the external perturbation frequency:

$$\begin{cases} f_A(f, \Phi_A) & ; \quad \Phi_A = \frac{2\pi t}{T} = 2\pi t f \\ f_B(f, \Phi_B) & ; \quad \Phi_B = \Phi_A + \pi \end{cases} \tag{4.28}$$

The choice of π is justified by the fact that $f(t)$ is, with a very good approximation, a sinusoidal function, so that the phase difference between its maximum and minimum values is π radians. By varying f and t, i.e. Φ_A, one searches for the maximum value of $\Delta f(f, \Phi_A) = f_A(f, \Phi_A) - f_B(f, \Phi_B)$. The maximum occurs for $f = f_1$ and at a particular value of Φ_A which is fixed once the external perturbation is settled.

The frequencies $f_A(f, \Phi_A)$ and $f_B(f, \Phi_B)$ are measured by counting the discriminated

high frequency oscillations during two identical phase intervals $\Delta\Phi = (2\pi\Delta t)/T$. The obtained countings are respectively $N_A = f_A\Delta t$ and $N_B = f_B\Delta t$. Their difference $\Delta N = N_A - N_B = \Delta f\Delta t$ is large only around the resonance frequency f_1. This results in a very good SNR in the measurement of $\Delta N(f)$. Moreover N_A and N_B are recorded at a relative time distance $(T/2)$ of the order of the millisecond, so that their difference ΔN is insensitive to an eventual long-term frequency instability of the high frequency oscillator. In order to achieve a better precision, the countings can be repeated during many consecutive periods T and then averaged.

4.6.1 Measurements on Wires in Transport Trays

A series of measurements of the oscillation frequency of the 40 μm silver-plated aluminum wires have been done in Pisa, in order to verify the mechanical stringing tension of the *Cathode10* wires.

The transport trays are laid down on the granite work table alongside CYLDCH and aligned to the longitudinal axis of the CMM. Then the trays are blocked through some fixing clamps and the connector of the HV and read-out electronic board is plugged to the *Cathode10* wire-PCBs. In Figure **??** (on the left) a picture of the experimental set-up is shown, together (on the right) with a picture of the support structure which holds the subwoofer in view of the direct measurement of the wires mounted on CYLDCH. Since all the *Cathode10* wires are connected together to ensure the common ground, except the first and the last wire for test purposes (see Section 4.1.1), the measurements were done with a two-channel read-out, conventionally named *ch0* and *ch1* in the following. The noise substraction with a reference channel was not done. The noise level was ≈ 10 mVp-p. The Coordinate Measuring Machine (CMM) was used to measure the distances among the markers centers of the wire-PCBs with an accuracy < 20 μm, through the method described in Section 4.2.1 for the acceptance procedure of the transport trays. In this way one has an indirect measurement of the wires length.

The length of the *Cathode10* wires when they are mounted on CYLDCH at the nominal distance of 1932 mm between the endplates is 1922.587 mm. This corresponds to a nominal distance along the z axis of CYLDCH between the soldering pads of the wire-PCBs of 1912 mm. In fact, $1912/\cos\theta_{stereo}$, with $\theta_{stereo} = 6.016^\circ$ for *Cathode10*, is just 1922.587 mm. At the nominal position, the distance between the central markers of the wire-PCBs on the transport tray is ≈ 1948.450 mm. From this central value, other four measurements have been done within ± 1 mm with a step of 0.5 mm. The additional strain $\Delta L = L - L_{NOM}$ is the difference between the current length L and the nominal

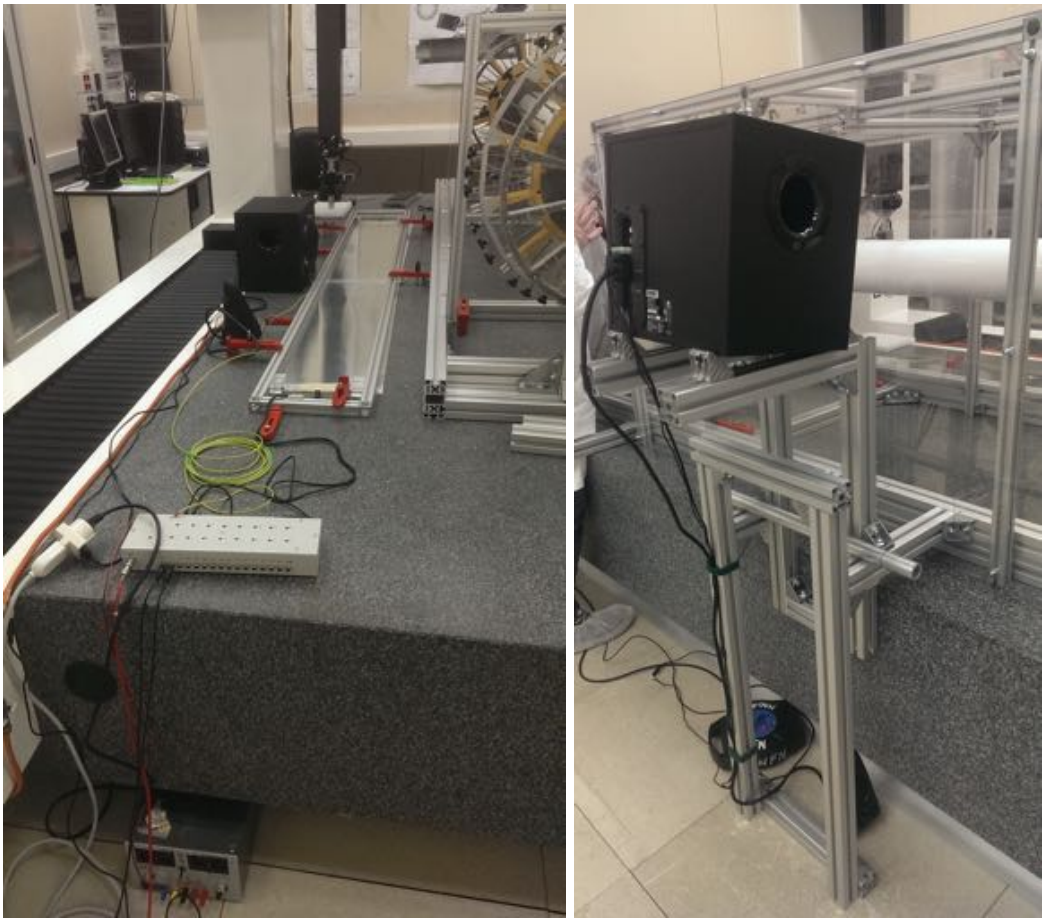

Figure 4.46: Left: experimental set-up for the measurement of the mechanical stringing tension of the *Cathode10* wires in the transport trays. Right: the support structure which holds the subwoofer in view of the direct measurement of the wires mounted on CYLDCH.

one L_{NOM}. The relaxed length $L_0 \approx L_{NOM} - 4$ mm is the wire length when zero tension is applied. In fact the wires breaking point has been measured to be at about $L_0 + 8$ mm and the working point is settled at 50% of the elastic range.

As described in Section 4.2.1, the misalignment among wire-PCBs in the transport trays leads to different lengths of the tested wires which are placed at the opposite sides of the wire-PCBs and the misalignment can also change when the trays are stretched. The measurements done in Pisa are reported in Figure 4.47 and Figure 4.48. The peak at 50 Hz is due to the AC current of the power line used as power supply for the read-out board. The linear dependence between f^2 and ΔL can be obtained from Equation 4.17 squared:

$$f^2 \propto \frac{T}{(L_{NOM} \pm \Delta L)^2} = \frac{T}{\left[L_{NOM}\left(1 \pm \frac{\Delta L}{L_{NOM}}\right)\right]^2} \propto \left(1 \pm \frac{\Delta L}{L_{NOM}}\right)^{-2} \approx 1 \pm 2\frac{\Delta L}{L_{NOM}} \tag{4.29}$$

since $\Delta L \ll L_{NOM}$. The elastic constant k is obtained from the *Hooke's law* since the pulling force $T = k\Delta L = f^2[\rho g \sigma(4L^2)]$. The elastic modulus, also known as Young modulus E_{YOUNG}, is computed from the ratio between the pulling force per unit wires cross sectional area T/σ and the wires relative elongation $\Delta L/L_0$:

$$E_{YOUNG} = \frac{(T/\sigma)}{(\Delta L/L_0)} \tag{4.30}$$

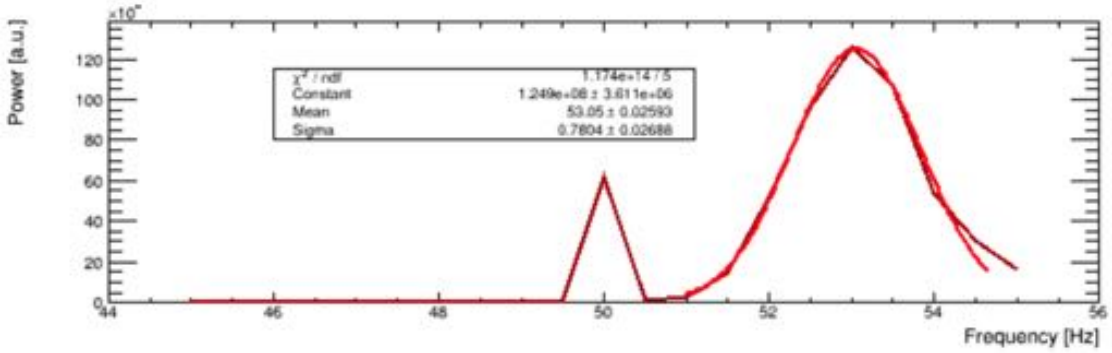

Figure 4.47: Example of resonance peak from the measurements done in Pisa. The fit with a Gauss function gives a frequency centered at ≈ 53 Hz. The bump at 50 Hz is due to the AC current of the power line used as power supply for the read-out board.

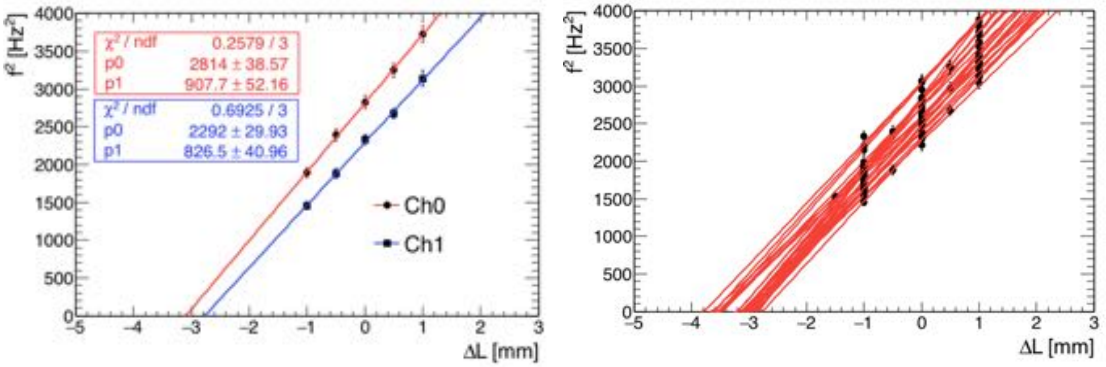

Figure 4.48: Left: the linear dependence between f^2 and ΔL. Right: aggregate plot with all the measurements.

The calculated Young modulus is $E_{YOUNG} \approx 63$ GPa. This is related to the elastic constant k by the *Hooke's law*:

$$T = k\Delta L = \frac{\sigma E_{YOUNG}}{L_0}\Delta L \quad \rightarrow \quad k = \frac{\sigma E_{YOUNG}}{L_0} \quad \rightarrow \quad E_{YOUNG} = \frac{kL_0}{\sigma} \tag{4.31}$$

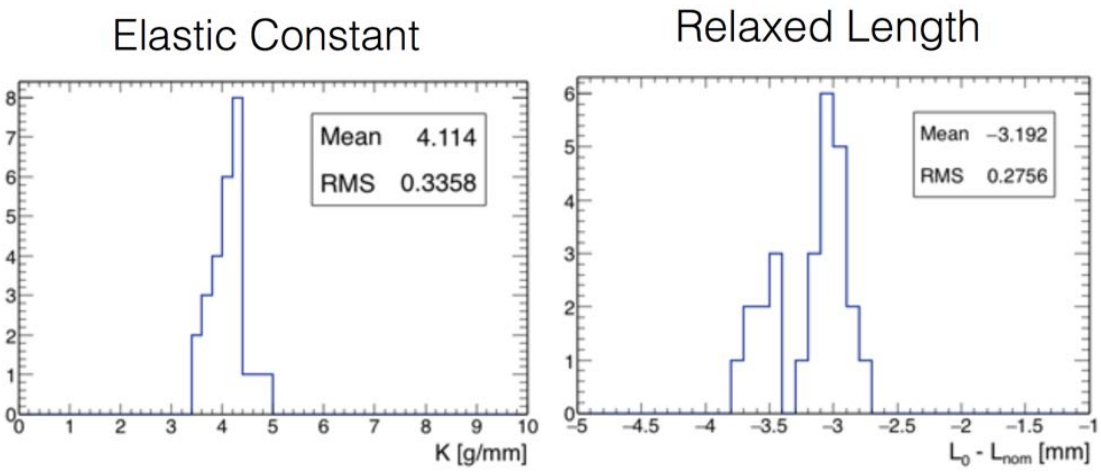

Figure 4.49: Left: Distribution of the elastic constant k. Right: Distribution of the additional strain ΔL.

The extrapolation to the length L_0 at zero applied tension shows a small deviation from the expected value of -4 mm. This means that probably the wires length is slightly longer than that expected, but this is not a critical issue since larger wires lengths do not lead to wires breaking when the end-plates are moved to their final position. This interpretation is not definitely confirmed. One should verify this offset by means of direct measurements of the wires mounted on CYLDCH. The RMS due to the differences between the two wires lengths in the same tray is 2.4 Hz and the linear regressions suggest a standard uncertainty of 0.9 Hz. An average uncertainty of the measurement < 1 Hz leads to an uncertainty in the measurement of the pulling force of ≈ 0.5 g. From Equation 4.17 one can obtain the measurement of the pulling force for *Cathode10* wires at the nominal length. Given a frequency $f_1 = 55$ Hz the resulting tension T is ≈ 17.2 g (to be compared to a nominal stringing tension of 19.25 g, see Table 4.5), using $\rho g = 3$ g/cm^3 for the silver-plated aluminum 40 μm-thick wires.

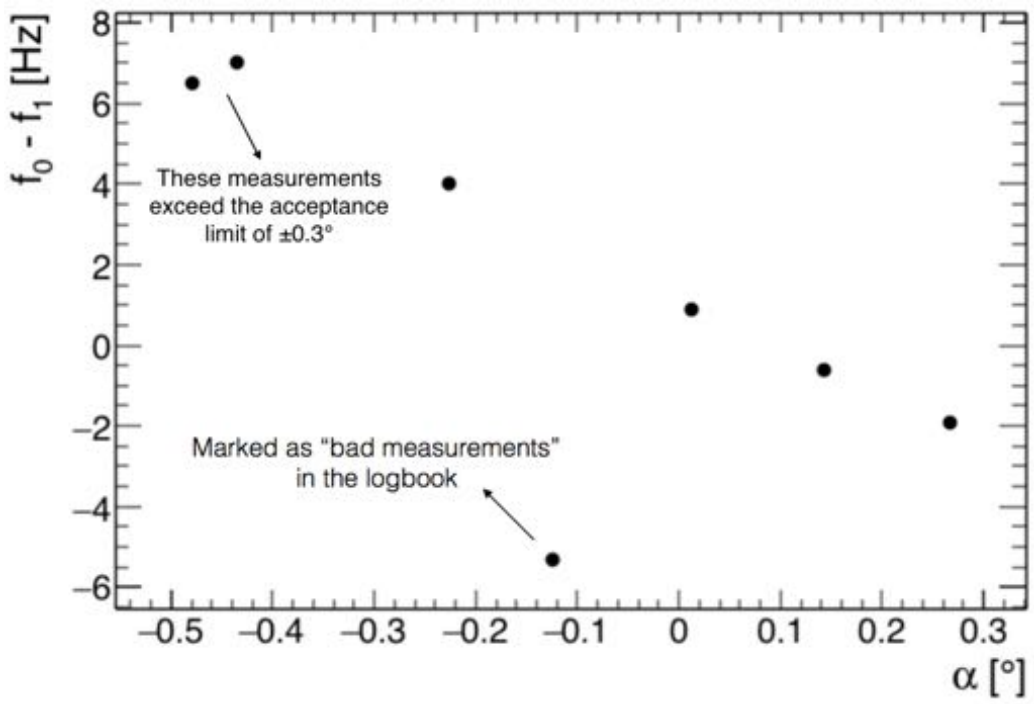

Figure 4.50: Difference between the frequencies measured from the two wires in the same tray ($ch0-ch1$) as a function of the misalignment angle α for a wire length corresponding to $L_{NOM} + 1$ mm.

Figure 4.49 shows the distributions of the elastic constant k and the additional strain ΔL for the wires measurements. Figure 4.50 shows the difference between the frequencies measured from the two wires in the same tray ($ch0-ch1$) as a function of the misalignment angle α for a wire length corresponding to $L_{NOM} + 1$ mm.

4.7 Problems Related to Ambient Humidity

During assembly of CYLDCH inside the cleanroom in the San Piero a Grado (Pisa) INFN facility, serious issues related to the ambient humidity arose, leading to the breaking of some wires. Both 40-μm and 50-μm silver-plated aluminum wires have been affected, while the 20-μm gold-plated tungsten wires are undamaged to date.

The problem has been deeply investigated: accelerated damaging test of wires immersed in water (distilled and with the addition of NaCl), optical inspections by means of different optical microscopes with increasing magnification powers and Scanning Electron Microscope (SEM) analysis in order to identify the material deposits on wires near the breaking point have been performed both in Pisa and Lecce.

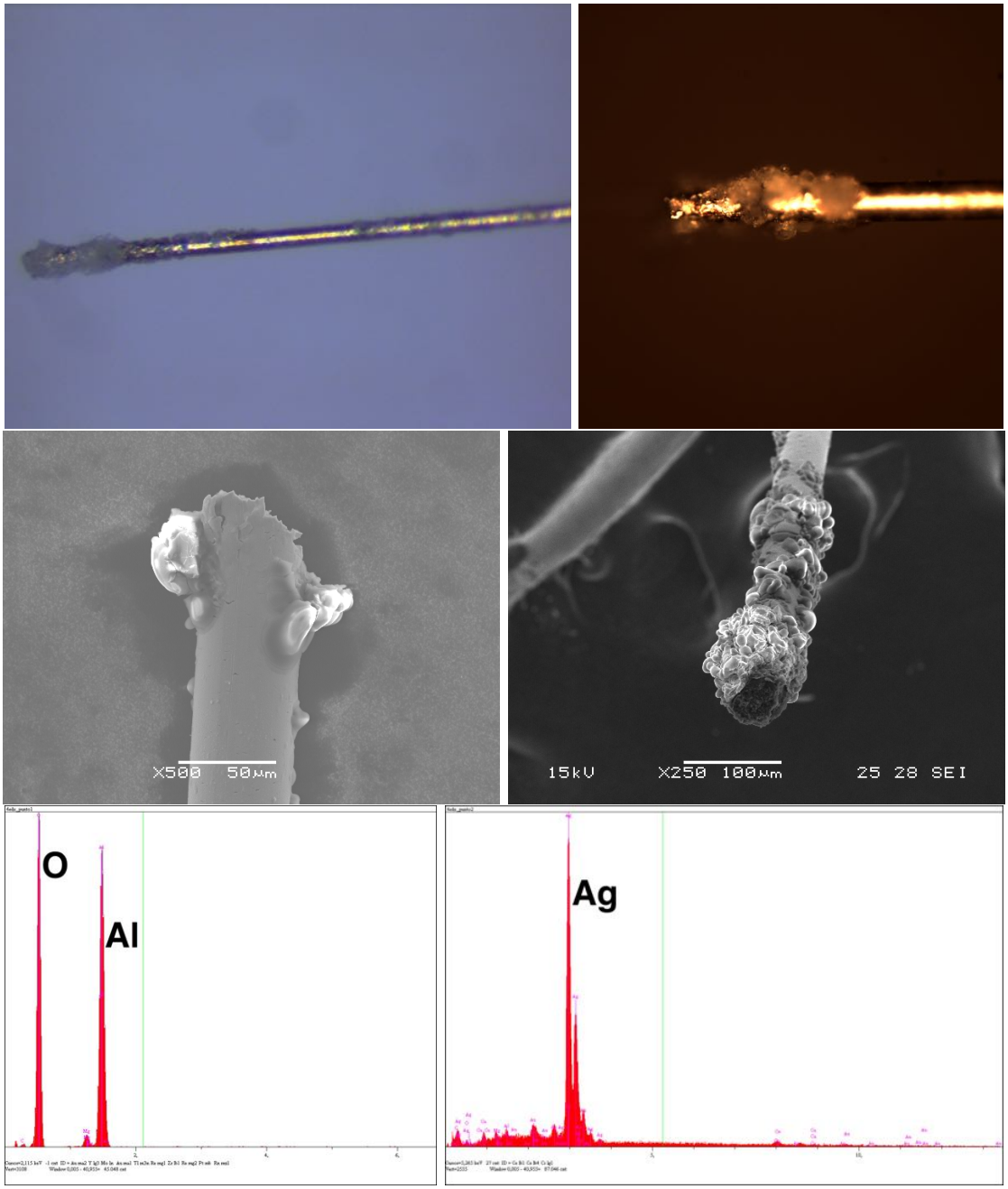

Figure 4.51: Some pictures from the investigations performed in Pisa and Lecce. The SEM analysis of the white deposits visible in the photographs near the breaking point are also shown. Far from the breaking point silver is the most abundant material, as expected given the Ag coating. Instead, the analysis of the white deposits near the breaking point shows the presence of oxygen and aluminum, suggesting the formation of aluminium oxide or hydroxide.

In Figure 4.51 some pictures from the aforementioned investigations are shown. The SEM analysis of the white deposits visible in the photographs near the breaking point are also shown. Far from the breaking point silver is the most abundant material, as expected given the Ag coating. Instead, the analysis of the white deposits near the breaking point shows the presence of oxygen and aluminum, suggesting the formation of aluminium oxide or hydroxide.

The conclusion, although not definitively confirmed, is that a galvanic corrosion between the wires silver coating and their aluminum core happens in presence of an electrolyte: the condensed water on the wires from air moisture. Water can reach the wires aluminum core through some cracks in the silver coating. The corrosion does not stop and progresses at the expense of the aluminum core until the breaking of the guard and cathode wires occurs. The breaking happens even at the nominal tension because of the weakening of the wires aluminum core.

Corrosion phenomena were not observed during assembly of the KLOE drift chamber, although the same types of wires were used: silver-plated 80-μm thick aluminum wires. This issue is unknown to the KLOE collaboration. The same aforementioned tests and investigations have been performed also on this kind of wires, leading to the same conclusions. The KLOE drift chamber was assembled in a cleanroom with temperature and humidity conditions strictly monitored ($\approx$ 22 °C and 50% of relative humidity). This did not allow the moisture condensation on the wires and the galvanic corrosion did not occur because of the absence of the electrolyte (water). During the MEG-II CYLDCH assembly, relative humidity values above 70% have been recorded, together with temperatures even below 18 °C. In fact for a period the air treatment system of the cleanroom did not work properly. From now on, CYLDCH assembly will continue with a strict monitoring of the dew point conditions in order to avoid the issues experienced previously.

Chapter 5

Pattern Recognition (PR) and Track Finding Algorithm

In a high-rate-interaction environment like the πE5 beam line at PSI with a muon stopping rate of 7×10^7 Hz foreseen for MEG-II, a large amount of hits are expected within the DAQ time window in all the sub-detectors of the experimental apparatus. The detector occupancy will be crucial especially for the new MEG-II CYLDCH due to its high granularity and geometry. In fact 1920 drift cells cover the whole azimuthal angle ϕ around the stopping target and run for about $\pm$100 cm along the beam direction z. For this reason an efficient Pattern Recognition (PR) and Track Finding algorithm is of primary importance for the MEG experiment upgrade.

The PR is the preliminary step needed before fitting a track. This one must determine a set of measured hits which contribute to the individual particle tracks. The PR algorithm must identify the hits which are part of the same track among all the hits scattered throughout the whole sensitive volume of the drift chamber and recorded in a preset acquisition time window. The positions of the hits identified at this stage to belong to one track then constitute the input for the following fitting procedure (see Chapter 6) which determines the best estimates for the position and momentum vector of a particle at any point along its trajectory. The list of hits has to be azimuthally sorted. A small amount of wrongly sorted hits is usually unavoidable and does not hurt the final track fitting procedure. In principle the fit should work even if the hits are completely unsorted, but the results are expected to have a lower accuracy because of the numerical uncertainties due to Multiple Coulomb Scattering (MCS) and energy-loss straggling during the long extrapolations in between the hits. The integration between the Track Finding and Track Fitting tasks is a crucial aspect that will be explained in

detail in this Chapter and in the next one.

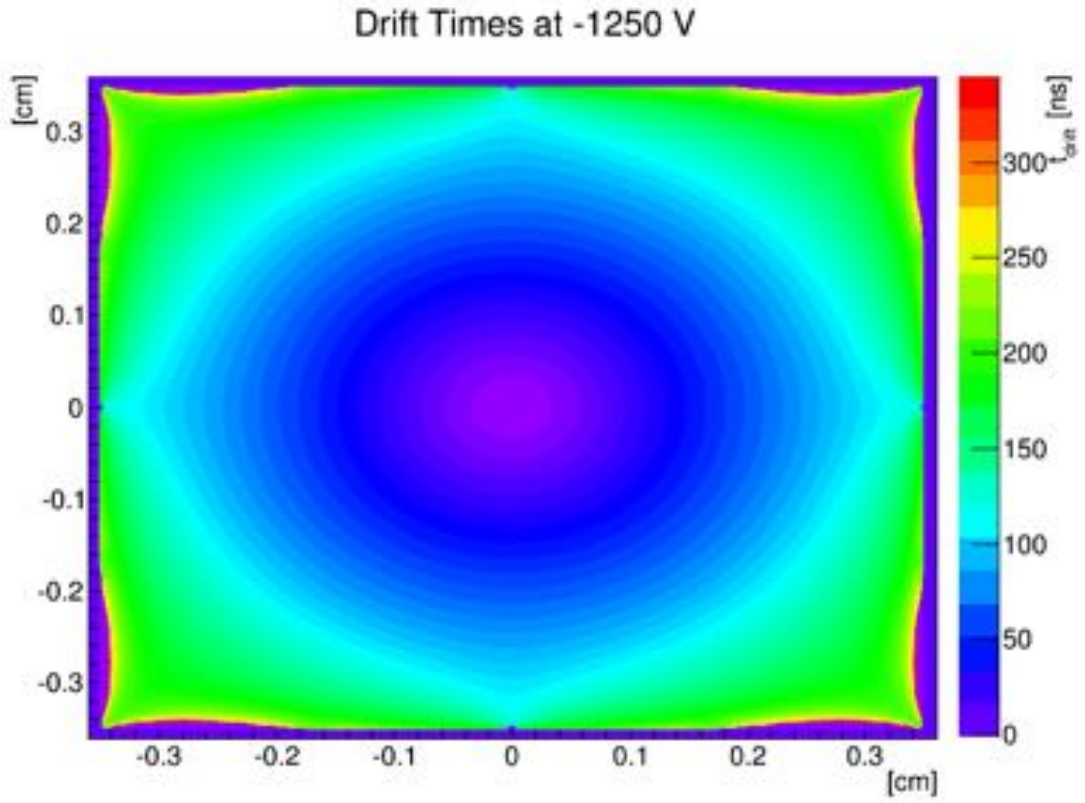

Figure 5.1: Example of simulation of a square-shaped drift cell with a width of 7 mm. The surfaces of constant drift time around the sense wire are highlighted. The isochrones cylindrical symmetry holds up to drift time values of ≈ 100 ns (≈ 3 mm), then for larger drift distances this approximation is lost. However, except in low field areas, all the electrons leave the whole drift cell clear in $\approx 200 \div 250$ ns.

In case of wire-based drift chambers, as the new MEG-II CYLDCH, a charged particle passing through a drift cell ionizes the tracker gas mixture, leaving a trail of primary ionization clusters along its flight path. The ionization electrons of every track segment are then accelerated by the electric field of the cell, drifting through the gas until they arrive in the proximity of the sense wire. In the zone around the wire the electric field density increases strongly and reaches its maximum value at the wire surface. Here the electrons amplification occurs in avalanche and the electrical signals which contain the information about the original location and ionization density of the segment are recorded by the sense wire. Hence the measurement consists in the drift time from the position of the energy deposit to the sense wire. The electric and magnetic field configuration

defines the surfaces formed by the points having the same drift time towards a fixed wire. These surfaces are called **isochrones** and all particles whose trajectories are tangent to an isochrone have equal drift time towards the central wire of the cell. Subsequently, the drift time measurement is converted into a position information by means of proper time-to-distance relations (t-xy tables). As aforementioned in Chapter 4, because of the stereo wires configuration of CYLDCH, the drift cell dimensions vary as a function of the radius and also slightly with the position along the drift chamber axis z. As a consequence, several t-xy tables have to be prepared taking into account the cell width and z position.

As reported in Section 3.2.3, the maximum measured drift time in drift cell prototypes of CYLDCH amounts to $200 \div 250$ ns. These results confirm the Garfield [60] simulations, as shown in Figure 5.1 for a square-shaped drift cell with a width of 7 mm as example. The colors, in this picture and from now on, show how many entries fall in each individual bin of the corresponding histograms. The isochrones are azimuthally uniform around the sense wire up to drift time values of ≈ 100 ns, corresponding to a distance from the wire of ≈ 3 mm. For larger drift distances the isochrones deviate from a circular shape. However, although the cylindrical symmetry approximation does not hold any more, except in low field areas, all the ionization electrons leave the whole drift cell in $\approx 200 \div 250$ ns.

When a coincidence of a signal-like photon in the LXe calorimeter and a positron in the Timing Counter (TC) fires the trigger signal, the acquisition time window is enabled, with a maximum length which cannot exceed $200 \div 250$ ns. For the study reported in this Chapter a simulated acquisition time window of 200 ns is used. With a foreseen muon stopping rate on the polyethylene target of 7×10^7 Hz, this corresponds to a pile-up of ≈ 14 e^+ tracks stemming from muon decays in the whole volume of CYLDCH. In the drift chamber a single positron helical trajectory makes in average almost two full turns. The average number of hits left in the drift chamber is about 90 for signal positrons. By considering the total number of Michel e^+ tracks collected in a single event during the 200 ns DAQ, the average number of hits is ≈ 600. The radius of the central hole is tuned to avoid that low-momentum Michel positrons enter the sensitive volume of CYLDCH. Given the momentum p_{BKG} of these background particles, they start to cross the drift chamber for $p_{BKG} > 45$ MeV. These are the numbers which the PR algorithm has to deal with. An extended study about the occupancy and geometrical acceptance of CYLDCH is reported in Section 5.3.1.

5.1 MEG Software and Event Generation

Before going forward with a detailed description of the Track Finding algorithm strategy, an overview of the MEG software is reported in order to clarify the connection between the different software tools that form the whole package. There are mainly two major MEG software packages: *meg* and *meg*2. The former contains the software for the first phase of MEG (until 2013) and is not of interest for this work, while the latter is dedicated to the upgraded MEG experiment (MEG-II). Both partitions follow the same concept. The Pattern Recognition (PR) task described in this Chapter and the Track Fitting task described in the next one have been developed inside the *meg*2 software package in view of the second phase of the experiment.

The MEG-II software package consists of the following sub-packages which are dedicated to different tasks:

- **gem4**: Monte Carlo simulation based on the Geant4 [61] toolkit for the simulation of the passage of particles through matter;
- **bartender**: DAQ electronics simulation and mixing of different kinds of simulated events;
- **analyzer**: online and offline data analysis and event display.

In Figure 5.2 the connections between the different programs are shown together with the output files produced by each package. The MEG DAQ system is based on *MIDAS* [1] (Maximum Integrated Data Acquisition System). During data taking runs, the DAQ apparatus stores the online information in *.mid* files. The offline software is based on *ROME* (ROOT-based Object oriented MIDAS Extension): a ROOT-based framework generator for event based data processing. It was developed in the MEG collaboration but it is designed as a general-purpose software, so that it can be used for other experiments too. In the *ROME* environment, the experimenter defines the analysis framework for his experiment in a very clear and compact way in XML files. The key concept of *ROME* is to generate most of the code of a project, except the analysis (or simulation) algorithms. It is written in C++ and structured in methods (tasks) and folders for data exchange. For more details about the MEG software see [59].

Simulation specific data are written in *sev* (sub-events) files and subsequently mixed by *bartender*. Simulation specific data after merging several sub-events by *bartender* are written in *sim* files. These files serve as input for the *analyzer* to compare Monte Carlo

[1] http://midas.psi.ch.

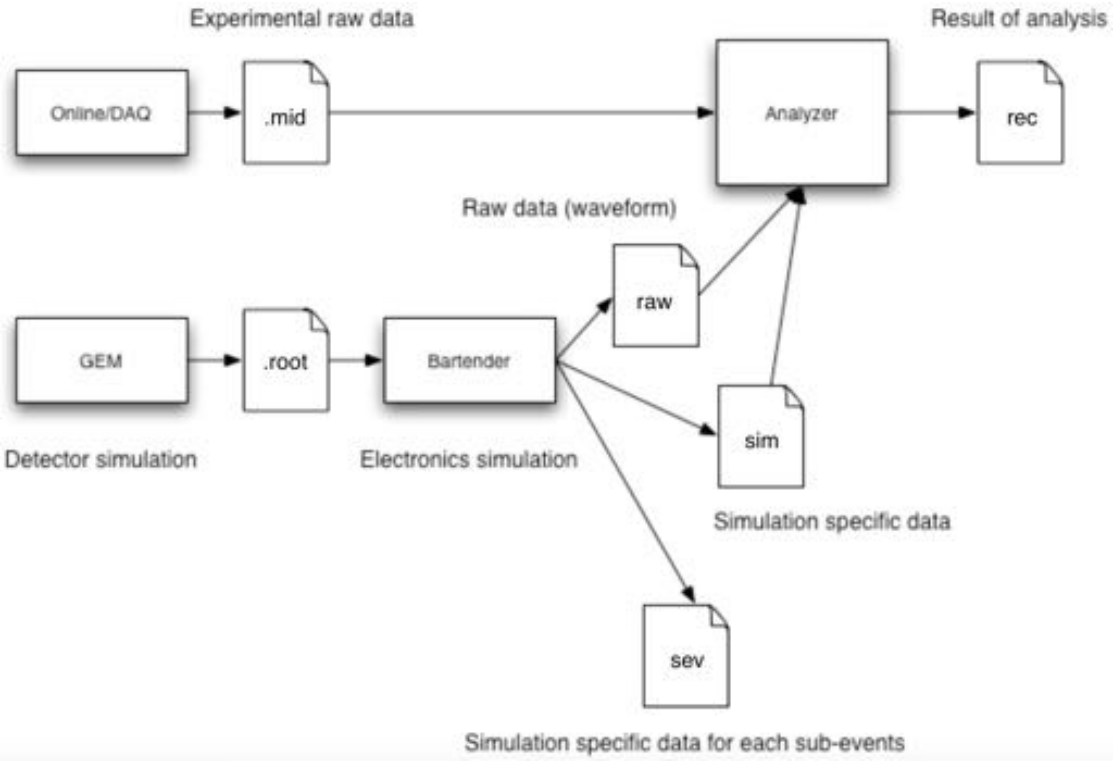

Figure 5.2: Connections between the different programs which form the MEG software package.

(MC) input and analyzed results. *Raw* files contain the raw data: real or simulated waveforms from each sub-detectors. Normally these files are output of *bartender* and input of *analyzer* for simulation data, but they can be also output of *analyzer* after pre-selection of experimental data. All these files are based on ROOT `TTree`.

For the development of the Track Finding algorithm a set of files has been produced through *gem*4 simulation program. During the generation phase the nominal geometry of CYLDCH (see Section 4.1) is loaded by *gem*4 code. The "global" reference frame of CYLDCH is shown in Figure 2.9 for the previous MEG detectors configuration, but it is the same for MEG-II. The z axis runs along the muon beam and the drift chamber axis, pointing from the upstream region to the downstream one. The x axis points in the opposite direction with respect to the LXe calorimeter and finally the y axis points upwards. As aforementioned in Section 4.1.1, the geometry is loaded by reading either dedicated geometry text files or an online database.

Separately generated files contain signal positron events from the $\mu^+ \to e^+\gamma$ decay process or Michel positron events from the $\mu^+ \to e^+\nu_e\bar{\nu_\mu}$ decay. These files are then

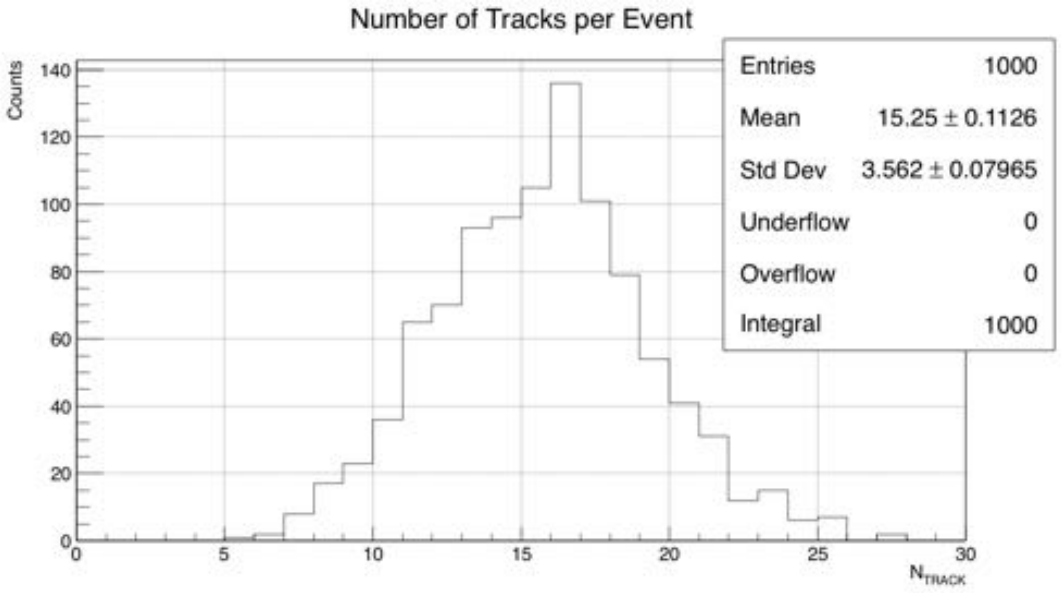

Figure 5.3: Total number of generated tracks for mixed events. Each mixed event consists in a signal positron surrounded by an average number of 14 Michel e^+'s. Obviously only the positron tracks which met the geometrical acceptance requirements hit CYLDCH.

mixed by using *bartender* in order to have one signal event together with the appropriate number (14) of background events. The analysis presented here was performed on a *bartender* file containing 1000 of such mixed events. A 200 ns acquisition time window extending from -50 ns up to $+150$ ns with respect to the signal e^+ time and a stopping rate of 7×10^7 μ^+/s, equal to that foreseen for MEG-II, are simulated. The distribution of the total number of tracks for mixed events is reported in Figure 5.3. Obviously only the positrons which meet the geometric acceptance conditions hit CYLDCH (see Section 5.3.1).

5.2 Pattern Recognition (PR) Algorithm

The Pattern Recognition algorithm is encoded into an *analyzer* task implemented inside the MEG-II software package (see Section 5.1). The task which performs PR is written in C++ and is called *MEGTCYLDCHSearchTriplets.cpp*. Its name reflects the basic concept behind the Track Finding algorithm which searches for triplets of nearby hits belonging to adjacent drift cell planes.

The only information exploited by the PR is the absolute hit wire number n_{wire} within one event, numbered from $i = 0$ to $i = 1919$, and a coarse measurement of the

hits z position. This latter is assumed to be known with a resolution $\delta z = 10$ cm from the difference in the arrival times of the signals at the two ends of the sense wire (see also Section 4.1). On the basis of n_{wire} the algorithm is able to load all information related to the wire geometry, i.e. its position vector at the CYLDCH center ($z = 0$), the direction cosines which provide its orientation and another number for the nominal half wire length. The position vector is used to compute the nominal wire radius R_{0i} and its azimuthal position ϕ_i at $z = 0$. Currently the sag displacement is not used and all the 1920 sense wires are considered as straight lines. The information of the wires plane n_{plane} is encoded into the MC files, even if it can be easily recovered by a simple calculation: $n_{plane} = n_{wire}\%192$, where 192 is the number of sense wires per plane.

5.2.1 Track Segments Finding Strategy

Since the occupancy of the CYLDCH drift cells is maximum for the innermost wires radii, the PR finding algorithm looks for triplets of close hits on the basis of the hit wire number, starting from the outermost drift cells plane.

Before starting the hits triplets searching, a merging procedure (Figure 5.4) of all pairs of hits recorded in consecutive sense wires within the same plane is performed, in order to reduce the combinatorial background which would occupy too much computing time. Each time a pair is found, the two sense wires involved are combined into an average virtual wire. However, no hits are lost, since the original information of the two wires is kept in memory and subsequently recovered to compute the drift distances relative to each hit sense wire.

As reported in Section 4.1, CYLDCH is formed by 10 layers of drift cells, numbered from 0 to 9, with alternating stereo angle. Thus, one can define two directions along the wires, corresponding to the positive and negative stereo angle, called the $\hat{U}$ orientation and the $\hat{V}$ orientation respectively. Depending on the projective view, the U-view or the V-view, the line of sight is parallel to all wires with the same sign of the stereo angle. The PR algorithm is based on the fact that positrons tracks cross almost parallel wires in planes belonging to the same view. If one considers a relative wires numbering, i.e. n_{wire} starting from 0 up to 191 for each of the ten wires planes, usually the difference in the hit wire number for hits in two consecutive planes of the same (U or V) view is $|\Delta n_{wire}| \leq 4$. Instead each sense wire of a view is crossed by 32 wires of the other view. In fact, being each sector 30° wide, wires starting in sector k in one end-plate end in sector $k \pm 2$ in the the other end-plate, depending on the sign of the stereo angle ($\Delta\phi = 60°$). In Figure 5.4 an example of a signal event in the xy plane is shown with the

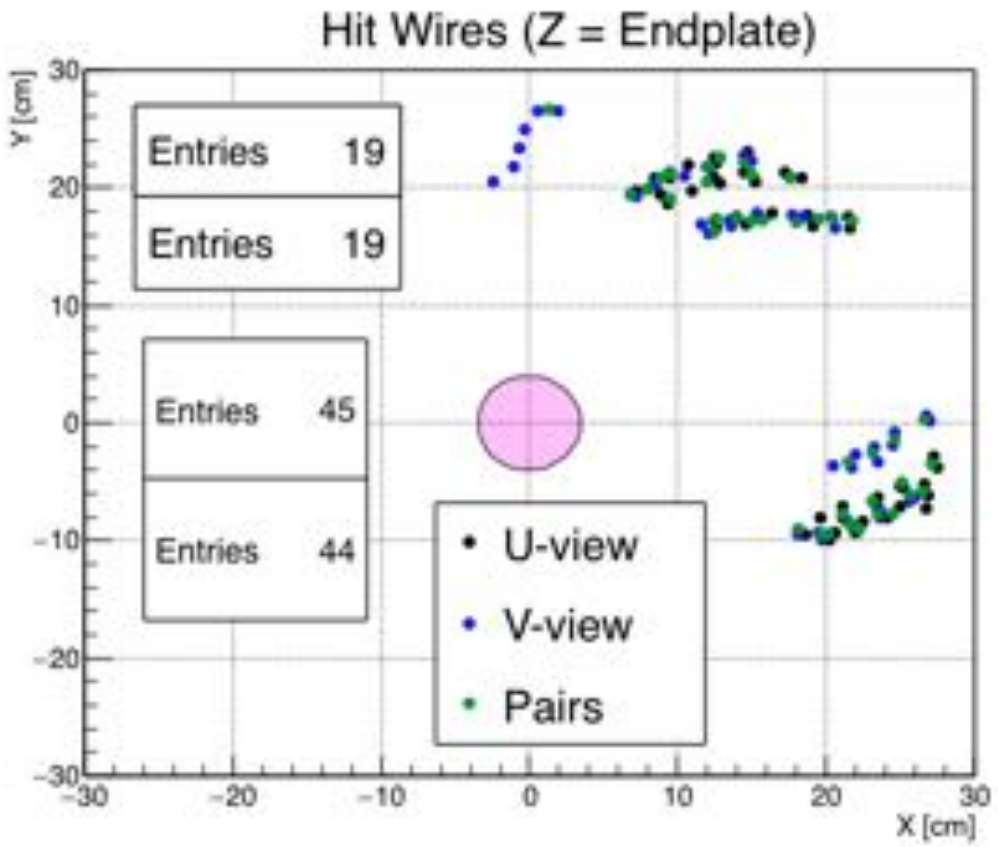

Figure 5.4: Example of signal event in the xy plane with the position of the corresponding hit wires on the U-view and the V-view (black and blue dots respectively). The green dots are the pairs of wires formed by the PR algorithm. At the center the polyethylene muon stopping target is highlighted.

position of the corresponding hit wires on the U-view (black dots) and on the V-view (blue dots). The green dots are the pairs of wires formed by the PR algorithm. At the center the polyethylene muon stopping target is highlighted.

The Track Finding algorithm strategy is schematically shown in Figure 5.5. In the example picture, two wires planes of the U-view are depicted in black, the outermost plane i and the innermost plane $i+2$, together with the wires plane $i+1$ of the V-view in blue. The e^+ track passing through the drift cells is depicted by the green arrow and the hit wires are the red ones. If the sense wire j in plane i (U-view) is hit, the PR finding algorithm checks for the presence in plane $i+1$ (V-view) of a hit sense wire within the interval $j \pm 16$. If the search is positive, for instance the wire $j+16$ is found to be hit,

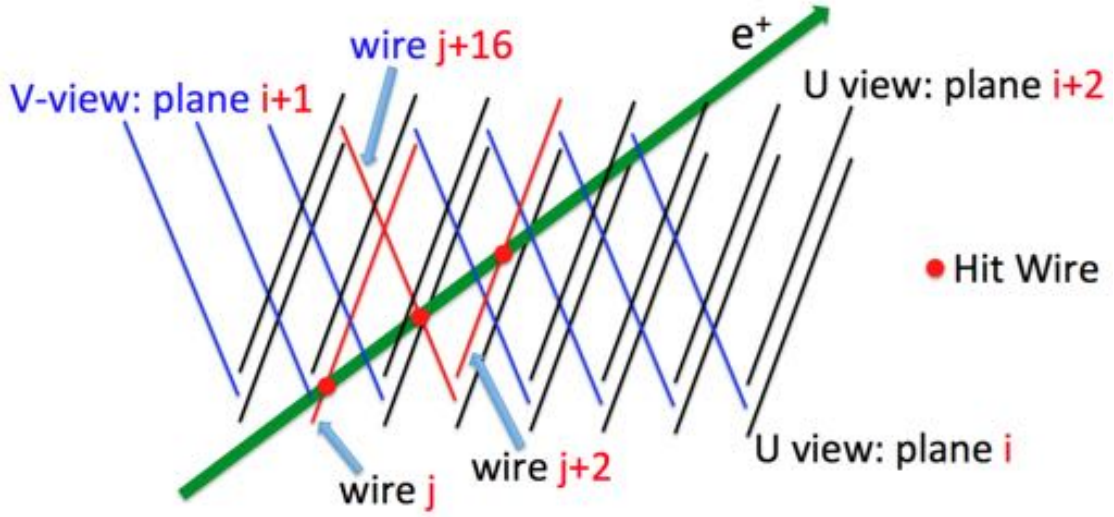

Figure 5.5: Schematic picture of the principle of operation of the Track Finding algorithm strategy based on the search for triplets of hits belonging to adjacent sense wires planes.

the compatibility of the z positions of the two hits in plane i and $i+1$ is verified. The z resolution is simulated in the code by requiring: $|z_j^i - z_{j+16}^{i+1}| < \delta z = 10$ cm. If this condition is met the searching algorithm continues with the plane $i+2$ (U-view) within the wires interval $j \pm 2$. If, for instance, the sense wire $j+2$ is found to be hit, the compatibility of the z positions of the two hits in plane $i+1$ and $i+2$ is checked again: $|z_{j+16}^{i+1} - z_{j+2}^{i+2}| < \delta z = 10$ cm. Before associating a new hit to the previously grouped ones, some spatial and angular contiguity criteria are required on the new measured hit position. The first is $\Delta x = \Delta y \leq 2$ cm and $\Delta z \leq 10$ cm among two consecutive hits. Concerning the angular contiguity, if $i+1$ is the index of the new hit to be added, the angle β between the two segments $(i-1, i)$ and $(i, i+1)$ in the transverse plane xy is computed and the requirement is $|\beta| < 60°$. This iterative algorithm goes on (plane $i+$..., up to the tenth plane) until the previous conditions are met in order to form a **track segment**.

An estimate of the hits coordinates is computed by the PR algorithm using the minimum distance between two hit wires of adjacent planes. Let us define their position vectors $\vec{r}_0$ and $\vec{r}_1$, and the direction cosines versors $\hat{v}_0$ and $\hat{v}_1$ parallel to the wires. Putting $\vec{\Delta}_r = \vec{r}_1 - \vec{r}_0$ and $\vec{\Delta}_v = \hat{v}_1 - \hat{v}_0$, the geometrical segment of minimum distance which connects the two hit wires is calculated as:

$$d_0 = -\frac{\vec{\Delta}_r \cdot \vec{\Delta}_v}{2(1 - \hat{v}_0 \cdot \hat{v}_1)} \tag{5.1}$$

and the intersection points between this segment and the wires leads to the reconstructed hits position, $\vec{w}_0$ and $\vec{w}_1$, on the wires:

$$\begin{cases} \vec{w}_0 = \vec{r}_0 + d_0 \hat{v}_0 \\ \vec{w}_1 = \vec{r}_1 + d_0 \hat{v}_1 \end{cases} \tag{5.2}$$

The same calculation is performed in the next iteration if the algorithm finds a hit wire in the next plane ($\vec{r}_2$ and $\hat{v}_2$) which meets the association criteria previously defined. Similarly, the segment of minimum distance between the wires (d_1) and the reconstructed hits position on the wires ($\vec{w}'_1$ and $\vec{w}_2$) are computed. Every time the average between the hit position on wire computed in two consecutive iterations is taken in order to obtain the final measured hit position on wire:

$$\vec{m}_i = \frac{\vec{w}_i + \vec{w}'_i}{2} \tag{5.3}$$

Obviously the mean is not calculated for the first and the last wires plane: $\vec{m}_{first} \equiv \vec{w}_{first}$ and $\vec{m}_{last} \equiv \vec{w}_{last}$.

The procedure is iterated for each hit sense wire as starting point from the outermost plane to the innermost one. When all the hit wires within the same plane are completed, the starting plane becomes the adjacent one at a smaller radius and so on. In fact a track segment can in principle start from any wires plane. When a hit wire is found to be part of a track segment, its wire number is considered as associated to this segment.

At the end of this stage all the hits within the identified track segments are temporarily sorted by plane, from the outermost to the innermost one, in order to make easier the next cleaning procedures described in Section 5.2.2, based on one-by-one hits comparisons among different track segments. The final sorting procedure is performed later, as described in Section 5.2.4.

5.2.2 Merging, Skipping and Cleaning Procedures

When the main Track Finding task is finished, a group of arrays containing the measured hits positions is stored in memory, each one corresponding to a track segment. Usually at this time the number of track segments is larger than the effective number of tracks left by positrons in the drift chamber sensitive volume. Thus a series of **merging**, **skipping** and **cleaning** procedures are performed separately by different methods of the PR algorithm

in order to reduce the number of duplicates. These tasks are summarized in Figure 5.6.

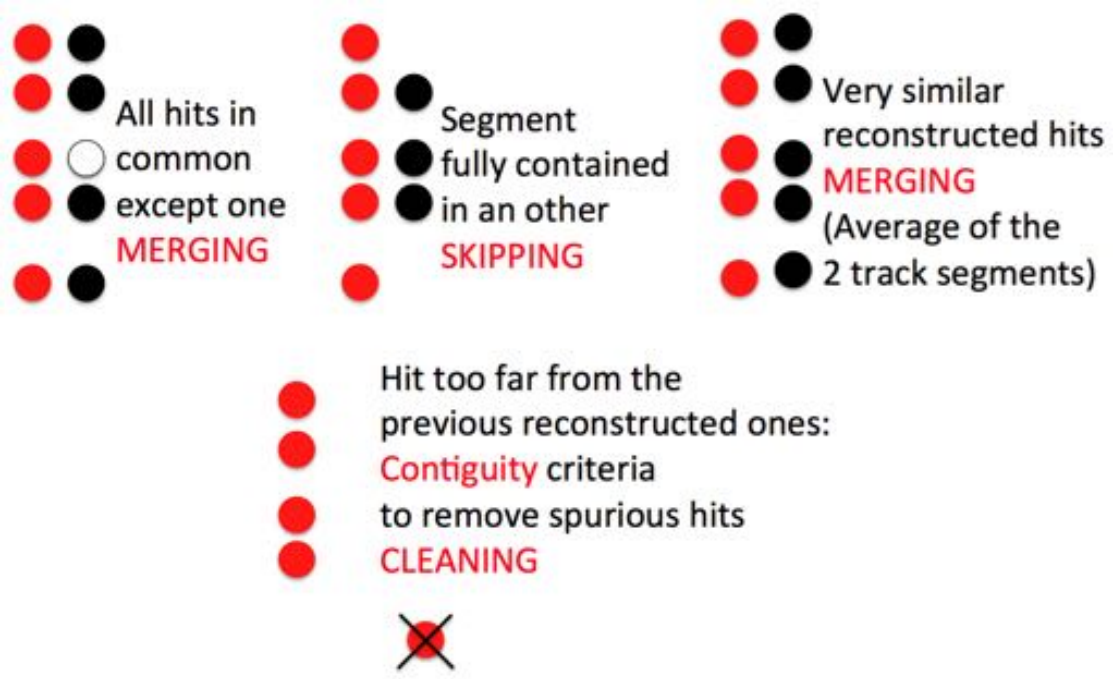

Figure 5.6: Schematic representation of the merging, skipping and cleaning tasks performed by dedicated methods of the PR algorithm.

If a segment is found to be fully contained in another one just stored in memory, taking also into account the fact that the segment under testing can begin in a different plane, then the shorter one is skipped and the hits positions are not stored in the corresponding array. If the tested track segments are found to have all the measured hits in common except one, then the two segments are merged and the resulting one is stored in memory. By comparing two track segments, sometimes the algorithm can find very similar reconstructed hits. In this case the hits positions of the two segments are averaged into one merged track segment. The similarity is established by computing the χ^2 between the recontructed hits positions within the corresponding planes and verifying that its value is under a certain predefined threshold[2]:

$$\chi^2 = \frac{1}{3N_{points}} \sum_{i=0}^{N_i} \sum_{j=0}^{N_j} \left[\left(\frac{x_i - x_j}{\sigma_{xy}} \right)^2 + \left(\frac{y_i - y_j}{\sigma_{xy}} \right)^2 + \left(\frac{z_i - z_j}{\sigma_z} \right)^2 \right] \delta P_i \, \delta P_j \qquad (5.4)$$

[2]After some preliminary studies, the merging was found to be efficient for a threshold value of 25.

where $\sigma_{xy} = 0.45$ cm and $\sigma_z = 3.2$ cm are the spatial resolution assumed for the measurement on the (x, y) plane and on the z direction respectively, N_i and N_j are the number of hits within the two segments, N_{points} is the total number of pairs of points corresponding to the same plane and δP_i δP_j ensures that the χ^2 receives contribution only if $P_i = P_j$, i.e. the hits are on the same plane. Every time a new hit is appended to an existing track segment by adding the corresponding hit wire in a plane, the hit position in that plane is computed again (see Section 5.2.1) taking into account the new wire.

Afterwards a cleaning procedure, based on the same contiguity criteria already described in Section 5.2.1, is performed in order to remove spurious hits. The requirements are slightly relaxed (a factor of 1.2) in order to take into account the possible small changes in the reconstructed hits positions caused by the merging procedures which add wires in the same planes. If a reconstructed position is found to be too far from the previous reconstructed ones, it is discarded. Moreover a method is dedicated to check the **continuation** between track segments by comparing the extreme hits positions of each segment. All the four combinations are verified in order to take into account the possible wrong hits sorting of the track segments. If the proximity is under a predefined tolerance ($\Delta x = \Delta y = 2$ cm and $\Delta z = 10$ cm) and the contiguity criteria are met, then the two segments are joined. Finally a **recovery** of not yet assigned hit wires is tried on the basis of their wire number which is compared to the wire numbers already associated to stored track segments. For the wires numbers comparison the criteria discussed in Section 5.2.1 are used. At the end a further filtering procedure is performed before storing the final hits information for the next Track Fitting task. By scrolling all the positions within the already identified hits arrays, the following requirement is applied among consecutive hits: $|z_i - z_j| < 3$ cm and $\sqrt{(x_i - x_j)^2 + (y_i - y_j)^2} < 5$ cm. If all the criteria are satisfied a new reconstructed hit is determined, whose contiguity with the segment is checked as discussed before.

5.2.3 Circle Fit

Once a set of hits is grouped in a track segment, a least-squares circle fitting procedure in the transverse plane xy is performed in order to obtain an estimate of the track segment bending radius R_{seg}. This value, together with the corresponding circle center, is important to calculate the seed momentum vector $\vec{p}_{seed}$, module and direction in space. The fit is done for each individual segment separately, since the track segment merging, even for different turns of the same e^+ helical trajectory, is delegated to the Track Fitting

task (see Chapter 6). The fitted momentum, the measured space positions of all the hits within the same segment and the seed hits time are the starting input information for the subsequent Track Fitting task in order to finally determine the best estimate of the positron kinematic variables (see Section 5.2.4).

Given the set of points of a track segment, say $\{(x_i, y_i) \mid 0 \leq i \leq N\}$, where (x_i, y_i) are the reconstructed hits coordinates on the transverse plane (x, y), the fitting algorithm operates as follows. Firstly, both the mean x and y hits coordinates are computed:

$$\bar{x} = \frac{1}{N}\sum_{i=0}^{N} x_i \quad ; \quad \bar{y} = \frac{1}{N}\sum_{i=0}^{N} y_i \tag{5.5}$$

Then a change of reference system is done: $u_i = x_i - \bar{x}$, $v_i = y_i - \bar{y}$ for $0 \leq i \leq N$. Hence the problem is solved first in (u, v) coordinates and then transformed back to (x, y). Let the circle have center (u_c, v_c) and radius R. The quadratic form:

$$S(R^2, u_c, v_c) = \sum_{i=0}^{N} (g(u_i, v_i))^2 \quad \text{where} \quad g(u_i, v_i) = (u - u_c)^2 + (v - v_c)^2 - R^2 \tag{5.6}$$

is minimized by differentiating S with respect to u_c, v_c and $\alpha \equiv R^2$:

$$\begin{cases} \frac{\partial S}{\partial \alpha} = 0 & \rightarrow & \sum_{i=0}^{N} g(u_i, v_i) = 0 \\ \frac{\partial S}{\partial u_c} = 0 & \rightarrow & \sum_{i=0}^{N} u_i g(u_i, v_i) = 0 \\ \frac{\partial S}{\partial v_c} = 0 & \rightarrow & \sum_{i=0}^{N} v_i g(u_i, v_i) = 0 \end{cases} \tag{5.7}$$

Expanding the second and third Equations in 5.7 and defining $S_u = \sum_{i=0}^{N} u_i = 0$, $S_{uu} = \sum_{i=0}^{N} u_i^2$, $S_{uuu} = \sum_{i=0}^{N} u_i^3$, $S_{uv} = \sum_{i=0}^{N} u_i v_i$, $S_v = \sum_{i=0}^{N} v_i = 0$, $S_{vv} = \sum_{i=0}^{N} v_i^2$, $S_{vvv} = \sum_{i=0}^{N} v_i^3$, $S_{uvv} = \sum_{i=0}^{N} u_i v_i^2$ and $S_{vuu} = \sum_{i=0}^{N} v_i u_i^2$, one obtains:

$$\begin{cases} u_c S_{uu} + v_c S_{uv} = \frac{S_{uuu} + S_{uvv}}{2} \\ u_c S_{uv} + v_c S_{vv} = \frac{S_{vvv} + S_{vuu}}{2} \end{cases} \tag{5.8}$$

Solving the system of Equation 5.8 gives the circle center (u_c, v_c). Then the original coordinate system is recovered: $(x_c, y_c) = (u_c, v_c) + (\bar{x}, \bar{y})$. Expanding the first Equation in 5.7, one gets the radius:

$$R = \sqrt{\alpha} = \sqrt{u_c^2 + v_c^2 + \frac{S_{uu} + S_{vv}}{N}} \tag{5.9}$$

An example of circle fit in the transverse plane xy for all the track segments of a signal

positron found by the PR algorithm in one event is shown in Figure 5.7. An individual fit is obtained for any segment. At the center the polyethylene muon stopping target is highlighted.

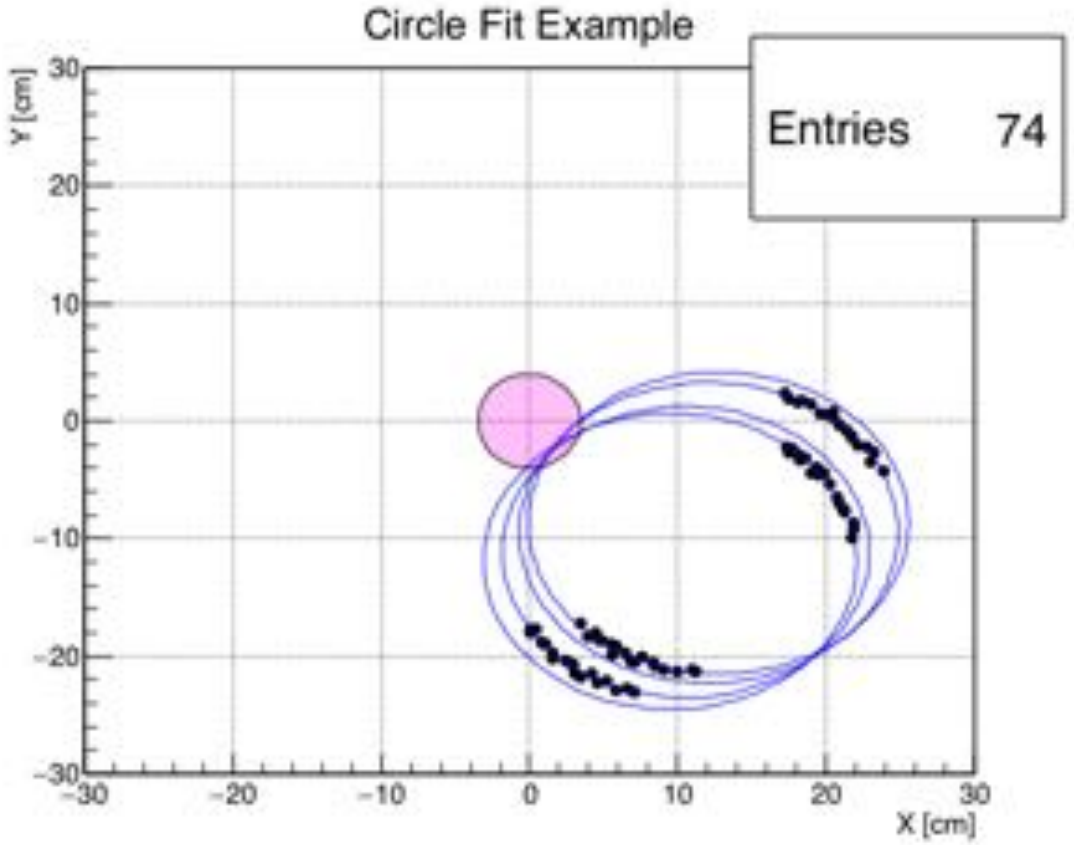

Figure 5.7: Example of circle fit in the transverse plane xy for all the track segments of a signal positron found by the PR algorithm in one event. At the center the polyethylene muon stopping target is highlighted.

Once the track segment bending radius R_{seg}, its average position along the CYLDCH axis z_{seg} and in the transverse plane ϕ_{seg} are determined, the local value of the longitudinal component of the magnetic field B_z (loaded in a 3D map stored in memory, see Section 2.2.2) is used to compute the seed transverse momentum vector $\vec{p}_{\perp seed}$. The momentum vector is tangent to the circle fit at the measured hits position. The pitch angle of the helix α_{seed} is obtained by the average transverse and longitudinal displacements, $\sqrt{\Delta x^2 + \Delta y^2}$ and Δz respectively (Figure 5.8), between the hits within the e^+ track segments which passed the quality cuts described in Section 5.3.2:

$$|\vec{p}_{\perp seed}| = \frac{qB_z(z_{seg}, R_{seg}, \phi_{seg})}{R_{seg}} \quad ; \quad \alpha_{seed} = \arctan\left(\frac{\Delta z}{\sqrt{\Delta x^2 + \Delta y^2}}\right) \tag{5.10}$$

Finally the seed total momentum vector is calculated: $\vec{p}_{seed} = \vec{p}_{\perp seed} / \cos\alpha_{seed}$.

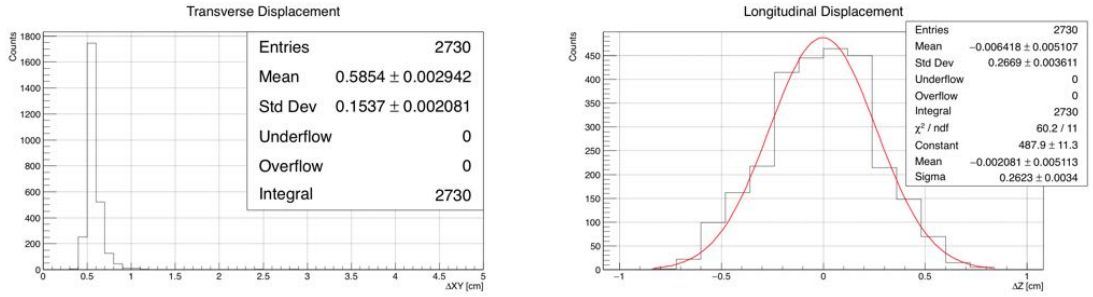

Figure 5.8: Average transverse and longitudinal displacement, $\sqrt{\Delta x^2 + \Delta y^2}$ and Δz respectively, between the hits within the signal e^+ track segments which passed the quality cuts described in Section 5.3.2.

5.2.4 Storing Information for Track Fitting

The hits within a track segment have to be sorted to help the Track Fitting task to reach its optimal accuracy and minimize the numerical uncertainties due to MCS and energy-loss straggling during the long extrapolations in between two consecutive hits. Hits sorting is performed according to their azimuthal angles ϕ_i. In the last part of the Track Finding task, the hits are arranged in a clockwise direction in the transverse plane xy, with increasing ϕ_i values in order to follow the natural e^+ helical trajectories through the CYLDCH sensitive volume.

The sorted hits list is then passed to the Track Fitting task (see also Section 6.1.2) as input, in form of instances of the specific classes `TrackCandidate` and `DCHHit`. By means of a dedicated method, the PR task fills `TrackCandidate` and `DCHHit` folders with the hits information from all the track segments found within each individual event. The `TrackCandidate` folders store the seed position, the seed momentum vector and the seed time t_0 of the first and last hits within the same segment. At present, t_0 is taken from the MC information, since the time provided by the Timing Counter (TC) is not yet used. The `DCHHit` folders store the measured hits positions and three lists of indices. Each hit has an entry in the three lists: the index relative to the azimuthally sorted hits array within the same track segment, the absolute hit index among all the

hits detected by the drift chamber and associated to track segments and the index of the track segment found within each single event. The space position measurements of all the hits in a track segment are provided both in the "global" coordinate system of the CYLDCH and in the "local" reference system of each drift cell. In these coordinates the z_{loc} axis coincides with the central sense wire, while the transverse plane $x_{loc}y_{loc}$ is perpendicular to the drift cell axis. By means of proper transformations the passage from one reference frame to the other and vice versa is ensured. These transformations are encoded into dedicated matrices: $L = G^{-1}$ from the "global" coordinates system to the "local" one and $G = L^{-1}$ for the inverse transformation. These matrices are a function of the absolute hit wire number n_{wire} since the "local" coordinates are defined with respect to each individual drift cell. Additional information is included into `DCHHit` folders, like the left-right ambiguities[3], the drift distances for each drift cell and the hit wire numbers.

Currently the signal waveforms acquired by the sense wires and simulated by *bartender* are not used in the PR algorithm to find the drift time related to the positron passage through the drift cell volume. The conversion of the drift time into the drift distance is simulated in the code by computing the Point Of Closest Approach (POCA) of a MC e^+ track to the corresponding hit wire. The distance between the POCA and the wire, i.e. the impact parameter, is calculated. A 100 μm gaussian smearing of the impact parameter is then performed in order to simulate a single-hit resolution similar to that obtained through direct measurements on drift cell prototypes, as reported in Section 3.2.1 and in [53]. In Figure 5.9 a schematic representation of this procedure is shown, together with the distribution of the energy loss for each signal e^+ hit in the CYLDCH gas mixture.

Let us define the MC hit position $\vec{p}_i$ and the versor $\hat{t}_i$ parallel to the linear approximation of the true e^+ track in the proximity of $\vec{p}_i$. Let $\vec{r}_i$ and $\hat{v}_i$ be the position vector and the versor of the hit sense wire ($\hat{n}_{wire}$) respectively. The position of the POCA in the "global" coordinates system $\vec{c}_i$ is obtained as:

$$\begin{cases} s_i = \frac{(\hat{t}_i \cdot \hat{v}_i)[\hat{v}_i \cdot (\vec{p}_i - \vec{r}_i)] - \hat{t}_i \cdot (\vec{p}_i - \vec{r}_i)}{1 - (\hat{t}_i \cdot \hat{v}_i)^2} \\ \vec{c} = \vec{p}_i + s_i \hat{t}_i \end{cases} \tag{5.11}$$

Subsequently $\vec{c}_i$ is computed into the "local" reference frame ($\vec{k}_i$) through the proper transformation matrix $L(\hat{n}_{wire})$. The impact parameter b_i is obtained and subsequently smeared with $\sigma_b = 100$ μm. The drift vector is defined in the "local" coordinates as

[3]The relation between drift time and space coordinate is not unique, since ionization electrons can reach a sense wire from two opposite sides. Thus, two space coordinates can correspond to the same measured signal time, one of them correct, the other a fake. This is the so-called left-right ambiguity.

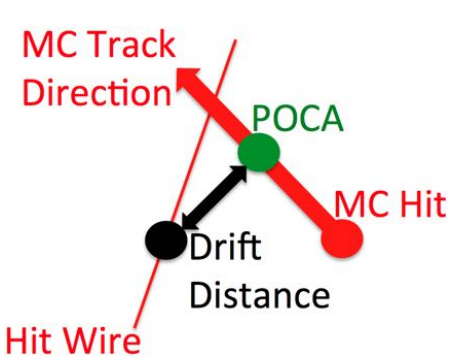

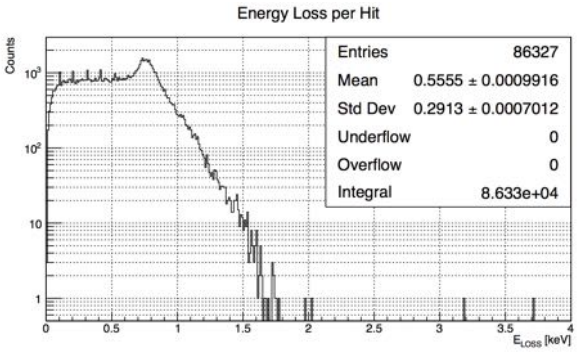

Figure 5.9: Left: schematic representation of the procedure used to directly obtain the hits drift distance from the corresponding hit sense wires. A 100 μm gaussian smearing on the impact parameter is performed in order to simulate a single-hit resolution similar to that obtained through direct measurements on drift cell prototypes. Right: distribution of the energy loss for each signal e^+ hit in the CYLDCH gas mixture.

$\vec{d_i} = (k_x, k_y, 0)$:

$$\vec{k_i} = L(\hat{n}_{wire})\vec{c_i} \quad ; \quad \vec{d_i} = (k_x, k_y, 0) \quad ; \quad b_i = \sqrt{k_x^2 + k_y^2} = |\vec{d_i}| \tag{5.12}$$

Similarly, the measured hit position on wire $\vec{m}_i$ (see Section 5.2.1) is calculated in the local reference system $(\vec{l_i})$. This position is then moved from the wire to its final position in space $\vec{L}_i$ by adding the drift vector $\vec{d_i}$. Finally, $\vec{L}_i$ is computed in the "global" reference system $(\vec{M}_i)$ through the proper transformation matrix $G(\hat{n}_{wire})$:

$$\vec{l_i} = L(\hat{n}_{wire})\vec{m}_i \quad ; \quad \vec{L}_i = \vec{l_i} + \vec{d_i} \quad ; \quad \vec{M}_i = G(\hat{n}_{wire})\vec{L}_i \tag{5.13}$$

The distribution of the drift distances in the CYLDCH cells is shown in Figure 5.10. The X-shape is due to the approach of the e^+ helical trajectory to the sense wires.

5.3 Pattern Recognition (PR) Performance

The performance of the Track Finding task has been firstly tested on 1000 events of pure signal positrons in order to refine contiguity criteria, fitting procedures and applied cuts for maximizing the algorithm efficiency. Thousand mixed events from *bartender* files have been also analyzed in order to simulate experimental conditions close to that of real future MEG-II data taking.

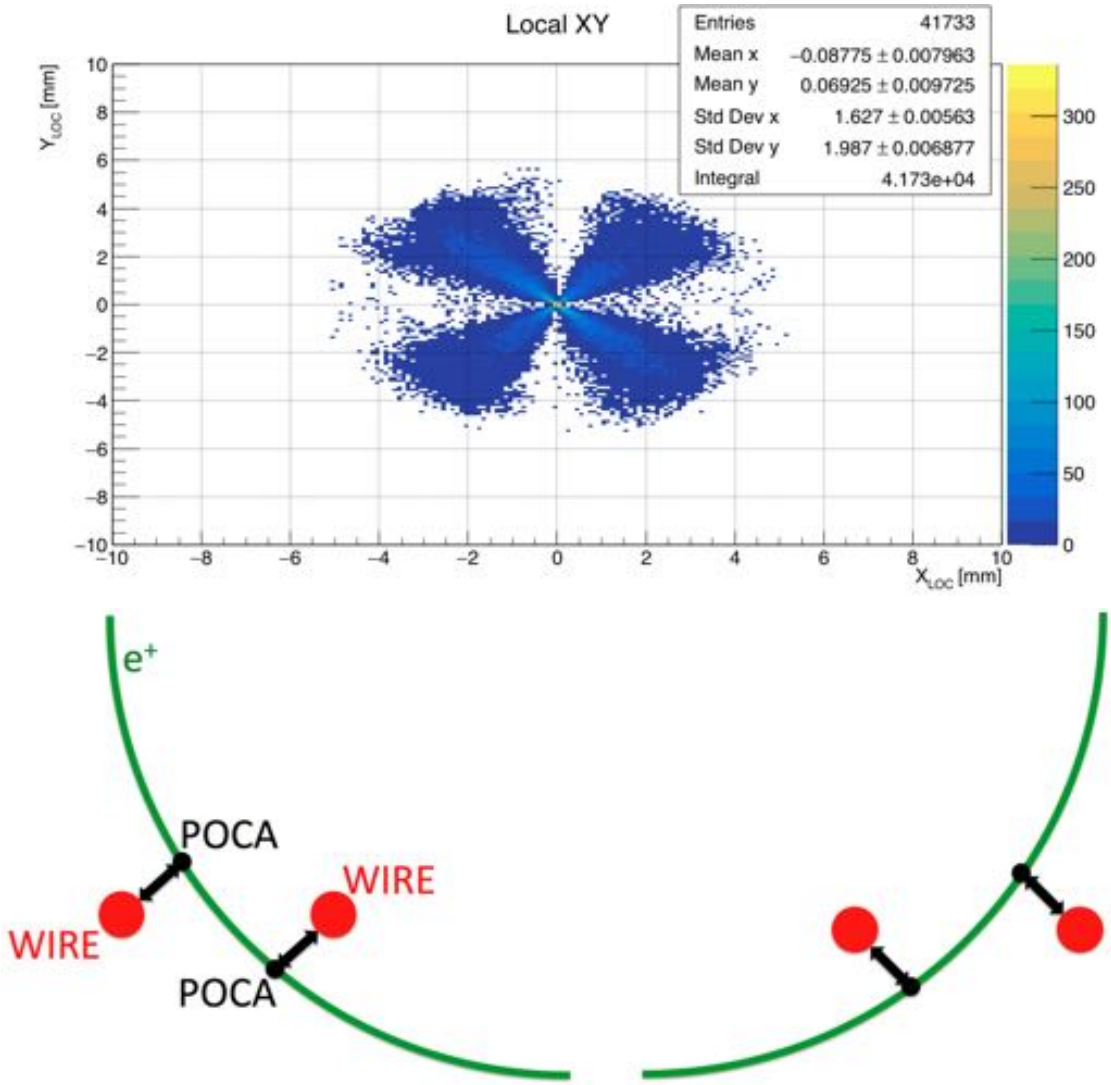

Figure 5.10: Above: drift distances distribution in the CYLDCH cells. Below: the X-shape is due to the approach of the e^+ helical trajectory to the sense wires.

5.3.1 Geometrical Acceptance and Occupancy

Before focusing on the performance of the PR algorithm, a study of the geometrical acceptance and occupancy of CYLDCH is presented in case of pure signal and mixed events. Signal positrons have been generated taking into account the combined acceptance of the MEG detectors. In fact, events are acquired only in case of a coincidence of a signal-like photon in the LXe calorimeter and a signal-like positron in the Timing Counter (TC). The geometrical acceptance of CYLDCH for signal positrons is determined by the por-

tion of solid angle covered by the photon detector, which is placed in the half-space $x < 0$ and covers about 11% of the whole solid angle, $120° < \phi < 240°$ and $|\theta| < 69.5°$ for the azimuthal and polar angle respectively (see Section 2.2.1). Hence a signal e^+ stemming from the muon stopping target as a result of a μ decay, in the opposite direction with respect to the corresponding signal γ detected in the LXe, enters the drift chamber sensitive volume at a maximum azimuthal angle ϕ of about $\pm 60°$. Positrons naturally turn clockwise in the transverse plane xy and this defines the CYLDCH acceptance edge for signal e^+.

The histograms in Figure 5.11 show the MC hits distribution in the CYLDCH sensitive volume for signal e^+ tracks (about 2/3 of the whole azimuthal angle ϕ is hit). The two black lines in the top histogram delimit the acceptance region covered by the MEG calorimeter and projected in the CYLDCH volume, while the two red circles depict the trajectory of a signal positron emitted from the center of the muon stopping target, highlighted in magenta in the plots, tangent to the acceptance edge lines. Obviously the muon beam spot on the target is not point-like, but its sizes are approximately 1.5×2 cm^2 FWHM (see Table 2.2). The solid black circle delimits the CYLDCH sensitive volume at the end-plates, while the two dashed black circles define the drift chamber sensitive volume at $z = 0$. The difference in the radial position is due to the CYLDCH hyperbolic profile given by the stereo configuration of the wires and this explains also the region with the highest occupancy, enclosed by the two dashed circles. The middle histogram shows a top view of the CYLDCH sensitive volume, with its radial dimensions at $z = 0$ and at $z = \pm 956$ mm highlighted through the solid black lines. The same is shown in the bottom histogram with a side view. The region with the highest occupancy along the CYLDCH axis is at about $|z| < 20$ cm, because of the proximity of the muon stopping target.

The same plots but for Michel positrons are shown in Figure 5.12. Michel positrons hit the CYLDCH sensitive volume uniformly in the whole azimuthal angle ϕ, since they are uncorrelated from the LXe calorimeter acceptance. The two dashed black circles define the drift chamber sensitive volume at $z = 0$ and contain the region with the highest occupancy. CYLDCH is designed to have the maximum acceptance for signal e^+, thus the detected hits are concentrated at the innermost radial position, as expected from the Michel e^+ momentum spectrum [57]. In fact, approximately 50% of the generated Michel positrons does not hit the drift chamber, passing through the central hole since their curvature radius is too small. Even in this case the region with the highest occupancy along the CYLDCH axis is at about $|z| < 20$ cm. This is shown in the two bottom histograms, for the top and side views respectively.

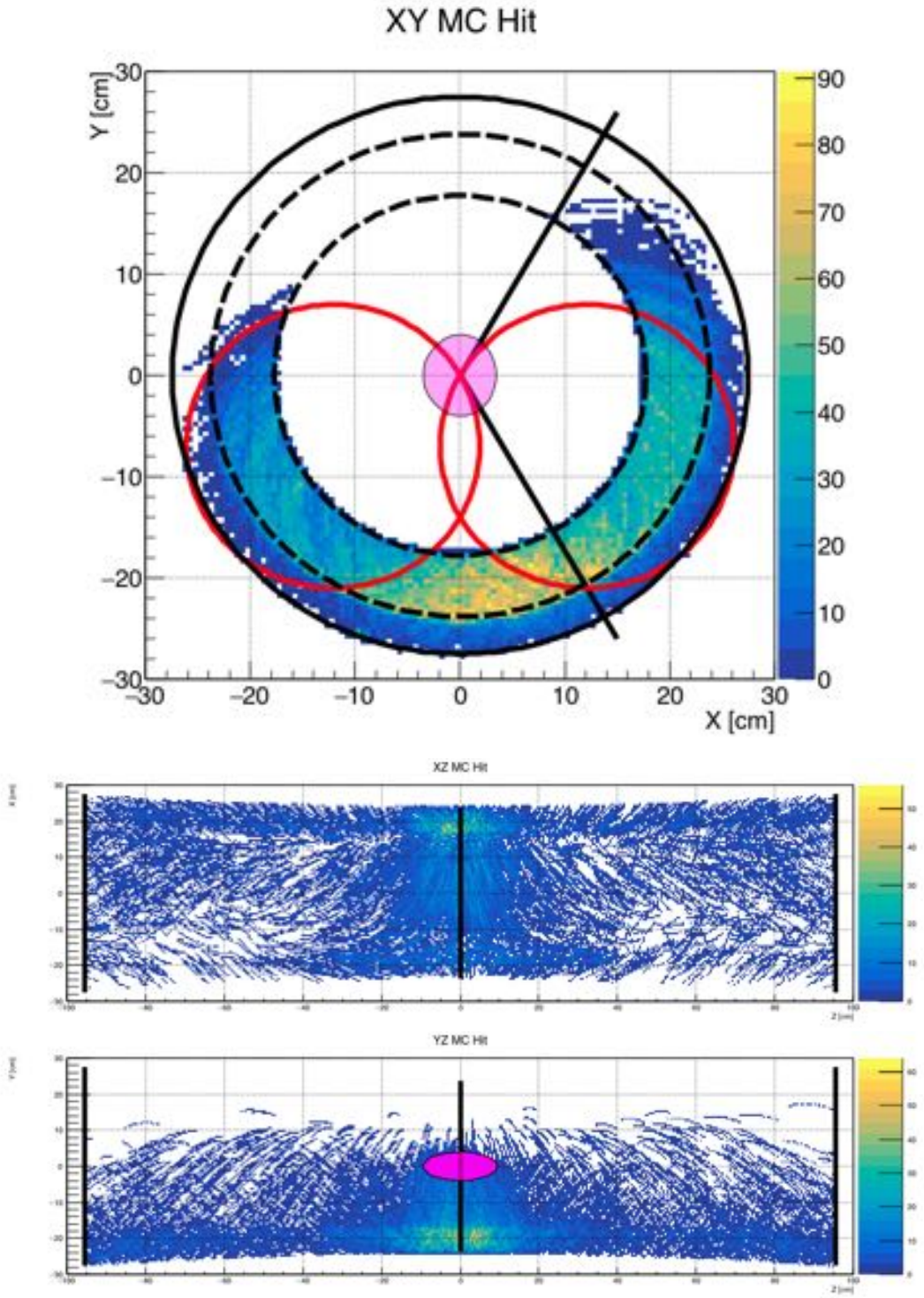

Figure 5.11: MC hits distribution in the CYLDCH sensitive volume for signal events. The two black lines in the top histogram delimit the acceptance region covered by the MEG calorimeter and projected in the CYLDCH volume, while the two red circles depict the trajectory of a signal positron emitted from the center of the muon stopping target, tangent to the acceptance edge lines. The solid black circle delimits the CYLDCH sensitive volume at the end-plates, while the two dashed black circles define the drift chamber sensitive volume at $z = 0$. The radial dimensions of the CYLDCH volume at $z = 0$ and at $z = \pm 956$ mm are highlighted through the solid black lines in the mid and bottom histograms.

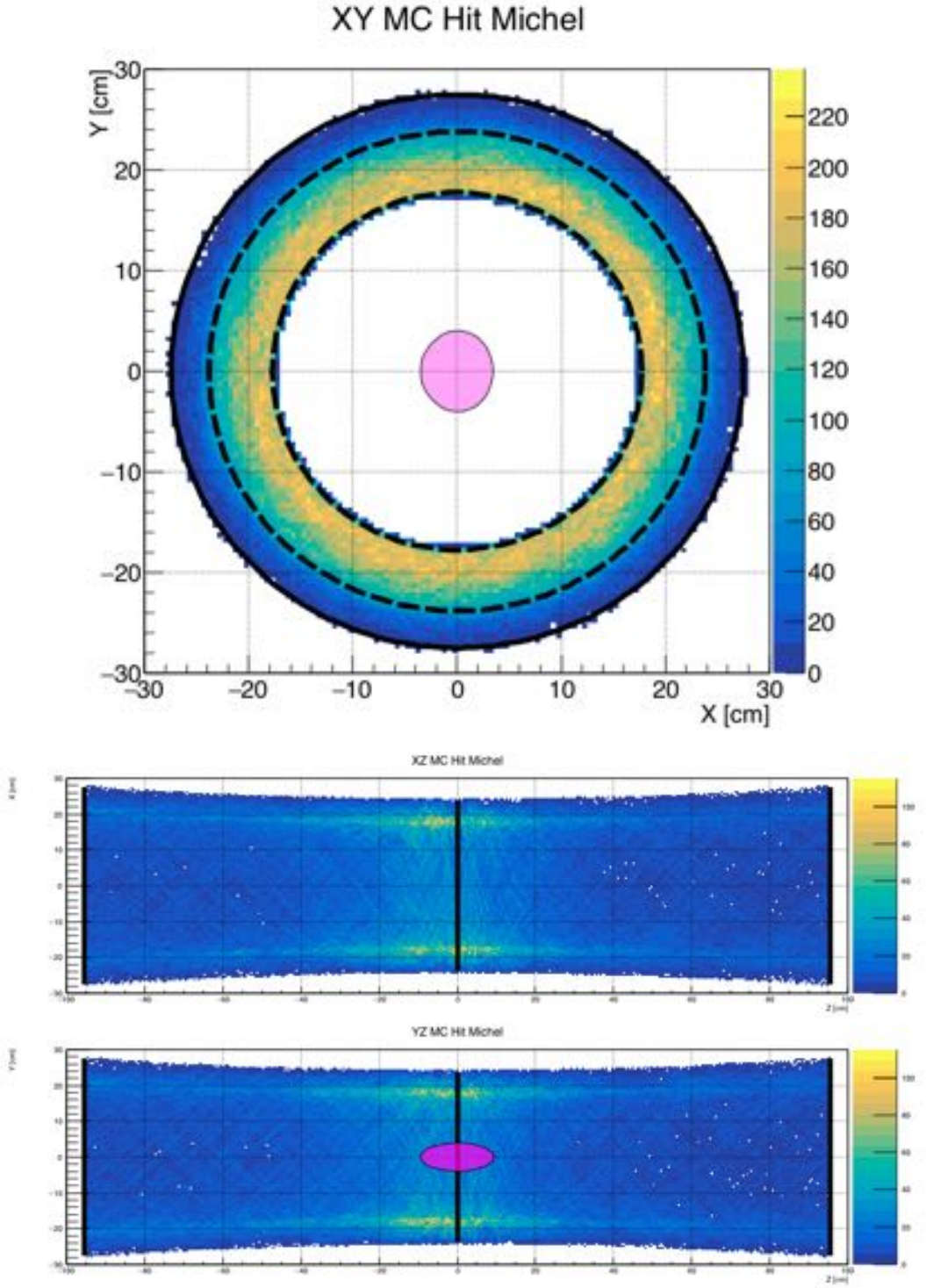

Figure 5.12: MC hits distribution in the CYLDCH sensitive volume for mixed events. The solid black circle in the top histogram delimits the CYLDCH sensitive volume at the end-plates, while the two dashed black circles define the drift chamber sensitive volume at $z = 0$. The solid black lines placed in the proximity of the end-plates and at the drift chamber center, in the mid and bottom histograms, highlight the hyperbolic envelope due to the stereo wires configuration.

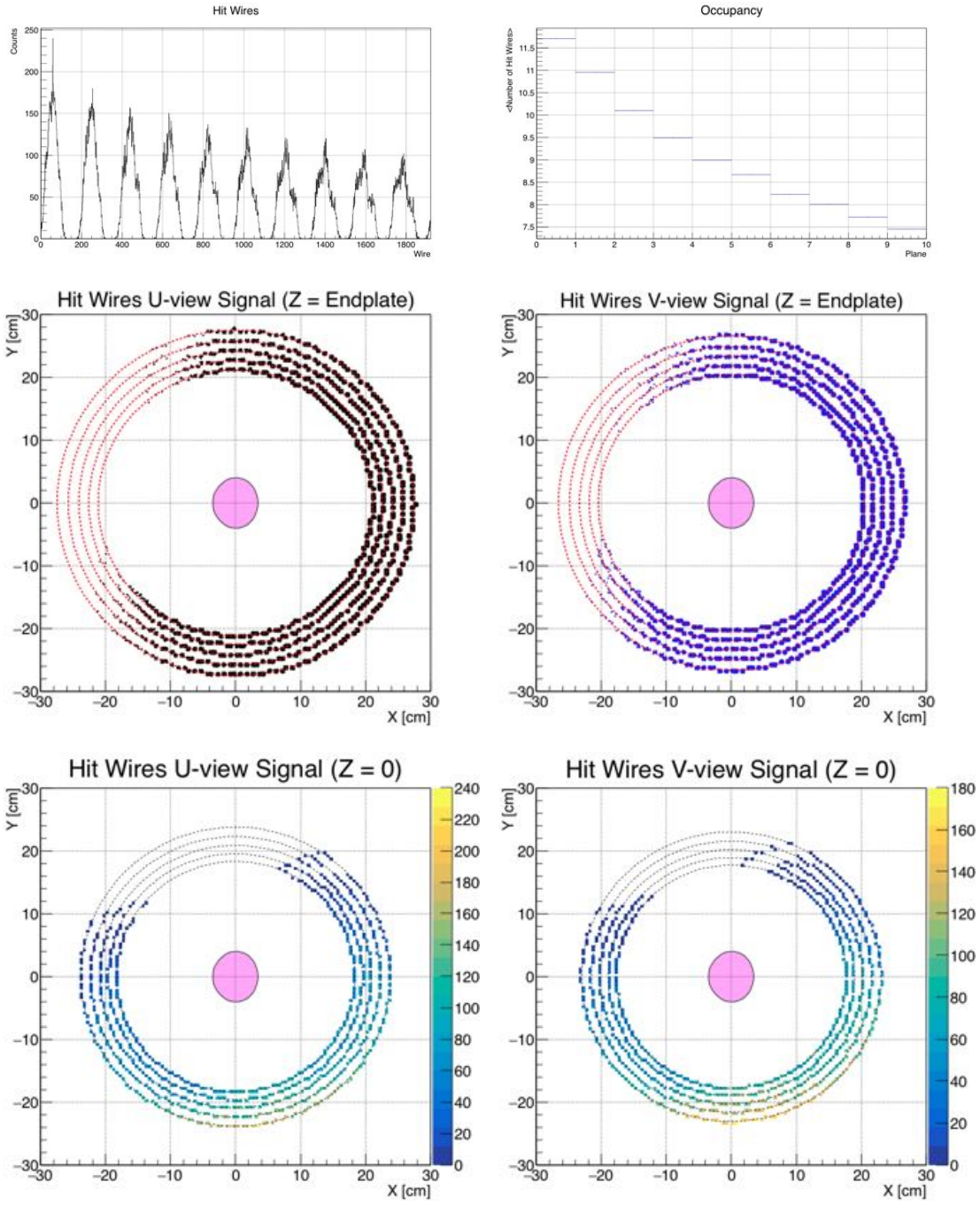

Figure 5.13: CYLDCH wires and planes occupancy for signal positrons.

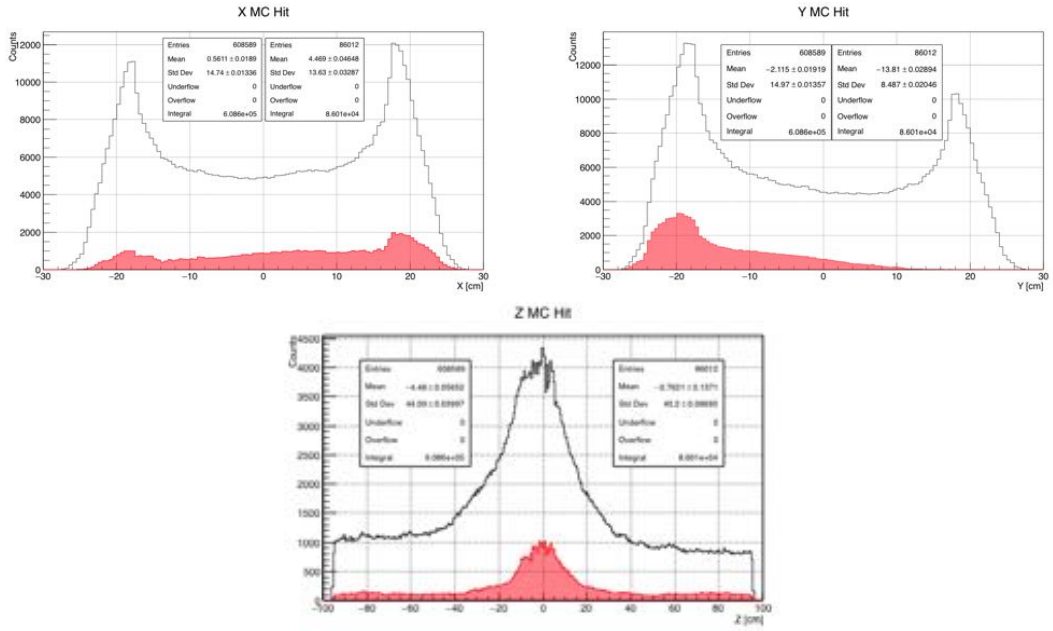

Figure 5.14: CYLDCH hits positions for mixed events projected on the x, y and z axes respectively. The contribution of the signal e^+ is highlighted in the red histograms and amounts to $\approx 14\%$ of the whole integral. This is in agreement with the separate analysis of pure signal and mixed events which shows that the average total number of hits detected in the drift chamber sensitive volume is ≈ 90 per signal event and ≈ 600 per mixed event respectively.

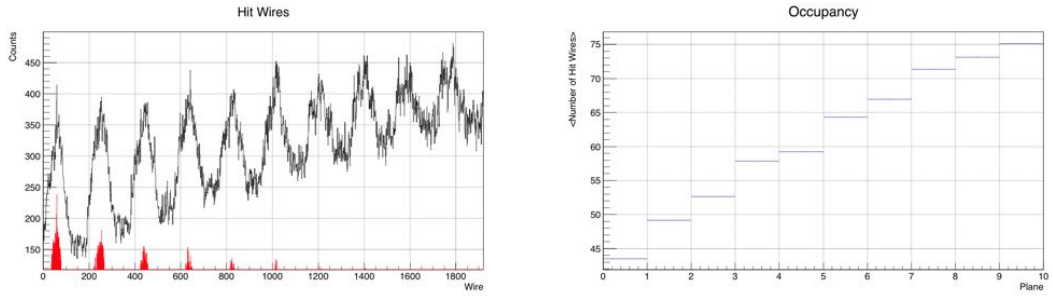

Figure 5.15: CYLDCH wires and planes occupancy for mixed events. The contribution of the signal e^+ is highlighted in the red histograms.

The solid black lines placed in the proximity of the end-plates and at the drift chamber center highlight the hyperbolic envelope due to the stereo wires configuration. The individual projections of the previous histograms on the x, y and z axes are shown in Figure 5.14. The contribution of the signal positrons, $\approx 14\%$ of the whole integral, is

highlighted in the red histograms. This value is in agreement with the entries of the occupancy plots shown in Figure 5.16 and 5.17. As aforementioned in the introduction to this Chapter, for a muon stopping rate of 7×10^7 Hz, foreseen for MEG-II, the expected average number of Michel positrons which are emitted during the 200 ns DAQ time window is ≈ 14. However the new drift chamber is designed to ensure the maximum geometrical acceptance for signal positrons. In fact, the analysis of pure signal and mixed events reveals that the average total number of hits in the CYLDCH sensitive volume is ≈ 600 per mixed event, versus a mean value of ≈ 90 per signal event.

The distribution of the hit wires number is shown in Figure 5.13 (top left) for signal events and in Figure 5.15 (left) for mixed events, with the contribution due to signal e^+'s highlighted by the red peaks. In both Figures also the average number of hit wires per plane is reported, respectively in the top right histogram in Figure 5.13 and in the right histogram in Figure 5.15. These latter provide the drift chamber occupancy as a function of the drift cells layer. Both the wires (numbered from 0 to 1919) and the wires planes (numbered from 0 to 9) are ordered from the outermost to the innermost radial position. In case of signal events the layers occupancy is maximal for the outermost wires planes, as expected. The periodicity of the peaks in the top left picture of Figure 5.13 is clearly 192, as expected from the two mid histograms of Figure 5.13, which show the positions of the hit wires at the CYLDCH end-plates for the U-view (black dots) and V-view (blue dots) respectively. The wires are correctly arranged at the nominal radial positions, highlighted with the dashed red circles (for each individual value see Figure 4.12). The wires occupancy is also shown in the two bottom histograms for the two views at $z = 0$: the 30° azimuthal rotation with respect to the mid plots is due to the stereo wires configuration (see Section 4.1). About 1/3 of the sense wires is never hit by signal positrons, as expected from the combined geometrical acceptance given by the CYLDCH and LXe calorimeter (Figure 5.11). The analysis of the mixed events shows that for the MEG-II real data taking conditions the occupancy of the CYLDCH drift cells is at its maximum for smaller radii (Figure 5.12 and Figure 5.15).

The average number of turns for positron tracks inside the CYLDCH sensitive volume before they hit the Timing Counter (TC) scintillating tiles is $\bar{N}_{turn} \approx 1.7$. This value is provided by the histogram in Figure 5.16 and Figure 5.17 (top left) which shows the distribution of the number of hits as a function of the turn for e^+ helical trajectories, respectively for signal and mixed events, with $\approx 14\%$ contribution due to signal e^+'s highlighted in the red histogram of Figure 5.17 (top left picture). The average hits occupancy is also shown for the first four turns individually (mid and bottom plots).

The drift chamber z occupancy as a function of the drift cells layer is further shown in

Figure 5.16 and Figure 5.17 (top right). The drift chamber occupancy per single drift cell at the innermost radius, near the muon stopping target, is about 23 kHz/cm for $|z| < 20$ cm. This value drops to about 13 kHz/cm for 20 cm $< |z| < 40$ cm, before decreasing down to about 5 kHz/cm or even less near the longitudinal end portions of the CYLDCH sensitive volume. This is in agreement with the plots shown in Figure 5.12. In the drift chamber core ($|z| < 20$ cm) the occupancy per single drift cell at the outermost radius is about 10 kHz/cm. Thus, the rate per cell ranges from about 0.8 MHz to about 1.7 MHz, resulting in a probability to have a hit cell within the simulated 200 ns acquisition time window ranging from about 16% to about 34%.

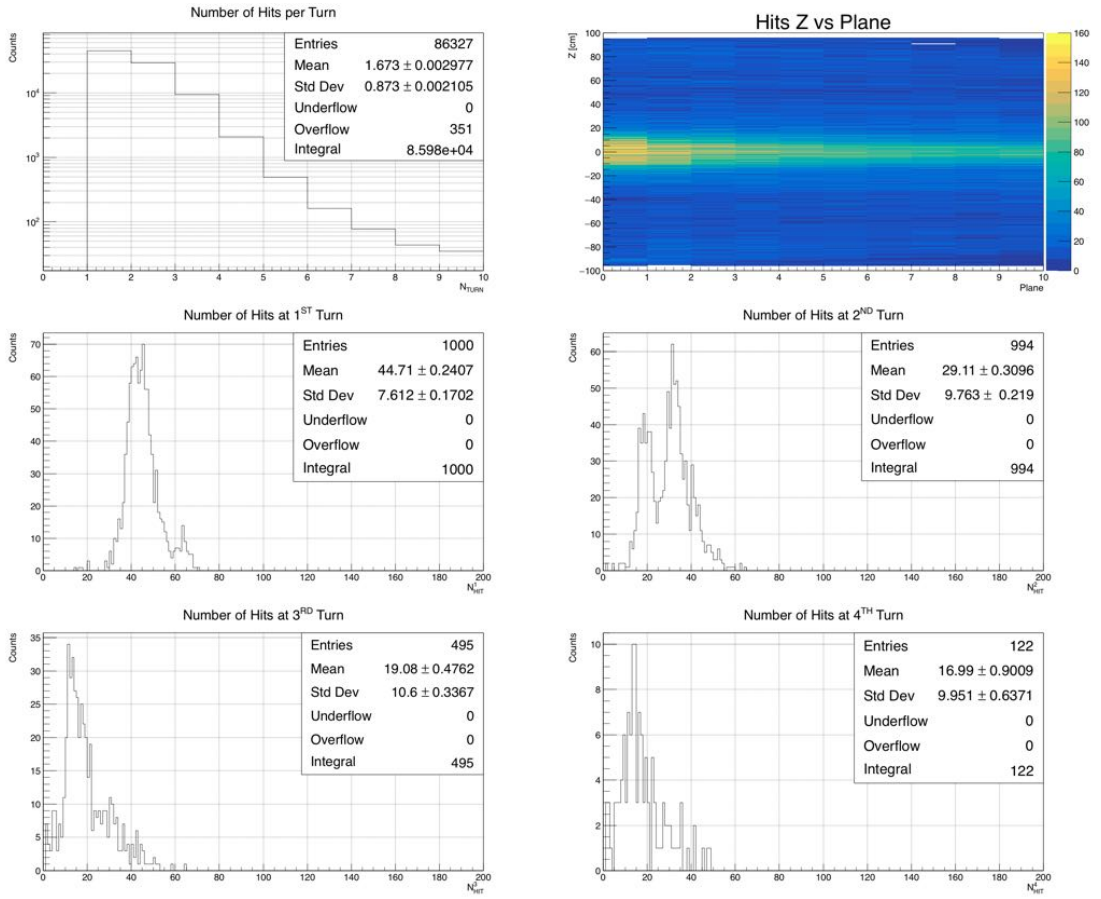

Figure 5.16: Distribution of the number of hits as a function of the turn for signal e^+ helical trajectories. The average number of hits as a function of the first four turns is shown individually; the average total number of hits per signal event is ≈ 90. The drift chamber z occupancy for the various wires plane is reported on the top right plot.

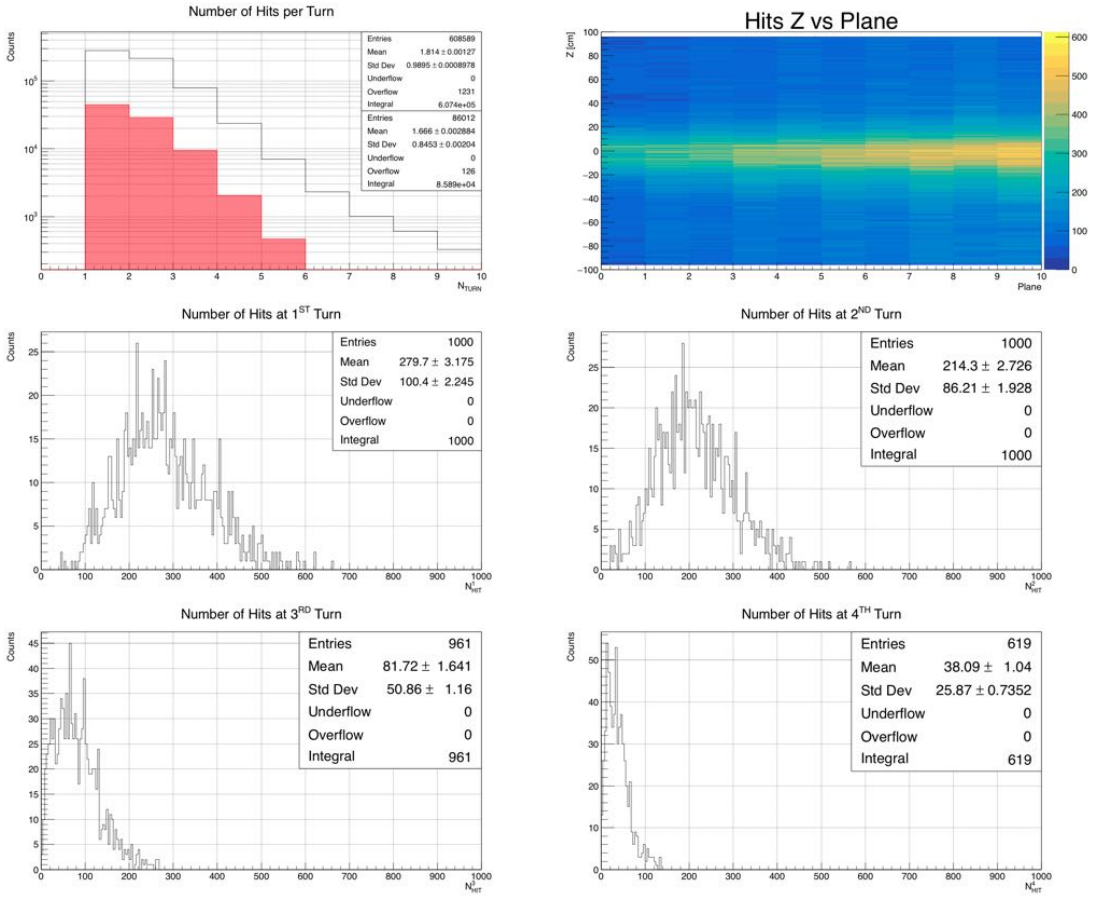

Figure 5.17: Average number of turns for positron tracks inside the CYLDCH sensitive volume before they hit the TC scintillating tiles, resulting from the analysis of the mixed events. The average number of hits as a function of the first four turns is shown individually; the average total number of hits per mixed event is ≈ 600. The drift chamber z occupancy depending on the wires plane is reported on the top right plot.

5.3.2 Efficiency

The distribution of the number of hits within signal events is presented in the black histogram of Figure 5.18 (top left plot). The number of hits found by the Track Finding task is highlighted in the red histogram in the same plot. By comparing the mean of the two histograms, one obtains that the average percentage of found hits is about 71%, ≈ 60.6 versus ≈ 86.4 from MC data. However, the top right plot shows the number of track segments per signal event and the corresponding number of identified ones in red: by comparing the two distributions one observes that the mean track segments finding efficiency is about 90%, ≈ 4.4 versus ≈ 4.9 from MC data. Regarding the number of hits

per track segment, the results are shown in the bottom plot, with the ones identified by the PR algorithm highlighted in red. Even in this case the ratio found/total amounts to about 72%, ≈ 14 versus ≈ 19.4 from MC data. This points out that usually the detected track segments contain less hits compared to the MC ones. However they are identified and stored correctly in about 90% of cases. A more detailed discussion about the missed hits is reported in the last part of this Section.

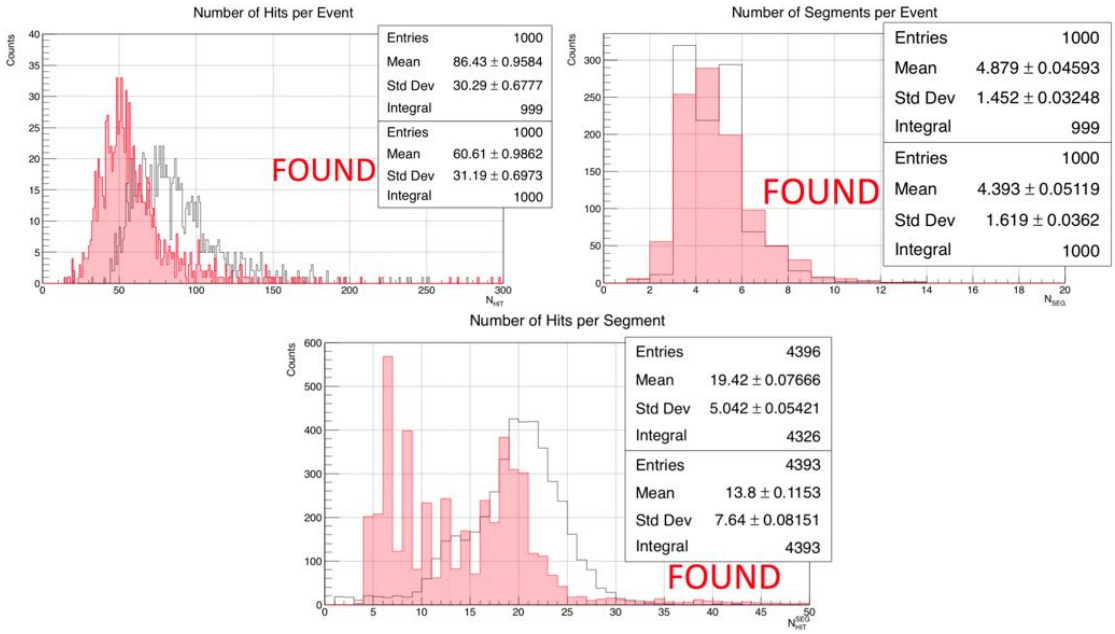

Figure 5.18: Top left: distribution of the number of hits within signal events (black histogram) with the found ones highlighted in red. Top right: number of track segments per signal event (black histogram), and the corresponding identified ones (red histogram). Bottom plot: number of hits per track segment (black histogram), with the ones identified by the PR algorithm highlighted in red.

The same plots, but stemming from the analysis of the mixed events, are reported in Figure 5.19. In this case the average percentage of found hits (top left picture) drops down to about 42% (≈ 610 versus ≈ 256), while regarding the average number of hits per track segment (bottom picture) the ratio found/total is $\approx 13.5/28 \approx 48\%$. However, the track segments finding efficiency (top right picture) amounts to $\approx 88.5\%$ (≈ 20 versus ≈ 22.6), a value not so different from the one obtained from the analysis of pure signal events ($\approx 90\%$). This means that, even in this case, the found track segments are shorter than the MC ones, containing approximately one half of the hits.

Before storing the final information which will be passed as input for the Track Fitting

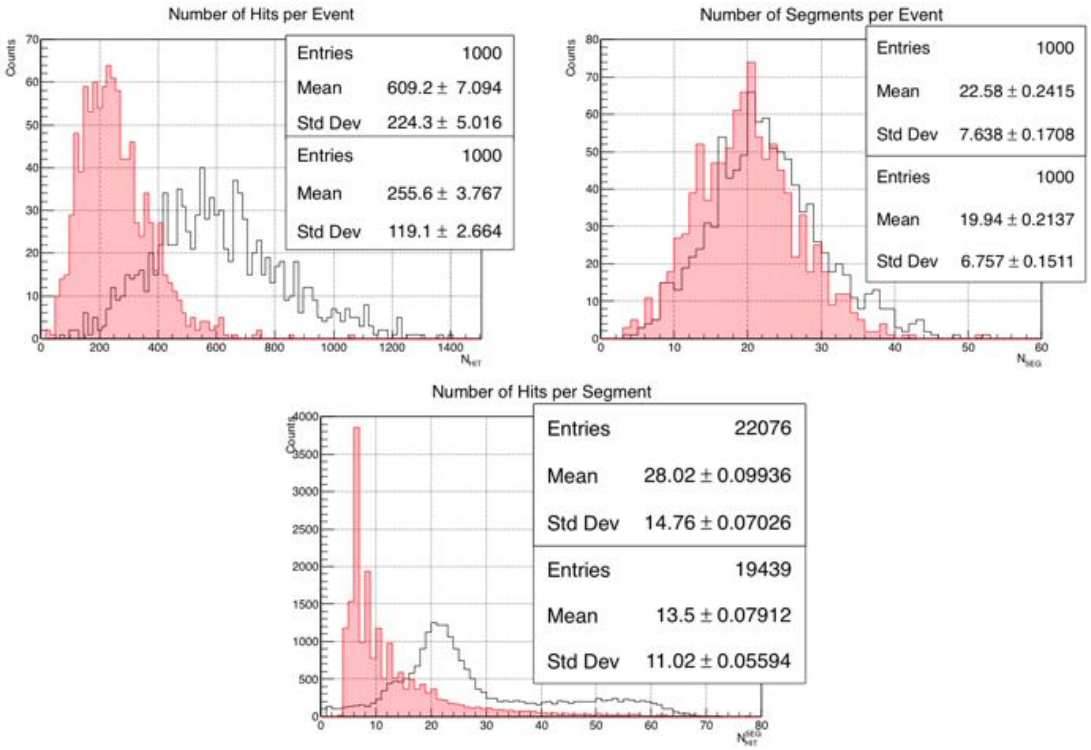

Figure 5.19: Top left: distribution of the number of hits within a mixed event (black histogram) with the found ones highlighted in red. Top right: number of track segments per mixed event (black histogram), and the corresponding identified ones (red histogram). Bottom plot: number of hits per track segment (black histogram), with the ones identified by the PR algorithm highlighted in red.

task, a series of selection cuts is applied to the identified track segments. These quality cuts are essentially based on the minimum number of hits found per track segment N_{hits}^{seg}. The first condition required is $N_{hits}^{seg} > 6$ since, although five parameters are in principle enough to characterize a helical trajectory, some preliminary studies have shown that practically the minimum amount of hits per single track segment to be correctly fitted by the Track Fitting algorithm, without failures (see Section 6.3), is seven. The same quality cut ($N_{hits}^{seg} > 6$) has been used during the final data analysis of the first phase of the MEG experiment. Moreover the selection cuts include requirements on the track segments radius (10 cm $< R_{seg} <$ 20 cm), obtained through the least-squares circle fitting procedure described in Section 5.2.3 and on the circle fit quality itself. Figure 5.20 shows the positions of the circle centers, as returned by the fits performed on the detected track segments, with superimposed the ones which have passed the quality cuts (top right plot). The same is reported for the track segments radius distribution (bottom

plot). The mean radius is compatible with the signal e^+ tracks curvature in the COBRA magnetic field, given the value of their momentum (≈ 52.8 MeV). The tail for small radii is due to short track segments badly fitted. In the top left plot the distribution of the average z positions of the track segments identified by the PR algorithm for the entire length of the CYLDCH sensitive volume is reported. Note that more than 52% of the found track segments is located within $|z| < 20$ cm, in agreement with the occupancy plots of Figure 5.16.

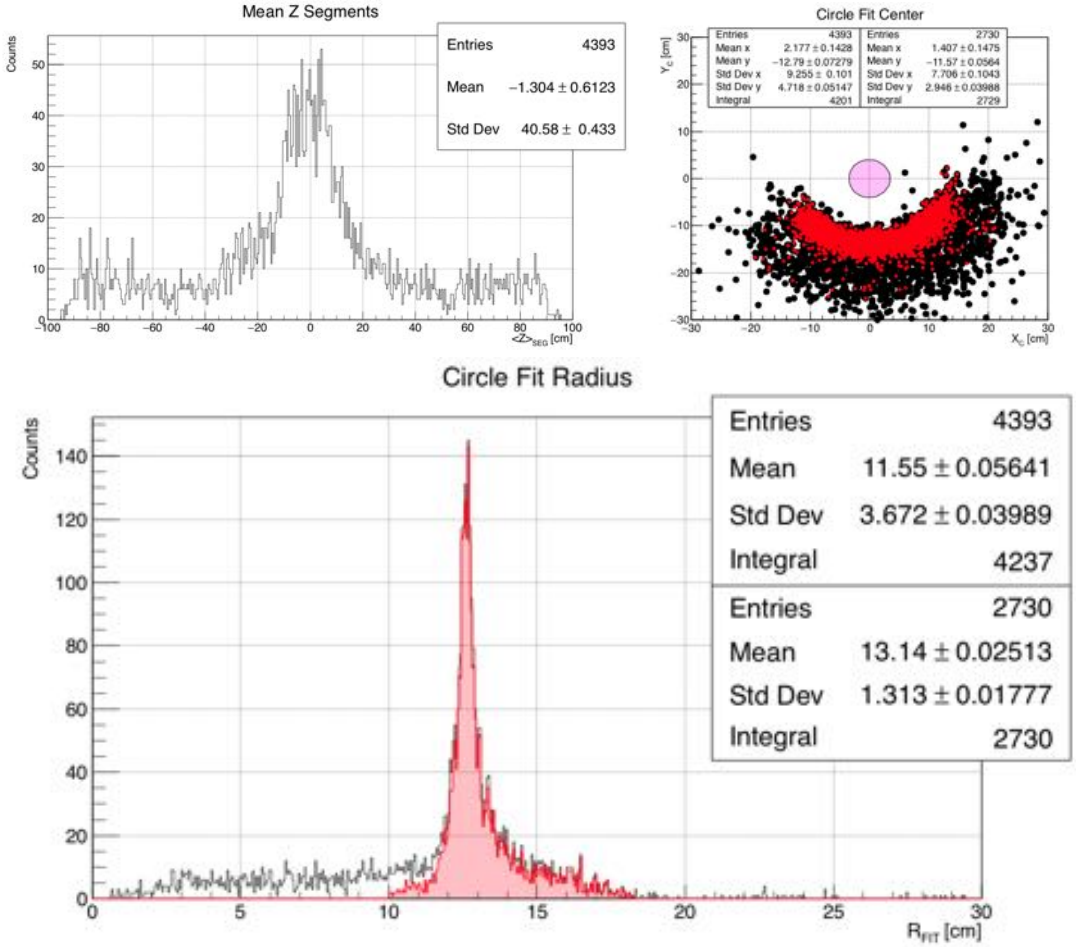

Figure 5.20: Top left: distribution of the average z positions of the track segments hits identified by the PR algorithm for signal events. Top right: positions of the circle centers, as returned by the fits performed on the detected track segments, with superimposed the ones which have passed the quality cuts. Bottom: the same for the distribution of track segments radii.

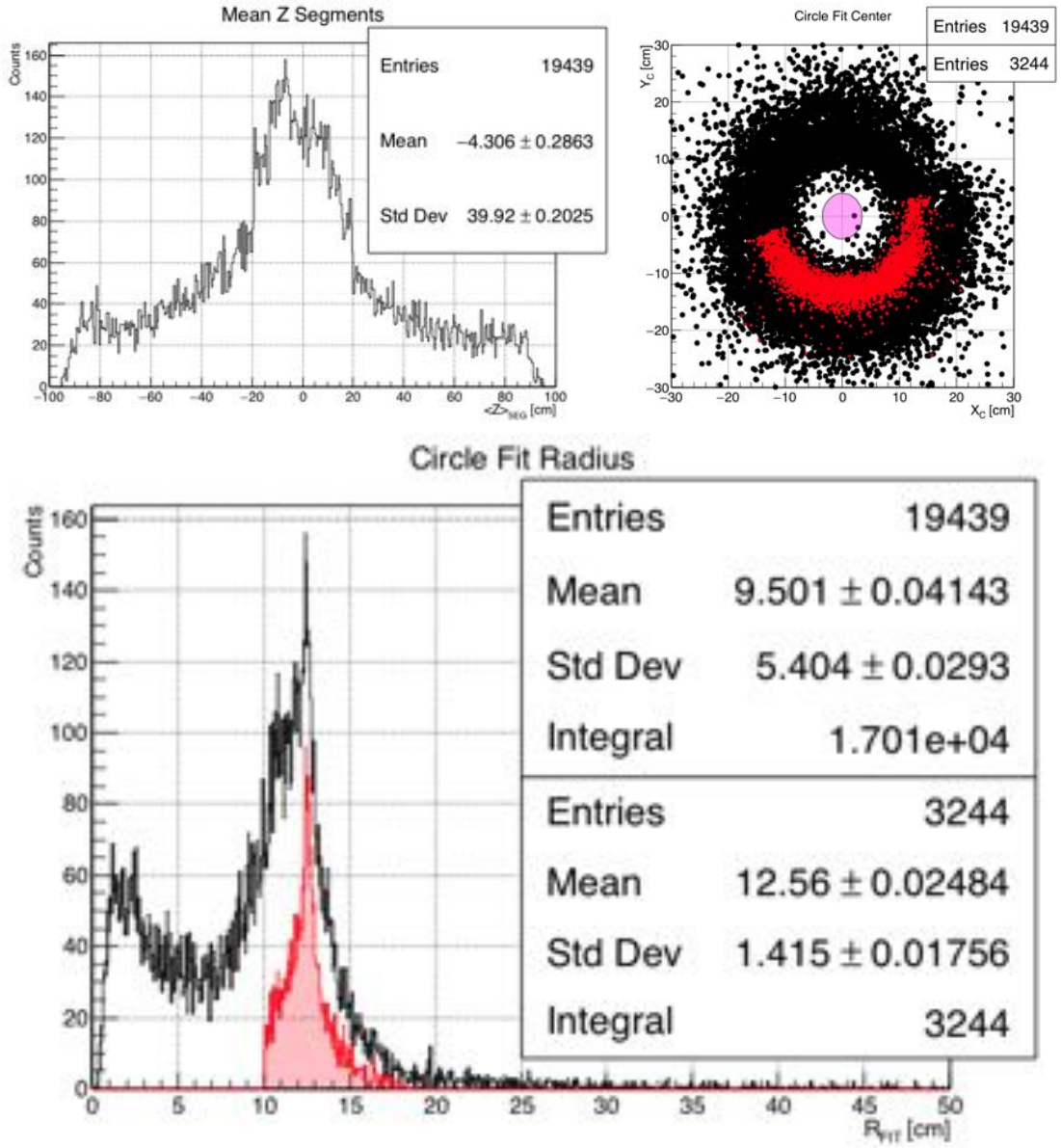

Figure 5.21: Top left: distribution of the average z positions of the track segments hits identified by the PR algorithm for mixed events. Top right: positions of the circle centers, as returned by the fits performed on the detected track segments, with superimposed the ones which have passed the quality cuts. Bottom: the same for the distribution of track segments radii.

Similarly, the same plots are shown in Figure 5.21 for mixed events. The percentage of the track segments found by the PR algorithm within $|z| < 20$ cm is larger than 47% (top left picture). Regarding the track segments radius (bottom picture), the peak in the black

histogram for $R_{seg} < 5$ cm is due to low-momentum Michel positrons. These ones are largely discarded by the quality cuts (red histogram); nevertheless the low-momentum background component lowers the mean value of the radius, by approximately 5 mm. The top right histogram shows the positions of the circle centers, as returned by the fits performed on the detected track segments. Mindful of the previous experience stemming from the signal events analysis, the quality cuts have been enriched with an azimuthal requirement on the circle fit center position on the xy plane, which must be located in $-166.8° < \phi < 13.2°$. This range is chosen by exploiting the histogram of Figure 5.20.

The track segments which pass the selection cuts described above are the so-called **track candidates**. These ones contain the hits which will be processed by the Track Fitting task. The number of track candidates per signal event is ≈ 3.2, as shown in Figure 5.22 (on the left). Thus in average one track segment, the shorter one, is discarded by the quality cuts (see Figure 5.18 for a comparison). The average number of track candidates increases in case of mixed events up to ≈ 3.8 (Figure 5.23 on the left). In priciple this value should not be different from that stemming from the signal events analysis (Figure 5.22 on the left), nevertheless the selection cuts practically can not clean all the background-derived track segments and an average increase of $\approx 18\%$ is noted. The mean number of hits within the track candidates is shown in the right pictures of Figure 5.22 for signal events and of Figure 5.23 for mixed events respectively. In the first case, the value increases from about 14 (all track segments, see Figure 5.18) up to about 16 (track candidates), to be compared with a MC value of about 19.4 ($\approx 82\%$). In the second case the mean value decreases by almost one hit: from ≈ 13.5 (Figure 5.19) to ≈ 12.6.

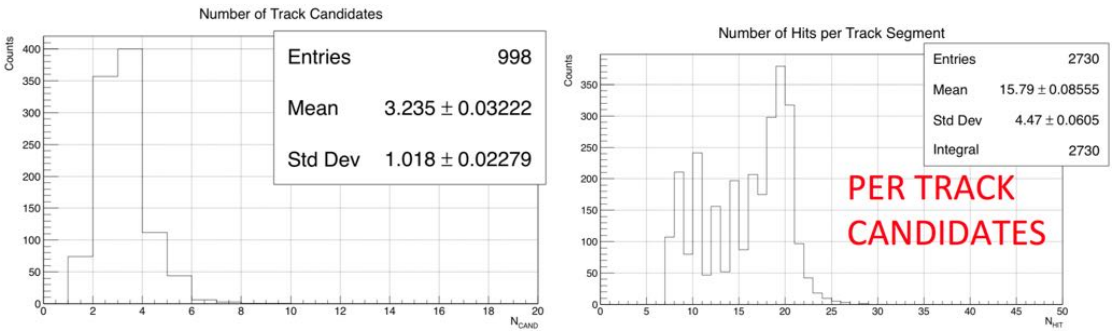

Figure 5.22: Left: number of track candidates per signal event. Right: number of hits within the track candidates.

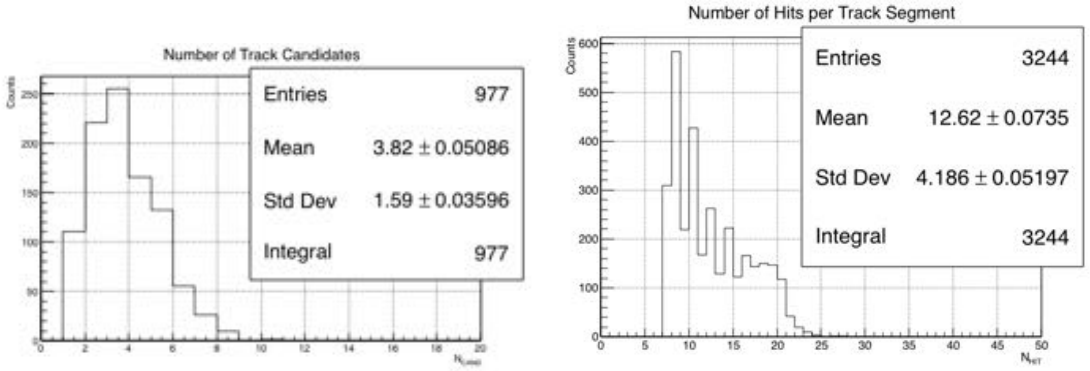

Figure 5.23: Left: number of track candidates per mixed event. Right: number of hits within the track candidates.

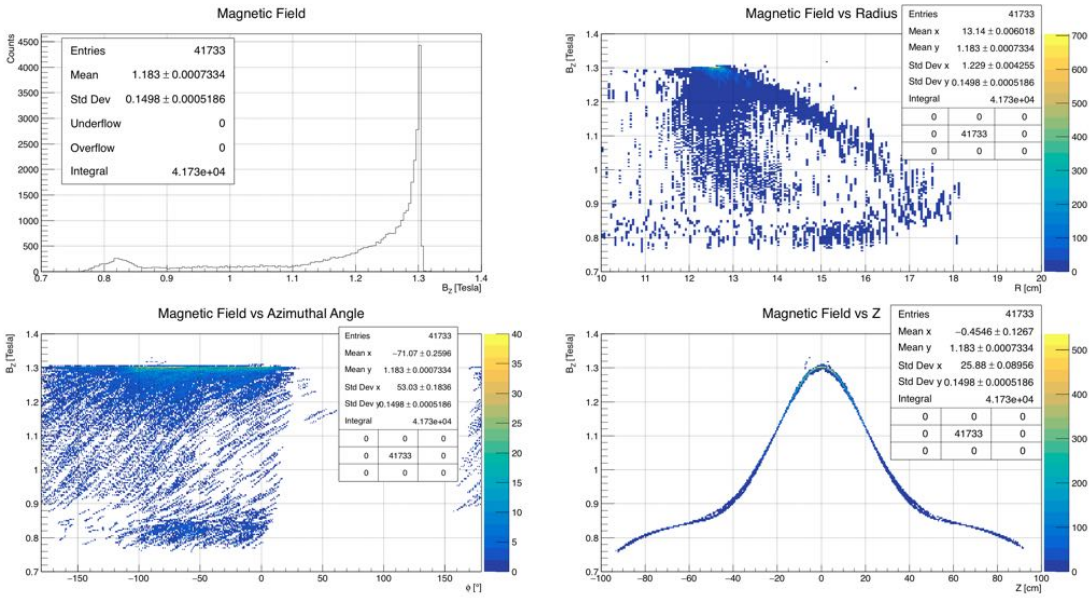

Figure 5.24: Longitudinal component of the magnetic field B_z (top left) provided by the COBRA superconducting magnet. B_z is also plotted versus the radius (top right), the azimuthal angle ϕ (bottom left) and the z position (bottom right) of the track candidates. The maximum magnetic field intensity is for small value of $|z|$ in the proximity of the muon stopping target.

In Figure 5.24, the value of the longitudinal component of the magnetic field B_z provided by COBRA is shown (top left). B_z is also plotted versus the radius (top right), the azimuthal angle ϕ (bottom left) and the z position (bottom right) of the track candidates. The maximum magnetic field intensity is reached for small value of $|z|$ in the

proximity of the target. The CYLDCH (2/3)-azimuthal acceptance for signal positrons is clearly visible in the bottom left picture, in agreement with the plots reported in Figure 5.11.

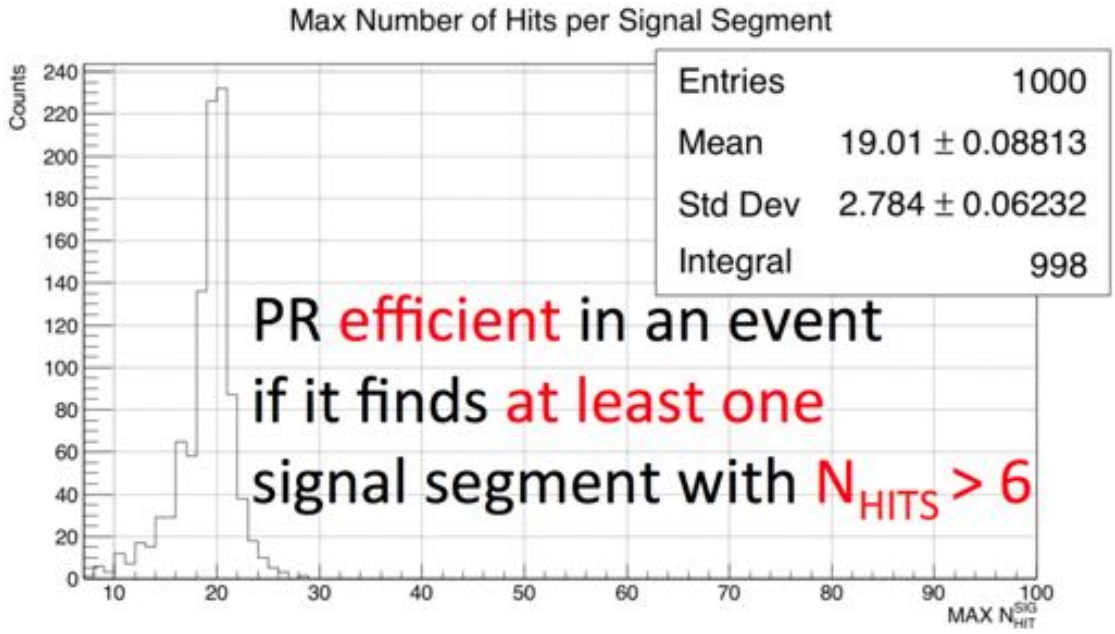

Figure 5.25: Distribution of the maximum number of hits per segment identified by the PR algorithm within each individual signal event. The average of the histogram is ≈ 19, showing that at least one long track segment is found. This simple plot allows to extract directly the efficiency on signal positrons reached by the Track Finding task (PR_{EFF}). The PR algorithm is considered efficient in one event if it finds at least one signal segment with a number of hits larger than six ($N_{hits}^{SIGseg} > 6$). PR_{EFF} is obtained by calculating the ratio between the integral of the portion of the histogram corresponding to $N_{hits}^{SIGseg} > 6$ and the total number of entries coincident with the number of signal events analyzed: $\mathrm{PR}_{EFF}^{SIG} = 99.8\%$.

The Pattern Recognition (PR) algorithm is considered **efficient** in one event if it finds **at least one signal segment with a number of hits larger than six** ($N_{hits}^{SIGseg} > 6$). In fact, as reported slightly above in this Section, some preliminary studies have shown that 7 is the minimum amount of hits per single track segment to be correctly fitted by the Track Fitting algorithm, without failures (see Section 6.3). The identification of signal segments in a mixed event is possible thanks to a MC flag that allows to monitor the hits types, signal or Michel e^+, within the track candidates. The histogram presented in Figure 5.25 shows the distribution of the maximum number of hits per signal segment identified by the PR algorithm within each individual signal event. The average of the

histogram is ≈ 19, showing that at least one track segment with a large number of hits is found. This simple plot allows to obtain directly the efficiency on signal positrons reached by the Track Finding task (PR_{EFF}) by calculating the ratio between the integral of the portion of the histogram corresponding to $N_{hits}^{SIGseg} > 6$ and the total number of entries coincident with the number of signal events analyzed: $\mathrm{PR}_{EFF}^{SIG} = 99.8\%$.

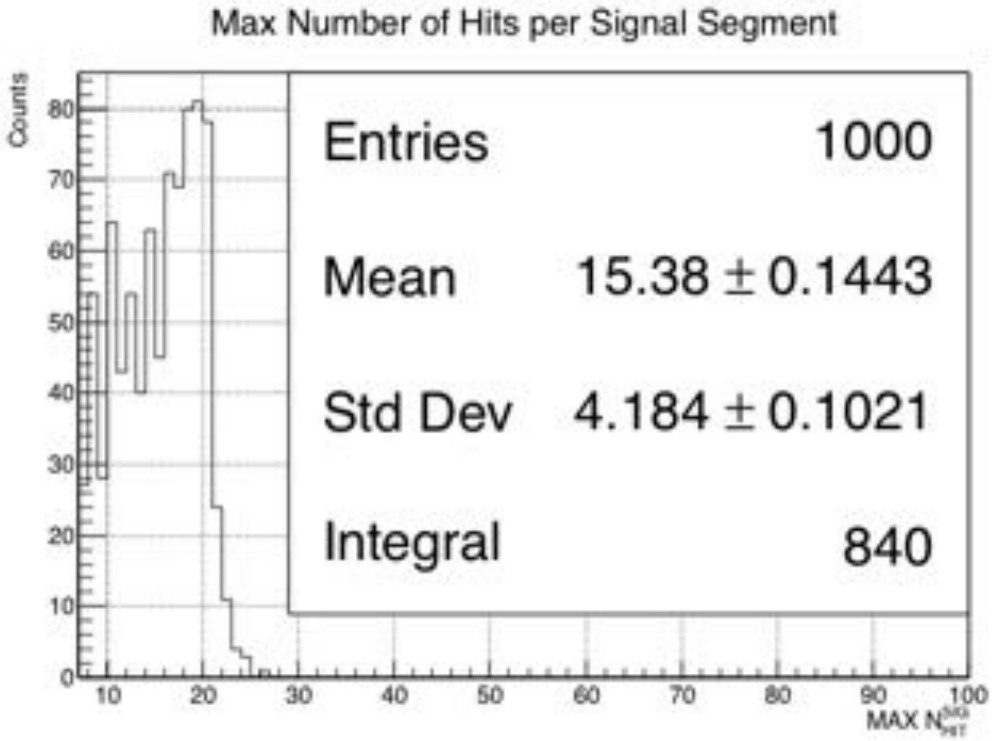

Figure 5.26: Distribution of the maximum number of hits per segment identified by the PR algorithm within each individual mixed event. The average of the histogram is ≈ 15.4, showing that at least one long track segment is found. This simple plot allows to extract directly the efficiency on signal positrons reached by the Track Finding task (PR_{EFF}). The PR algorithm is considered efficient in one event if it finds at least one signal segment with a number of hits larger than six ($N_{hits}^{SIGseg} > 6$). PR_{EFF} is obtained by calculating the ratio between the integral of the portion of the histogram corresponding to $N_{hits}^{SIGseg} > 6$ and the total number of entries coincident with the number of signal events analyzed: $\mathrm{PR}_{EFF}^{MIX} = 84\%$.

The mixed events analysis shows a drop of the PR algorithm efficiency on signal, due to the harsher environment caused by the background Michel positron recorded during the simulated 200 ns acquisition time window, which increases the average number of hits to be processed from ≈ 90 up to ≈ 600. The distribution, centered at ≈ 15.4

hits, of the maximum number of hits per signal segment identified by the PR algorithm within each individual mixed event (Figure 5.26), leads to a PR efficiency on signal of $\mathrm{PR}_{EFF}^{MIX} = 84\%$. In all these cases the Track Fitting algorithm is capable to process the track segments and to return a value for the e^+ kinematic variables needed to classify the detected events. This value is not so far from the presumed 90% efficiency on signal positrons of the new drift chamber (see Table 3.2).

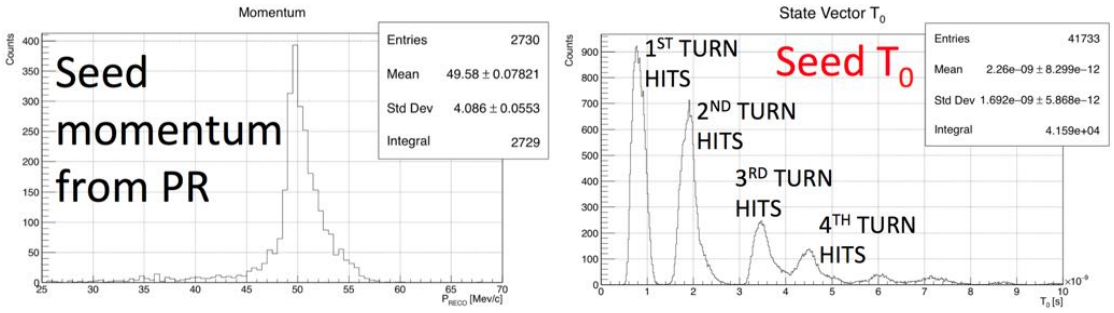

Figure 5.27: Seed momentum p_{seed} and seed positron time t_0 for signal events.

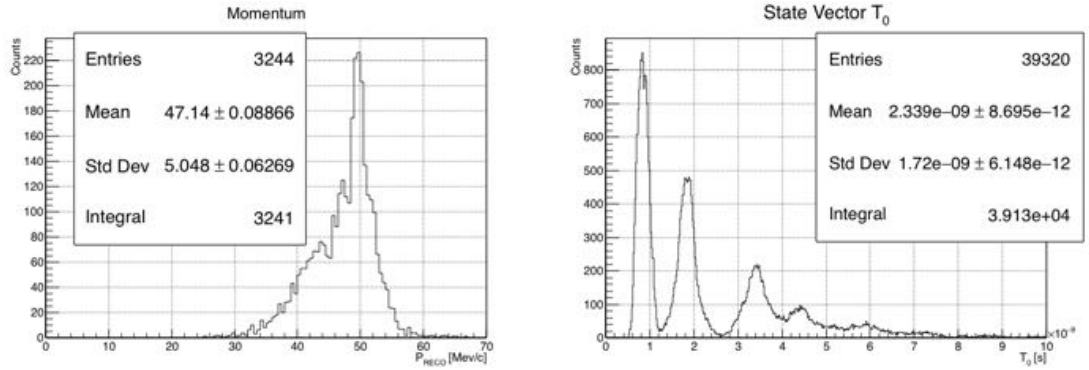

Figure 5.28: Seed momentum p_{seed} and seed positron time t_0 for mixed events.

Nevertheless, several further improvements have to be implemented into the Pattern Recognition algorithm. For instance, an extrapolation procedure based on the first hits in one track segment to get a prediction of the next hit position should be implemented in order to avoid unnecessary calculation and to reduce the combinatorial background. Moreover, the full analysis chain, from the waveforms of the hit sense wires which provide the ionization clusters drift times within the CYLDCH cells, the use of the cluster timing technique (see Section 3.2.3) to get a minimum-biased estimate of the e^+ track impact parameter with respect to the wire, to the final hits reconstruction, needs still to be implemented.

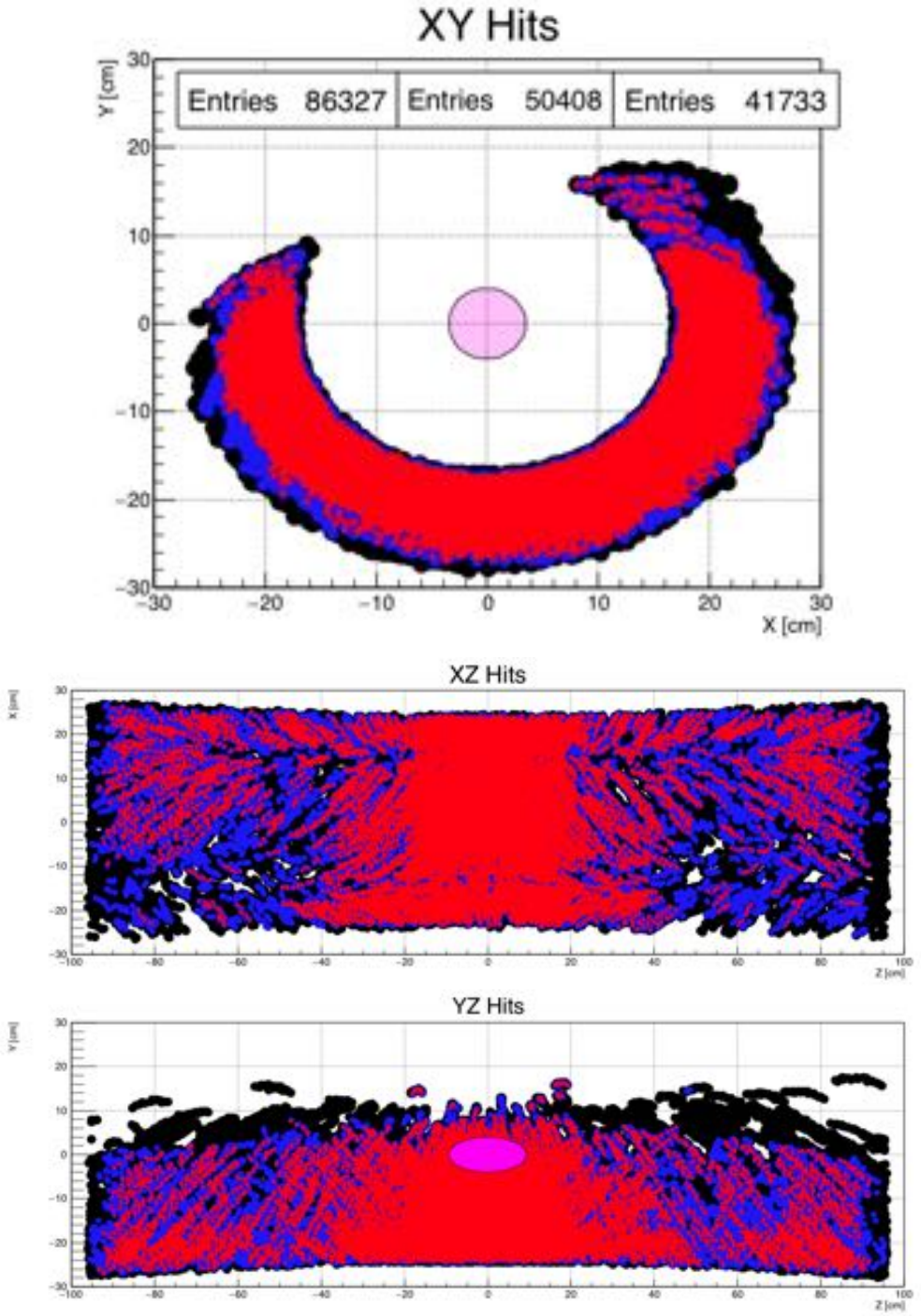

Figure 5.29: Aggregate positions of the hits belonging to the track candidates identified by the Track Finding task, for all 1000 signal events analyzed (red dots), together with all the reconstructed hits, before the filtering procedure based on the quality cuts (blue dots), and the MC ones (black dots).

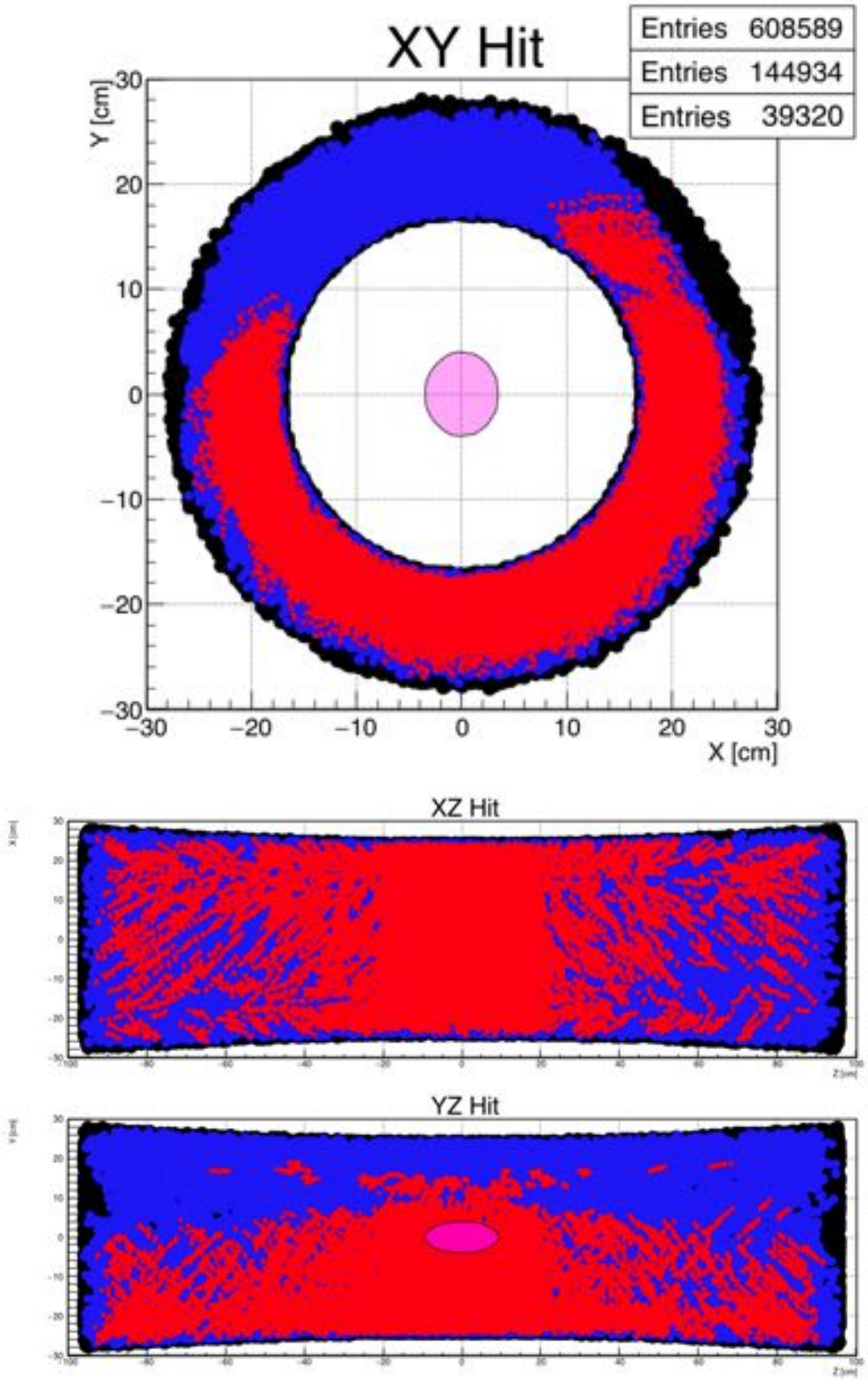

Figure 5.30: Aggregate positions of the hits belonging to the track candidates identified by the Track Finding task, for all 1000 mixed events analyzed (red dots), together with all the reconstructed hits, before the filtering procedure based on the quality cuts (blue dots), and the MC ones (black dots).

The aggregate positions of the hits belonging to the track candidates identified by the Track Finding task, for all the 1000 signal and mixed events analyzed, are shown with the red dots in Figures 5.29 and 5.30 respectively; in the same Figures all the reconstructed hits, before the filtering procedure based on the quality cuts, are shown with blue dots and all the MC hits with black dots. No hits are found out of the CYLDCH geometrical acceptance, as expected. Figures 5.27 (signal events) and 5.28 (mixed events) show the seed momentum p_{seed} (left), as obtained from the procedure described in Section 5.2.3, and the seed positron time t_0 (right), presently taken from the MC hits time, since the Timing Counter information is not yet used. The peaks due to hits belonging to different turns of the e^+ trajectory are clearly visible. All this information is stored into instances of the specific classes `TrackCandidate` and `DCHHit`, as described in Section 5.2.4 and then passed as input to the Track Fitting procedure presented in Chapter 6.

Intrinsic Inefficiency and Execution Time

As discussed in Section 5.3.2, the PR algorithm has an intrinsic inefficiency of $\approx 30\%$ (pure signal events) and of $\approx 50\%$ (mixed events) in associating individual hits to one track segment.

Figure 5.31 is useful to clarify the origin of this intrinsic inefficiency. In the example picture the positions of the hit sense wires at the center of CYLDCH ($z = 0$) are shown on the U-view (black dots) and on the V-view (blue dots). At the center the polyethylene muon stopping target is highlighted. The recontructed hits (red dots) are also shown, together with the MC ones for this particular signal event. When only the sense wires belonging to one view (the V-view in the example) are hit, the track segment is lost since the PR algorithm can not combine the stereo information from adjacent wires planes to reconstruct the hits positions in space. Usually this happens near the acceptance edge of signal positrons and close to the inversion point of the positrons helical trajectories. In fact, when the e^+ track is tangent to a wires plane, then usually only one view is hit and the stereo information can not be used. In this particular case, when the inversion point is within a long e^+ track segment, the PR algorithm can also split the single track segment into two separate track segments, shorter than the original one.

Concerning the PR task execution time, the average values for signal and mixed events are respectively: $T_{PR}^{SIG} \approx 1.3$ s/event and $T_{PR}^{MIX} \approx 1.7$ s/event on a computer running Scientific Linux 6.6 and featuring a 64-bit quad-core AMD Opteron Processor 2356 clocked at 1.15 GHz.

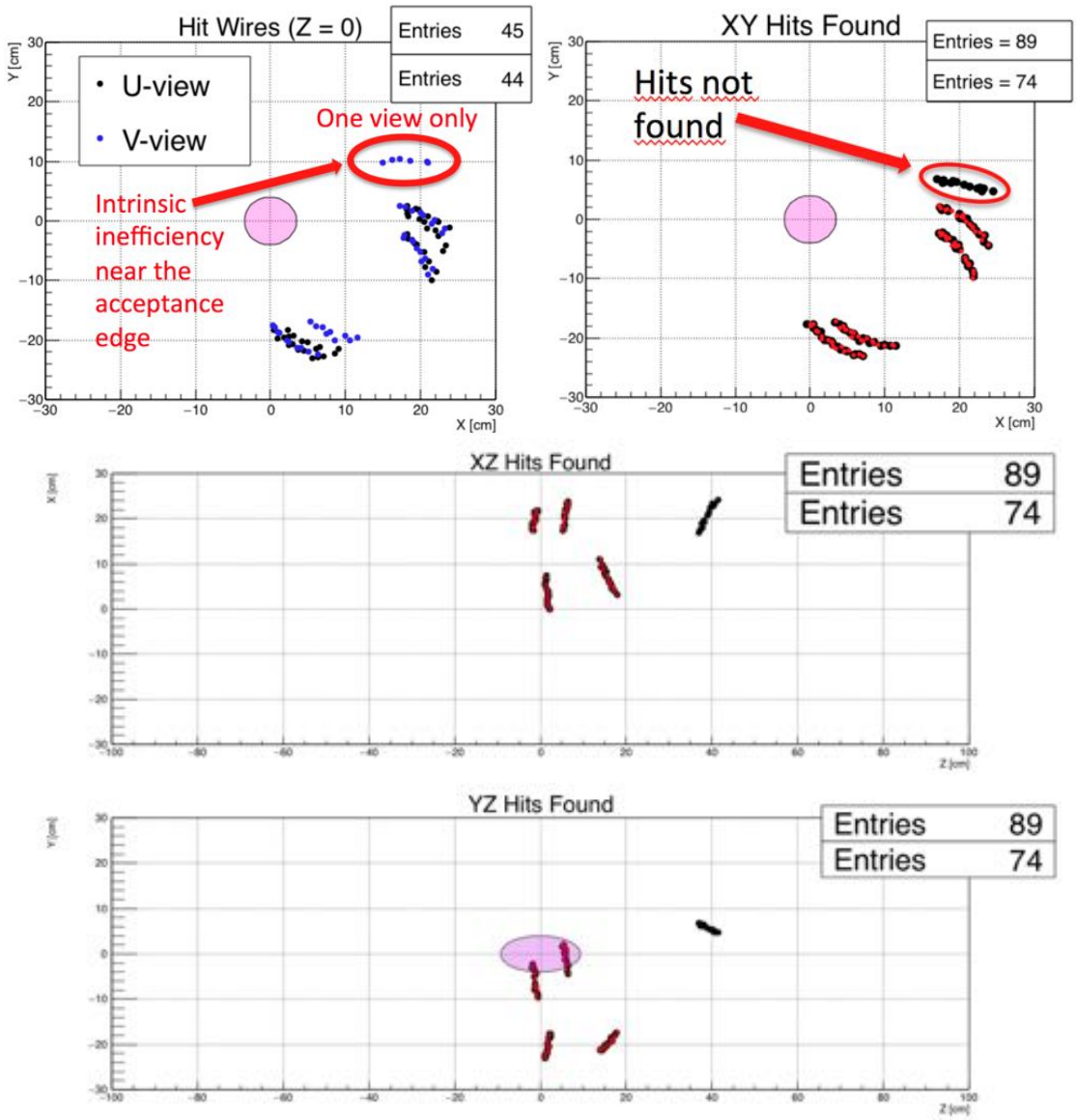

Figure 5.31: Intrinsic inefficiency of the Track Finding algorithm: near the acceptance edge sometimes some track segments are lost since only the sense wires belonging to one view (the V-view in the example) are hit. Hence the PR algorithm can not combine the stereo information from adjacent wires planes to reconstruct the hits positions in space. At the center the polyethylene muon stopping target is highlighted.

The data processing was always performed in interactive mode, which in principle should overestimate the computing time, since input-output operations are more efficiently handled in batch mode. Moreover, the quoted computing time includes the filling of several test histograms which could be switched off when the selection procedures and

cuts will be optimized. Nevertheless, T_{PR}^{SIG} and T_{PR}^{MIX} do not scale with the average number of hits within signal and mixed events: ≈ 90 versus ≈ 600 respectively. This is due to long memory-reset operations of a big number of large-size arrays and folders used by the algorithm. Code optimizations and cleaning are then needed to make the PR task faster and less memory-demanding.

Chapter 6

Track Fitting

Spectrometers in high energy nuclear physics have the purpose of measuring the momentum vector of charged particles deriving from high-energy collisions and decays of particles or nuclei by tracking them in magnetic fields. The hits position along the particle trajectory is determined by ionization detectors, like Drift Chambers (DC), Multi-Wire Proportional Chambers (MWPC) or Time Projection Chambers (TPC). Once the Pattern Recognition algorithm identifies hits belonging to one track, these position measurements serve as input for the fitting algorithm, which determines the best estimates for the particles momentum at any point along their trajectories. Tracks of charged particles in magnetic fields are usually described by five parameters and the corresponding covariance matrix.

The ability to extrapolate a track described by these parameters and their covariances, taking into account the effects of materials and magnetic fields, to different positions in the spectrometer is mandatory for track fitting. The toolkit that will be used for the MEG upgrade is GENFIT, in place of the old one used for the first phase of the MEG experiment, GEANE [13]. GEANE is distributed as part of CERN's Virtual Monte Carlo (VMC) package and is written in FORTRAN; GENFIT is written in C++ and contains a tested Kalman Filter (KF). The Track Fitting algorithm is implemented inside the MEG-II software package (see Section 5.1), encoded into an *analyzer* C++ task called *MEGTDCHKalmanFilterGEN.cpp*. KF is a progressive fitting algorithm and is commonly used for track fitting in particle spectrometers since it has much better performances than global minimization approaches in the presence of materials and inhomogeneous magnetic fields, as that of COBRA.

6.1 GENFIT (a GENeric track-FItting Toolkit)

GENFIT is a novel track fitting toolkit, independent of the specific event topology, detector setup or magnetic field geometry and hence usable in many particle physics experiment. This goal is achieved by combining fitting algorithms, track representations and measurement geometries into a framework with a completely modular design. It is implemented in a C++ library, available as free software in a stand-alone package. GENFIT, originally developed in the framework of the PANDA experiment software [11] [15], was used by other experiments and it is now at its second release (GENFIT2).

GENFIT provides an extensible modular open-source framework that performs track fitting and other related tasks and eliminates the redundancy of writing track fitting programs for every experiment. All particle physics experiments need to identify and classify processes based on detectors signals. Combining these signals to reconstruct particle trajectories is the task called "tracking". Suitable collections of measurements must be combined into track candidates by PR algorithms, and tracks must be fitted. Track Finding and Track Fitting are then not independent. Provided suitable collections of measurements, GENFIT can fit, combine and refine the single measurements, also using information from different subdetectors.

6.1.1 The GENFIT Pillars

The track fitting algorithm operates on the following entities, the three pillars on which GENFIT is based.

Raw Measurements

They contain the *raw measurements* from a detector, i.e. the vectors $\vec{m}_k$ of the reconstructed hits coordinates and the corresponding covariance matrix V_k for the k^{th} hit. In GENFIT the detector measurements are always defined in **detector planes**. These can either be physical or virtual. The situation which is assumed before fitting is that one or several detectors have made measurements of the particle trajectory. The unique *a priori* assumption is that the hits have been sorted by the Pattern Recognition (PR) algorithm before they are provided as input of the fitting procedure.

GENFIT has been designed to overcome the hit dimensionality problems related to the different nature of particle detectors. It comes with predefined measurement classes for various detector types, including silicon strip detectors or Multi-Wire Proporitonal Chamber (MWPC), planar detectors (silicon pixel detectors), Drift Chambers (DC) and

Time Projection Chambers (TPC). In fact the dimensionality of detector hits is not limited. For example, one-dimensional hits constrain the track only along the coordinate axis in the detector plane on which they are measured. Two-dimensional hits are used to constrain the track in two dimensions in their detector planes. In the case of non-planar detector like wire-based Drift Chambers (DC) the tracking information is not delivered in physical detector planes, but the concept of **virtual detector plane** is introduced. The measurement, from now on **wire-measurement**, consists in the drift time relative to a wire position, i.e. a surface of constant drift time around the wire through which the particle passed tangentially. For wire-measurements GENFIT provides functions to construct the so-called virtual detector planes and compute the measurement coordinates and covariance in the coordinate system of that plane. In fact the hit information encoded in the surface of constant drift time is converted into a position measurement in a virtual reference plane, perpendicular to the track, defined by the spanning vectors $\vec{u}$ and $\vec{v}$. The fitting algorithm is then able to perform a χ^2-minimization of the sum of squared orthogonal distances, normalized to the errors, between the track and the detector measurements, i.e. the residuals.

The natural, most general choice for the virtual reference plane is that orthogonal to the track in the Point Of Closest Approach (POCA). For this reason the detector plane for a space-point hit must contain the hit point and the POCA of the track to the hit point (Figure 6.1). GENFIT also allows to compensate for detector deformations, misalignment, wire sag and drift-time corrections.

Track Representation

A charged particle track in a magnetic field is described by a set of track parameters and a corresponding covariance matrix which are defined at a given position along the track. In GENFIT the track parameters are always defined in reference planes (physical or virtual detector planes). After the detector plane k is defined, the reconstructed hits can provide the measurement coordinate vector ($\vec{m}_k$) and the hit covariance matrix (V_k). In order to use a track model in a track fitter one needs to be able to extrapolate the track parameters to different positions in the spectrometer.

GENFIT exploits an extrapolation code based on a Runge-Kutta iterative algorithm from GEANT3. The combination of *track-parameterization* and *track-extrapolation* functionality is called *track representations*. GENFIT has been designed to handle different track models with different propagation mechanisms and parameterizations, even within the same event. The Runge-Kutta track representation folder is called `RKTrackRep`. It

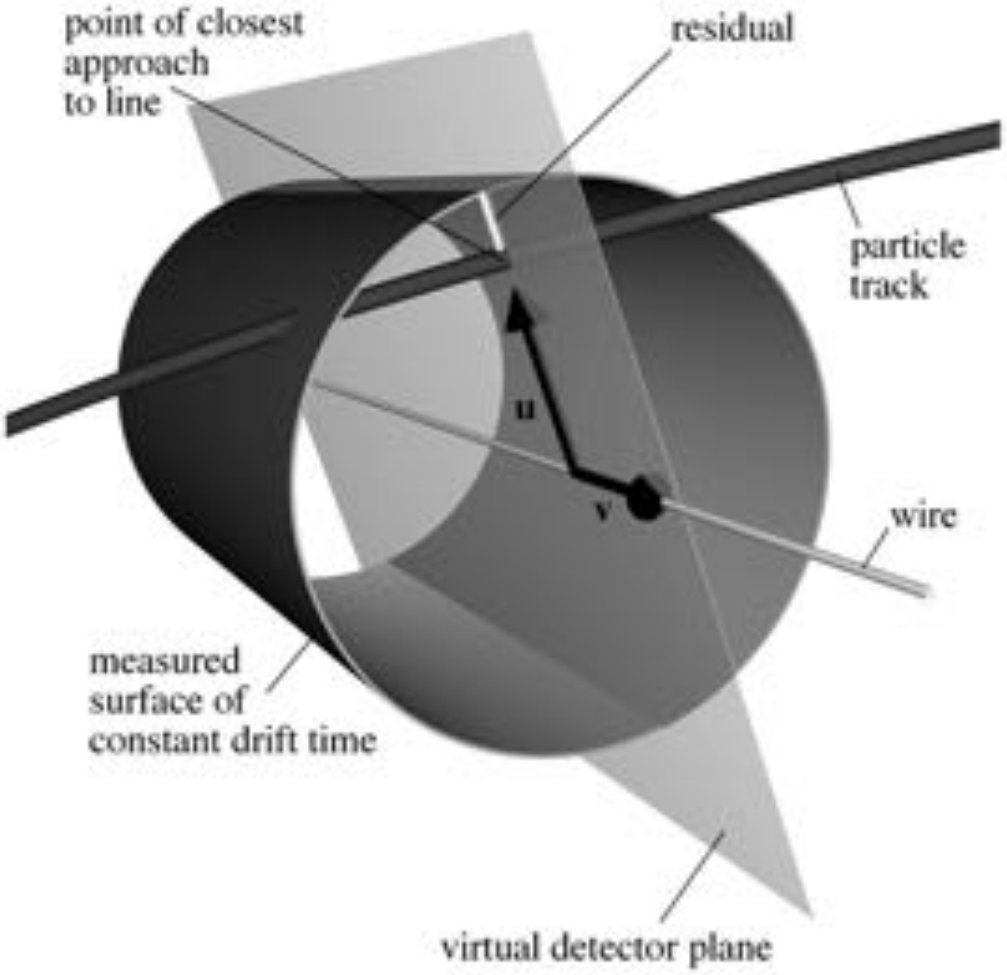

Figure 6.1: The virtual detector plane defined by the spanning vectors $\vec{u}$ and $\vec{v}$) for a wire-based Drift Chamber (DC).

holds the data of the **state vector** for the k^{th} hit ($\vec{x}_k$), together with its covariance matrix (C_k) as well as the reference plane at which these are calculated. In the Kalman Filter (KF) algorithm two important coordinate systems are defined:

- the coordinate system of measurements of a detector ($\vec{m}_k$), which is defined by the two versors ($\hat{u}$ and $\hat{v}$) spanning the individual detector plane. The u and v coordinates defined here must not be confused with the two projective views U and V, parallel to the CYLDCH wires with positive and negative stereo angles respectively (see Chapter 4);

- the coordinate system of state vectors ($\vec{x}_k$), which describe the state of tracks in

a given detector plane. For particle tracking in magnetic fields these are usually 5-dimensional vectors. They hold the charge and magnitude of the 3-momentum of the particle ($q/|\vec{p}|$) and the location and direction of the momentum vector with respect to a detector plane (two coordinates each). The only requirement to the choice of coordinate systems is that there must exist a linear transformation H_k, the so-called *projection matrix*, which transforms state vectors $\vec{x}_k$ into the coordinate system of the detector measurements $\vec{m}_k$, i.e. $\vec{m}_k$ and $H_k\vec{x}_k$ are in the same coordinate system. The projection matrix H_k can be determined once known the coordinate system of the track representation and the reconstruction hit.

An abstract interface class interacts with the detector geometry included via the `TGeo` classes of ROOT. The magnetic field maps are accessed via the interface class called `GFAbsBField`. During the fitting procedure, material properties are used to calculate the following effects: energy loss and energy-loss straggling for charged particles according to the Bethe-Bloch formula, Multiple Coulomb Scattering (MCS) using the Highland formula [24] and soft bremsstrahlung energy loss and energy-loss straggling for e^- and e^+. The step size used for the Runge-Kutta extrapolation should be as large as possible to save unnecessary computation, while still being small enough to keep errors reasonably small. An adaptive step-size calculation is done, taking into account magnetic field inhomogeneities and curvature. In order to calculate material effects correctly, the extrapolation stops at material boundaries and the step size is limited by the maximum allowed relative momentum loss in the material.

The `RKTrackRep` folder provides different methods to find the Point Of Closest Approach (POCA) of the track to non-planar measurements. These are used to construct the aforementioned virtual detector planes. They are calculated dinamically for every extrapolation of a track to a detector hit. In the case of Drift Chambers (DC) the `ExtrapolateToLine` routine finds the POCA of the track to a given line or wire. The corresponding virtual detector plane contains the wire and the POCA and is extended to contain the whole wire, as shown in Figure 6.1. The origin vector of the plane ($\vec{o}$) is set to the hit position and the spanning vectors lie perpendicular ($\hat{u}$) and along ($\hat{v}$) the wire, with the versor perpendicular to the plane ($\hat{w} = \hat{u} \times \hat{v}$) pointing along the momentum vector $\vec{p}$. The wire position and drift time are then measurements of the u coordinate. For CYLDCH the v coordinate is measured via the crossing wires by exploiting the stereo configuration. A consistent help in constraining the v coordinate is given by the difference in the arrival time of signals at both ends of the wire and by charge subdivision which are a measurement of the coordinate along the wire with a resolution of about 10

cm or even better.

The orientation of the plane directly depends on the track parameters, thus the virtual detector planes have to be calculated each time a hit is to be used in a fitting step, i.e. the span vector $\vec{u}$ is chosen dinamically. The intersection of the virtual detector plane and the measurement covariance gives the covariance in that plane through the projection matrix (H_k). The matrix H_k provides the only link between a given track parameterization and the hit coordinate system. For instance, the 3-dimensional hit vector and the 3×3 covariance matrix of a space-point hit are transformed into a 2-dimensional vector and a 2×2 covariance matrix. Even if the errors of the space-point hits were uncorrelated, the matrix V_k will in general contain a correlation which is taken into account in the fit.

Different track representations can be used in parallel by fitting the same track, i.e. the same sets of hits, simultaneously. For instance, different mass hypotheses can be done and via the χ^2 of the fit one can obtain a clue to the particle identity. Again, in the early phase of an experiment one can compare different track representations to identify the one which leads to the best results. If a fit is performed with several track representations the same set of reconstructed hits will provide a different matrix H_k for each track representation.

Fitting Algorithms

The Fitting Algorithms use the raw measurements and the track representations to calculate the fit results. In general the fitting algorithms are iterative procedures, capable to produce an optimal esitmate of a system state (including its covariance) from a series of noisy measurements defined in the corresponding detector planes k (Figure 6.2). Basically the algorithms work in two consecutive steps (Figure 6.3). During the **prediction step** a starting state and its covariance on plane k are extrapolated to the next plane $k+1$ by means of the numerical extrapolation code. It takes into account MCS, energy loss and all the possible physical effects which can affect the charged particle motion through the matter. During the **update step** the information from the predicted state and the current measurement are combined. This is the **filtering procedure** which is nothing but a *weighted mean* between the new measurement x_n and the prediction x_p, taking into account the corresponding errors, respectively σ_n and σ_p. The filtered position x_f can be written as:

$$x_f = \frac{\frac{1}{\sigma_p^2}x_p + \frac{1}{\sigma_n^2}x_n}{\frac{1}{\sigma_p^2} + \frac{1}{\sigma_n^2}} = \frac{\sigma_n^2}{\sigma_p^2 + \sigma_n^2}x_p + \frac{\sigma_p^2}{\sigma_p^2 + \sigma_n^2}x_n \tag{6.1}$$

The fitting procedure can be done in the forward and backward directions. Usually both the forward and backward fit are performed in order to refine the reconstructed track parameters. This double passage is repeated even more than one time, until a convergence criterion is satisfied. The convergence criteria and the hit processing are treated below in deeper details.

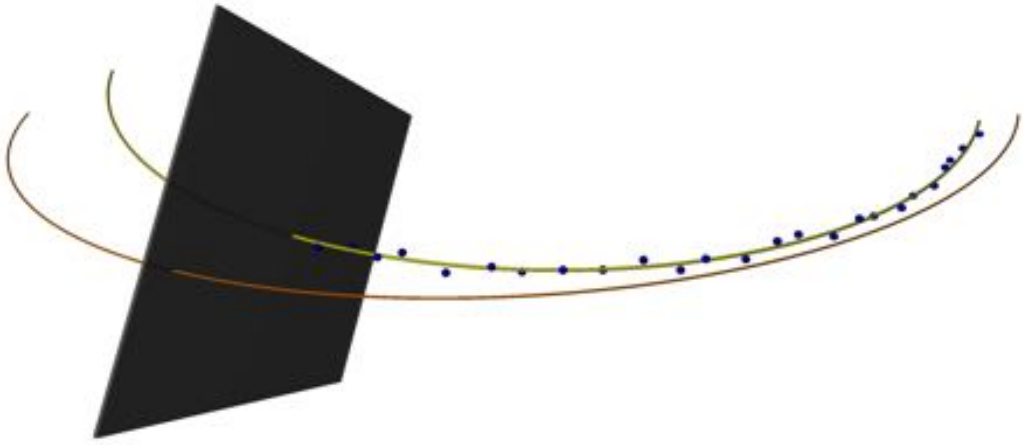

Figure 6.2: Example of track fitting: from a series of noisy measurements (blu points) and a seed value for the track parameters (orange track), the fitting algorithm is able to obtain the best estimate for the track parameters (yellow track).

In GENFIT, four different *track fitting algorithms* are currently implemented: two smoothing Kalman Filters (one which linearizes the transport around the state predictions and one which linearizes it around a reference track); a *Deterministic Annealing Filter* (DAF); a General Broken Lines (GBL) fitter.

Thanks to the modular implementation of GENFIT, the classes which represent the fitting algorithms just carry out their linear algebra without knowing the dimensions of the state vectors $\vec{x}_k$ and the measurement vectors $\vec{m}_k$. The projection matrix H_k is provided by the reconstruction hit class to transform the state vectors and covariance matrices of a specific parameterization into the measurement vector coordinate system. The projection matrix H_k ensures that the dimensionalities of the vectors and matrices in the fitting algorithm are compatible with each other (a practical example is shown

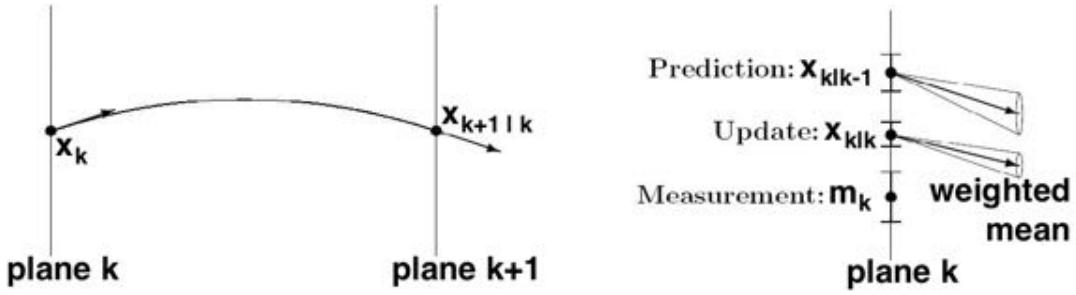

Figure 6.3: Schematic view of the prediction and update steps for every iterations of the track fitting algorithm.

below).

The general structure of objects for track fitting in GENFIT is shown in Figure 6.4. The arrows indicate the interactions between the objects.

6.1.2 Kalman Filter (KF) Input

The reconstructed hits folders are created from the position information acquired in the detectors. The Pattern Recognition (PR) algorithm, which precedes the use of GENFIT, determines which of these detector hits belong to a certain track and fills (see also Section 5.2.4):

- an instance of the track candidate `TrackCand` class which stores the state vectors at the first and last hit positions of the found track. Basically it contains the seed position and the seed momentum vector for the first and last hits within the track candidates provided by the Pattern Recognition (PR) algorithm, plus a dummy initial covariance matrix which will be subsequently initialized by GENFIT with the detector resolutions;

- an instance of the `DCHHit` class which stores the indices k and the measured positions of all the raw detector hits found by the PR to belong to the same track (not only the two initial and final seed hits, but even all the intermediate measurements). The measurements are provided by the PR in the "global" coordinate system of the MEG detector. Moreover additional information is included, as the left-right ambiguity, the drift distance of the charged particle ionizing the CYLDCH gas, the hit position in the "local" coordinate system of each CYLDCH drift cell and the hit wire number corresponding to the current measurement.

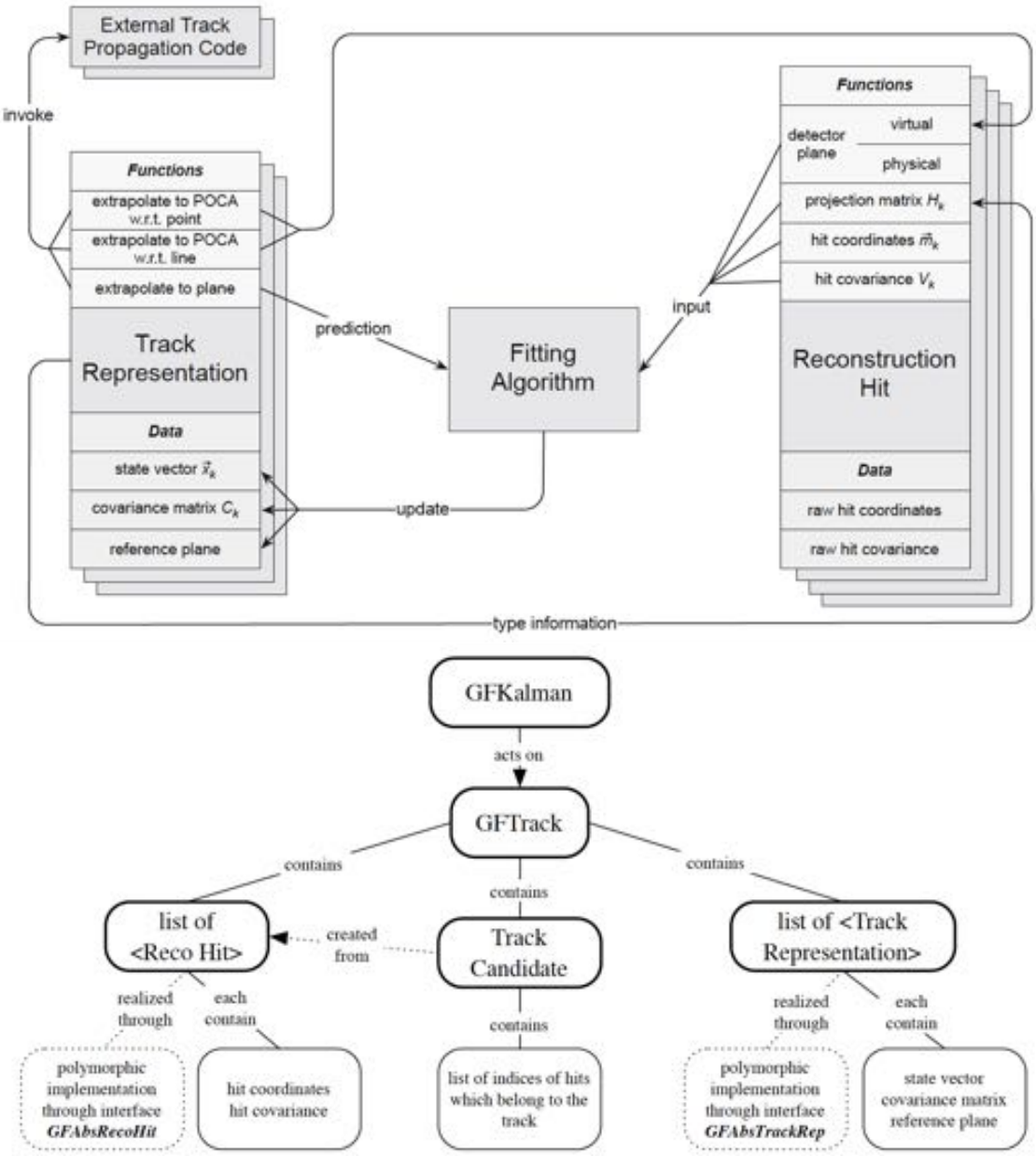

Figure 6.4: General structure of objects for track fitting in GENFIT: Reconstruction Hit (raw measurement), Track Representations and Fitting Algorithms. The arrows indicate the interactions between the objects.

Once filled, the `TrackCand` and `DCHHit` folders serve as helper classes and are provided as input to the Kalman Filter (KF) algorithm. The KF task is capable to build and properly fill an instance of the `Track` class from the two input objects through the GENFIT task `MeasurementFactory`. Afterwards, this `Track` object can be processed by the various fitting algorithms.

All per-track data are stored in the corresponding `Track` object. This can hold a sequence of `TrackPoint` objects, which can contain the measurements, `FitterInfo` objects, which can keep all fitter-specific information and `FitStatus` objects, which can store general information (number of iterations, convergence, etc...) and fit properties (χ^2, NDF, p-value, track length, etc...). Usually only a part of this information needs to be stored on disk. The user can decide which data to keep. A `Track` can contain one or more track representations corresponding to the different particle hypotheses that would be fitted. One of them must be selected as the cardinal track representation. This can be done by the user or by GENFIT which selects the track representation that best fits the measurements, i.e. has the lowest χ^2. GENFIT provides the possibility to store several measurements of the same type in one `TrackPoint` object and there are several ways to handle multiple measurements. For example, in DCs the wire-measurements produce two measurements on the virtual detector plane, which represent the passage of a particle on either side of the wire (left-right ambiguity).

The track fitting algorithm which will be used for MEG-II is the Deterministic Annealing Filter (DAF). The DAF is a robust track fitter and a powerful tool for the rejection of outliers, i.e. measurements distant from the other observations. In this particular type of KF the measurement residuals are used to determine the proper weigths between iterations. The weigths are converted in assignment probabilities for the measurements. The DAF is particularly suitable to resolve the left-right ambiguities of wire-measurements and for this reason it is usually employed for track-fitting in drift chambers: the weighted average of the individual measurements is calculated and the side closest to the algorithm prediction is selected. The weights must be initialized and the basic solution is to give to both left and right measurements the same weight. The wire positions are taken as measurements in the first iteration and their covariance is set to twice the mean of the individual ones. Thus all wire positions have the same covariance, regardless of how far from the actual trajectory. This sistematically false estimate of the covariance seed biases the fit. GENFIT provides a novel technique to initialize the weights that improves the fitting efficiency. Smaller weights are assigned to measurements with larger drift radii. This leads to a larger covariance since the wire position is expected to be farther away from the trajectory. Conversely measurements with smaller drift radii, which are closer

to the track path, get larger weights and accordingly a smaller covariance. After this so-called *annealing scheme*, the fit is considered to have converged if the absolute change of all weights is less than a pre-settable threshold. In any case a maximum number of iterations is set. This number is user-adjustable too.

The start parameters (seed) are extrapolated to all `TrackPoint` objects and at every algorithm iteration the prediction is updated taking into account the measurements and the relative weights (Figure 6.3). A linearization procedure around the predictions can be used. In order to save computing time, if the change is very small the state predictions are not updated.

It is also possible to let the fitter sort the measurements along the track, improving the fitting accuracy. A minimum and maximum number of iterations can be set as convergence criteria. After performing a minimum number of iterations, GENFIT checks if the fit p-value has changed less than a certain amount since the previous iteration. However, with this criterion tracks with a p-value close to zero are often considered as converged even though the χ^2, albeit big, is still changing significantly, indicating that the fit is still improving. In order to cure this issue, a non-convergence criterion has been introduced so that if the relative change in χ^2 from one iteration to the next is larger than an user preset threshold (usually 20%) the fit will continue. In addition to these convergence criteria, the fit is regarded to have converged if none of the prediction states has been updated since the previous iteration.

GENFIT features a sophisticated 3D event display which allows to visualize fitted tracks. Detector geometry, detector planes, measurements and tracks with their covariances, forward and backward fits with predictions and updates can be drawn. Furthermore, GENFIT uses the mechanisms of ROOT to enable the user to save the fit results to files. That is why all data classes in GENFIT are derived from ROOT's `TObject` class. ROOT is in principle capable to persist all C++ STL (Standard Template Library) containers, but nevertheless comes with its own container classes which have certain advantages. For instance, the track representations in the `Track` class are stored in a `TObjArray`.

6.2 The Concept of the Kalman Filter (KF) Algorithm

The basic functionalities required for any procedure of track fitting are the extrapolation of tracks to the position of the hits in the detector and the calculation of the distance between the hits and tracks, i.e. the residuals. If one defines the unknown true state vector $\tilde{x}_k$ of a system from a series of noisy measurements, the Kalman filter is an

efficient recursive regression algorithm that finds the optimum estimate $\vec{x}_k$ together with its corresponding covariance matrix C_k. The state vector contains the track parameters and the index k indicates that the state vector and its covariance matrix are given at the k^{th} hit detector plane. The state vectors $\vec{x}_k$ used with the Runge-Kutta track representation (`RKTrackRep`) have the following structure:

$$\vec{x}_k = \left(\frac{q}{|\vec{p}|}, \frac{du}{dw}, \frac{dv}{dw}, u, v \right)^T \tag{6.2}$$

where q denotes the particle charge, p is the particle momentum and the detector plane is spanned by the versors $\hat{u}$ and $\hat{v}$ defined above, with the normal versor $\hat{w} = \hat{u} \times \hat{v}$ which has the same direction of momentum $\hat{p} = \vec{p}/|\vec{p}|$.

One filter step of the algorithm is defined as the inclusion of the measurement information of one more hit into the state vector. Figure 6.5 should help the understanding of the procedure. Before the recursion step the state vector $\vec{x}_{k-1}$ and its covariance matrix C_{k-1} contain the information of all hits up to the index $k-1$. In the prediction step (red lines and crosses) the state vector and covariance matrix are extrapolated to the detector plane of hit k by the track-following code. The predicted state vector and covariance matrix are denoted by $\vec{x}_{k|k-1}$ and $C_{k|k-1}$ respectively. This latter is the sum of the propagated track covariance matrix and a *noise matrix* which takes into account effects like MCS and energy-loss straggling. Then the algorithm computes the update (green dots) for the state vector and the covariance matrix through the filtering procedure, i.e. a weighted mean (see Equation 6.1) which takes into account the measurement $\vec{m}_k$ (black squares) such that the filtered track comes closer to the measured hit than the predicted one. The final fit is depicted by the magenta trajectory.

The impact of including a new hit on the track direction depends on the relative size of the covariance matrix of the hit and of the track, which is matematically expressed in form of the so-called **Kalman Gain**. The elements of the covariance matrix C_k shrink with the inclusion of more hits, thus reducing the impact of a single hit on the value of the state vector. The hit processing, briefly described above and sketched in Figure 6.5, is presented now in more details (for a more rigorous treatment of the KF mathematics see Appendix B):

1. the new virtual detector plane k is calculated for a non-planar detector as described above;

2. the track is extrapolated to this detector plane in order to obtain the state vector prediction ($\vec{x}_{k|k-1}$) and covariance matrix ($C_{k|k-1}$);

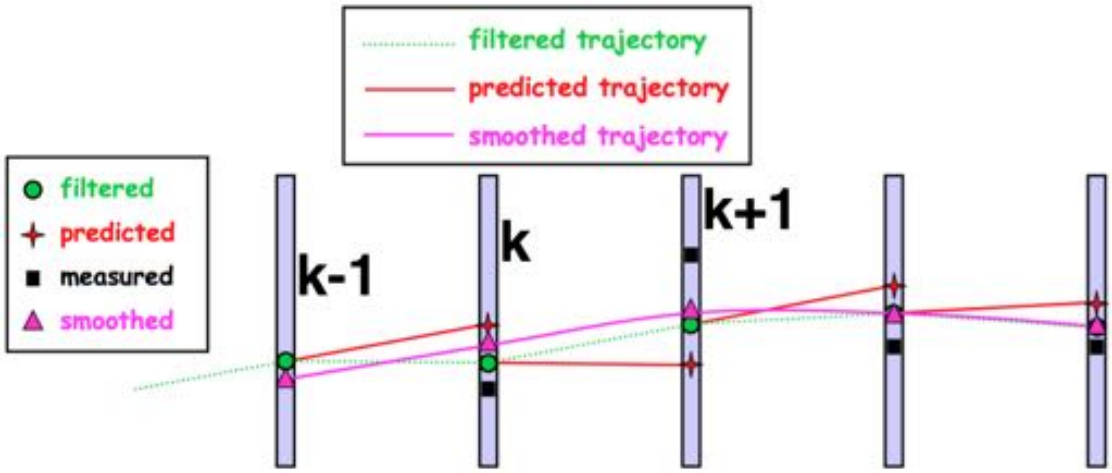

Figure 6.5: Schematic view of the prediction and update steps with the filtering procedure based on the measured positions on the detector planes.

3. the covariance matrix V_k for the measurement $\vec{m}_k$ is acquired by transforming the raw hit covariance information into the specific detector-plane coordinate system. In the case of wire-based DCs the raw hit covariance contains the position resolution and the drift time resolution;

4. the projection matrix H_k (see Section 6.1.1) is obtained. This point is the only place in the full-modular structure of GENFIT where track representations and raw measurements are explicitly synchronized. Each hit class (wire-measurement in case of wire-based DCs) has to define at this point which track representations it supports to ensure the full compatibility between hits and state vectors. This is necessary because the linear transformation matrix H_k depends on the choice of coordinate system for the state vectors and covariance matrices (see the practical example below). This is especially important if two different track representations are used to fit the same track;

5. the weight of the residual or Kalman Gain is calculated:

$$K_k = C_{k|k-1} H_k^T (H_k C_{k|k-1} H_k^T + V_k)^{-1} \tag{6.3}$$

where $(H_k C_{k|k-1} H_k^T + V_k) = R_k$ is the covariance of the residual;

6. the residual vector is calculated:

$$\vec{r}_{k|k-1} = \vec{m}_k - H_k \vec{x}_{k|k-1}; \tag{6.4}$$

7. the reference plane, the state vector and the covariance matrix are updated:

$$\vec{x}_{k|k} = \vec{x}_{k|k-1} + K_k \vec{r}_{k|k-1} \tag{6.5}$$

$$C_{k|k} = (I - K_k H_k) C_{k|k-1} \tag{6.6}$$

   where I is the unit matrix of corresponding size;

8. the χ^2-increment is calculated:

$$\chi^2_k = \vec{r}^T_{k|k} (V_k - H_k C_{k|k} H_k^T)^{-1} \vec{r}_{k|k} \tag{6.7}$$

   with the filtered residual:

$$\vec{r}_{k|k} = \vec{m}_k - H_k \vec{x}_{k|k} \tag{6.8}$$

   which adds $\dim(\vec{m}_k)$ degrees of freedom to the total χ^2.

A Practical Example

As a practical example, one can consider CYLDCH in order to determine the 5-dimensional trajectory model for a charged particle in a magnetic field. The detector measures the u and v coordinates in the virtual detector plane defined by the normal versor $\hat{w} = \hat{u} \times \hat{v}$ and the state vector is $\vec{x}_k = (q/|\vec{p}|, du/dw, dv/dw, u, v)^T$, as described above. In particular the surface of constant drift time is converted into the position measurement u. The v coordinate is measured via the crossing wires by exploiting the CYLDCH stereo configuration with the constraint given by the difference in the arrival time of the signals at both wire ends. The 2×5 projection matrix H_k is then:

$$H_k = \begin{pmatrix} 0 & 0 & 0 & 1 & 0 \\ 0 & 0 & 0 & 0 & 1 \end{pmatrix} \tag{6.9}$$

In this way all matrices and vectors automatically appear with the correct dimensions:

- $\vec{m}_k$ and $\vec{r}_{k|k-1}$ are 2-vectors;
- V_k is a 2×2 matrix;

- the Kalman Gain K_k is a 5×2 matrix;
- χ^2_k is a scalar which is calculated from 2 degrees of freedom: $\vec{r}_{k|k}$ is a 2-vector and $(V_k - H_k C_{k|k} H_k^T)$ is a 2×2 matrix.

After the Kalman steps have been performed in the forward direction on all the hits of the track found by the PR (assuming forward sorting), the fit results can still be biased due to the wrong starting values $\vec{x}_0$. This bias can be reduced by the repeated application of the procedure in the opposite order of hits (backward fit), using the previous fit results as starting values for the track parameters. The track is then defined on the plane of the first hit after one forward-backward fitting iteration. Several of these passages can be performed to further minimize the bias due to the large uncertainties of the track parameter starting values. Before the fit is repeated the covariance matrix must be reset: the diagonal elements are multiplied by a large factor $O(1000)$ and the off-diagonal elements are set to zero, otherwise the magnitude of the track errors would shrink with the inverse square root of the number of fitting passes. In this way the same information in not included in the track several times.

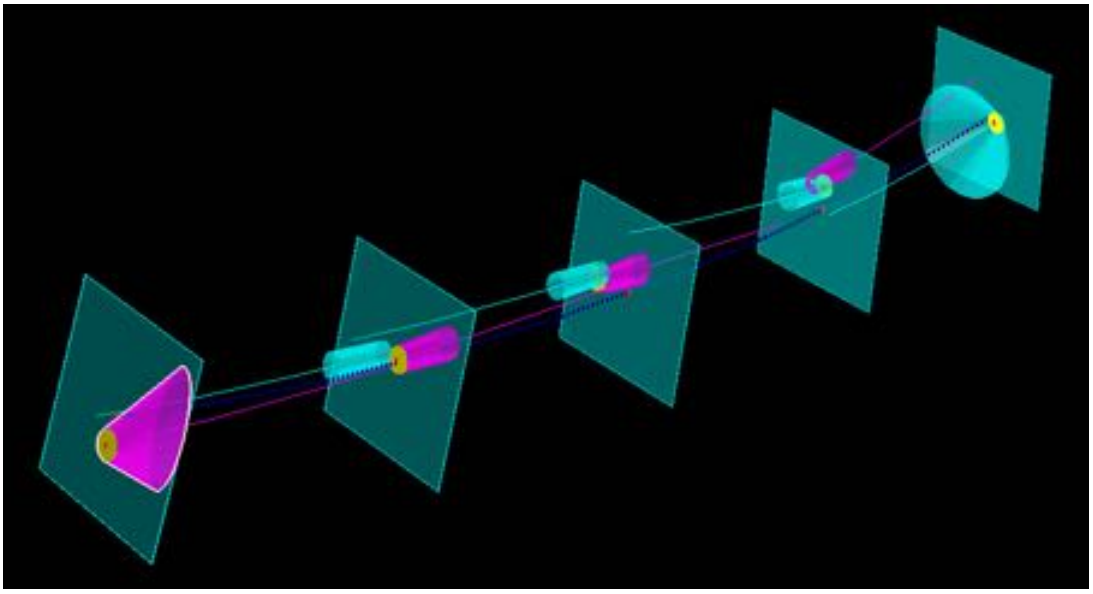

Figure 6.6: Example of a forward-backward fit procedure (see text).

In Figure 6.6 an example of a forward-backward fit procedure is shown. The detector measurements (red dots) are defined in the detector planes (cyan squares) with the corresponding hit covariances (yellow circles). The first and the last hits are respectively on the right and on the left of the picture. The forward fit is shown in cyan, while

the backward one in magenta. The prediction steps are represented with the broken full line from the starting surface to the next. As one can see, the starting point for the next prediction step is not the one obtained from the previous prediction step. In fact, during the update step the information from the predicted state and the current measurement are combined in a weighted mean such that the track comes closer to the hit than the predicted one (filtering procedure, see Figure 6.5). The cones show the evolution of the track covariance during the prediction step. The blue-dotted line which crosses all the detector planes is the final track reconstructed from the fit results after one forward-backward iteration.

6.3 Kalman Filter (KF) Performance

In this Section the results deriving from the Track Fitting procedure by exploiting the KF method are reported. In order to verify the maximum achievable performance of the algorithm, we used pure MC track segments belonging to signal events, directly providing them to the Track Fitting task, without passing through the PR; the distribution of the reconstructed positron momentum is shown in Figure 6.7 and the fit with a gaussian function results in a momentum resolution $\sigma_p^{MC} \approx 74$ keV. The mean of the distribution amounts to 52.82 MeV. Let's then use the candidates identified by the PR within signal events and mixed events respectively. In all the cases 1000 events were processed.

In general, despite the events type, the fitting procedure is performed firstly for all the individual track candidates found by the PR algorithm within the same event. Then the Track Fitting task tries to merge the track segments, even for different turns of the positron helical trajectory through the CYLDCH sensitive volume. The merging is crucial to improve the final fit results. In fact the best accuracy is achieved for merged e^+ tracks, since a large number of hits better constrains the track parameters. Conversely, MCS contribution, together with the energy-loss straggling in long track extrapolations, increases the numerical uncertainties. At the end, the KF algorithm tries to further extrapolate the e^+ flight path firstly to the external surface of the target and then to the target plane. In order to distinguish among the two extrapolations, from now on the first is called "target extrapolation", while the second is called "vertex extrapolation" in the plots. In Figure 6.7, the difference between the true number of generated tracks (1000) and the found ones (1058) is due to the merging inefficiency: $\approx 5\%$. Two track candidates are merged in a single one if the differences between the corresponding state vectors of the extrapolated tracks to the vertex satisfy the following requirements: $|\Delta p| < 5$ MeV, $|\Delta\theta| < 0.2$ rad, $|\Delta\phi| < 0.2$ rad, $|\Delta z| < 10$ cm, $|\Delta r| < 10$ cm and $|\Delta t| < 20$ ns, where p

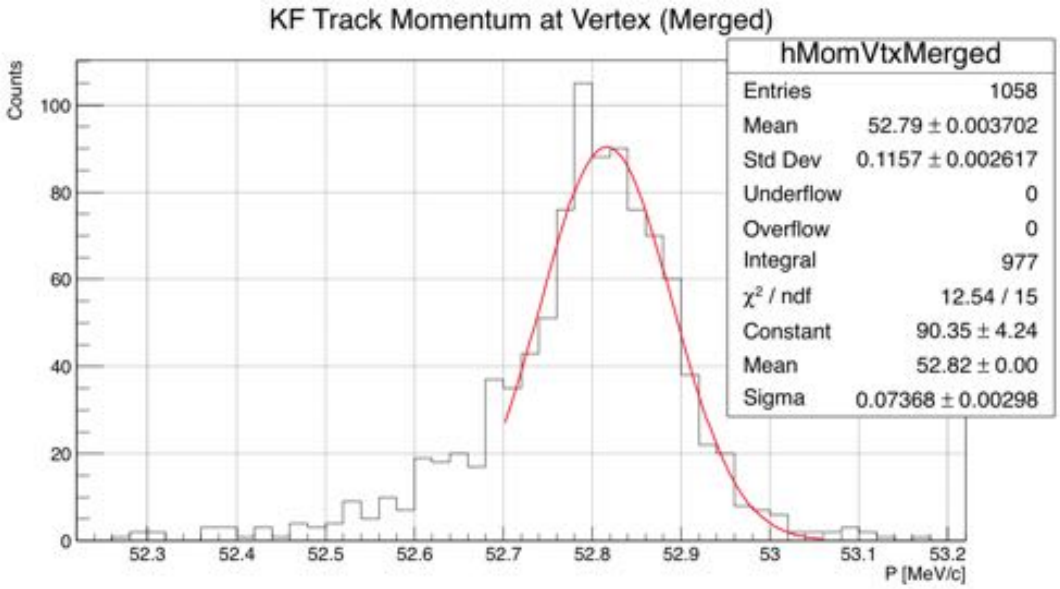

Figure 6.7: Maximum achievable performance of the Track Fitting task: positron momentum resolution on MC track segments directly processed by the KF method.

is the momentum, θ and ϕ are the positron emission angle, z and $r = \sqrt{x^2 + y^2}$ are the longitudinal and radial position at vertex and t is the time associated to the extrapolated e^+ track.

6.3.1 Fitting and Merging Efficiency

The Track Fitting algorithm was capable of fitting all the individual track candidates without failures. This is shown in Figures 6.8 and 6.9 (on the left) for the signal and mixed events respectively (black histograms). The bin 0 of the histogram is filled if a track candidate is not fitted, while the bin 1 if it is successfully fitted. The red histograms show the number of merged track segments. Even in this case the fit has been successful, except in one case in which the KF has failed to fit a merged track for mixed events (Figure 6.9 on the left). For signal events, in theory an ideal merging should result in 1000 final merged tracks, since this is the number of pure signal positron tracks processed. The merging efficiency for signal events amounts to $\approx 77\%$. The number of merged tracks is even lower for mixed events ($\approx 50\%$), thus the merging efficiency needs to be improved.

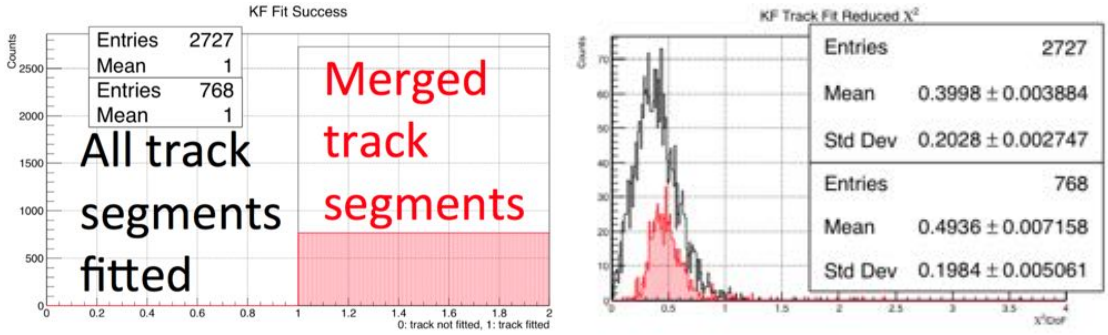

Figure 6.8: On the left: fitting and merging efficiency for track candidates within signal events. On the right: reduced χ^2 distribution, as obtained by the KF fit to the individual tracks candidates (black histogram) and to the merged ones (red histogram) respectively.

Figures 6.8 (signal events) and 6.9 (mixed events) show on the right also the reduced χ^2 distribution, as obtained by the KF fit to the individual tracks candidates (black histograms) and to the merged ones (red histograms) respectively.

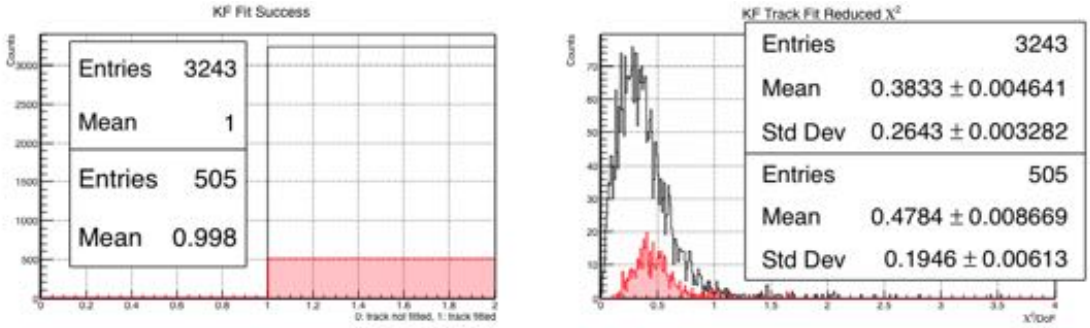

Figure 6.9: On the left: fitting and merging efficiency for track candidates within mixed events. On the right: reduced χ^2 distribution, as obtained by the KF fit to the individual tracks candidates (black histogram) and to the merged ones (red histogram) respectively.

The distribution of the number of tracks survived after the merging procedure is reported, for signal and mixed events respectively, in the top left pictures of Figures 6.10 and 6.11 (red histograms), together with the initial number of individual track segments (black histograms) passed from the PR to the Track Fitting task. The average number of track candidates is similar for signal (≈ 3.2) and mixed (≈ 3.8) events, since the selection cuts applied in the PR task are optimized to search for signal positron track segments, rejecting most of the Michel e^+ background. Therefore an ideal merging procedure should result at the end in one positron track. Nevertheless the merging inefficiency leads to an average of ≈ 2.2 and ≈ 3.2 survived tracks for signal and mixed events respectively.

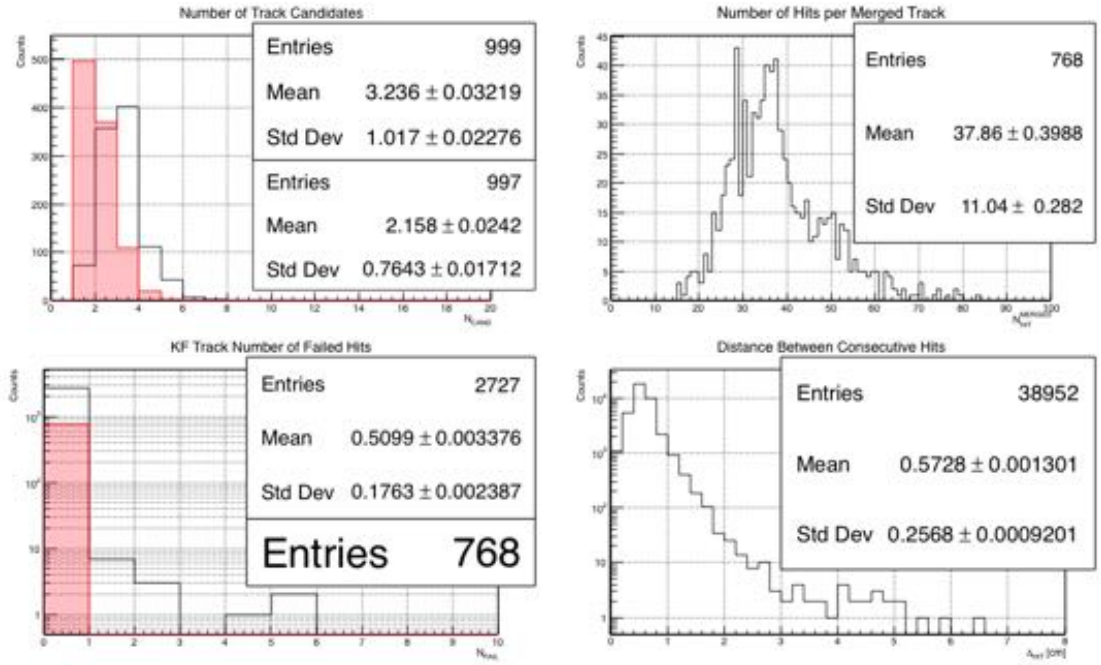

Figure 6.10: Signal events. Top left: distribution of the number of tracks survived after the merging procedure (red histograms), together with the number of track candidates (black histograms) passed from the PR to the Track Fitting task. Top right: distribution of the number of hits per merged tracks. Bottom left: distribution of the number of hits filtered away (rejected) by the KF algorithm for the fit of individual track segments (black histograms) and of merged tracks (red histograms). Bottom right: distribution of the distance between consecutive hits within single track candidates.

The distribution of the number of hits per merged track candidates is shown in the top right picture. The average is ≈ 37.9 and ≈ 29.2 for signal and mixed events respectively, versus mean values of ≈ 15.8 and ≈ 12.6 for single track segments (see Figures 5.22 and 5.23).

In the bottom left pictures of Figures 6.10 and 6.11, the distribution of the number of hits filtered away (rejected) by the KF algorithm is plotted for the fit of the individual track segments (black histograms: the average number of discarded hits for signal and mixed events is ≈ 0.5 and ≈ 0.6 respectively) and for the merged tracks (red histograms: no hits are discarded).

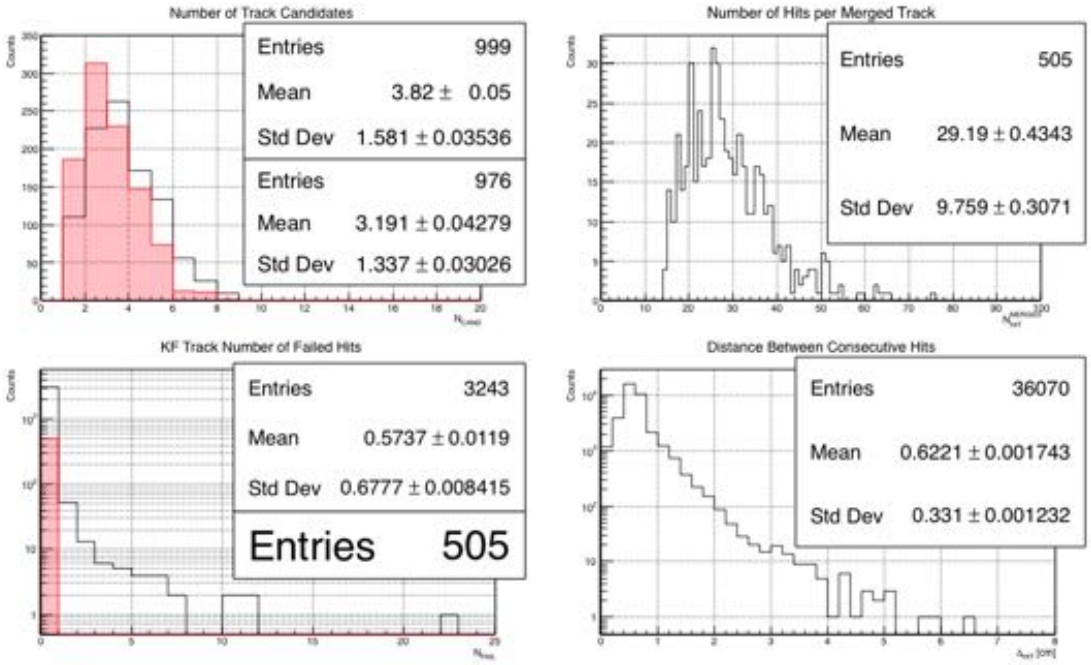

Figure 6.11: Mixed events. Top left: distribution of the number of tracks survived after the merging procedure (red histograms), together with the number of track candidates (black histograms) passed from the PR to the Track Fitting task. Top right: distribution of the number of hits per merged tracks. Bottom left: distribution of the number of hits filtered away (rejected) by the KF algorithm for the fit of individual track segments (black histograms) and of merged tracks (red histograms). Bottom right: distribution of the distance between consecutive hits within single track candidates.

Finally the bottom right pictures of Figures 6.10 and 6.11 show the distribution of the distance between consecutive hits within single track candidates. The average distance amounts to ≈ 6 mm for both signal and mixed events, in agreement with the plots of Figure 5.8. Note the logarithmic scale on the y axis in the bottom plots of Figures 6.10 and 6.11.

The distribution of emission angles θ (left plot) and ϕ (right plot) of the positron reconstructed tracks extrapolated to the target surface are reported in Figures 6.12 and 6.13 for signal and mixed events respectively. As usually, black histograms are for individual track candidates, while the red histograms are for merged tracks. The distributions, apart from some boundary effects, are within the expected acceptance regions (see Section 5.3.1).

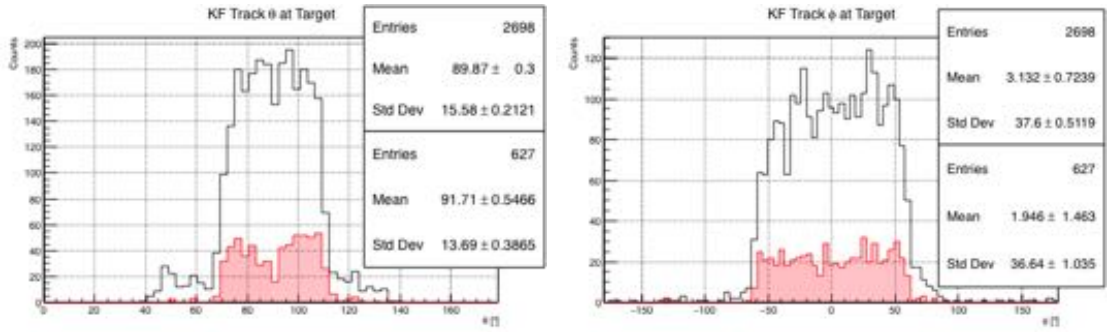

Figure 6.12: Emission angles θ (left plot) and ϕ (right plot) of the positron reconstructed tracks extrapolated to the target surface from the signal events analysis. The black histograms are for individual track candidates, while the red histograms are for merged tracks. The distributions, apart from some boundary effects, are within the expected acceptance regions.

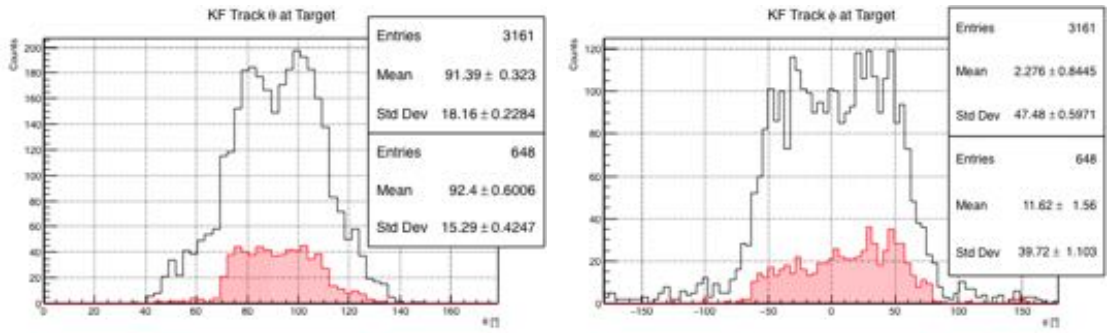

Figure 6.13: Emission angles θ (left plot) and ϕ (right plot) of the positron reconstructed tracks extrapolated to the target surface from the mixed events analysis. The black histograms are for individual track candidates, while the red histograms are for merged tracks. The distributions, apart from some boundary effects, are within the expected acceptance regions.

The extrapolation of the reconstructed positron tracks to the target surface provides the histograms of Figures 6.14 and 6.15, for the signal and mixed events respectively. The plots are done for the transverse plane xy (top) and for the side view yz (mid and bottom). The top left and mid pictures refer to individual track candidates, while the top right and bottom pictures are for merged tracks, where the larger number of hits better constrains the track parameters, reducing the numerical uncertainties. The profile of the target is highlighted with the red ellipses.

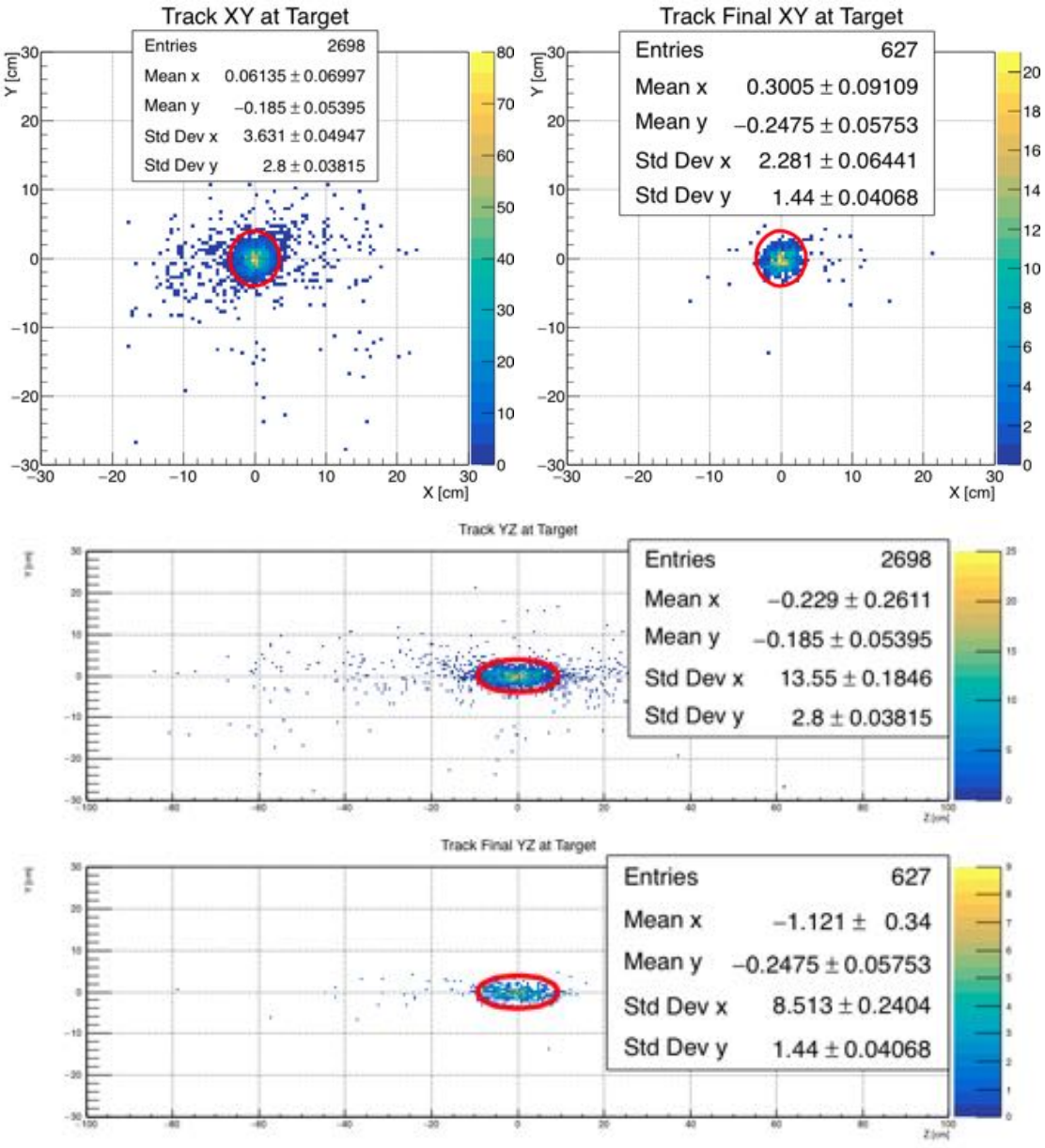

Figure 6.14: Extrapolation of the reconstructed positron tracks to the target surface for signal events. The top left and mid pictures refer to individual track candidates, while the top right and bottom pictures to merged tracks, where the larger number of hits better constrains the track parameters, reducing the numerical uncertainties. The profile of the target is highlighted with the red ellipses.

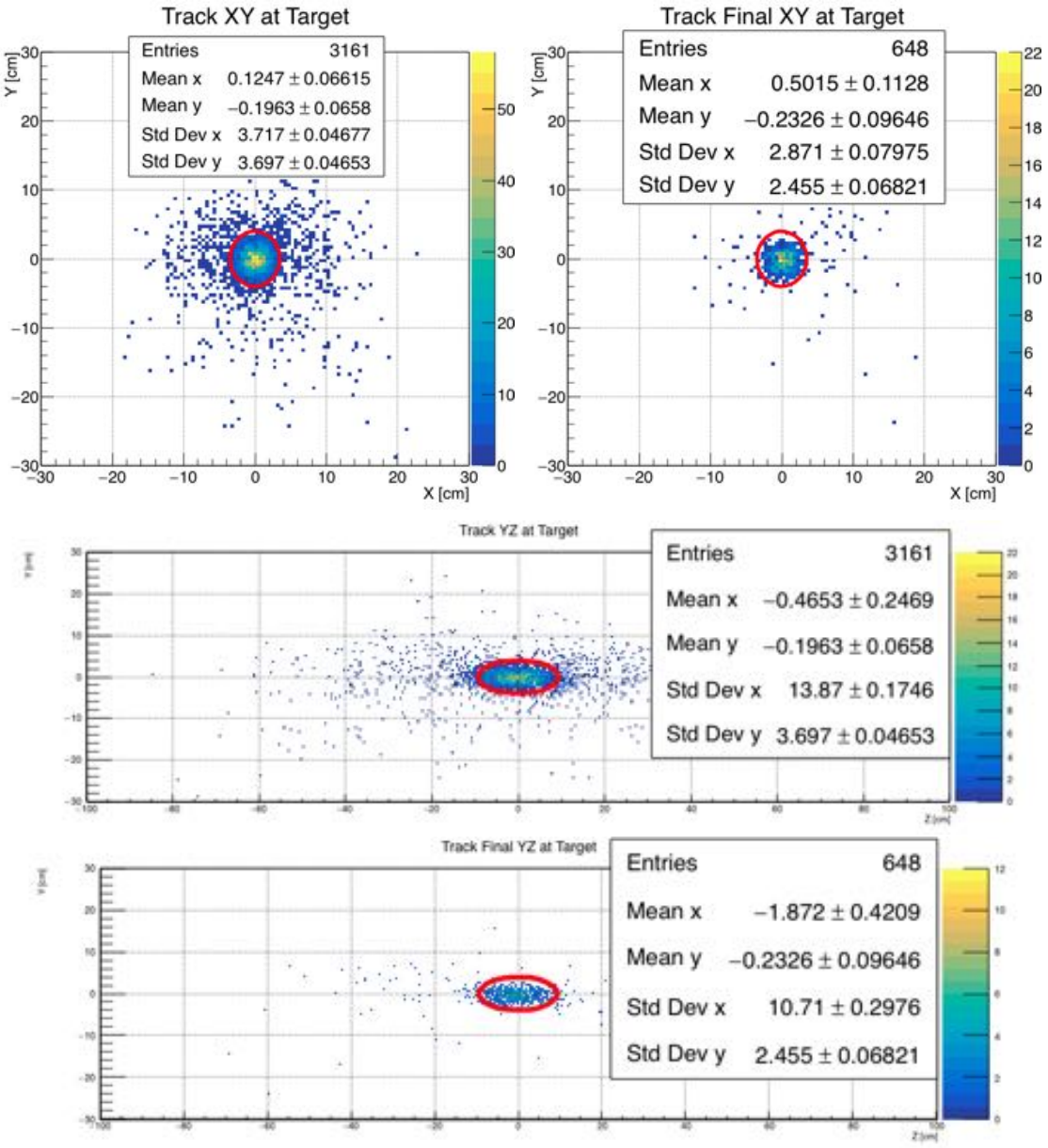

Figure 6.15: Extrapolation of the reconstructed positron tracks to the target surface for mixed events. The top left and mid pictures refer to individual track candidates, while the top right and bottom pictures to merged tracks, where the larger number of hits better constrains the track parameters, reducing the numerical uncertainties. The profile of the target is highlighted with the red ellipses.

6.3.2 Expected Momentum and Angular Resolutions for MEG-II

The results presented in this Section provide an estimate of the momentum and angular resolutions foreseen for MEG-II, by employing the Pattern Recognition (PR) algorithm described in Chapter 5 to provide the input information to the Track Fitting task.

The distributions of the final reconstructed positron momentum are shown in Figures 6.16 and 6.17 for merged tracks, extrapolated to the vertex by the KF algorithm, belonging to signal and mixed events respectively. By performing a fit with a gaussian function, the corresponding widths are $\sigma_p^{SIG} \approx 83$ keV and $\sigma_p^{MIX} \approx 92$ keV, while in both cases the mean amounts to 52.8 MeV. The improvement with respect to the expected value (130 keV, see Table 3.2) resulting from the mixed events analysis, closer to the real DAQ experimental conditions, is $\approx 41\%$ and more than a factor of 4 compared to the momentum resolution obtained in the first phase of the MEG experiment (380 keV, see Table 3.2). Nevertheless further improvements can be done both in the PR (see Section 5.3.2) and in the Track Fitting task, especially in order to improve the track segments merging efficiency and increase the current low statistics.

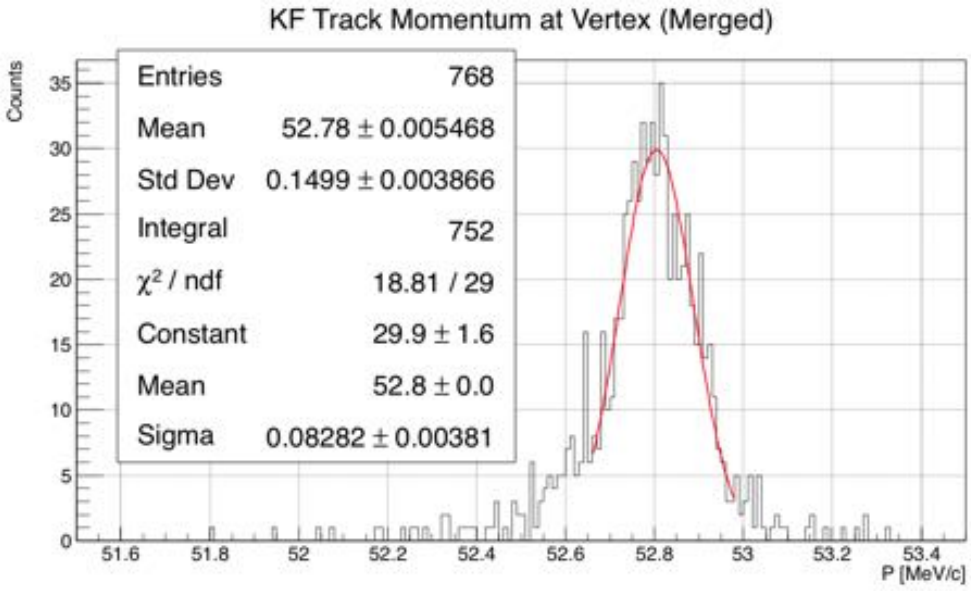

Figure 6.16: Momentum resolution on merged track candidates extrapolated to the vertex (target plane) for signal events.

The θ and ϕ angular resolutions are obtained by comparing the emission angles of the reconstructed positron tracks, extrapolated to the target surface, with the MC emission angles of the generated positrons. No requirements on the reconstructed positron mo-

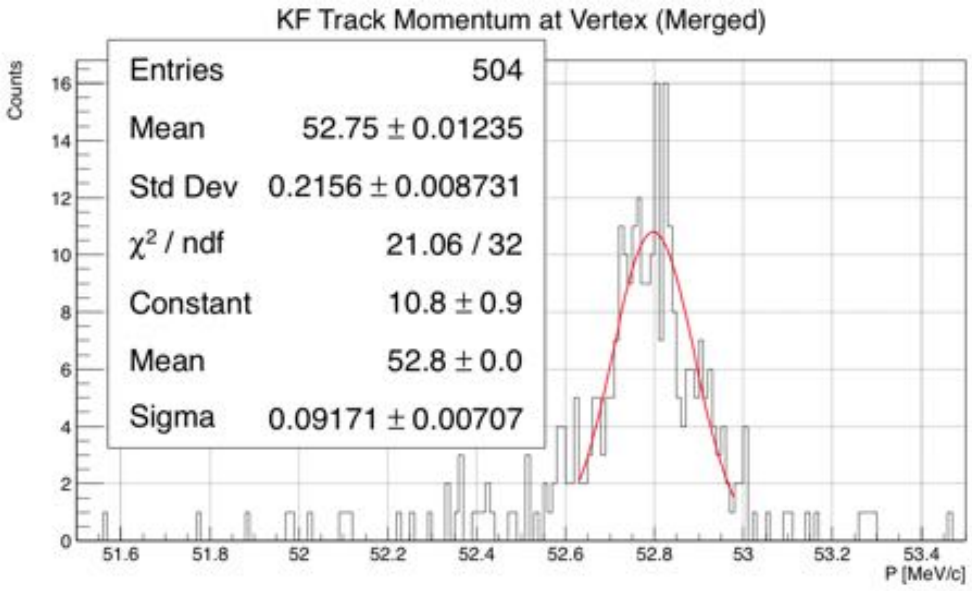

Figure 6.17: Momentum resolution on merged track candidates extrapolated to the vertex (target plane) for mixed events.

mentum are applied. The results are shown in Figures 6.18 and 6.19 for signal and mixed events respectively. The corresponding distributions (top picture for the angle θ and bottom picture for the angle ϕ) are fitted with a gaussian function leading to: $\sigma_\theta^{SIG} \approx 5.4$ mrad, $\sigma_\phi^{SIG} \approx 4.5$ mrad, $\sigma_\theta^{MIX} \approx 6.5$ mrad, $\sigma_\phi^{MIX} \approx 7$ mrad. On the angular side, the resolutions obtained from the pure signal events analysis match the expected values ($\delta\theta_e = 5$ mrad and $\delta\phi_e = 4$ mrad, see Table 3.2). Instead the results stemming from the processed mixed events are worse than those foreseen for MEG-II. Nevertheless both σ_θ^{MIX} and σ_ϕ^{MIX} are significantly better compared to the angular resolutions obtained in the first phase of the MEG experiment ($\delta\theta_e = 9$ mrad and $\delta\phi_e = 11$ mrad, see Table 3.2). The results discussed here are a starting point and future improvements in both the PR and KF will enhance the current reconstructed resolutions and efficiency. We are repeating these studies with enlarged statistics in order to make the results more robust and single out possible critical points of the PR and merging procedures. In particular, different and less demanding merging requirements are under test.

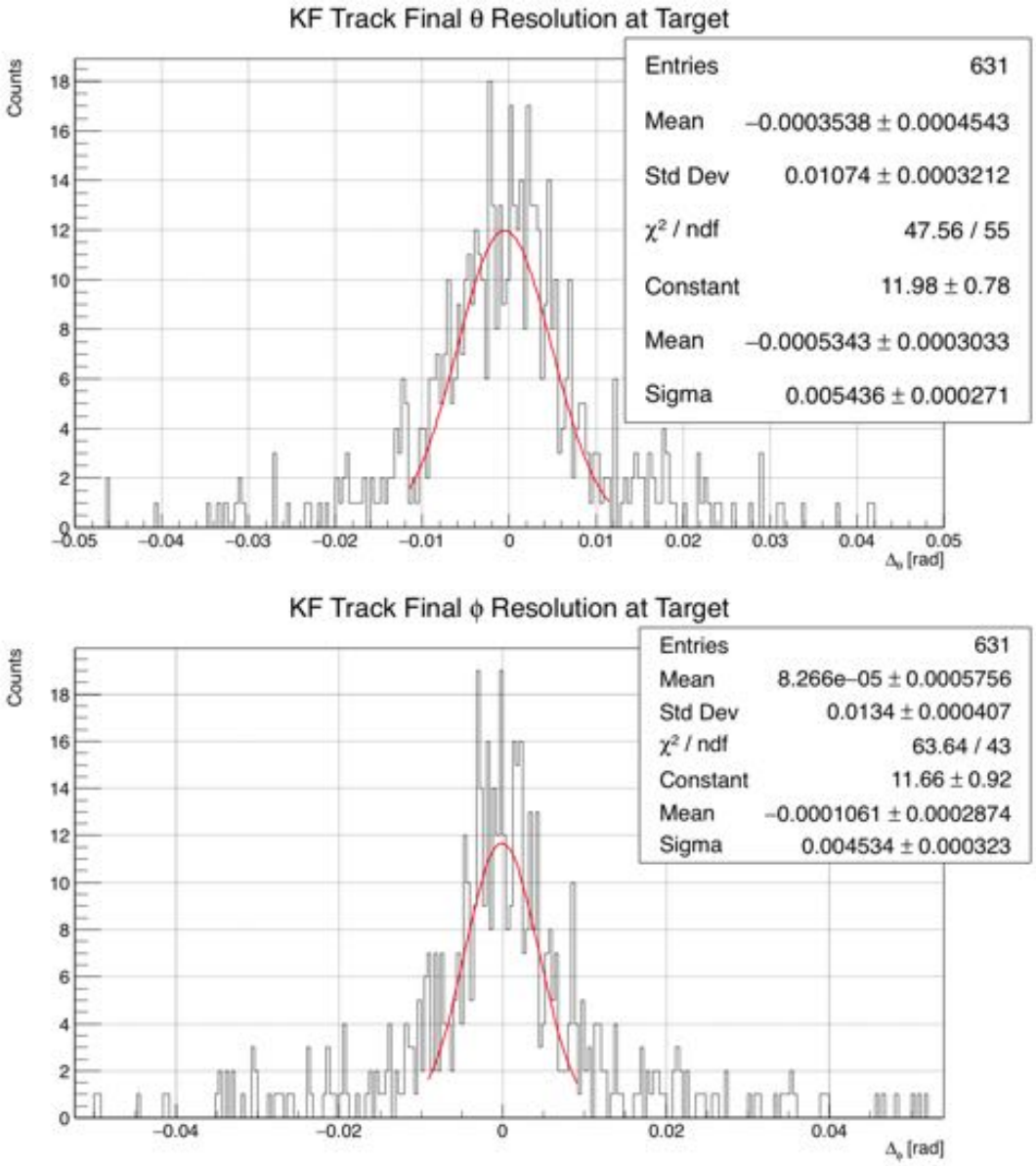

Figure 6.18: Angular resolutions on the emission angles θ and ϕ for merged track candidates extrapolated to the target surface for pure signal events.

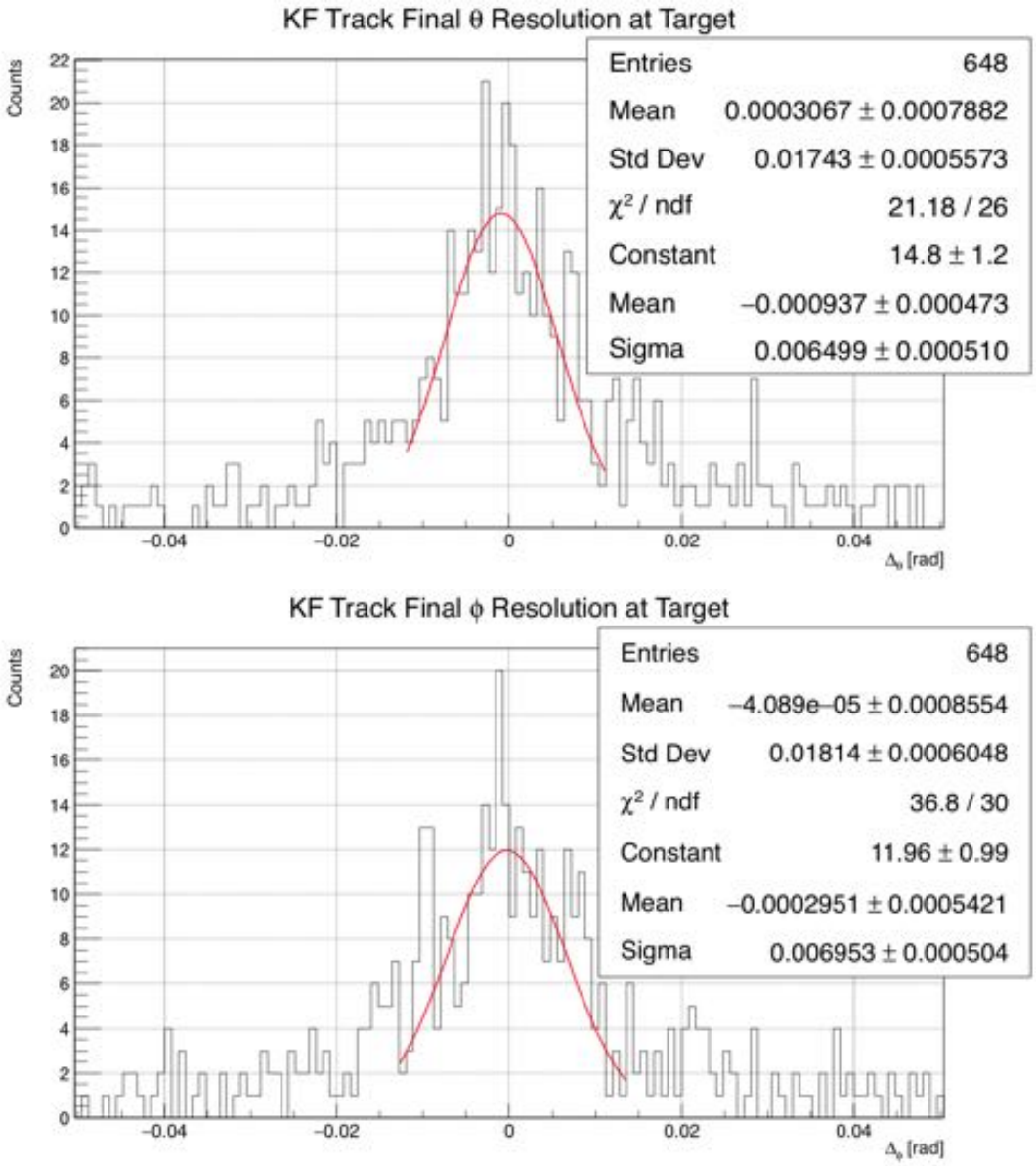

Figure 6.19: Angular resolutions on the emission angles θ and ϕ for merged track candidates extrapolated to the target surface for mixed events.

Chapter 7

Conclusions

The MEG experiment, with its first phase of operations at the Paul Scherrer Institut (PSI), set the most stringent constraint on the Charged Lepton Flavor Violating decay process $\mu^+ \to e^+\gamma$. The analysis of the full data set, corresponding to $\approx 7.5 \times 10^{14}$ muons stopped in the target, collected from 2009 to 2013 at a stopping rate of 3×10^7 μ^+/s, has resulted in the new best upper limit on the BR($\mu^+ \to e^+\gamma$) $\leq 4.2 \times 10^{-13}$ at 90% Confidence Level (C.L.), imposing one of the tightest constraints on models predicting LFV-enhancements through New Physics Beyond the Standard Model.

While the Liquid Xenon calorimeter and the Timing Counter almost met their requirements, on the positron side the performances of the MEG-I Drift Chambers (DC) were significantly worse than the design values, even with performances deterioration over time. An upgrade (MEG-II) of the current experimental apparatus has been approved and is presently under construction, with the aim of reaching a sensitivity enhancement of at least one order of magnitude compared to the final MEG-I result. MEG-II consists in improving the detectors figures of merit and in more than doubling the muon stopping rate.

The new MEG-II CYLindrical Drift CHamber (CYLDCH) is crucial to improve the angular and momentum resolutions on the final state e^+ kinematic variables and thus minimizing the background sources. Great attention has been put on the CYLDCH design aspect to overcome the DCs limitations and ensure the proper operation at high rate with a long-term detector stability. The new drift chamber features a high granularity low-mass single sensitive volume, with a total number of 13056 wires forming 1920 drift cells arranged in a stereo configuration. Nevertheless, the amount of material crossed by the positrons is lower than the MEG-I DCs, thus reducing Multiple Coulomb Scattering and background γ enhancements due to e^+ Annihilation-In-Flight in the CYLDCH ma-

terials. The expected improvements on the positrons momentum and angular resolutions are approximately of a factor three (from ≈ 380 keV down to ≈ 130 keV) and of a factor two (from ≈ 10 mrad down to ≈ 5 mrad) respectively.

The preparation of the new drift chamber involves the common effort of several working groups within the MEG-II collaboration. The assembly is taking place in Pisa and the final delivery at PSI is planned in 2017. Before starting the construction, further improvements, mainly concerning the drift chamber geometry, have been made with respect to the original project, in order to guarantee the best CYLDCH performances. During assembly, problems related to ambient humidity have been encountered, leading to wires breakings. The CYLDCH construction will continue with a strict monitoring of the environmental conditions.

Due to the higher μ stopping rate foreseen during the MEG-II operations and to the CYLDCH high granularity and geometry, a large amount of hits are expected in the new detector. For this reason an efficient Pattern Recognition (PR) and Track Finding algorithm is of primary importance. The CYLDCH performances have been studied by means of simulations of both pure signal events and signal events mixed to the expected background positrons, closer to the real future DAQ experimental conditions. The PR finding efficiency of signal track segments is $\mathrm{PR}_{EFF}^{SIG} = 99.8\%$ and $\mathrm{PR}_{EFF}^{MIX} = 84\%$ for signal and mixed events respectively. The latter value is not so far from the expected 90% efficiency on signal positrons of the new drift chamber. Nevertheless, several further improvements have to be implemented into the PR algorithm, since it is still at an early stage: for instance, an extrapolation procedure based on the first hits in one track segment to get a prediction of the next hit position should be implemented to avoid unnecessary calculation and to reduce the combinatorial background. Moreover, code optimizations and cleaning are needed to make the PR task faster and less memory-demanding.

The achievable positron momentum and angular resolutions have been evaluated too. The track segment information reconstructed by the PR has been passed as input to the Track Fitting task which will be used for MEG-II. This one exploits the GENFIT2 framework which features a Kalman Filter fitting procedure. The algorithm tries to merge the single track segments before performing the final track fit. The results on the e^+ momentum side are: $\sigma_p^{SIG} \approx 83$ keV and $\sigma_p^{MIX} \approx 92$ keV for signal and mixed events respectively. This is a good starting point since the reconstructed values are below the momentum resolution adopted for MEG-II and much better (a factor four) than the MEG-I e^+ momentum resolution. Regarding the resolution on the polar (θ) and azimuthal (ϕ) angles, the results are: $\sigma_\theta^{SIG} \approx 5.4$ mrad, $\sigma_\phi^{SIG} \approx 4.5$ mrad, $\sigma_\theta^{MIX} \approx 6.5$ mrad, $\sigma_\phi^{MIX} \approx 7$ mrad. On the angular side, the resolutions obtained from the pure

signal events analysis match the expected values, while the results stemming from the processed mixed events are a little bit worse than that foreseen for MEG-II. Nevertheless, both σ_{θ}^{MIX} and σ_{ϕ}^{MIX} are significantly better compared to the MEG-I angular resolutions. Further improvements can be done both in the PR and in the Track Fitting task, especially in order to improve the track segments merging efficiency. New selection procedures and cuts are under test and studies with enlarged statistics are ongoing in order to make the results more robust and single out possible critical points.

Appendix A

Wire Displacement

Let's define the coordinates y (downwards) and z (horizontal) in order to derive a formula for the wire displacement. For every wire element with length dz, the weight dw is:

$$dw = dz\rho g\sigma \tag{A.1}$$

where ρ and σ are the density and the cross sectional area of the wire respectively and $g = 981$ cm/s^2 is the gravitational acceleration. The weight must be compensated by the vertical component of the tension at that point which is equal to the difference of the slopes at the two ends of the wire element dz multiplied by the pulling force T:

$$dw = -T[y'(z + dz) - y'(z)] \tag{A.2}$$

In this approximation one assumed that the pulling force is the same for all the z positions, the variation due to the weigth of the wire being negligible for practical cases. Combining the previous equations one obtains:

$$\begin{array}{l} -\frac{[y'(z+dz)-y'(z)]}{dz} = \frac{\rho g\sigma}{T} \\ -y'' = \frac{\rho g\sigma}{T} \end{array} \tag{A.3}$$

The general solution of the differential Equation A.3 is the parabola function A.4:

$$y(z) = \left(\frac{\rho g\sigma}{2T}\right) z^2 + C_1 z + C_2 \tag{A.4}$$

Given the wire length L, the bound condition: $y = 0$ at $z = \pm L/2$, i.e. the wire displacement is null at the wire ends kept at a fixed position, determines the coefficients C_1 and C_2 and the solution becomes:

$$y(z) = \left(\frac{\rho g \sigma}{2T}\right)\left(\frac{L^2}{4} - z^2\right) \tag{A.5}$$

Appendix B

Mathematics of the Kalman Filter

The equations of the Kalman filter (KF) in the so-called **Gain Formalism** are presented below in an easy-to-follow derivation. In Table B.1 the variables used for the calculations are presented.

The Kalman Filter (KF) is a Minimum Square Estimator and its goal is to minimize the expectation value $\mathrm{E}(|\tilde{x}_k - \vec{x}_{k|k}|^2)$. It can be expressed in terms of the covariance matrix $C_{k|k}$:

$$\begin{aligned} C_{k|k} = \mathrm{Cov}(\tilde{x}_k - \vec{x}_{k|k}) = \mathrm{E}([\tilde{x}_k - \vec{x}_{k|k} - \mathrm{E}(\tilde{x}_k - \vec{x}_{k|k})][\tilde{x}_k - \vec{x}_{k|k} - \mathrm{E}(\tilde{x}_k - \vec{x}_{k|k})]^T) = \\ = \mathrm{E}([\tilde{x}_k - \vec{x}_{k|k}][\tilde{x}_k - \vec{x}_{k|k}]^T) \end{aligned} \tag{B.1}$$

where the identity $\mathrm{E}(\tilde{x}_k - \vec{x}_{k|k}) = 0$ is used. This latter holds true if the model for $\tilde{x}_k$ is correct and the starting values $\vec{x}_{0|0}$ are simmetrically distributed around the correct values for the track. For the components one has:

$$C_{k|k,ij} = \mathrm{E}([\tilde{x}_{k,i} - \vec{x}_{k|k,i}][\tilde{x}_{k,j} - \vec{x}_{k|k,j}]) \tag{B.2}$$

Then the minimization acts on:

$$\begin{aligned} \mathrm{E}(|\tilde{x}_k - \vec{x}_{k|k}|^2) = \mathrm{E}(\textstyle\sum_{i=1}^{N}(\tilde{x}_{k,i} - \vec{x}_{k|k,i})^2) = \\ = (\text{the expectation value is a linear operator}) = \\ = \textstyle\sum_{i=1}^{N} \mathrm{E}((\tilde{x}_{k,i} - \vec{x}_{k|k,i})^2) = \sum_{i=1}^{N} C_{k|k,ii} = \mathrm{Tr}(C_{k|k}) \end{aligned} \tag{B.3}$$

The **Kalman Gain** (weight of the residuals) is introduced through the *Kalman gain matrix* K_k with the assumption that the filtered, updated state vector $\vec{x}_{k|k}$ is:

k	Hit index.
$\tilde{x}_k$	Unknown true state vector.
$\vec{\nu}_k$	Noise of the position measurement.
$\vec{m}_k = H_k\tilde{x}_k + \vec{\nu}_k$	Hit coordinate vector.
H_k	**Projection matrix**. It has the dimensions $\dim(m_k) \times \dim(\tilde{x}_k)$ and consists in a linear transformation from the vector space of state vectors to the vector space of detector measurements.
$V_k = \mathrm{Cov}(\vec{\nu}_k)$	Covariance of measurement noise $\vec{\nu}_k$.
$\vec{x}_{k\|k-1}$	**Predicted state vector** at the detector plane of hit k. It contains all information of the hits up to the index $k-1$ and is extrapolated from there.
$C_{k\|k-1} = \mathrm{Cov}(\tilde{x}_k - \vec{x}_{k\|k-1})$	**Predicted covariance matrix**. It contains all information of the hits up to the index $k-1$ and is extrapolated from there.
$\vec{r}_{k\|k-1} = \vec{m}_k - H_k\vec{x}_{k\|k-1}$	Residual vector of the measurement and the extrapolated track.
$R_k = H_kC_{k\|k-1}H_k^T + V_k$	Covariance of the residual (see derivation below).
$K_k = C_{k\|k-1}H_k^T R_k^{-1}$	Optimal **Kalman Gain** or weight of the residuals (see derivation below).
$\vec{x}_{k\|k} = \vec{x}_{k\|k-1} + K_k\vec{r}_{k\|k-1}$	**Updated state vector**.
$C_{k\|k} = (I - K_kH_k)C_{k\|k-1}$	**Updated covariance matrix** with I the identity matrix of corresponding dimensionality (see derivation below).

Table B.1: Variables for the derivation of the KF equations in the *Gain Formalism*.

$$\vec{x}_{k|k} = \vec{x}_{k|k-1} + K_k \vec{r}_{k|k-1} \tag{B.4}$$

Then the covariance matrix is updated:

$$\begin{gathered} C_{k|k} = \mathrm{Cov}(\tilde{x}_k - \vec{x}_{k|k}) = \mathrm{Cov}(\tilde{x}_k - [\vec{x}_{k|k-1} + K_k \vec{r}_{k|k-1}]) = \\ = \mathrm{Cov}(\tilde{x}_k - [\vec{x}_{k|k-1} + K_k \vec{m}_k - H_k \vec{x}_{k|k-1}]) = \\ = \mathrm{Cov}(\tilde{x}_k - [\vec{x}_{k|k-1} + K_k H_k \tilde{x}_k + \vec{\nu}_k - H_k \vec{x}_{k|k-1}]) = \\ = \mathrm{Cov}([\tilde{x}_k - \vec{x}_{k|k-1}] - K_k H_k [\tilde{x}_k - \vec{x}_{k|k-1}] - K_k \vec{\nu}_k) = \\ = \mathrm{Cov}([I - K_k H_k][\tilde{x}_k - \vec{x}_{k|k-1}] - K_k \vec{\nu}_k) \end{gathered} \tag{B.5}$$

In the next step, two rules for calculating vectors ($\vec{x}_k$) covariances are used:

- $\mathrm{Cov}(\vec{x}_1 \pm \vec{x}_2) = \mathrm{Cov}(\vec{x}_1) + \mathrm{Cov}(\vec{x}_2)$ if $\vec{x}_1$ and $\vec{x}_2$ are uncorrelated. Since $\vec{\nu}_k$ is a property of the detector, it is completely uncorrelated and the previous assumption holds.
- $\mathrm{Cov}(A\vec{x}) = A\mathrm{Cov}(\vec{x})A^T$ where A is a matrix.

Then going ahead with the calculation:

$$\begin{gathered} C_{k|k} = \mathrm{Cov}([I - K_k H_k][\tilde{x}_k - \vec{x}_{k|k-1}] - K_k \vec{\nu}_k) = \\ = \mathrm{Cov}([I - K_k H_k][\tilde{x}_k - \vec{x}_{k|k-1}]) + \mathrm{Cov}(K_k \vec{\nu}_k) = \\ = [I - K_k H_k]\mathrm{Cov}(\tilde{x}_k - \vec{x}_{k|k-1})[I - K_k H_k]^T + K_k \mathrm{Cov}(\vec{\nu}_k) K_k^T = \\ = [I - K_k H_k] C_{k|k-1} [I - K_k H_k]^T + K_k V_k K_k^T = \\ = [I - K_k H_k] C_{k|k-1} [I - K_k^T H_k^T] + K_k V_k K_k^T = \\ = C_{k|k-1} - K_k H_k C_{k|k-1} - C_{k|k-1} H_k^T K_k^T + K_k H_k C_{k|k-1} H_k^T K_k^T + K_k V_k K_k^T = \\ = C_{k|k-1} - K_k H_k C_{k|k-1} - C_{k|k-1} H_k^T K_k^T + K_k [H_k C_{k|k-1} H_k^T + V_k] K_k^T = \\ = C_{k|k-1} - K_k H_k C_{k|k-1} - C_{k|k-1} H_k^T K_k^T + K_k R_k K_k^T \end{gathered} \tag{B.6}$$

with the covariance of the residual:

$$R_k = H_k C_{k|k-1} H_k^T + V_k \tag{B.7}$$

This identity can be derived in the following way:

$$\begin{gathered} \mathrm{Cov}(\vec{r}_{k|k-1}) = \mathrm{Cov}(\vec{m}_k - H_k \vec{x}_{k|k-1}) = \mathrm{Cov}(H_k \tilde{x}_k + \vec{\nu}_k - H_k \vec{x}_{k|k-1}) = \\ = \mathrm{Cov}(H_k [\tilde{x}_k - \vec{x}_{k|k-1}] + \vec{\nu}_k) = H_k \mathrm{Cov}(\tilde{x}_k - \vec{x}_{k|k-1}) H_k^T + \mathrm{Cov}(\vec{\nu}_k) = \\ = H_k C_{k|k-1} H_k^T + V_k = R_k \end{gathered} \tag{B.8}$$

The Kalman filter is successful if $\mathrm{Tr}(C_{k|k})$ is minimal:

$$\frac{\partial \mathrm{Tr}(C_{k|k})}{\partial K_k} = 0 \tag{B.9}$$

Following the derivation rules for derivatives of traces of matrices [54] one obtains:

$$\begin{gathered}\frac{\partial \mathrm{Tr}(C_{k|k})}{\partial K_k} = \frac{\partial \mathrm{Tr}(C_{k|k-1} - K_k H_k C_{k|k-1} - C_{k|k-1} H_k^T K_k^T + K_k R_k K_k^T)}{\partial K_k} = \\ = -\frac{\partial \mathrm{Tr}(K_k H_k C_{k|k-1})}{\partial K_k} - \frac{\partial \mathrm{Tr}(C_{k|k-1} H_k^T K_k^T)}{\partial K_k} + \frac{\partial \mathrm{Tr}(K_k R_k K_k^T)}{\partial K_k} = \\ = -C_{k|k-1}^T H_k^T - C_{k|k-1} H_k^T + K_k R_k^T + K_k R_k = \\ = -2C_{k|k-1} H_k^T + 2K_k R_k = 0\end{gathered} \tag{B.10}$$

And finally one obtains the Kalman gain matrix K_k (weight of the residuals):

$$K_k = C_{k|k-1} H_k^T R_k^{-1} \tag{B.11}$$

In fact R_k and $C_{k|k-1}$ are both covariances and hence symmetrical. The last step is the derivation of the simplified form of the updated covariance matrix:

$$\begin{gathered}C_{k|k} = C_{k|k-1} - K_k H_k C_{k|k-1} - C_{k|k-1} H_k^T K_k^T + K_k R_k K_k^T = \\ = C_{k|k-1} - K_k H_k C_{k|k-1} - C_{k|k-1} H_k^T K_k^T + C_{k|k-1} H_k^T R_k^{-1} R_k K_k^T = \\ = C_{k|k-1} - K_k H_k C_{k|k-1}\end{gathered} \tag{B.12}$$

Leading to:

$$C_{k|k} = (I - K_k H_k) C_{k|k-1} \tag{B.13}$$

Ringraziamenti

Innanzitutto un sincero e profondo ringraziamento è rivolto all'intero gruppo MEG di Pisa, perché mi ha dato l'opportunità unica di lavorare alla progettazione, agli algoritmi di Pattern Recognition e direttamente alla costruzione della nuova camera a deriva dell'esperimento MEG-II. L'accoglienza, la disponibilità e la semplicità dimostratami sono stati fin da subito un punto di riferimento e un grande mano nell'inserimento in un gruppo che mi ha insegnato tante cose.

Una menzione particolare meritano i due relatori Alessandro Baldini (anche per il reclutamento) e Fabrizio Cei per la competenza, l'aiuto, la comprensione e la vicinanza in tutte le occasioni. Vorrei ringraziare anche Marco Grassi, che nel frattempo è diventato direttore, vero padre del nuovo rivelatore e poi Donato Nicolò e Giovanni Signorelli per i consigli.

E come non ringraziare i "giovani" di MEG e zone limitrofe, ragazzi eccezionali, che mi hanno accompagnato in questi mesi trascorsi all'INFN: MarcoV (chi è in MEG sa perché devo aggiungere la prima lettera del nome...), Luca e Davide per le chiacchierate, di lavoro e non, e per i caffè offerti.

Ringrazio Fabrizio Raffaelli e i tecnici INFN, Giulio, Sandro, Aldo, Marco, per il lavoro insieme, le chiacchierate, i racconti di un tempo che fu, i pranzi a San Piero con l'indimenticabile "pinolo"...

Ringrazio Giada e "i ragazzi" di Pellizzi, passati e presenti: Hikmat, Mario, Alberto e Stefano.

E poi gli amici della nostra bellissima Siena...Salvo, Simone e Elisa, Ale e Francesca, gli amici dell'AstroStaff e tutti gli altri, di Newcastle e non...basta ho detto tutto.

Un grazie immenso va alla mia famiglia, a Mamma e Babbo, ai Nonni, perché mi hanno permesso di fare tutto questo, perché ci sono sempre e comunque, senza chiedere nulla in cambio. E alla famiglia di Sara: Lucia, Stefano, Viola, Ernesto...persone speciali...grazie!

Sara...beh...le parole non servono, lei sa...grazie.

Bibliography

[1] A. M. Baldini et al. (MEG Collaboration). *MEG Upgrade Proposal*. arXiv:1301.7225 (February 4, 2013).

[2] F. Bedeschi, R. Tenchini, J. Walsh. *What Next: White Paper of CSN1. Proposal for a long term strategy for accelerator based experiments*. Frascati Physics Series (May 29, 2015).

[3] K. G. Wilson. *Non-Lagrangian Models of Current Algebra*. Physical Review, Volume 79, Number 5 (March 25, 1969).

[4] A. J. Buras. *Weak Hamiltonian, CP Violation and Rare Decays*. arXiv:hep-ph/9806471v1 (June 24, 1988).

[5] Y. Kuno, Y. Okada. *Muon Decay and Physics Beyond the Standard Model*. Review of Modern Physics (January 12, 2001).

[6] R. H. Bernstein, P. S. Cooper. *Charged lepton flavor violation: An experimenter's guide*. Physics Reports 532 (2013) 27-64.

[7] A. de Gouvea, P. Vogel. *Lepton flavor and number conservation, and physics beyond the standard model*. Progress in Particle and Nuclear Physics 71 (2013) 75-92.

[8] D. J. H. Chung, L. L. Everett, G. L. Kane, S. F. King, J. Lykken, L. T. Wang. *The soft supersymmetry-breaking Lagrangian: theory and applications*. Physics Reports 407 (2005) 1-203.

[9] G. J. Feldman, D. Cousins. *Unified Approach to the Classical Statistical Analysis of Small Signals*. Physical Review D 57 (1998) 3873.

[10] W. Blum, W. Riegler, L. Rolandi. *Particle Detection with Drift Chambers*. Springer-Verlag Berlin Heidelberg (2008).

[11] C. Höppner, S. Neubert, B. Ketzer, S. Paul. *A novel generic framework for track fitting in complex detector systems*. Nuclear Instruments and Methods in Physics Research A 620 (2010) 518-525.

[12] J. Rauch, T. Schlüter. *GENFIT - a Generic Track-Fitting Toolkit*. arXiv:1410.3698v1 (October 14, 2014).

[13] M. Innocente, V. Mairie, E. Nagy. *GEANE: Average Tracking and Error Propagation Package*. CERN Program Library, W5013-E (1991).

[14] R. E. Kalman. *A New Approach to Linear Filtering and Prediction Problems*. Transactions of the ASME-Journal of Basic Engineering, Series D 82 (1960) 35-45.

[15] PANDA Collaboration. *Technical Progress Report*. Technical report, Facility for Antiproton and Ion Research, Damstadt, Germany (February 2005).

[16] J. Adam et al. (MEG Collaboration). *The MEG detector for $\mu^+ \to e^+\gamma$ decay search*. European Physics Journal C (2013) 73:2365.

[17] J. Adam et al. (MEG Collaboration). *New Constraint on the Existence of the $\mu^+ \to e^+\gamma$ Decay*. Physical Review Letters 110, 201801 (May 13, 2013).

[18] V. Karimäki. *Effective circle fitting for particle trajectories*. Nuclear Instruments and Methods in Physics Research A305 (1991) 187-191.

[19] A. Sharma. *Properties of some gas mixtures used in tracking detectors*. SLAC-J-ICFA-16-3, SLAC-JOURNAL-ICFA-16-3 (July, 1998).

[20] M. Gupta. *Calculation of radiation length in materials*. PH-EP-Tech-Note-2010-013.

[21] M. Chew, J. E. O'Meara, W. Tuzel. *Gravitational wire sag in nonrigid drift chamber structures*. Nuclear Instruments and Methods in Physics Research A 323 (1992) 345-349.

[22] P. Ciambrone et al. *Automated wire tension measurement system for LHCb muon chambers*. Nuclear Instruments and Methods in Physics Research Section A: Accelerators, Spectrometers, Detectors and Associated Equipment 545, Issues 1-2, Pages 156-163 (June 11, 2005).

[23] G. Bowden. *Stretched Wire Mechanics*. SLAC-PUB-11465.

[24] V. L. Highland. *Some practical remarks on multiple scattering*. Nuclear Instruments and Methods 129, Issue 2, Pages 497-499 (November 15, 1975).

[25] G. Flucke, P. Schleper, G. Steinbrück, M. Stoye. *A Study of the Full Scale CMS Tracker Alignment using High Momentum Muons and Cosmics*. CMS NOTE-2008/008 (February 11, 2008).

[26] S. Ritt. *Design and performance of the 6 GHz waveform digitizing chip DRS4*. 2008 IEEE Nuclear Science Symposium Conference Record (October, 2008).

[27] H. Friederich et al. *A scalable DAQ system based on the DRS4 waveform digitizing chip*. Real Time Conference (RT), 2010 17th IEEE-NPSS (May, 2010).

[28] V. Blobel. *Millepede II. Linear Least Squares Fits with a Large Number of Parameters*. Institut für Experimentalphysik, Universität Hamburg (2007).

[29] S. H. Neddermeyer and C. D. Anderson. *Note on the Nature of Cosmic-Ray Particles*. Phys. Rev. 51, 884-886 (May 15, 1937).

[30] M. Conversi, E. Pancini, and O. Piccioni. *On the Disintegration of Negative Mesons*. Phys. Rev. 71, 209 (February 1, 1947).

[31] E. P. Hincks and B. Pontecorvo. *Search for Gamma-Radiation in the 2.2-Microsecond Meson Decay Process*. Phys. Rev. 73, 257 (February 1, 1948).

[32] A. Gando et al. (KamLAND Collaboration). *Constraints on θ_{13} from a three-flavor oscillation analysis of reactor antineutrinos at KamLAND*. Physical Review D 83, 052002 (March 4, 2011).

[33] U. Bellgardt et al. (SINDRUM Collaboration). *Search for the decay $\mu^+ \to e^+e^+e^-$*. Nuclear Physics B 299, Issue 1, Pages 1-6 (March 28, 1988).

[34] W. Bertl et al. (SINDRUM II Collaboration). *A search for μ-e conversion in muonic gold*. European Physics Journal C 47, 337-346 (2006).

[35] M. Ahmed et al. (MEGA collaboration). *Search for the lepton-family-number non-conserving decay $\mu^+ \to e^+\gamma$*. Phys. Rev. D 65, 112002 (June 7, 2002).

[36] A. Ferrari (KLOE collaboration). *The KLOE drift chamber*. Nuclear Instruments and Methods in Physics Research A 494 (2002) 163-172.

[37] Mu3e Collaboration. *Research Proposal for an Experiment to Search for the Decay $\mu \to eee$*. https://www.psi.ch/mu3e/DocumentsEN/ResearchProposal.pdf.

[38] N. Berger (Mu3e Collaboration). *The Mu3e Experiment*. Nuclear Physics B - Proceedings Supplements, Volumes 248-250, Pages 35-40 (March-May, 2014).

[39] R. M. Carey et al. (Mu2e Collaboration). *Proposal to search for $\mu^- N \to e^- N$ with a single event sensitivity below 10^{-16}*. FERMILAB-PROPOSAL-0973 (October 10, 2008).

[40] L. Bartoszek et al. (Mu2e Collaboration). *Mu2e Technical Design Report*. arXiv:1501.05241v2 (October, 2014).

[41] D. Bryman et al. (COMET Collaboration). *An Experimental Search for Lepton Flavor Violating $\mu^- - e^-$ Conversion at Sensitivity of 10^{-16} with a Slow-Extracted Bunched Proton Beam*. http://comet.kek.jp/Documents_files/main-proposal.pdf (November 30, 2007).

[42] Y. G. Cui et al. (COMET Collaboration). *Conceptual Design Report for Experimental Search for Lepton Flavor Violating μ^--e^- Conversion at Sensitivity of 10^{-16} with a Slow-Extracted Bunched Proton Beam (COMET)*. http://comet.kek.jp/Documents_files/comet-cdr-v1.0.pdf (June 23, 2009).

[43] R. Akhmetshin et al. (COMET Collaboration). *Letter of Intent for Phase-I of the COMET Experiment at J-PARC*. http://comet.kek.jp/Documents_files/PhaseI-LoI-draft-v1.1.pdf (March 11, 2012).

[44] R. Akhmetshin et al. (COMET Collaboration). *Experimental Proposal for Phase-I of the COMET Experiment at J-PARC*. http://comet.kek.jp/Documents_files/Phase-I-Proposal-v1.2.pdf (July 12, 2012).

[45] R. Akhmetshin et al. (COMET Collaboration). *COMET Phase-I Technical Design Report*. http://comet.kek.jp/Documents_files/PAC-TDR-2014/PAC-Review-20141110.pdf (September, 2014).

[46] G. Cvetič et al. *Muonium-antimuonium conversion in models with heavy neutrinos*. arXiv:hep-ph/0504126v2 (April 19, 2005).

[47] L. Willmann et al. *New Bounds from Searching for Muonium to Antimuonium Conversion*. arXiv:hep-ex/9807011v1 (July 10, 1998).

[48] R. Abela et al. *Improved Upper Limit on Muonium to Antimuonium Conversion*. Physical Review Letters, Volume 77, Number 10 (September 2, 1996).

[49] SuperKEKB website: http://www-superkekb.kek.jp.

[50] M. De Gerone et al. *Design and test of an extremely high resolution Timing Counter for the MEG II experiment: preliminary results.* Journal of Instrumentation, Volume 9 (February, 2014).

[51] T. Mori. *Les Rencontres de Physique de la Vallée d'Aoste. Results and Perspectives in Particle Physics.* https://agenda.infn.it/conferenceDisplay.py?confId=10549 (March 8, 2016).

[52] A. M. Baldini et al. (MEG collaboration). *Search for the Lepton Flavour Violating Decay $\mu^+ \to e^+\gamma$ with the Full Dataset of the MEG Experiment.* arXiv:1605.05081v2 (May 18, 2016).

[53] A. M. Baldini et al. *Single-hit resolution measurement with MEG II drift chamber prototypes.* arXiv:1605.07970v1 (May 25, 2016).

[54] K. B. Petersen, M. S. Pedersen. *The Matrix Cookbook.* http://matrixcookbook.com (November 15, 2012).

[55] Particle Data Group website: http://pdg.lbl.gov.

[56] H. A. Bethe. *Molière's Theory of Multiple Scattering.* Phys. Rev. 89, 1256 (March 15, 1953).

[57] L. Michel. *Energy Spectrum of Secondary Electrons from μ-Meson Decay.* Nature, Volume 163, Issue 4155, pages 959-960 (1949).

[58] L. Malter. *Thin Film Field Emission.* Phys. Rev. 50, 48 (July 1, 1936).

[59] F. Cei et al. *The architecture of MEG simulation and analysis software.* Eur. Phys. J. Plus (2011) 126:60.

[60] Garfield++ website: http://garfieldpp.web.cern.ch/garfieldpp/.

[61] Geant4 website: https://geant4.web.cern.ch/geant4/.